NANOCOMPOSITE CATALYTIC MATERIALS FOR CLEAN ENERGY PROCESSES

by

Thomas James Sanders

B. S. in Chemical Engineering, Wayne State University, 2003

Submitted to the Graduate Faculty of

the Swanson School of Engineering in partial fulfillment

of the requirements for the degree of

Doctor of Philosophy

University of Pittsburgh

2008

UNIVERSITY OF PITTSBURGH

SWANSON SCHOOL OF ENGINEERING

This dissertation was presented

by

Thomas James Sanders

It was defended on

April 25th, 2008

and approved by

Robert M. Enick, PhD, Professor, Chemical and Petroleum Engineering Department

Steven R. Little, PhD, Professor, Chemical and Petroleum Engineering Department

James Miller, PhD, Professor, Chemical Engineering Department, Carnegie Mellon University

Dissertation Director: Götz Veser, PhD, Professor, Chemical and Petroleum Engineering Department

NANOCOMPOSITE CATALYTIC MATERIALS FOR CLEAN ENERGY PROCESSES

Thomas James Sanders, Ph.D

University of Pittsburgh, 2008

Nanomaterials have gained much attention as catalysts since the discovery of exceptional CO oxidation activity of nanoscale gold by Haruta. However, many studies avoid testing nanomaterials at the high-temperatures relevant to reactions of interest for the production of clean energy (T > 700°C). The generally poor thermal stability of catalytically active noble metals has thus far prevented significant progress in this area.

We have recently overcome the poor thermal stability of nanoparticles by synthesizing a platinum barium-hexaaluminate (Pt-BHA) nanocomposite which combines the high activity of noble metal nanoparticles with the thermal stability of hexaaluminates. This Pt-BHA nanocomposite demonstrates excellent activity, selectivity, and long-term stability in CPOM.

Pt-BHA is anchored onto a variety of support structures in order to improve the accessibility, safety, and reactivity of the nanocatalyst. Silica felts prove to be particularly amenable to this supporting procedure, with the resulting supported nanocatalyst proving to be as active and stable for CPOM as its unsupported counterpart.

Various pre-treatment conditions are evaluated to determine their effectiveness in removing residual surfactant from the active nanoscale platinum particles. The size of these particles is measured across a wide temperature range, and the resulting "plateau" of stability from 600-900°C can be linked to a particle caging effect due to the structure of the supporting ceramic framework. The nanocomposites are used to catalyze the combustion of a dilute

methane stream, and the results indicate enhanced activity for both Pt-BHA as well as ceria-doped BHA, as well as an absence of internal mass transfer limitations at the conditions tested. In water-gas shift reaction, nanocomposite Pt-BHA shows stability during prolonged WGS reaction and no signs of deactivation during start-up/shut-down of the reactor.

The chemical and thermal stability, low molecular weight, and wealth of literature on the formation of mesoporous silica materials motivated investigations of nanocomposite silica catalysts. High surface area silicas are synthesized via sol-gel methods, and the addition of metal-salts lead to the formation of stable nanocomposite Ni- and Fe- silicates.

The results of these investigations have increased the fundamental understanding and improved the applicability of nanocatalysts for clean energy applications.

TABLE OF CONTENTS

LIST OF TABLES

LIST OF FIGURES

ACKNOWLEDGMENTS

Thank you Götz for all of the helpful advice, the thoughtful discussions, and the beneficial guidance. It has been my pleasure to grow and learn in your research group.

Thank you lab mates, especially Sudipta, Tengfei, Vanessa, Anthony, Michael, Rahul, and Yi, for the discussions we had and the experiences we shared. I will never forget my experiences at Pitt because of you.

Thank you to the numerous undergraduates I had the pleasure to mentor during my studies, especially Phae, Wyatt and Peter. Your hard work was a great help and you have taught me to be a more patient tutor.

Thank you to the staff of the Chemical Engineering and Mechanical Engineering and Materials Science departments at Pitt, especially Al Stewart, Cole Van Ormer and Andi Kulovits. The technical training I received and useful discussions we shared were a great benefit.

Thank you to the Department of Energy Hydrogen Fuels Initiative and the National Science Foundation for funding.

Thank you to my friends and family, especially Mom, Dad, Brian, and most of all Lori. The fun times, love, and support has made the time fly. You have enriched my life and supported me through good times and bad. I couldn't have done it without you.

1.0 INTRODUCTION

It has been well established that the world is facing an energy challenge of staggering proportions as we move through the 21st century. Numerous studies have indicated that petroleum production has peaked or is in the process of peaking[1, 2]. Near the end of 2007 the price of crude oil reached an inflation-adjusted record high of $100 per barrel. The growing concern about fossil fuel supply is coupled with concern about global warming due to anthropomorphic CO_2 emissions. The Intergovernmental Panel on Climate Change has stated that there is unequivocal evidence that global warming is occurring and that it is very likely due to human based sources of green house gases[3]. These issues are exacerbated by the tremendous economic growth (and correspondingly tremendous growth in energy demand) in developing countries such as China and India. It has become clear that fundamentally different methods of energy production need to be developed in order face these difficult challenges.

Catalysis can play a major role in reducing the demand for fossil resources and transitioning toward a sustainable energy future. Moving toward more selective catalytic reactions has the ability to reduce energy demand for many traditional energy production reactions. Catalytic reactions also reduce the formation of unwanted byproducts, thus eliminating the need for energy intensive separation and/or further reaction steps. Anastas and Warner list the use of catalytic systems as one of their 12 principles of green chemistry, the goal of which is the reduction/elimination of hazardous substances in the design of chemical

processes[4]. In order to unlock the potential of catalysis, more research is needed into the rational design of catalysts, especially at the atomic scale.

The field of nanoscience has opened up new areas of interest for the construction of interesting and novel catalytic systems. Nanoscale materials make ideal catalytic materials in many ways. Because of their small size, they inherently have increased surface areas, which is of obvious importance in catalysis. In parallel to that, nanomaterials contain a larger fraction of the active metal on their surface, thus better utilizing the (often expensive) active component. Haruta and coworkers were the first to show that nanomaterials can exhibit novel activity over their (inert) macroscale equivalents. They studied gold nanoparticles in CO oxidation reaction[5]. While bulk gold has long been known to be inert, Haruta's nano-sized (~3nm) gold was an excellent catalyst for this reaction. Follow-up studies have posited a number of reason for the novel activity exhibited by nanomaterials – from quantum size effects[6], support interactions[7], and an increased fraction of edge and defects[8, 9]. This work inspired much of the current interest in nanocatalysts. Yet nanomaterials are challenging systems to apply in industrial practice at high temperatures – poor thermal stability of the delicate structure leads to rapid sintering. Additionally, modern nanoscale fabrication techniques have become increasingly sophisticated in recent years. The tools of nanoscience now allow for the fabrication of a wide variety of structures of various chemical compositions. The use of these nanoscale techniques for the formulation of new and interesting structures has outpaced our ability to characterize these structures and to apply them in industrially relevant applications.

Therefore, there is a great opportunity in applied research of nanoscale catalytic materials, which will be explored in this thesis. Previous work in our group has demonstrated the synthesis of thermally stable nanocomposite Pt-barium hexaaluminate (BHA) catalysts and

their long term stability in catalytic partial oxidation of methane[10-14]. In this work this class of nanocomposites is explored further. Notably, detailed investigations are presented regarding the origin of the tremendous thermal stability of platinum particles within the Pt-BHA catalyst.

We seek to fundamentally understand science behind the synthesis techniques used and how we can manipulate the synthesis in a rational manner to induce changes in the final product. To this end, the tailoring of the nanocomposite structure is explored via varying the experimental parameters of the synthesis, by changing the chemical precursors used, and by changing the post-synthesis parameters. In particular, the synthesis of nanoscale silica is examined.

Nanomaterials are often problematic to employ in industrial practice. The fine powder form in which nanomaterials are typically synthesized create concerns regarding pressure drop, flow maldistribution, and fluid by-pass, as well as health and environmental concerns due to particle handling and possible particle entrainment. However, conventional procedures such as pelletizing, for example, typically result in compacting or collapsing of the catalyst structure. For these reasons, we have explored supporting the nanocomposite powder on various structured support materials in order to make them more amenable to industrial application.

To-date our work has focused on the partial oxidation of methane reaction as a test reaction for thermally stabilized Pt-BHA nanocomposites. However, the high activity and stability of these materials is desirable in other reactions as well. The flexibility of the nanocomposite is therefore explored by testing in reaction systems of interest for energy production. Nanocomposite catalysts are tested in both catalytic methane combustion, an important reaction for clean-up of lean fuel mixtures, and water-gas shift, an important reaction for increasing the H_2/CO ratio in synthesis gas mixtures.

1.1 THE FUTURE OF ENERGY PRODUCTION

The past two centuries have seen a transition from solid fuels like wood and coal, to liquid fuels such as petroleum. Today approximately 90% of U.S. vehicular fuel needs are met by petroleum[15]. This transition was motivated by the large energy density of petroleum when compared to previously available energy sources, which made it economical and practical for use as a transportation fuel. Unfortunately, it is well known that petroleum is a finite resource that is rapidly being depleted[1, 2]. As naturally-occurring petroleum reserves are consumed, there has been increasing demand for other energy sources such as natural gas. Natural gas can be catalytically converted to synthesis gas, an important precursor for many synthetic chemical products. Additionally, synthesis gas can be used in Fischer-Tropsch processes to produce liquid fuels to replace petroleum. Finally, the hydrogen component of synthesis gas can be separated for use in fuel cells.

Natural gas, like petroleum, is a finite resource. For this reason, it can be easy to dismiss it as a mere stop-gap for our energy problems. However, it can be considered as an important transition fuel as society moves toward renewable energy and a carbon-free energy-dense economy. Additionally, there has been increasing interest in producing methane from renewable resources such as corn or switch grass. The successful development of technologies to economically utilize natural gas in an environmentally friendly manner is one of the main goals of the proposed research. Reactions for conversion of methane to syngas, including partial oxidation and steam reforming, are high-temperature and require the use of catalysts. As discussed before, high temperatures often result in sintering of the active metal component of the catalyst, resulting in significant loss in activity. A thermally-stabilized nanocatalyst is thus

highly desirable for these reactions. Section 2.3 gives a detailed background of these catalytic fuel processing applications.

1.2 THE ROLE OF CATALYSIS

In general, most chemical reactions do not show the required degree of selectivity towards a specific reaction product, and catalysts are hence used in about 90% of all chemical processes to reduce energy requirements, selectively increase the yield of the desired product, and to minimize byproduct formation. Many important reactions and technologies are catalytic, including: the above mentioned Fischer-Tropsch process for converting coal or natural gas to liquid fuels, ammonia synthesis via the Haber process, automobile catalytic converters, and catalytic cracking in petroleum refining. Clearly, catalysis is already a key technology, and it can be anticipated that this importance of catalysis is going to further increase as we progress through the 21st century, both for the development of novel chemical processes as well as for clean energy production.

An increasingly important area of catalysis research is the rational design of materials that have precisely controlled atomic composition. This field has the goal of constructing catalysts with highly specific and targeted physical and chemical properties. Highly sophisticated molecular simulations and experimental techniques are increasingly able to determine the composition of a catalyst that is ideal for any particular reaction system. Recent advances in nanotechnology have given us the ability to construct materials to exact chemical specifications.

1.3 NANOTECHNOLOGY AND NANOCATALYSIS

Nanotechnology is the rapidly expanding field of the design, synthesis, characterization and application of materials and devices on the nanoscale. One of the major advantages of nanotechnology and nanomaterials is the dramatically increased surface-to-volume ratio of nanoscale materials over their macro-scale counterparts. This makes these materials ideal for catalysis, where surface area is a critical parameter. Additionally, nanotechnology has taught us that materials can take on fundamentally different properties when they are constructed with nanoscale dimensions. Nanoscale semiconductors can confine the motion of conduction band electrons, in a structure known as a quantum dot. Carbon nanotubes show enhanced strength and unique thermal and electrical properties. As discussed previously, nanoscale domains of gold are very active in carbon monoxide oxidation, while bulk gold is chemically inert[5]. Thus, the application of nanotechnology to catalysis has become an important research field. In particular, nanocomposite materials hold vast potential for catalysis because they allow the targeted combination of characteristics which can reconcile contrasting demands such as high activity (achieved via small particles) and good stability (which typically requires larger particles).

The major goal of this thesis work is to build upon the principles learned from this growing field and to successfully implement them in novel catalysts for use in important reactions for clean energy production. Towards this goal, we seek to improve the current understanding and control of mechanical, thermal and chemical properties of nanocatalysts. Specifically, we aim to develop a fundamental understanding of nanocomposite catalysts via systematic investigation (i.e. synthesis, characterization, and catalytic tests) of metal/oxide nanocomposites. Section 2.1 discusses the techniques used in the synthesis of these nanoscale

materials, including sol-gel, microemulsion, and surfactant templating. Section 2.2 discusses some of the limitations imposed on nanocatalysts by virtue of their nanoscale dimensions, including limited thermal stability and mass transport limitations within the internal structure.

1.4 OVERVIEW

In the present thesis chapter 2.0 will give an overview of the current state-of-the-art in fuel processing, nanoscale synthesis techniques, and some of the limitations of nanocatalysts. After that, Chapter 3.0 gives a detailed description of the experimental methods, including the synthesis steps, characterization techniques, and a description of the reactive setups used. Next, Chapter 4.0 discusses the synthesis of metal/oxide nanocomposites type catalysts. This work primarily focuses on Pt nanocrystals supported in barium hexaaluminate ceramic structures (Pt-BHA) and understanding the reasons for the excellent thermal stability of platinum particles within the structure of these materials observed previously. However, efforts are discussed to vary both the metal and ceramic components of the nanocomposite structure. This chapter also includes efforts to tailor the structure via variation of the synthesis properties, investigation of pre-treatment conditions including calcination and washing, and reactive evaluation of the nanocomposites in catalytic partial oxidation of methane, water-gas shift, and methane combustion. Subsequently, Chapter 5.0 discusses the synthesis of nanoscale silicate materials. Silica is an important support material in many catalytic reactions because it is chemically inert and shows high thermal stability. It includes a discussion of two methods used to form nano-silica and the results of parameter variation on the resulting materials. Next, Chapter 6.0 describes the formulation of hierarchical supported nanocomposites in order to overcome the

difficulties and shortcomings inherent to working with finely grained nanocomposite powders. It includes a detailed characterization of the various structures tested, as well as evaluation of these structures in CPOM reaction. Finally, Chapter 7.0 concludes this work with a summary and outlook.

2.0 BACKGROUND

2.1 NANO-SYNTHESIS TECHNIQUES

Nanotechnology is the burgeoning field of study involving materials with at least one characteristic dimension of size less than 100 nm. Materials in this size range demonstrate unique properties not present in their bulk-form counterparts due to increased surface-to-volume ratio, surface energy, electronic structure, and surface disorder. These properties have motivated an exceptional amount of research interest in nanomaterials. For example, nanomaterials have recently been investigated for their potential applications in the fields of bio-materials, coatings, data-storage, optics, high-performance ceramics, fuel-cells, and catalysis[16-22].

In terms of the synthesis of nanoscale materials, there are two main approaches: top-down and bottom-up. Top-down approaches take a macro-scale material and modify it to give it nano-scale characteristics. The most recently developed methods of lithography[23] (e-beam, deep ultraviolet, extreme ultraviolet) are examples of top-down approaches that have been critical in the advancement of the semiconductor and microelectromechanical systems industries. While lithography exhibits very precise control over the size and composition of nanoscale objects, it is limited for use in catalytic applications by its 2D nature. Bottom-up approaches seek to use controlled growth of chemical precursors to form a wide variety of nanoscale materials. Physical

vapor deposition[24], wet-chemical syntheses[25, 26], and flame aerosol techniques[27, 28] are typical examples of bottom-up techniques.

Wet-chemical techniques are particularly promising for the synthesis of nanoscale catalysts because the growth of the nanoparticles can be controlled by surfactant based templating. Two main types of templating are commonly distinguished: exotemplating and endotemplating. Exotemplating utilizes self-assembled surfactant structures as scaffolds for the growth of nanoparticles[29-33]. These techniques typically result in long-channeled highly-ordered porous materials, such as Mobil catalyst material 41 (MCM-41)[34]. While these materials have garnered much attention in the materials synthesis field, they suffer from diffusion limitations due to their inherently large aspect ratio which limit their utility as nanocatalysts[35]. Endotemplating techniques show more promise for nanocatalyst purposes. This subset of templating methods utilizes the self-assembly of a surfactant monolayer on the surface of the nanoparticle to control the primary particle size, and has received significant research interest[14, 36-50].

The wet chemical catalyst techniques used in this thesis are discussed below. The sol-gel technique (sec. 2.1.1) is widely employed in the synthesis of xero- and aerogel type materials. More recently, the use of microemulsions has been explored as a controlled environment for the synthesis of nanomaterials (sec. 2.1.2).

2.1.1 Sol-gel technique

The sol-gel technique is a well-established technique for the formation of practically relevant materials, and numerous reviews have been written[51, 52], including some about their direct relevance in catalysis[53]. The sol-gel synthesis technique is named for two of the intermediary

steps, the sol and the gel, formed as intermediates on the way to a nanostructured solid. The sol consists of either a colloidal dispersion or an inorganic precursor (typically an alkoxide). During the sol-gel process, this sol undergoes hydrolysis and condensation to form the gel, a polymeric network of the precursor containing the reaction solvent. If we consider the sol-gel reaction of a metal alkoxide (MOR), the hydrolysis (eq. [1]) and condensation (eq. [2]) are shown below[53]:

[1] --MOR + H_2O -> --MOH + ROH

[2] --MOH + --MOR -> --MOM-- + ROH *or* --MOH + --MOH -> --MOM-- + H_2O

As equation [2] demonstrates, the product of the sol-gel reaction is a metal oxide network (--MOM--) infiltrated by the solvent system, typically a mixture of alcohol and water. After this network has formed, the gel experiences aging before the final drying step. This aging period can have a large impact on the structure of the final material. The gel may experience syneresis (removal of solvent due to shrinkage of the gel) or coarsening (dissolution and re-precipitation of metal oxide framework) during the aging process.

Following aging, it is necessary to dry the gel. Traditionally, drying is performed by evaporation of the solvent in a heated oven. The resulting material is termed a xerogel. This drying method often results in a low surface area material. This results because the pore network experiences a capillary pressure due to the liquid-vapor interface within the pores. This pressure acts to collapse the pore network and leads to low surface area materials which are not ideal for catalysis[53]. Significant work has been done to avoid this liquid-vapor capillary pressure during the drying process. Supercritical drying[54] circumvents the liquid-vapor phase boundary by converting the liquid to a supercritical fluid at high temperature and pressure and by subsequently removing the fluid from the pores of the structure. Typically the native solvent is replaced with CO_2 (supercritical at mild conditions, 304K and 7.39 MPa) to facilitate the process

of achieving supercritical conditions. The resulting material is termed an aerogel. Alternatively, the liquid-vapor phase boundary is avoided at low temperature/pressure by way of freeze drying. In this manner, the frozen solid solvent is removed directly as a vapor via sublimation.

One of the important aspects of sol-gel is the high degree of synthetic flexibility the technique offers. Any of the reaction parameters that affect the hydrolysis or condensation reactions (eqs. [1] and [2] above) has a potential to control the material properties of the final structure. These parameters include temperature, pH, amount and type of precursor, type of solvent, and water content. By tuning these parameters it is possible to form a wide variety of highly porous materials that have direct application in catalytic applications.

Another important aspect of sol-gel technique, in terms of catalytic systems, is the ability to form multiple component (e.g. active noble metal and high-temperature stable ceramic) materials in a single step. This not only simplifies the synthesis of these materials, it also can lead to a more intimate contact between the various components. This intimate contact could become important in catalytic reactions involving multiple active sites (transport between the sites enhanced) or involving a catalyst-support interaction. Perhaps most importantly, a number of studies have shown that in metal – oxide materials formed via sol-gel, the metal component is at least partially buried within the oxide material. This leads to enhanced thermal and mechanical stability of the active metal component[55, 56].

2.1.2 Microemulsion templating

Microemulsion based techniques are particularly appealing for nanocatalyst synthesis because they are simple, easily controlled, and highly customizable. A microemulsion is defined as a thermodynamically stable and optically transparent mixture of water and oil made possible by

the addition of a surfactant and (in most cases) a co-surfactant[57]. Both normal (oil droplets dispersed in water) and reverse (water droplets dispersed in oil) exist. Microemulsions are highly flexible due to the fact that many experimental parameters can be used to influence their final properties, including: water-to-oil ratio, structure and concentration of surfactant, co-surfactant, and precipitating reagents. The micelles that form in microemulsions are nano-sized, and serve as well defined and highly controlled 'nanoreactors' for the chemical synthesis of nanoparticles[58]. If the reactants or precursors in the synthesis of a particular nanomaterial are labeled A and B, the reaction can be induced in one of 2 ways: by mixing a microemulsion containing species A and a second microemulsion containing species B, or by direct addition of reactant A to a microemulsion which already contains species B. The difference between these techniques is the diffusion mechanism which controls the reaction parameters: the rate of micellular mixing, or the rate at which the precursor diffuses through the surfactant layer and into the micelle. The first use of microemulsions for catalyst synthesis was demonstrated in 1982 by Boutonnet *et al*[59]. Today they are prolific across many catalytic applications, including hydrogenation[44, 60-63], combustion[36, 38, 40, 64-66], electrocatalysis[67, 68], as well as NO-CO reduction reactions[44, 69].

As with any system, there are drawbacks to the application of microemulsions for catalyst synthesis. The most significant problem involves the separation of the nanoparticles from the surfactant component. The surfactant plays an important role in maintaining the small size of primary particles, yet must be removed to ensure adequate catalytic activity[70]. This problem is further complicated in nanoparticulate systems because the surfactant molecules adsorb more strongly to the particle surface. A careful combination of liquid extraction, freeze-drying, and

calcination has been found to ensure surfactant removal while maintaining a high-surface area and active nanocatalyst[38].

2.2 LIMITATIONS OF NANOCATALYSTS

Nanocatalysts have traditionally been limited in practical application due to problems associated with their inherently small size. Nanoscale domains of metal are more susceptible than larger particles to thermal sintering due to the known phenomena of melting point depression[71]. Additionally, some nanocatalysts are configured with the active site located within a torturous nanosized pore. This can lead to significant internal transport limitations depending on the reaction conditions and size of the reactant molecules.

2.2.1 Thermal stability

In order to gain widespread use as catalysts, nanocatalysts need to be developed that overcome the major weakness inherent to nanomaterials: a lack of thermal stability. To this day, even the most stable mesoporous materials only can withstand temperatures of ~800°C[72], which is insufficient for the reactions mentioned in the above section. Extension of this stable temperature range to ~850°C has been demonstrated by incorporating zeolite-like order into the pore walls and through the use of porogens[73-75]. Yet even these highly-specialized catalysts lack the high-temperature stability needed.

Moving to metal nanoparticles will only stress the thermal and hydrothermal stability of these catalysts further. Thermodynamics favor the sintering of smaller particles into larger ones

at applicable temperatures for catalysis[76]. A quantitative relationship between the melting point and particle size of nanomaterials was postulated almost a century ago by Pawlow[77], and more recently was modified by Borel *et al* to be more accurate[78]. The modified form postulated by Borel, which matches well with experimental data, shows that the reduction in melting point from the bulk form for a particular material is proportional to the inverse of the particle diameter. This means that as particles become smaller, their thermal stability decreases at a similar rate. Recent studies even suggest that nanoparticles demonstrate a stronger sintering rate than predicted[79, 80]. Typical procedures to stabilize metal nanoparticles used in nanomaterials research, such as ceramic or polymer coating[21], cannot be applied in catalysis because they block the active sites on the particle surface. Essentially, the low thermal stability of noble metal nanoparticles has prevented any systematic investigation of their applicability for high-temperature fuel processing.

2.2.2 Mass transport limitations

Another critical factor in the applicability of nanoparticles for catalysis concerns the catalyst formulation. Using the raw nanoparticulate powder in a typical industrial process will result in handling problems and a prohibitive pressure drop. The typical solution for this involves mixing the liquid microemulsion with a solid support structure and allowing the particles to adhere to the support during the phase separation and drying steps. This process is typically not very well controlled, and presents a significant limitation to the realization of the full potential of the nanoscale characteristics of the catalyst. Recent research studies have attempted to overcome this problem by supporting the catalyst in a mesoporous MCM-41 structure [81, 82], or by encapsulation of the nanoparticles in the structure of mesoporous SBA-15 by sonication or *in-*

situ synthesis of nanoparticle and mesoporous support[83-85]. As mentioned above, the large aspect ratio of these mesoporous materials are subject to transport limitations, as the reactant gas has to pass through a narrow channel in order to reach the catalyst active site. These mass transport limitations are expected to become more prevalent in high-temperature reactions when the surface reaction rate increases at a faster rate than mass transport (e.g. CPOM, methane combustion)[86].

This problem is referred to frequently in research concerning catalytic applications of mesoporous materials; however, only one published study investigates the matter. Nyugen and co-workers studied the catalysis of perovskite embedded inside mesoporous silica for methane combustion[35]. They found that mass transport limitations set in at T ~ 380°C as evidenced by an observed decrease in activation energy from 25.5 kcal/mol at T < 380°C to 18.5 kcal/mol for larger temperatures. M.-O. Coppens *et al* have attempted to circumvent mass transport limitations by incorporating a population of macropores with the mesopores[87]. Significant questions about the thermal/mechanical stability of these materials as well as the extent to which they can prevent mass transport limitations remain. In general, mass transport is a key issue for nanocatalysts, and further research is clearly needed.

2.3 FUEL PROCESSING APPLICATIONS

2.3.1 Catalytic partial oxidation of methane (CPOM)

Catalytic partial oxidation of methane to synthesis gas (CPOM) is chosen as a test reaction to evaluate the activity and stability of nanocomposite catalysts due to its industrial importance as well as its high-temperature and short-contact time reaction conditions. In CPOM, methane reacts directly with oxygen or air to form synthesis gas (CO and H_2) in a one-step reaction:

$$CH_4 + 0.5\ O_2 = CO + 2\ H_2\ (\Delta H_R^0 = -37\ kJ/mol)$$

Syngas is an important chemical intermediate principally used to produce hydrogen, but is also used in the synthesis of numerous other molecules, including methanol, polyurethanes, polycarbonates, acetic acid, ammonia, and synthetic liquid fuels (Fischer-Tropsch)[88]. The reaction is typically catalyzed by noble (Pt, Rh) or transition (Ni, Ru, Ir) metals supported on high surface area supports such as Al_2O_3. CPOM is considered a promising alternative to the traditional industrial route for methane utilization, that of steam reforming of methane (SRM) [89, 90]:

$$CH_4 + H_2O = CO + 3\ H_2\ (\Delta H_R^0 = 210\ kJ/mol)$$

CPOM has many advantages over SRM in terms of clean energy and/or hydrogen production. SRM is a highly endothermic reaction, and therefore is a major energy consumer. CPOM, on the other hand, is mildly exothermic, allowing it to be run autothermally. SRM is generally heat transfer limited, necessitating extremely large reactor volumes and long contact times (~1s). This limits the implementation of SRM to large scale, centralized facilities. CPOM has no such limitation (contact time <10ms), and could be run in small scale, decentralized reactor units that would allow implementation in many of the remote locations where natural gas

is typically found. Finally, SRM produces syngas with a H_2/CO ratio of 3, whereas in CPOM this ratio is 2. A ratio of 2 is more favorable for downstream utilization of syngas (e.g. methanol production or Fischer Tropsch)[89]. Many SRM reactors are typically followed by a water-gas shift reactor (sec. 2.3.2) in order to adjust this ratio, thus increasing the complexity and expense of the typical SRM process.

Replacing energy-intensive, large-scale, and centralized SRM with energy efficient, small-scale, and decentralized CPOM will only be possible if suitable catalysts are found for CPOM. Recent work in our group has shown that thermally stabilized Pt-barium hexaaluminate (BHA) nanocomposite catalysts are active, selective, and stable for long periods (>100h) of CPOM reaction[10-14]. The beneficial properties of CPOM, as well as our expertise in the area[91-94] make it an ideal test reaction for further investigation of the catalytic activity and thermal stability of other nanocomposite catalysts. In particular, this thesis extends the utility of Pt-BHA catalysts for CPOM by supporting the nanocomposite onto a variety of macroscale structures (see sec. 6.0)

2.3.2 Water-gas shift (WGS)

The water-shift reaction is another important, industrially relevant reaction for the production of clean energy and hydrogen. The WGS reaction is a proven technology for increasing the H_2/CO ratio of syngas mixtures. In water-gas shift, carbon monoxide is reacted with water vapor in a mildly exothermic reaction, producing carbon dioxide and hydrogen:

$$CO + H_2O = CO_2 + H_2 \ (\Delta H_R^0 = -41 \text{ kJ/mol})$$

The reaction is typically equilibrium controlled, with higher conversions attained at low temperatures due to the exothermicity of the reaction. To overcome the limitations of slow

kinetics at low temperatures, WGS is historically run in a two reactor system. The first reactor is high-temperature WGS (320-450°C) typically run over iron oxide catalysts. The second reactor is low-temperature WGS (200-250°C) run over Cu-ZnO based catalysts. CoO-MoO/Al_2O_3 catalysts have also been investigated because they show good reactivity throughout both high and low temperature regimes, and are sulfur tolerant[95].

A number of recent experimental studies highlight the interest in developing improved WGS catalysts. The group of Flytzani-Stephanopoulos has pointed out the weaknesses of Cu-ZnO catalyst in practical application (specifically, for removal of CO from the feed stream of a Polymer Electrolyte Membrane (PEM) fuel cells), including their sensitivity to temperature excursions, pyrophoricity in air, and the cumbersome pre-activation steps needed. Their group investigated a number of alternative reaction systems: Cu and Ni loaded La-CeO_2 significantly lowered the activation energy of WGS (compared to metal free La-CeO_2) while requiring no pre-activation steps[96]. Cu on CeO_2 catalysts were also found to be suitable for high-temperature WGS, with the surface properties of the CeO_2 being crucial to high activity[97]. An *in-situ* study of Cu-CeO_2 WGS shift catalysts indicates that the active site involved both metallic copper and O vacancies in the CeO_2 support[98]. Wen *et al* studied Cu-MoO_2 catalysts and found significant WGS activity above 350°C. By examining the structure of the Cu-MoO_2 catalyst *in-situ,* they found an interplay between Cu-MoO_2, $CuMoO_4$, and $Cu_6Mo_5O_{18}$ species, with interfacial interactions between Cu and MoO_2 leading to WGS activity[99]. An IR study of a wide variety of metals on ceria was conducted by Jacobs *et al* that focused on the role of the metal in reducing the CeO_2. Metals with higher reduction temperature were better at reducing the CeO_2, and this led to better activity in WGS reaction[100].

In the area of low-temperature WGS, low content (<0.6 atomic %) Pt and Au catalysts supported on nanocrystalline CeO_2 were found to be the most active catalysts investigated[101, 102]. Time resolved X-ray diffraction and absorption methods indicate that the active site for Au-CeO_2 is the gold-ceria interface[103]. In another study, leaching of Au metal from Au-CeO_2 catalysts (while retaining atomically dispersed gold) resulted in a 5 fold drop in turn-over frequency – leading the authors to conclude that nanocrystalline gold is the important source of activity in these materials[104]. Pt-CeO_2 catalysts were shown to be ~20% more active than Au-CeO_2, thus indicating that the metal type plays an important role in the WGS mechanism[105]. In Pt-CeO_2 catalysts, the decomposition of formate ions which form around the edges of the metal particles is proposed as a rate limiting step[106-109]. The activity of the reaction has been shown to increase with Pt loading, due to the promotion of formate decomposition[110, 111]. The effect of doping Pt-CeO_2 catalysts with zirconia was examined, and a maximum WGS rate was found with increasing Zr content[112]. Another study found that Pt-thoria catalysts showed slightly increased conversion over Pt-ceria[113]. One main concern with Au and Pt based ceria catalysts has been severe deactivation during start-up/shut-down. The issue can be linked to the formation of cerium (III) hydroxycarbonate which causes catalyst deactivation. The Flytzani-Stephanopoulos group was able to decompose this unwanted compound through the addition of as little as 0.5vol% O_2 in the reactive stream during start-up/shut-down[114].

The abundant experimental work in WGS has been complemented by a number of theoretical studies. Rodriguez and coworkers have conducted density functional theory (DFT) analysis of a variety of catalyst structures in WGS reaction. A study comparing WGS activity of Cu and Au nanoparticles (with 29 atoms each) to bulk (100) surfaces of each metal showed that nanoparticles were more active than their bulk counterparts, and that copper in either form is

more active than gold. The higher activity of the nanoparticles was attributed to a larger fraction of low-coordinated edge and corner sites as well as increased particle fluxionality. Additionally, the activity of Au nanoparticles on CeO_2 was higher than for the same particles on ZnO, indicating that the support is playing a role in the water-gas shift mechanism[115]. DFT was also used to investigate the activity of C- and Mo- terminated Mo_2C catalysts compared to Cu (111). Their results indicate that O (remaining from water decomposition) on the surface of Mo-Mo_2C strongly deactivate that surface, whereas C-Mo_2C surfaces are show higher activity in the presence of O atoms[116]. Their results indicate that pre-treatment should not be overlooked when preparing a WGS catalyst.

The water-gas shift reaction is an important fuel processing and hydrogen production reaction and is shown experimentally and theoretically to be remarkably sensitive to the surface properties, composition, and structure of both the metal particles and oxide support. Additionally, many of the tested WGS catalysts demonstrated a significant metal-support interaction, leading to improved activity in some cases, and deactivation in others. This indicates that the intimate contact between metal particle and support as well as the small stable nanoparticle size offered by previously mentioned nanocomposite catalysts[10-14] might make them particularly well-suited for WGS.

2.3.3 Catalytic methane combustion

Catalytic combustion has gained increasing attention as a means to produce energy with lowered greenhouse gas and NO_x emissions. NO_x emissions are eliminated in this type of combustion because the flame temperature is typically much lower than that required for the formation of thermal NO_x (~2000K)[117]. Catalytic combustion has also been developed for the abatement of

lean (low fuel to air ratio) mixtures of hydrocarbons (e.g. the exhaust mixture from a natural gas fueled vehicle). The elimination of methane from these exhaust gases is of particular importance because methane is a much more potent greenhouse gas than CO_2. A main advantage in catalytic combustion is the stability of the reaction compared to pure flame combustion, leading to increased efficiency.

Catalytic combustion of methane is best described as interplay between both homogeneous and heterogeneous combustion pathways. The reaction equation is shown below.

$$CH_4 + 2\ O_2 = CO_2 + 2\ H_2O\ (\Delta H_R^0 = -802.3\ kJ/mol)$$

The abundant amount of heat generated from this exothermic reaction ($\Delta T_{adiabatic} \approx 276K$ for abatement of a 1vol% stream of methane) poses the difficult challenge of finding catalytic materials which are active and stable under high-temperature conditions. Thermal cycling to temperatures as high as ~1000°C, as well as a harsh chemical environment (typical in automobile exhaust treatment) can cause catalyst deactivation by sintering, metal vaporization, corrosion, or erosion[118]. An additional challenge for practical application of a combustion catalyst is the typically low temperatures available at start-up. An ideal catalyst would be able to initiate light off of the fuel mixture at temperatures as low as 400°C[38].

Ceramics (e.g. metal oxides) have been focused on as materials for catalytic combustion, due to their robustness in extreme conditions. Hexaaluminates (e.g. $BaAl_{12}O_{19}$), in particular, show better sintering resistance than other complex oxides (e.g. $MgAl_2O_4$, $LaAlO_3$, $SrZrO_3$ and $LaTiO_3$) in the demanding environment of methane combustion[118]. $Sr_{0.8}La_{0.2}MnAl_{11}O_{19}$ appears to be the hexaaluminate with the best combination of catalytic activity and high surface area[119]. The addition of small quantities of Mn appears to be important for obtaining hexaaluminates with good sintering resistance[120]. Zarur and Ying developed high temperature stabilized barium

hexaaluminate ($BaAl_{12}O_{19}$, BHA) nanomaterials and tested them in catalytic combustion. They found when that when igniting a stream of 1vol% methane, a CeO_2 doped BHA exhibited a dramatically decreased light-off temperature (~400°C) when compared to nanostructured BHA (~600°C), or conventional BHA (~700°C)[38]. These hexaaluminates offer resistance to sintering at high temperatures, but are orders of magnitude less active than noble metal based catalysts[121].

Some researchers have attempted to incorporate noble metals, which offer the potential of higher reaction rates (and thus lower ignition temperatures) into high temperature stabilized supports. Most noble metals and their oxides are not suitable for these high-temperature systems due to sintering at moderate temperatures (500-900°C) or even metal volatilization (>1200°C)[122]. A heterogeneous dispersion of metal oxides on hexaaluminate has even been shown to increase sintering rates of these materials, seemingly limiting the possibility of a metal – hexaaluminate composite[122]. However, some progress has been made for low-temperature combustion (T<1000°C) by incorporating Pd into various oxide supports[86, 123-126]. Notably, strong metal-support interactions are seen when Pd is supported on Al_2O_3-36NiO and SnO_2.

Catalytic combustion is another important reaction for clean energy production and clean transportation technologies (e.g. natural gas vehicles). Overall, there is still a need for combustion catalysts which incorporate the high-temperature stability of hexaaluminates with the high activity of noble metals. In this thesis, I have extended the use of metal-oxide nanocomposite catalysts to methane combustion. These materials have previously shown a high level of activity and stability in high-temperature CPOM reaction at ~1000°C, indicating that similar levels of activity and stability should be attainable for combustion of lean methane streams at ~700°C[10-14].

3.0 EXPERIMENTAL

3.1 MICROEMULSION TEMPLATED SOL-GEL SYNTHESIS

The standard synthesis for nanocomposite materials in this work is a sol-gel synthesis occurring within a Winsor type IV microemulsion. The type IV classification indicates that there are no separate oil or water phases, simply a continuous microemulsion phase[127, 128]. This method is used for the formation of various catalysts in section 4.0 and in the formation of supported catalysts in section 6.0 . This synthesis was adapted originally from the work of Ying[36], and has been previously used for the formation of nanocomposite catalysts in our group[10-14]. A sample recipe for a typical batch of 10 wt% Pt-BHA is shown in **Table 1**. The metal weight loading is calculated based on complete incorporation of the aluminum metal into the BHA structure of the final product.

The surfactant used in the synthesis (abbreviated PEPP) is poly(ethylene glycol)-*block*-poly(propylene glycol)-*block*-poly(ethylene glycol) and has a number weighted molecular weight M_n = 2000. De-ionized water was obtained from a Milli-Q filtration system. All other materials were obtained from Sigma-Aldrich and used as received, with the exception of the anhydrous isopropanol which was transferred to an air tight vessel containing nitrogen gas, and sparged with a stream of nitrogen gas to remove any dissolved oxygen.

Table 1: *Components in the microemulsion templated sol-gel synthesis of 10 wt% Pt-BHA. All chemicals listed are reagent grade.*

Microemulsion		**Supplier**	**MW [g/mol]**	**moles**	**Mass [g]**
PEPP	(surfactant)	Sigma	2000.00	0.0075	15.0
1-Pentanol (>99%)	(co-surfactant)	Sigma	88.15	1.9853	175.0
2,2,4 Trimethylpentane (>99%)	(oil phase)	Sigma	114.23	0.3939	45.0
De-ionized H_2O (Milli-Q)	(water)	in-house	18.00	0.7111	12.8
$H_2PtCl_6 \cdot 6\ H_2O$ (>37.5% as Pt)	(metal salt)	Sigma	409.82	0.0012	0.475
Metal Alkoxides					
Al-isopropoxide (99.99%)		Sigma	204.24	0.0320	6.5360
Ba-isopropoxide (99.9%)		Sigma	255.51	0.0027	0.6822
Anhydrous 2-propanol (99.5%)		Sigma	60.10	1.6328	98.13

The microemulsion portion of the synthesis is formed by first combining the PEPP, 2-pentanol, and 2,2,4 trimethylpentane in a round bottom schlenk flask. The chloroplatinic acid hexahydrate is then dissolved in the de-ionized water, and this metal-salt solution is added to the other components. The entire mixture is stirred for approximately 5 minutes in order to form an optically transparent and thermodynamically stable microemulsion.

The metal-alkoxide portion of the synthesis is formed by carefully mixing the proper amounts of Al- and Ba-isopropoxides under an inert atmosphere to prevent unwanted hydrolysis of the reagents due to moisture in the air. All schlenk vessels are evacuated, flamed with a Bunsen burner, and filled with nitrogen gas twice before use. The isopropoxides are dissolved in anhydrous 2-propanol and refluxed at 90°C for approximately 2 hours, all while maintaining the inert nitrogen environment.

The metal alkoxides are then slowly added to the microemulsion via siphon, while stirring the mixture rapidly. The sol-gel reaction begins to take place and the mixture becomes

significantly more viscous. The mixture is stirred for approximately 70 hours at room temperature to allow for aging. After this time temperature-induced phase separation is used to separate the gel phase (2 hours in a 4°C environment). The gel is washed with 200 ml of acetone (99.9%, J.T. Baker) four times in order to remove excess surfactant and organic material. The washed gel is then freeze-dried by using liquid nitrogen and a high-vacuum pump. The dried yellow powder which results is then ready for calcination. Calcination of the powdered catalysts takes place in a standard tube furnace oven. Typical conditions are 600°C for five hours in an atmosphere of flowing air. Where necessary, the catalyst was reduced at the calcination temperature for ½ hour in flowing hydrogen.

Modifications to this procedure have been made during the investigations presented herein, and will be noted in the particular section where the modifications have been made. Most typically, the amount and/or type of metal salt is modified in order to achieve a different weight loading or metal composition. In some cases, the amount and/or type of surfactant was altered to investigate the effect on the final product. The calcination conditions (temperature, atmosphere) were also varied as noted.

3.2 CHARACTERIZATION

3.2.1 Porosimetry

Nitrogen porosimetry testing is done on a Micromeritics ASAP 2020 surface area and porosity analyzer. Samples are degassed for 3 hours at 200°C under high vacuum prior to each test. The typical test involved a 6-point BET analysis for total surface area measurement and an 84-point

BJH analysis (adsorption and desorption) with Halsey thickness curve correction and standard BJH correction for pore size and volume determination.

3.2.2 Chemisorption

Chemisorption experiments for total platinum surface area determination for the nanocatalyst are conducted on a Micromeritics Chemisorb 2750 pulse chemisorption system. Samples are reduced for 15 minutes in 10% H_2/Ar with a subsequent flush with He for 15 minutes all at 400°C prior to performing CO pulsing with He as a carrier gas at room temperature. The surface area of Pt was determined using a stoichiometry factor of 1 for CO on Pt, with assuming a Pt active site having surface area of 0.08 nm^2 (Chemisorb 2750 User Manual).

3.2.3 X-ray diffraction (XRD)

X-ray diffraction measurements were performed with a high-resolution powder X-ray diffractometer (Phillips PW1830, USA) in line focus mode using a monochromatic Cu radiation at the wavelength of 1.54 Å. The beam voltage was 40kV at a current of 30mA. The XRD patterns were recorded between 15 and 90° (2θ) in steps of 0.08° intervals with a minimum 0.2 s counting time at each step. Longer counting times were used to obtain higher resolution in some samples.

3.2.4 Transmission electron microscopy (TEM)

Catalyst morphology and platinum particle size are determined by transmission electron microscopy using a JEOL-2000FX and/or JEOL-200CX electron microscope and scanning electron microscopy using a Phillips XL30 electron microscope. Samples for the transmission electron microscopic measurements were obtained by placing a drop of sample suspension in acetone on a copper type-B support grid (Ted Pella Inc.), followed by air drying to remove the solvent. Measurement of mean platinum particle diameter from TEM micrographs was performed by hand using ImageJ software[129].

3.2.5 Mass spectroscopy (MS)

Analysis of exhaust gas during various calcination procedures was determined using a Balzers Quadstar GSD 300 mass spectrometer. This system gives time resolved, qualitative measurement of gas composition.

3.3 REACTIVE TESTING

3.3.1 Catalytic partial oxidation of methane (CPOM)

All catalysts (powdered, structured, or supported) are wedged between two 10cm long inert cordierite extruded monoliths, wrapped in a layer of alumina cloth, and inserted into a quartz-glass tube, which is part of a quartz-metal hybrid reactor. K-type thermocouples were used to

monitor reaction temperature on either end of the catalyst zone, with typical reaction temperatures between 700-1000°C for all configurations tested. Mass flow controllers (MKS Instruments Inc.) are used to feed methane (4.0 grade, Valley National Gas) and synthetic air (0.1 grade, Valley National Gas). All tests were run autothermally at 4SLM total flow rate, unless otherwise noted. Typical residence times varied between 9 and 38 ms for the different catalyst configurations (at standard inlet conditions). The exit gas passes through a condenser to eliminate H_2O from the stream. The composition is determined using a double oven gas chromatographic system (Shimadzu GC-14B). The GC determines the composition of CH_4, N_2, O_2, H_2, CO, and CO_2. The amount of H_2O is back-calculated from the measured exit-gas quantities and assuming that the C/H ratio does not change during the course of the reaction. Atomic balances are typically within +/-5%. Example calculations of conversion, selectivity and atom balance, as well as details of the column, oven, and detector configurations are located in Appendix B.

3.3.2 Water-gas shift (WGS)

Powdered catalytic materials are inserted into a 5 mm ID quartz glass tube. The catalysts are supported within the tube on either end by plugs of quartz glass felt. The tube is placed within a high temperature tube furnace such that the catalyst zone is fully within the heated zone of the furnace. Additionally, the catalyst zone is situated toward the far end of the tube furnace (with respect to the flow of gas) in order to allow adequate pre-heating of the reaction gas mixture. A K-type thermocouple is used to monitor reaction temperature and it was inserted such that the tip of the thermocouple is within 1 mm of the end of the catalyst zone. The temperature in the reaction zone is controlled by the temperature of the furnace, and is typically

between 200-600°C. Mass flow controllers (MKS Instruments Inc.) are used to feed a mixture of 15.21% CO, 35.09% H_2, 9.65% CO_2, and 40.05% He (mixture provided by Valley National Gas). Water is injected via syringe pump (Braintree Scientific, Inc.) directly into the feed gases which are flowing through a heated line maintained at 200°C. The composition of the mixture after water addition is 21.8% H_2O, 9.4% CO, 21.8% H_2, 6.0% CO_2, and 24.8% He. The total flow rate of gas is typically around 100 cubic centimeters per minute. Space velocities are typically ~120,000 h^{-1} (at standard inlet conditions) leading to contact times of ~100ms. The exit gas passes through a condenser to eliminate H_2O from the stream. The composition is determined using an Agilent 3000A Micro GC. The GC determines the composition of CH_4, O_2, CO, H_2, He, and CO_2. The system is capable of detecting N_2, ethylene, ethane, and acetylene, but none of these gases were detected during the experiments. Methane production as a result of methanation was limited to very low amounts (<1 vol%) at temperatures above 500°C. The inert Helium feed is used as an internal standard, and is used to calculate the total gas flow rate after water condensation and to back-calculate the concentration of water leaving the reactor. Atomic balances (C/O and C/H) are typically within +/-10%. Example calculations of conversion, selectivity and atom balance, as well as details of the column, oven, and detector configurations are located in Appendix B.

3.3.3 Methane combustion

Powdered catalytic materials are inserted into a 5 mm ID quartz glass tube. The catalysts are supported within the tube on either end by plugs of quartz glass felt. The tube is placed within a high temperature tube furnace such that the catalyst zone is fully within the heated zone of the furnace. Additionally, the catalyst zone is situated toward the far end of the tube furnace (with

respect to the flow of gas) in order to allow adequate pre-heating of the reaction gas mixture. A K-type thermocouple is used to monitor reaction temperature and it was inserted such that the tip of the thermocouple is within 1 mm of the end of the catalyst zone. The temperature in the reaction zone is controlled by the temperature of the furnace, and is between 300-800°C. Mass flow controllers (MKS Instruments Inc.) are used to feed a ~1% mixture of methane (4.0 grade, Valley National Gas) in synthetic air (0.1 grade, Valley National Gas). All tests are designed to run isothermally, with the measured temperature in the reaction zone being no more than 20°C greater than the furnace set point. The total flow rate of gas is typically around 100 ml/min, but is adjusted for some studies to normalize the contact time to the amount of active surface area in the catalyst. Residence times varied between 20 and 60 ms for the different catalyst configurations (at standard inlet conditions). The exit gas passes through a condenser to eliminate H_2O from the stream. The composition is determined using an Agilent 3000A Micro GC. The GC determines the composition of CH_4, N_2, O_2, and CO_2. The system is capable of detecting H_2, CO, ethylene, ethane, and acetylene, but none of these gases were detected during the experiments. Atomic balances are typically within +/-5%. Example calculations of conversion, selectivity and atom balance, as well as details of the column, oven, and detector configurations are located in Appendix B.

4.0 METAL-OXIDE NANOCOMPOSITE CATALYSTS

4.1 PREVIOUS WORK

Dr. Veser's research group has synthesized platinum barium hexaaluminate (Pt-BHA) nanocomposites previously[10-14]. The approach used is a microemulsion templated sol-gel synthesis which results in metal nanoparticles embedded in a ceramic matrix. The materials formed have a very open structure, without the long channels typically associated with mesoporous materials. They consist of ~10nm platinum particles embedded in a high-temperature stable barium hexaaluminate matrix. The material shows a narrow Pt-particle size distribution with uniform spatial distribution (see **Figure 1** left inset). Even more interestingly, they show an increased resistance to sintering as indicated by a delayed appearance of the Pt reflex in XRD measurements (see **Figure 1**). Catalytic testing in CPOM reaction shows enhanced hydrogen yields when compared to traditional Pt and Rh on alumina catalysts (see **Figure 2** left graph). This activity is realized with very low amounts of Pt, resulting in 90% of the catalytic activity achieved with only ~1mg of Pt for the setup utilized, a reduction of two orders of magnitude from the conventional catalyst (see **Figure 2** right graph). These nanomaterials are both active and stable for CPOM reaction at T ~ 1000°C, an increase of ~200°C from any previously reported study. Their significantly improved catalytic activity,

when compared to conventional catalysts, is a strong indication that mass transport limitations are minimized.

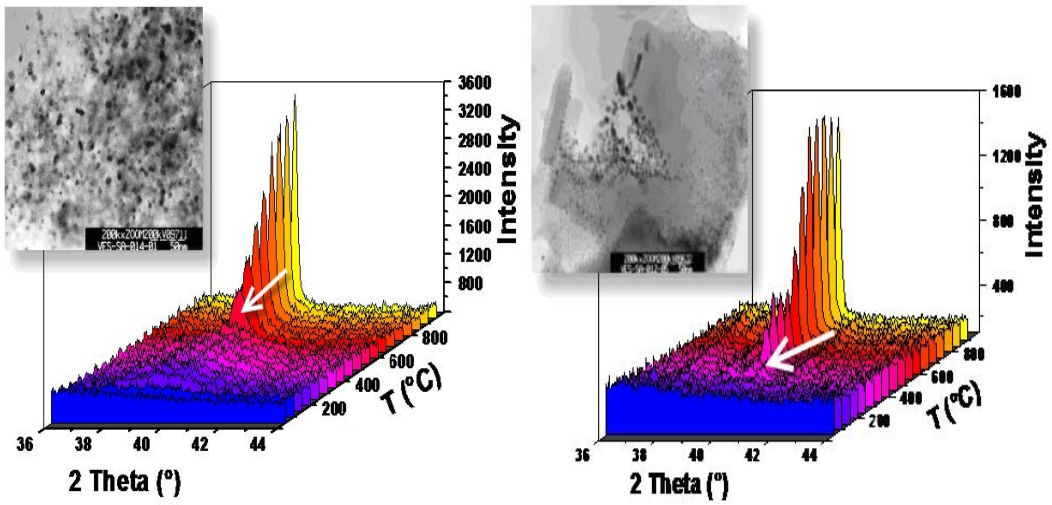

Figure 1: *Structure and stability of Pt-BHA nanocomposites. Left: XRD of Pt reflex for reverse-microemulsion templated sol-gel synthesis. Right: same reflex for post-impregnated BHA nanoparticles with Pt. Insets: TEM micrographs of indicated materials.*

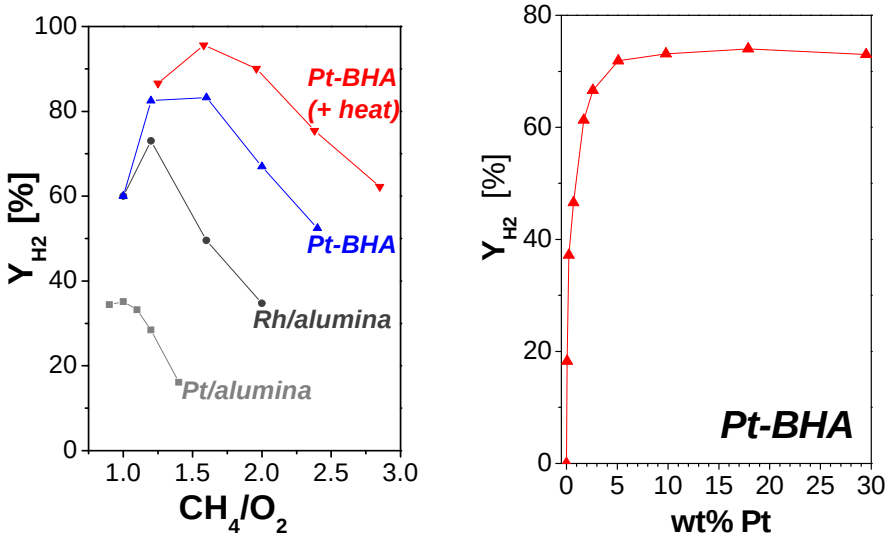

Figure 2: *Left: CPOM reaction over Pt-BHA and traditional Pt and Rh/alumina catalysts. 5.0 SLPM of CH_4/O_2, autothermal except: (+heat) sample was continuously heated by a heating tape at 800°C. Right: Hydrogen yield in CPOM versus percentage weight of Pt in Pt-BHA. 5 SLPM of CH_4/O_2=2.0.*

Overall, the described Pt-BHA nanocomposite catalyst appears to overcome both of the major limitations of nanocatalysts: thermal stability and mass transport limitations. The goal of the research in this chapter is to further characterize and investigate these novel materials, investigate the flexibility of this synthesis route, and test these materials for further reactions of interest for fuel processing applications.

4.2 EVALUATION OF PRE-TREATMENT

Catalyst pre-treatment is the series of steps undertaken between the time the material is synthesized and its use in a reaction. These steps vary widely depending on the composition of the catalyst and the reaction conditions of interest. Typical pre-treatment steps might include drying, calcination, oxidation, or reduction. For catalysts prepared from solutions containing surfactants (e.g. microemulsions), washing is typically an important step. The manner in which each of these steps is conducted will strongly affect the properties of the final material. The goal here is to establish the effect of various pre-treatments on nanocomposite Pt-BHA catalysts. Both calcination (in inert, reducing, and oxidizing conditions) and washing (see appendix) are investigated.

4.2.1 Calcination conditions

The calcination process serves a number of different purposes: removal of residual surfactants, heat treatment of the ceramic structure, and crystallization/stabilization of metal nanoparticles.

The environment (inert/oxidizing/reducing), length of time, temperature, and ramping rate of the calcination can strongly affect the morphology, composition, and size of metal nanoparticles in the final product. The effect of each of these parameters on the properties of Pt-BHA nanocomposites is investigated. Calcination temperature is an important factor in the high-temperature stability of the Pt particles, so its effect will be reported in more detail in section 0.

4.2.1.1 Duration of calcination

Calcination is expected to influence the morphology of the BHA and the Pt particle size. If the material is unstable at the calcination temperature of interest, a loss of surface area and pore volume, and an increase in Pt particle diameter are expected. The amount of time that the nanocomposite is held at a particular calcination temperature is an important experimental consideration. Adequate time must be given to remove residual surfactants, but extended time may cause significant degradation of the catalyst material.

A calcination temperature of 600°C is used because it is sufficiently high to combust residual surfactants (remaining from the reverse-microemulsion synthesis), and is the calcination temperature for a number of the reaction tests done previously with these materials[13]. A single batch of Pt-BHA is calcined at this temperature over a total of 50 hours. The sample is removed periodically from the calcination oven to perform nitrogen porosimetry and TEM measurements.

Figure 3 shows the results of the nitrogen porosimetry (BET surface area) and TEM measurements (Pt particle average size). The specific surface area of the sample (solid line) shows a steady degradation from ~325 to ~250 m^2/g as the calcination proceeds. The average Pt particle size (dashed line) is unaffected by the decreasing surface area, remaining ~13nm over the entirety of the 50 hours.

Figure 4 shows the pore size distributions obtained from BJH analysis of the nitrogen isotherms. The pore structure is essentially unaffected by the length of time calcined at 600°C.

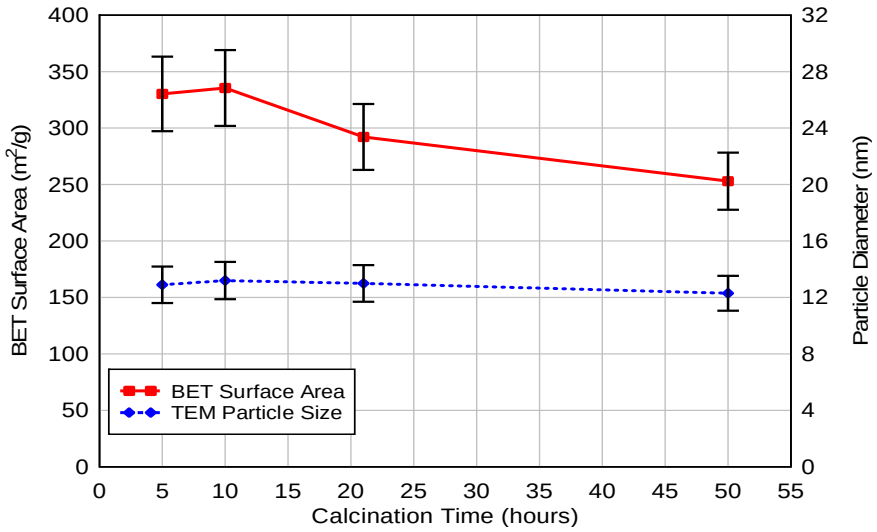

Figure 3: *Specific surface area and diameter of Pt particles in Pt-BHA vs. length of calcination. Calcination T=600°C. Vertical bars estimate 10% error due to experimental and measurement variability.*

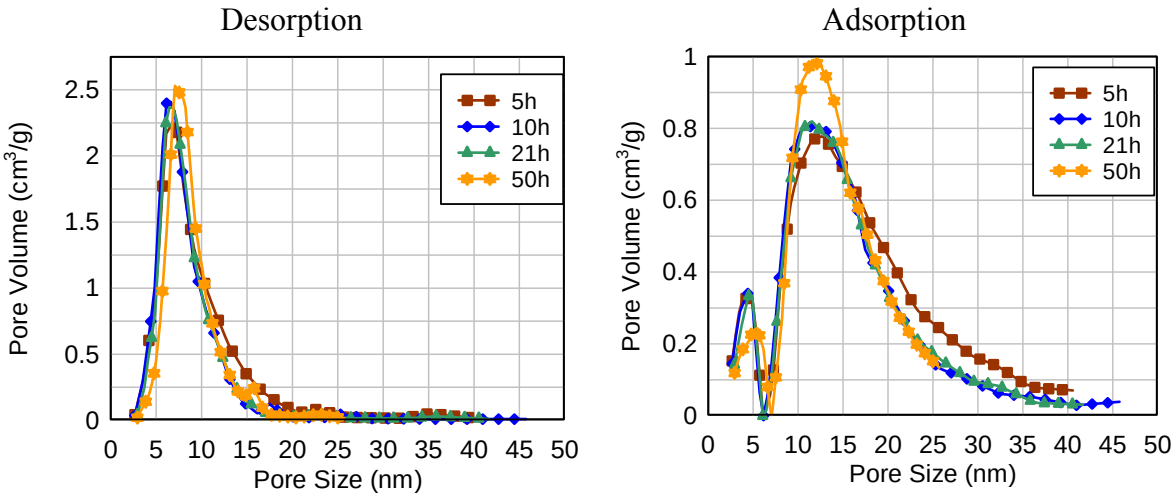

Figure 4: *Pore size distribution of Pt-BHA calcined for extended time periods, determined from BJH analysis of nitrogen adsorption isotherms. Left: size of pore necks from desorption isotherm. Right: size of pore cages from adsorption isotherm.*

These results indicate that the Pt-BHA nanocatalyst is thermally stable at 600°C, as one would expect considering the previously measured catalytic stability in CPOM reaction at much higher temperatures. The small decrease in specific surface area unaccompanied by a change in pore structure indicates that the majority of the material is stabilized, yet a small fraction of the ceramic structure (perhaps around the edges of the particulates) undergoes sintering without a significant decrease in pore volume. This localized sintering effect does not lead to Pt particle growth or changes in the pore structure, and thus it is unlikely to affect the catalytic activity of the nanocomposite. The results strongly confirm that the high-temperature stability of these materials is not simply a short-term kinetic effect, but a true thermal stability.

4.2.1.2 Environment

One of the major concerns with using any form of surfactant-templating approach (sol-gel, microemulsion) to form nanomaterials is the presence of hard-to-remove surfactant residues after synthesis. This is especially important for nanocatalysts, where surface accessibility of reactant molecules is crucial to the functionality of the material. Typically, removal is achieved via calcination – thermal degradation of surfactant material at high-temperatures (T > 450°C) in air. This type of treatment, while being highly effective at removing carbonaceous species, often leads to fundamental changes in surface properties, morphology, and structure of the remaining material. The combustion of long chain hydrocarbons (which is essentially what calcination consists of) is an extremely exothermic process (e.g. -10,700 kJ/mol for hexadecane combustion). The likely result of these exothermic reactions is higher temperatures (than the oven set point) at the surface of the calcined material. Most importantly for the purposes of Pt-BHA, this leads to Pt particle growth and therefore loss of catalytically active surface area. It therefore becomes important to develop a calcination procedure which can effectively remove

carbonaceous species from Pt particles and BHA pore structure while retaining (as much as possible) the nanoscale characteristics of the original, uncalcined material. One direction of interest is the use of an alternative reaction environment. Goworek and coworkers found that they could effectively remove the surfactant template from MCM-41 silica via treatment with hydrogen at temperatures as moderate as 250°C[130]. Their success in applying hydrogen calcination to the high aspect-ratio pores of MCM-41 indicates that similar treatments may be successful for Pt-BHA nanocomposites.

Separate fractions of a single batch of 10wt% Pt-BHA are calcined at 600°C in three different atmospheres – oxidative (flowing air), reducing (flowing hydrogen), and inert (flowing nitrogen). TEM is used to characterize the size and distribution of Pt-particles within the resulting calcined powders.

Figure 5 shows representative images of the Pt-BHA material after each of the calcination treatments, alongside the corresponding Pt particle diameter distributions. Both hydrogen and nitrogen treatment resulted in very narrow and small Pt particle size distributions (~2-3nm). Air treatment results in much larger particles (~9nm) with a wide size distribution. Additionally, the sample calcined in nitrogen appears to have BHA particles which are smoother and less textured than the hydrogen and air samples. This smooth appearance is the result of residual surfactant residing in the pore structure, as this appearance is typically evident in samples that are calcined at temperatures below the temperature of surfactant removal (~450°C).

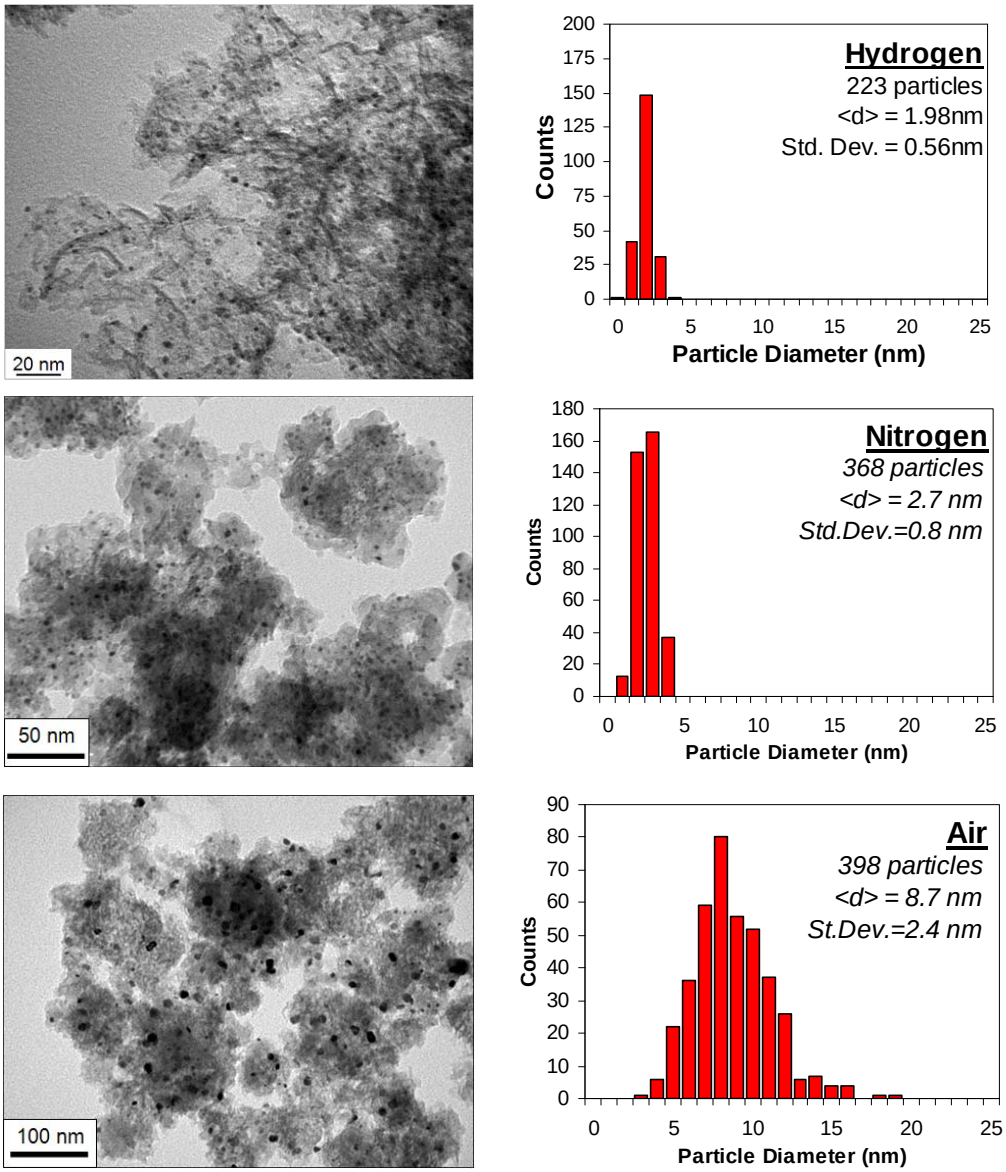

Figure 5: *TEM micrographs of 10 wt% Pt-BHA calcined at 530°C in hydrogen (top), and 600°C in flowing nitrogen (middle) and air (bottom) alongside particle size distributions.*

These results indicate that surfactant removal via combustion in flowing air results in strong growth of Pt particles. Calcination in nitrogen or hydrogen indicates that a very small particle size can be maintained at high temperatures in the absence of combustion reactions. There are two possible explanations for restrained particle growth in either treatment, both

resulting from poor removal of surfactant from the nanocomposite. The first is that the surfactant overlayer that remains on the platinum particles prevents sintering at high temperature. The other possibility is that surfactant combustion (and the resulting temperature excursion from this exothermic process) is responsible for particle sintering, and because this process does not occur or is limited during calcination, the nanoparticles remain small. It is not apparent from TEM images alone which explanation (or a combination of both) is responsible. Nitrogen treatment is expected to remove very little of the surfactant, because it relies solely on thermal degradation of the surfactant chains. Hydrogen treatment appears to be somewhat more effective at surfactant removal, when one considers the textured and porous appearance of the Pt-BHA nanocomposite compared with the smooth appearance of the nitrogen sample.

Another question arises in terms of the calcination environment – is a stagnant gas atmosphere sufficient for surfactant removal, or is continuous refreshing of the gases within the calcination chamber necessary? To obtain the answer, Pt-BHA nanocomposites are calcined in stagnant nitrogen for 5 hours, stagnant air for 5 hours, and stagnant air for 5 hours followed by flowing air for 1 hour. The resulting materials are examined with TEM and the resulting images and particle size distributions are shown in **Figure 6**.

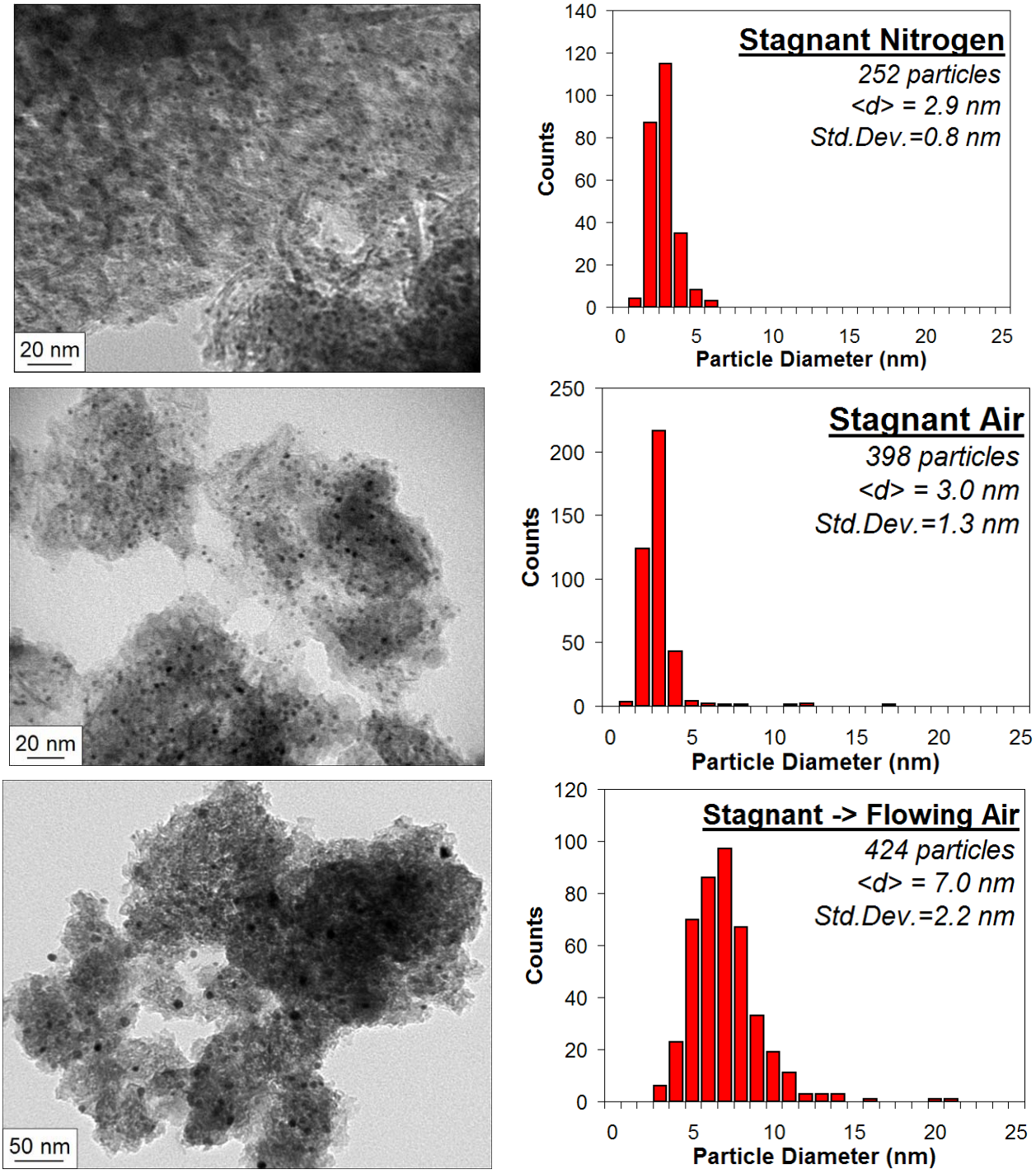

Figure 6: *TEM micrographs of 10wt% Pt-BHA calcined at 600°C in stagnant N_2 (top), stagnant air (mid), and flowing air following stagnant air (bottom) alongside particle size distributions.*

As expected from the treatment in flowing nitrogen, the sample calcined in stagnant nitrogen (top micrograph and histogram) does not show significant particle growth, and the BHA structure has a smooth appearance in the micrograph – indicating that residual surfactant remains in the structure. Interestingly, stagnant air calcination (middle micrograph and histogram) shows similar characteristics – a much smaller particle size than in the flowing air treatment, as well as a smooth texture. The stagnant environment is not sufficient to effectively remove residual surfactant. This makes sense if one considers that the surfactant combustion reaction requires an abundance of oxygen, and in the stagnant environment the oxygen is likely rapidly depleted at the surface of the Pt-BHA, leading to O_2 diffusion-limited surfactant removal. The presence of a few larger particles (>10nm) in the stagnant air sample are probably the result of surfactant calcination that occurs before these diffusion limitations become prevalent. When the sample calcined in stagnant air is then exposed to flowing air (bottom micrograph and histogram), one observes the rapid growth of platinum particles, and the emergence of a textured, porous appearance of the Pt-BHA in the micrograph. This further confirms that continuous refreshment of the oxygen atmosphere is necessary for effective calcination.

Flowing air calcination appears to be the most effective at removing surfactant – as well as being responsible for the most growth of the platinum nanoparticles. Flowing hydrogen treatment also shows potential, as evidenced by the porous, textured appearance of samples calcined in flowing hydrogen, as well as the promising results for this type of treatment by Goworek[130]. Both techniques are examined in further detail in the following sections.

Air Calcination

This section will describe the effect that calcination in air has on the structure and properties of the Pt-BHA nanocomposite. Mass spectrometry (MS) is used to monitor the

evolution of gases from the material, CO pulse chemisorption is used to evaluate the platinum surface area, and nitrogen porosimetry is used to evaluate the pore structure.

MS is used to monitor the calcination process as it proceeding. By observing the evolution of gases from the catalysts as they are heated it is possible to deduce the reactions taking place, and the temperature required for these reactions. These observations also allow one to evaluate the effectiveness of each treatment method.

Samples of pure BHA or 10 wt% Pt-BHA are placed into a quartz-glass U-tube reactor. Air or hydrogen is flowed through the sample at a rate of 30 cc/min. The U-tube is placed into a temperature-controlled reaction oven. The temperature in the oven is increased slowly over time, with typical ramping rate less than 5°C/min. The exhaust gases from the sample are monitored using MS. Mass numbers of interest are monitored continuously over time, and the full range of mass numbers (1-100) is periodically scanned to confirm which gases are evolving from the sample. Results of air calcination are shown in **Figure 7** and **Figure 8** while hydrogen calcination is shown below in **Figure 12**.

In air calcination (**Figure 7**), the combustion of hydrocarbon chains (residual surfactant) results in the evolution of CO_2 and water vapor. Both gases show similar temperature profiles for both Pt-BHA and pure BHA. Water vapor begins to form at ~200°C, and is no longer observed above ~450°C. CO_2 forms rapidly above ~150°C and also levels off at ~450°C. Partial oxidation products – CO and H_2 – were not observed in either sample. These results confirm previous MS measurements of CO_2 evolution which indicated that surfactant combustion was complete above ~450°C for this class of materials[13]. From these results it is also concluded that the Pt nanoparticles do not play a significant role in the surfactant removal process via combustion – as indicated by parallel pure BHA and Pt-BHA temperature profiles.

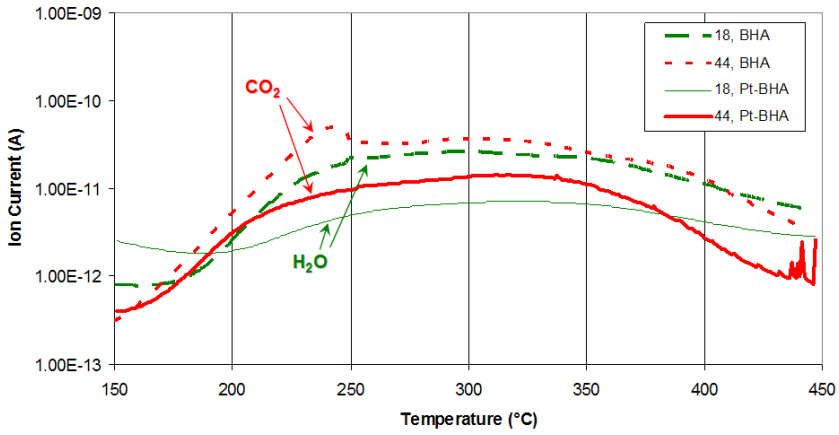

Figure 7: *Mass spectrometry of BHA and Pt-BHA calcined in air. Ramping rate = 4°C/min.*

The ramping rate of calcination in air becomes an important parameter as a result of the strong exothermicity of the surfactant combustion. As the ramping rate increases, there is a stronger possibility for uncontrolled burning of the surfactant due to feedback between the exothermic reaction and the rapidly increasing oven temperature. Uncontrolled surfactant combustion would result in steep temperature gradients within the material, and premature deactivation of the catalyst.

The effect of temperature ramping rate was examined in pure BHA and Pt-BHA nanomaterials. The air calcination was performed at three different ramping rates – 4, 5, and 7.5°C per minute. In each case the temperature was monitored with a thermocouple placed directly within the bed of nanomaterial. The exhaust gases were monitored with mass spectrometry. The results are shown for Pt-BHA in **Figure 8** – CO_2 signal is measured as a function of temperature at each ramping rate. Ramping rate experiments for pure BHA did not result in any temperature anomalies, so the results are not presented. At 4°C/min a smooth evolution of CO_2 is observed through the temperature range of interest. At both of the higher ramping rates, a strong evolution of CO_2 is measured – at ~250°C for 5°C/min and ~225°C for

7.5°C/min. In both cases a strong temperature overshoot was observed – as indicated by the backtracking of the CO_2 trace. Additionally, a noticeable decrease in oxygen signal was observed. As calcination continues past the temperature "spike", a lower CO_2 signal (relative to the sample that did not "spike") is measured between the "spike" temperature and ~350°C.

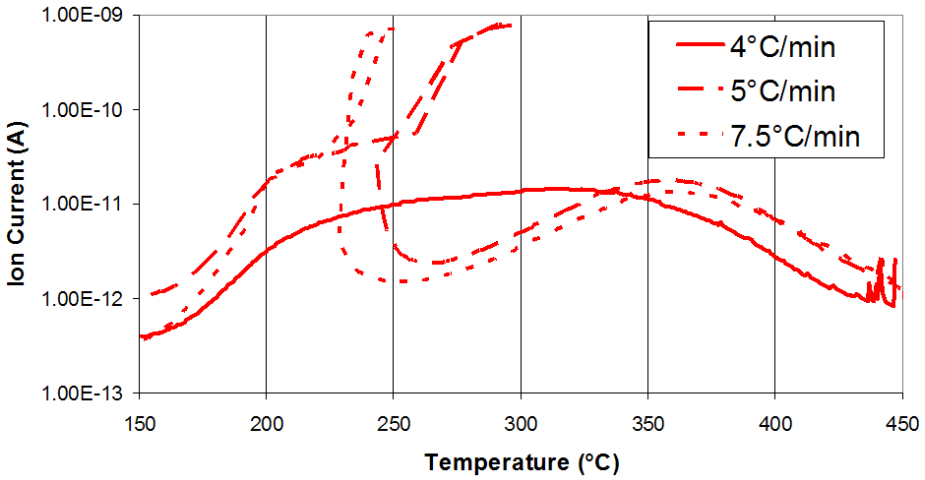

Figure 8: *Mass spectrometry measurement of CO_2 evolution from Pt-BHA calcined in air at temperature ramping rates of 4, 5, and 7.5°C/min.*

These observations indicate that uncontrolled surfactant ignition occurs in Pt-BHA nanocomposites when the temperature ramping rate is above 4°C/min. As the ramping rate increases, the feedback between the exothermic reaction and the increasing oven temperature grows stronger, and the ignition occurs at lower temperature. The resulting ignition consumes a large portion of surfactant at a lower temperature than when no ignition is observed. Although the measured maximum temperature of the ignition was relatively low, it is certainly possible (given the typically strong temperature gradients of combustion reactions) that localized temperatures within the nanostructure reached much higher temperatures.

The uncontrolled ignition of surfactant and subsequent temperature spike is expected to result in localized hot spots within the nanocomposite and consequently to sintering of Pt

nanoparticles. To test this hypothesis, the particle size of two samples is studied with TEM: one which did not experience an ignition event (4°C/min) and one which did (5°C/min). Both samples were calcined to a maximum temperature of 450°C. The resulting particle size distributions are shown in **Figure 9**.

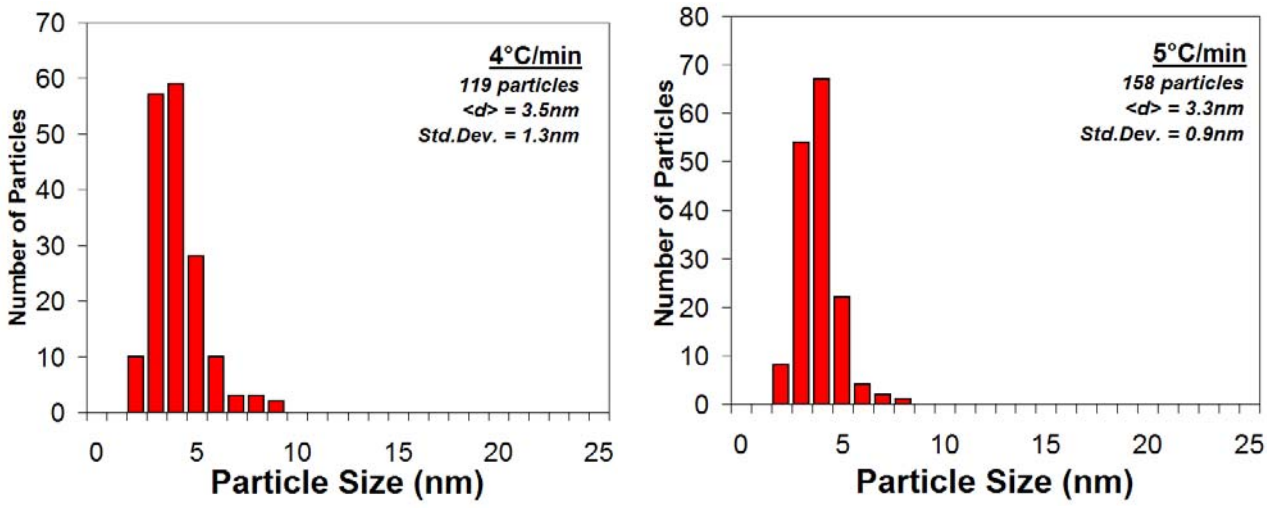

Figure 9: *Particle size distributions of Pt-BHA calcined in air at temperature ramping rates of 4°C/min (left graph) and 5°C/min (right graph). Determined from TEM images. Calcination T = 450°C.*

The particle size distributions of both samples are virtually indistinguishable. Both have mean diameter of ~3.4 nm with a standard deviation of ~1.1 nm. This indicates that localized heating does not occur, or at least does not result in significant particle growth at this temperature. Based on the inconsequential nature of this localized heating, subsequent air calcinations are typically run at 10-20 °C/min.

Another useful comparison basis for the effectiveness of the calcination treatments is the amount of exposed Pt surface area, which can be determined by pulse CO chemisorption. This measurement is an indication of the effectiveness of each treatment at removing surfactant from the surface of the Pt particles. Each treatment method is evaluated in a series of experiments

varying the calcination temperature (between 250-600°C) and duration of calcination (15m vs. 5h). Each sample was first calcined in the respective atmosphere for the indicated amount of time, removed from the oven for CO chemisorption measurement, and then returned for calcination at the next highest temperature. All samples were reduced for 5 minutes in hydrogen at 250°C after the calcination to ensure all platinum was in the zero-valent state. After the highest temperature is reached, the sample was imaged with TEM to obtain Pt particle size distributions. The results for air treatment are shown in **Figure 10**, with results for hydrogen treatment in **Figure 14**, below.

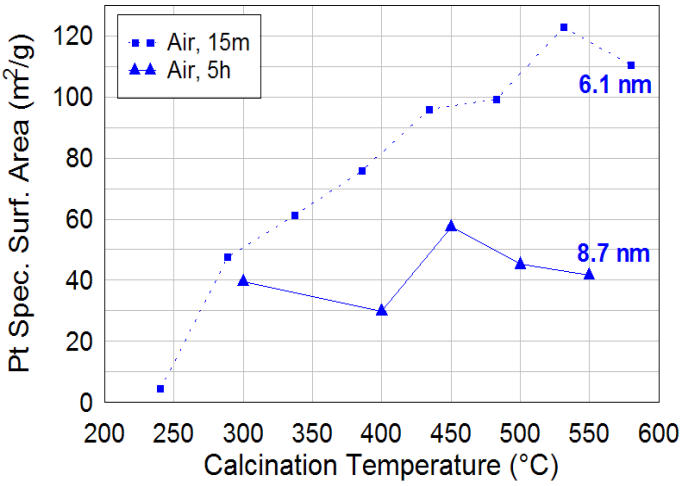

Figure 10: *Platinum specific surface area, determined via pulse CO chemisorption, of Pt-BHA catalysts calcined in air. Calcination was performed for both 15 minutes (dashed lines) and 5 hours (solid lines). Numbers indicate average Pt particle size, determined from TEM images, at the highest temperature measured.*

Figure 10 shows the results of the CO chemisorption measurement and the average Pt particle diameter at the highest temperature for air treatment. Calcination in air for 15 minutes is very effective at exposing platinum surface area (maximum of ~120 m^2/g @ 530°C). This effect

is kinetic, however, because similar treatment for 5 hours strongly reduces the measured Pt surface area (~40 m^2/g @ 550°C). Average Pt particle diameter increases by ~3nm in the sample treated for 5 hours as well.

Air treatment for 15 minutes effectively removes the majority of the surfactant from the surface of the particles while simultaneously retaining the small size of the nanoparticles. Extended treatment in air results in complete surfactant removal, but particle sintering under these conditions results in much lower Pt surface area.

An additional CO chemisorption measurement was made for calcination in nitrogen (included here for completeness). After 5 hours of calcination at 580°C, the resulting Pt surface area is ~10 m^2/g, further confirming the poor removal of surfactant in nitrogen treatment.

In order to determine the relative effectiveness of each treatment method at removing residual surfactant, a comparison is made between the actual and "theoretical" specific surface area. The "theoretical" specific surface area is a calculation of the specific surface area for perfectly spherical particles (without any occlusion) having the same size distribution as the particles measured in each of the samples (a weighted average). The fraction of surface area exposed is thus the actual surface area measured divided by the theoretical surface area, expressed as a percentage. **Table 2** lists the results of these calculations for the samples treated in both air and hydrogen.

Table 2: *Calculation of fraction surface area exposed for 10 wt% Pt-BHA catalysts calcined in hydrogen or air. Pt density = 21.09g/cm^3.*

Treatment method	Average Pt particle diameter [nm]	Measured Pt specific surface area [m^2/g]	Max theoretical specific surface area [m^2/g]	Fraction of surface area exposed [%]
Air, 15 mins, 580°C	6.1	110.5	59.0	187.3
Air, 5 hours, 550°C	8.7	41.7	35.2	118.5
H_2, 15 mins, 530°C	1.84	59.6	172.9	34.5
H_2, 5 hours, 530°C	1.98	31.9	161.5	19.8

The samples treated in air actually have a higher measured surface area than the "maximum" theoretical, 187.3% and 118.5% for 15 minutes and 5 hours respectively. An important factor must be considered in this calculation – even if the surfactant is completely removed from the nanocomposite, some fraction of the Pt particles will still be occluded by the ceramic structure. This fraction depends on how well embedded the Pt particles are in the ceramic walls – close to 0% for particles just contacting the surface of the BHA, and closer to 100% for particles which are 'buried' within the walls. Thus the theoretical specific surface areas reported here can be treated as a "maximum" specific surface area for that sample.

For Pt-BHA calcined in air it appears that most (if not all) of the surfactant has been combusted – surface areas are significantly higher than the theoretical maximum, and particle sizes are significantly larger than in hydrogen treated samples (discussed below). An explanation for the measured surface area being larger than "maximum" lies in the presence of very small (< 1 nm) Pt particles. These particles would contribute significantly to an increase in the measured specific surface area, while their presence would not affect the "maximum" because they are not resolved in the TEM micrographs and not included in the particle size distribution. The shape of the platinum particle distribution for the sample calcined for 15

minutes is right-skewed (see top graph in **Figure 19**). This means that a large fraction of the particles are smaller than the reported average, and also that there is an increased probability that particles below the detection limit of the TEM measurement are present. Additionally, smaller particles are more difficult to discern from the BHA framework – likely resulting in under-reporting of particles of smaller sizes. The smaller particles would have a larger "maximum" surface area, and would hence decrease the egregious value of 187.3% surface area exposed reported here. The BHA (without any Pt particles) does not adsorb any measurable quantity of CO, as determined in a separate investigation.

Residual surfactants will strongly influence the measurable pore volume/size in Pt-BHA nanocomposites. The surfactant might coat the walls of the pores – making them appear to be smaller in diameter and volume. It also might completely block some pores, leading to a decrease in pore volume without a corresponding decrease in pore diameter. Due to the potential influence of residual surfactant on pore structure, nitrogen porosimetry is used to evaluate the pore structure of Pt-BHA nanocomposites after both air and hydrogen treatments. BJH analysis of the nitrogen adsorption isotherms results in pore size distributions for each of the samples. **Figure 11** compares the pore structure for treatment in air for 15 minutes and 5 hours, with BHA calcined at 600°C in air for 5 hours included as a reference.

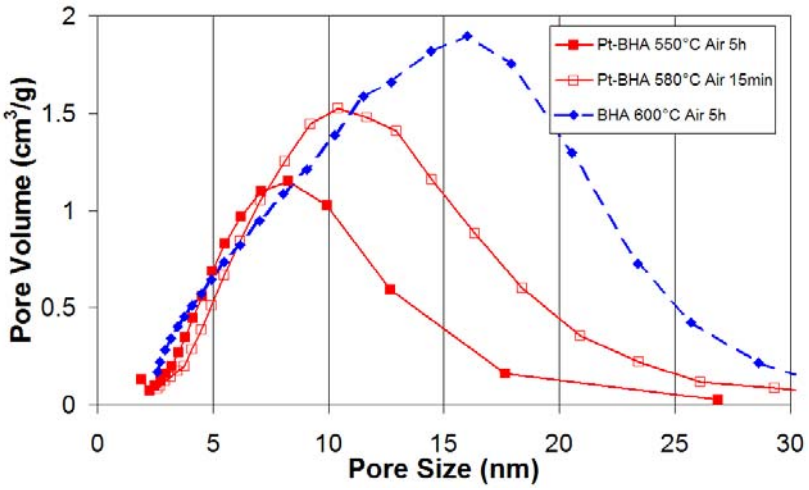

Figure 11: *Comparison of pore size distribution for BHA and Pt-BHA nanostructures calcined in air, determined by BJH analysis of nitrogen adsorption isotherms.*

For the samples calcined in air, the Pt particles are expected to have a large effect on the measured pore structure. Residual surfactant is not expected to influence the pore structure significantly because earlier measurements (Pt surface area) indicate that it is removed by the air treatment. Comparing the pure BHA (dashed line, solid diamond) with the Pt-BHA treated for 5 hours (solid line, filled squares), a strong decrease in both pore size and pore volume is observed. The pore volume decrease occurs exclusively in the largest pores, while smaller pores remain unaffected. Recalling that the adsorption isotherm yields information about both pore necks and pore cages, it is clear that this observation is entirely consistent with Pt particles residing in the larger BHA pore cages. Thus the observed pore structure is primarily that of the pore necks connecting the cages in the structure. This further supports our concept for the thermal stability of the Pt particles – the idea that each particle resides within a thermally stabilized pore cage in the BHA ceramic matrix. This cage restricts the growth of the Pt particle at high temperatures, leading to excellent thermal stability in extreme environments. The sample calcined for 15 minutes (solid line, open squares) does not show as strong a decrease in pore volume (for pore

diameters > 8nm) as the sample calcined for 5 hours. Earlier measurement indicates that the average Pt particle size is ~3 nm smaller for the material calcined for 15 minutes. This observation is also consistent with particles residing within the pore cages – in this case the particles are smaller and they occlude less of the pore volume in each cage.

Hydrogen calcination

This section discusses samples that have undergone calcination in hydrogen. The samples are analyzed with the same characterization tools (MS, pulse chemisorption, nitrogen porosimetry) as in the previous section on air calcination.

MS is used to evaluate the reactions taking place during hydrogen calcination. The results, plotted in **Figure 12**, indicate the formation of short chain hydrocarbons and a small amount of water vapor. Methane, ethane, and some propane are present in various concentrations in the exhaust stream, depending strongly on the calcination temperature. Interestingly, the temperature profile for pure BHA and Pt-BHA differ significantly. In pure BHA (top graph), all three hydrocarbons begin to form at ~200°C. Ethane and propane reach maximum at ~350°C, and are no longer detected above 550°C. Methane reaches its maximum closer to ~450°C and tapers off slowly as temperatures increase to 550°C. In Pt-BHA, ethane and propane evolution are roughly constant for large temperature ranges (300-375°C for ethane, 250-375°C for propane) before leveling off above 425°C. Methane production peaks strongly ~400° and is completed at ~475°C.

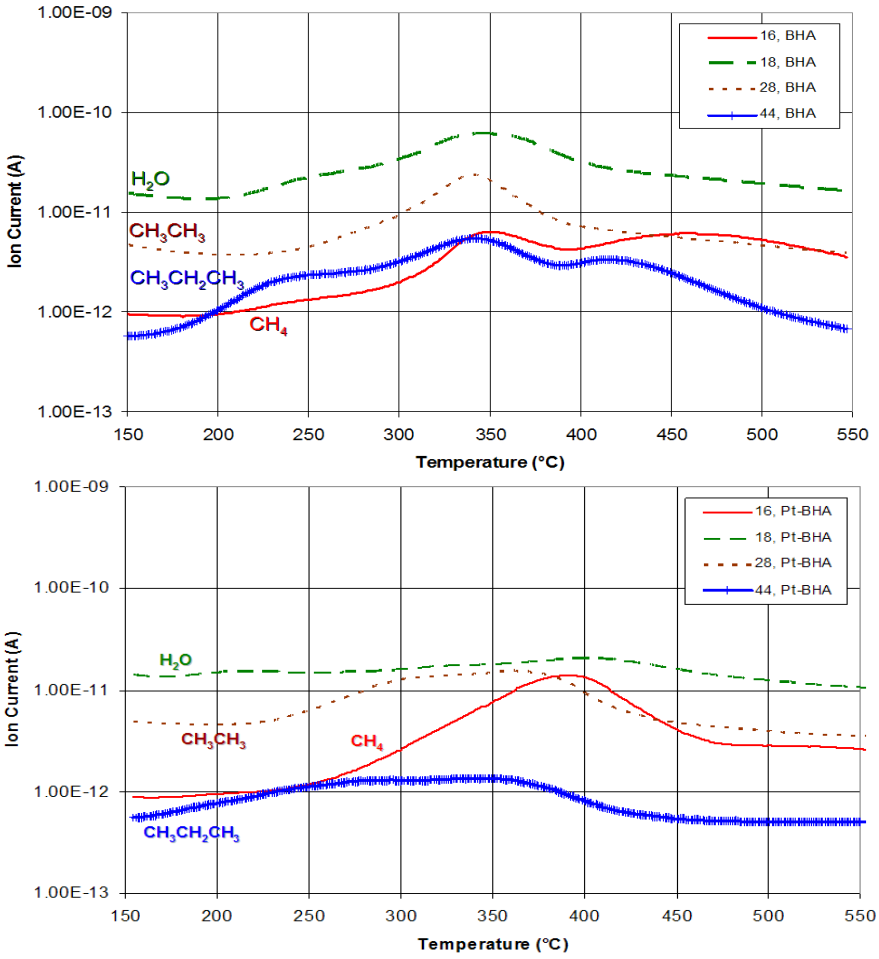

Figure 12: *Mass spectrometry of BHA (top graph) and Pt-BHA (bottom graph) calcined in hydrogen. Ramping rate = 5°C/min.*

These results indicate that high-temperature hydrogen treatment results in hydrogenolysis of residual carbonaceous species on the surface of the nanocomposite, and removal of a portion of these species as short-chain alkanes. This is not surprising since Pt has long been known to be an excellent catalyst for hydrocarbon hydrogenolysis[131]. In contrast with air treatment, Pt particles strongly influence the kinetics of surfactant removal in hydrogen treatment. Notably, the maximum methane evolution occurs at a lower temperature in Pt-BHA than pure BHA, a strong indication that catalytic reaction is occurring. When Pt particles are present in the catalyst

the reaction favors the production of methane (rather than ethane or propane) in the exhaust gas. These larger carbon species may be more strongly bound to the surface of the Pt nanoparticles. Studies of *n*-hexane hydrogenolysis over Pt catalysts have indicated that C-C bond cleaving is the likely rate-limiting step in systems containing excess hydrogen[132]. It is a strong possibility that slow C-C cleavage combined with strong affinity of longer chain molecules with the Pt surface is resulting primarily in the removal of surfactant as methane.

Incomplete surfactant removal by hydrogen treatment is confirmed by an additional MS analysis. After calcining in hydrogen as shown in **Figure 12**, a sample of 10 wt% Pt-BHA is calcined in air (while monitoring exhaust gas with MS). The result of this subsequent calcination is shown in **Figure 13**. The MS trace indicates that additional surfactant species are removed as combustion products – CO_2 and water vapor.

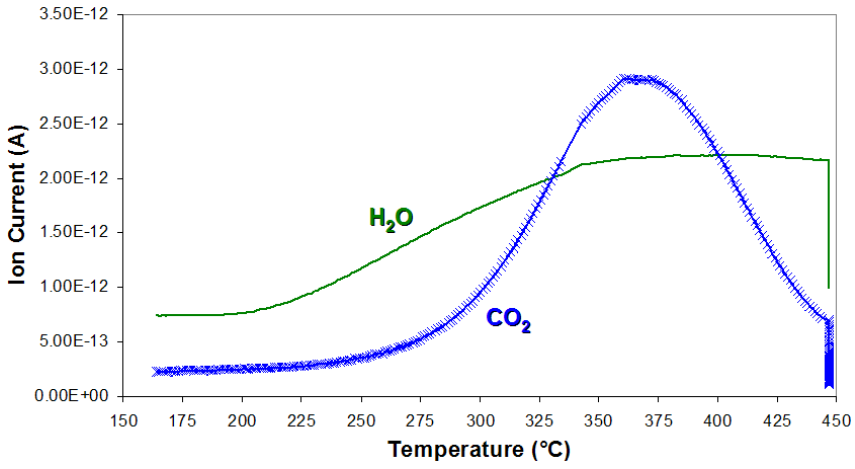

Figure 13: *Mass spectrometry of Pt-BHA calcined in air following hydrogen calcination up to 450°C. Ramp rate 5°C/min.*

Two important observations are made when comparing the evolution of the CO_2 peak in this testing with previous monitoring of air calcination of uncalcined samples (**Figure 7**). In simple air calcination, the onset of CO_2 evolution was at ~175°C. When the air calcination is

performed following hydrogen calcination, the onset of CO_2 evolution is delayed until ~275°C. This indicates that the surfactant residue remaining after hydrogen calcination is more difficult to remove, and thus requires a higher temperature. The second observation is in regards to the relative intensity of the CO_2 peak. In pure air calcination the peak is about an order of magnitude stronger in intensity than in the current measurement. This indicates that only a small portion of the original surfactant remains as difficult-to-oxidize residue after the hydrogen treatment.

Surfactant residue remaining after hydrogen treatment likely affects the availability of platinum surfaces within the catalyst – some of the residue may reside atop the platinum particles. Therefore, CO pulse chemisorption is used to evaluate the platinum surface area in samples after hydrogen treatment, and the results are shown in **Figure 14**. In these results, an interesting cross-over point is seen at ~330°C. Above this temperature, the trend is similar to air treatment (see **Figure 10**), with short calcination being marginally more effective at removing surfactant ($60 m^2/g$ vs. $30 m^2/g$ @ 530°C). This coincides with a ~0.1 nm increase in particle size for the longer treatment. Below the cross-over point long term calcination is more effective at exposing Pt surface area (~$55 m^2/g$ @ 300°C) than short term calcination (~$30 m^2/g$ @ 300°C). The cross-over temperature appears to be the temperature where difficult-to-remove surfactant species are removed. Below this point, prolonged treatment is necessary to remove surfactant and achieve large platinum surface areas. Above this point, a brief hydrogen treatment is effective at removing residual surfactant, while retaining small platinum particles and hence larger platinum surface areas.

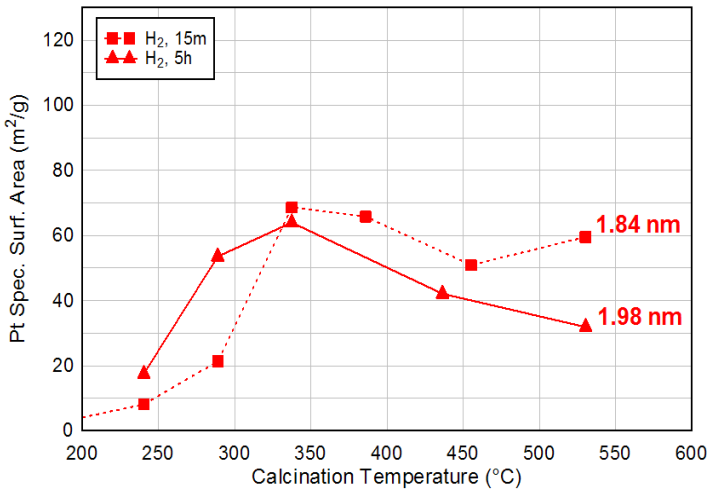

Figure 14: *Platinum specific surface area, determined via pulse CO chemisorption, of Pt-BHA catalysts calcined in hydrogen. Calcination was performed for both 15 minutes (dashed lines) and 5 hours (solid lines). Numbers indicate average Pt particle size, determined from TEM images, at the highest temperature measured.*

Hydrogen treatment shows potential as an effective method for removing residual surfactant while minimizing particle sintering. Measured Pt surface area for hydrogen treatment at 530°C is on-par with similar treatment in air, and the diameter of the resulting particles is more than 4 times smaller (2 nm vs. 9 in air). This indicates that surfactant removal is incomplete during hydrogen treatment, as much larger platinum surface areas are expected for these smaller particles.

The strong increase in Pt surface area for the sample calcined for 5 hours in the low-temperature regime also indicate that long-term, low temperature calcination in hydrogen could be effective. Goworek found that hydrogen calcination at ~250°C was an effective method for removal of surfactant template from MCM-41 materials, resulting in a carbon residue-free MCM-41. Prolonged calcination for 21 hours in hydrogen at 230°C resulted in a Pt surface area of only ~20 m^2/g, which is nearly identical to the result after 5 hours at this temperature (this data not included in the figure). The resulting low surface area (given the small platinum particle

size) indicates that Gowerek's results are not completely reproducible for Pt-BHA nanocomposites – surfactant residue remains on the platinum particles.

Further confirmation of remaining surfactant is seen when the fraction of the theoretical "maximum" platinum surface is analyzed for hydrogen treated samples. The results of this analysis are seen in the bottom two rows of **Table 2**. Samples treated in hydrogen, for 15 minutes and 5 hours, indicate that less than half of the "maximum" surface area of the particles is exposed, 34.5% and 19.8% for the 15 minute and 5 hour samples respectively. The results reiterate that hydrogen treatment is ineffective at completely removing surfactant from the surface of the Pt particles. This is a possible indication of why very small particles are observed for samples calcined in pure hydrogen – the surfactant residue residing on the surface of the particles restricts their growth.

BJH analysis of nitrogen isotherms are used to evaluate the role that this residual surfactant has on the pore structure of the hydrogen treated samples. The resulting pore size distributions for hydrogen treated BHA are shown in **Figure 15**. The pore size distribution for pure BHA calcined in air is also included as a reference (see discussion of **Figure 11**, above).

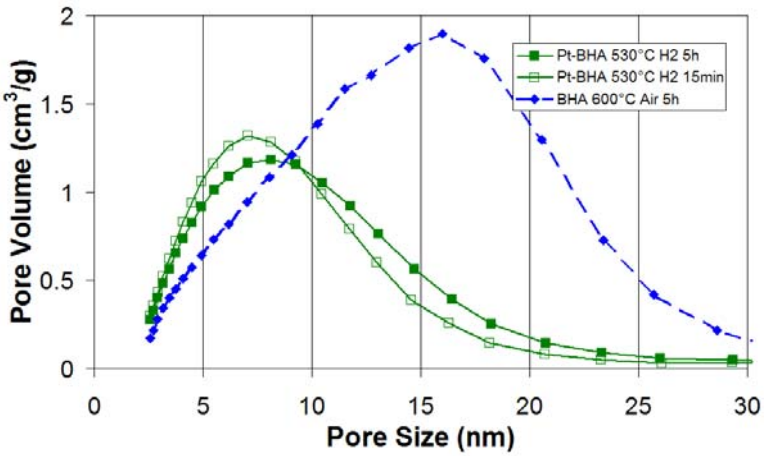

Figure 15: *Comparison of pore size distributions Pt-BHA nanostructures calcined in hydrogen (and BHA calcined in air for reference), determined by BJH analysis of nitrogen adsorption isotherms.*

In samples calcined in hydrogen (**Figure 15**), surfactant remains on the nanocomposite and is expected to strongly influence the observed pore structure. Both samples (15m and 5h) show similar pore structures, with strong decreases in pore volume for large diameter pores, yet increased pore volume for the smallest pores (diameter < 9 nm). Comparing the samples treated with hydrogen with the BHA sample calcined in air, one notices an increase in pore volume at small pore diameters. This effect is slightly more pronounced in the sample calcined for 15 minutes in hydrogen. This observation is consistent with hydrogen treatment being more selective at removing the surfactant in the smaller pore necks. This results in the observation that there is a larger volume of necks (per gram of sample) than in the pure BHA material, which can be assumed to be surfactant-free based on CO pulse chemisorption analysis of similarly treated Pt-BHA samples (see discussion of air calcination, above). The decrease in pore volume for larger diameters observed in hydrogen treated samples compared with the air-treated pure BHA is presumably due to the presence of small Pt particles in the pore cages and necks which

are coated with a layer of residual surfactant thick enough to completely block the majority of the pore cage structure.

Summary

Calcination of Pt-BHA and BHA nanomaterials was performed in three different calcination environments – nitrogen, air, and hydrogen. Nitrogen treatment was ineffective at removing residual surfactants. The resulting materials had very small Pt nanoparticles (~2nm), but virtually no exposed Pt surface area. Calcination in air resulted in complete surfactant removal via combustion. The Pt particles in these materials had very large specific surface areas, but grew significantly – up to diameter of ~9 nm @ 580°C. Porosimetry indicates that particle growth occurs primarily in the large pore cages of the BHA structure – an observation that correlates well with the observed thermal stability of this class of nanocomposites. Hydrogen treatment is marginally effective - surfactant removal proceeds via hydrogenolysis, but subsequent air calcination indicates that surfactant removal is incomplete. Platinum particles remained ~2 nm, similar to samples treated with nitrogen, but significant Pt surface area was measured. Porosimetry indicates that surfactant removal occurs primarily from the small diameter pore necks, with larger pore cages clogged by surfactant-laden Pt particles.

4.2.2 Washing of catalyst

From the testing of various calcination methods discussed previously, it is observed that residual surfactant in the pore network may be playing a role in the final structure of the nanocomposite and stability of the Pt nanoparticles. It seems likely that removing the surfactant in a controlled manner prior to calcination will result in more stable, better defined, and more ordered

nanocomposite. Washing the uncalcined, surfactant-laden material with a suitable solvent is a logical choice. A successful washing step would eliminate the exothermic combustion of the surfactant, which should effectively result in the nanoparticles experiencing lower calcination temperatures at any given point. For example, Lutensol XP30 surfactant contains 16 carbons and can be approximated (to simplify thermodynamic calculations) by hexadecane. The combustion reaction for hexadecane is shown below and is significantly larger than the heat of reaction for CPOM (-37 kJ/mol). Even for the relatively small amount of surfactant remaining, this could be detrimental to the stability of the platinum particles.

$$C_{16}H_{34} + 49/2\ O_2 \Longrightarrow 16\ CO_2 + 17\ H_2O \qquad \Delta H_r = -10700\ kJ/mol$$

Washing might also lead to a significant growth of the Pt particles. Previous results have indicated that residual surfactants are important for maintaining small particle sizes during calcination in nitrogen or hydrogen. If these surfactants are removed prior to calcination, significant growth of Pt particles is expected at lower temperatures.

A number of different washing techniques, including: physical mixing in water, acetone, and methylene chloride, as well as refluxing in acetone and methylene chloride are evaluated as washing techniques to remove surfactant material prior to calcination. These solvents are chosen to cover a wide range of hydrophobic and hydrophilic surfactant species which may be present on the surface of the catalysts. Somewhat less conventional techniques such as oxygen plasma and ozonolysis are also examined. Results of these treatments and possibilities for future research in this area are included in Appendix C.

4.3 TAILORING VIA SYNTHESIS PARAMETERS

One of the key aspects of the Pt-BHA nanocomposite synthesis method – microemulsion templated sol-gel – is the numerous ways that it allows for tailoring the catalyst structure. Simply changing the relative molar ratio of water-to-surfactant (R_W value) allows for some level of control over the size of the micelles within the microemulsion. The Pt-BHA precursors react within each of these micelles, and so there is a strong possibility that their size will influence the final structure of the nanocatalyst. A preliminary investigation of the properties of Pt-BHA as a function of R_W value is given in Appendix D.

Another important handle that the microemulsion-based synthesis method affords is the concentration and structure of the templating surfactant. The surfactant plays an important role in determining the size and surface properties of the micelles within the microemulsion, and therefore an important role in the structure of the nanocatalyst for the same reason that the R_W value does. Additionally, the surfactant (in one form or another) remains on material as it dries, and is removed via combustion during the calcination procedure. Thus, the surfactant has the potential to influence the properties of the nanocomposite throughout the entire synthesis process. A preliminary investigation of one particular surfactant property – hydrophilic chain length – is given in Appendix D.

4.4 INVESTIGATION OF NANOPARTICLE HIGH-TEMPERATURE STABILITY

The temperature of calcination is one of the most important parameters in the pre-treatment of a catalytic material, especially for noble-metal based nanocomposites. Generally, a catalyst is

calcined to a temperature above the reaction temperature of interest. This ensures that any changes imparted by the high-temperature take place within the controlled calcination environment, and not during the reaction itself. The most widely recognized deactivation phenomena for supported metal catalysts is sintering of the active metal component[133]. Sintering of the support ceramic might also occur during the high-temperature treatment, leading to changing pore structure and surface area[134]. Surfactant residue remaining from previous synthesis steps can be removed from the active surface, thus improving the catalyst activity[70]. Calcination at high-temperature may induce crystallization of particular phases of a catalyst material, typically resulting in decreased stability[135]. Finally, solid-state reactions between active metal and support can become important at high temperatures in some systems, most notably NiO-MgO[136].

The effect of calcination temperature on the size of the active Pt nanoparticles is particularly important as their size determines the total amount of active sites available, and thus the activity of the catalyst. Some studies have found that the particle size itself (regardless of geometric considerations such as increased surface area) may be responsible for increased activity in nanomaterials[5]. Many reactions that are important for clean energy production, such as CPOM and catalytic methane combustion, run at particularly high temperatures (T > 800°C). At these temperatures, platinum particles are expected to sinter, leading to catalyst deactivation[133]. However, previous studies have indicated that significant particle growth does not occur for Pt-BHA nanocomposites, even after long periods of exposure to high-temperature conditions[13, 14]. The goal of this study is thus to determine the reason for the high-temperature stability previously observed.

4.4.1 Pt particle size with increasing temperature

Because of the strong influence that high-temperature calcination is expected to have on the size of noble metal nanoparticles, as well as the increased catalytic activity of nanoparticle catalysts, it was decided to investigate the size of the Pt particles as a function of temperature. In this way, we can further develop our understanding of these novel nanocomposite catalysts and move toward establishing the origin of high-T stability.

Platinum particle size distributions are determined from TEM images of Pt-BHA nanocomposite calcined for 5 hours in air at 50°C intervals in the range of 250°C to 1200°C. Histograms of the Pt particle size distributions are shown for select temperatures (300, 600, 900, and 1200°C) in **Figure 16** (right side) along with representative TEM images (left side). From 300-900°C, the platinum particles remain homogeneously distributed within the ceramic BHA matrix (see TEM images), and as the calcination temperature increases, the average particle size increases (2.7nm @ 300°C to 8.7nm @ 600°C to 15.3nm @ 900°C) and the distribution of particles becomes wider (σ = 0.65nm @ 300°C to σ = 2.4 nm @ 600°C to σ = 4.6nm @ 900°C). This behavior is expected – continual growth of metal particles is typical across this temperature range. The size of the particles at 300°C and 600°C agrees reasonably well with published literature. At 300°C particles with average diameters of 2.56 and 2.77 nm are found on carbon black[137]. At 600°C, ~8 nm particles are present on carbon nanotubes[138], while ~12 nm particles are found on alumina at this temperature[139]. Data for platinum particle sizes at 900°C is not found in the published literature, with most papers claiming severe particle sintering and/or catalyst deactivation at these temperatures. Interestingly, that is not the case for these nanocomposite materials. At 1200°C, the platinum particles are poorly distributed, and have grown drastically in size (d_{Pt} > 100 nm). Previous work in our group indicates that this

temperature roughly corresponds to crystallization of the amorphous BHA matrix and collapse of the pore network[13].

The stability of Pt particles up to 900°C confirms our previous work showing excellent high-temperature stability of these nanocomposite materials[13, 14]. In order to track the Pt particle growth as the calcination temperature increases, and gain further understanding of the mechanism of growth, the mean Pt particle size is plotted versus calcination temperature in **Figure 17** (squares, left axis). Four distinct temperature regimes are present: a low temperature regime (T<550°C) where small Pt particles (d_{Pt} ≈3nm) are stable, a transition region (550<T<650°C) where strong particle growth (d_{Pt} ≈13nm) occurs, a stabilization regime (650<T<950°C) where the Pt particles remain stable d_{Pt} ≈13-15nm; and a high temperature region (T>950°C) where extensive Pt particle growth sets in. The specific platinum surface area, determined by CO pulse chemisorption, is also plotted in **Figure 17** (diamonds, right axis). The specific Pt surface area shows an increase in the low-temperature regime at ~450°, followed by a strong decrease in the transition region, leveling off at low (~3 m^2/g) values in the high temperature region before decreasing to <1 m^2/g at 1000°C and above.

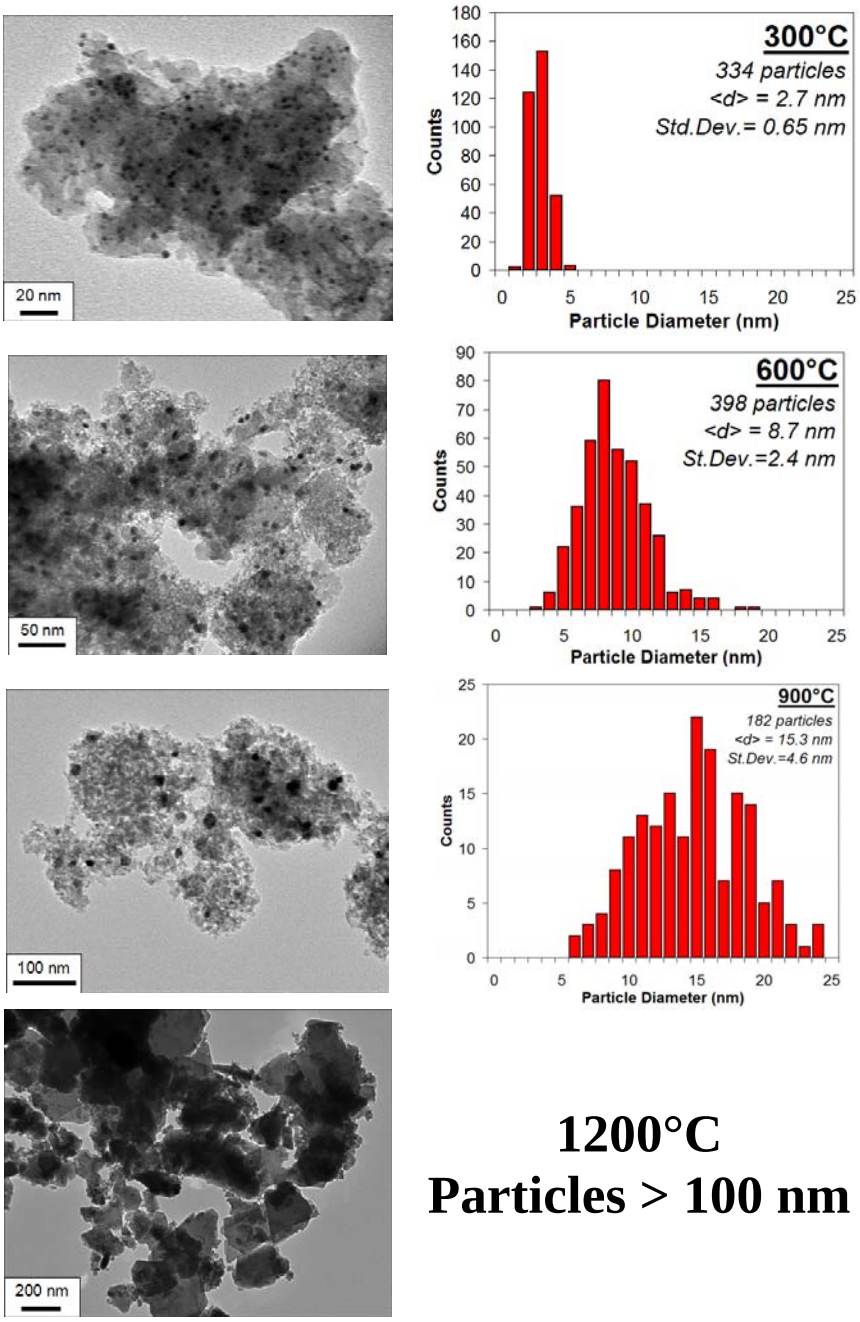

Figure 16: *TEM pictures of Pt-BHA and corresponding particle size distributions for samples calcined at 300, 600, 900, and 1200°C for 5 hours in flowing air.*

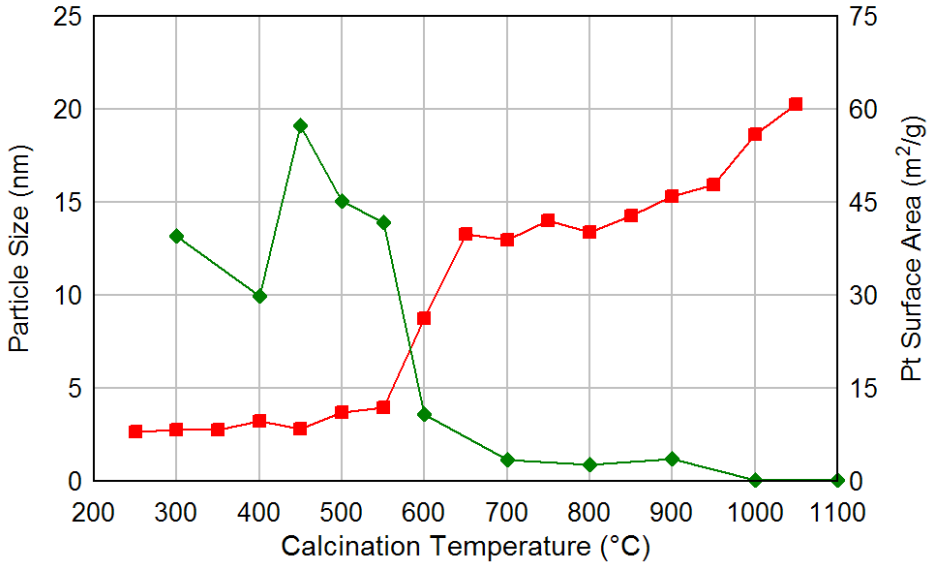

Figure 17: *Mean platinum particle size (left axis, squares) and specific platinum surface area (right axis, diamonds) versus calcination temperature. Calcination was in flowing air for 5 hours. Platinum surface area was determined via pulse CO chemisorption after each sample was reduced in H2 for 30 minutes.*

In the low temperature regime, the platinum particles are kinetically stable at their small sizes, as evidenced by the lack of particle growth. The reaction temperature it too low to allow sufficient particle mobility for sintering. The strong increase in the platinum surface area at 450°C can be attributed to surfactant removal in the form of CO_2 (surfactant combustion) as described previously[13]. In the transition region, sintering begins to take place as seen by the sharp increase in Pt particle size and the strong decrease in Pt surface area. As temperature increases, the particles become increasingly mobile and they are prone to sintering. For the Pt nanoparticles within the BHA matrix, however, very little particle growth occurs across a wide temperature range (650 – 950°C). This effect is highly surprising – with this strong increase in temperature the particles are expected to become increasingly mobile and sintering should proceed rapidly. It is not until temperatures as high as 1000°C are reached that further

significant Pt particle growth is measured, and not until 1200°C that the particles destabilize completely. This unexpected stability accounts for the strong, sustained catalytic activity of these materials in high temperature reactions such as CPOM[14]. The ability to maintain nano-sized active metal particles at high temperature is tremendously important in the field of catalysis. These nanocomposites have the potential to open up reaction systems previously thought inaccessible to metal catalysts – high temperature reactions such as catalytic combustion. It is important, therefore, to fully understand the mechanism behind particle stability if it is to be applied in other reaction systems. The fundamental reason for the unexpected stability of platinum particles within the Pt-BHA nanocomposite – attributed to a particle "caging" effect - is explored further in section 4.4.4.

4.4.2 Controlling Pt particle size at moderate temperatures

Interest in nanocatalysts has grown considerably since the discovery of novel reactivity for these materials in narrow size regimes. For example, gold nanoparticles become excellent oxidation catalysts at a diameter of ~3 nm[6]. In order to identify novel chemical reactivity associated with the size of the active nanoparticles, one must be able to reliably form a nanocomposite with a narrow active particle size distribution within the "nano-effect" regime where novel reactivity is expected.

As discussed in section 4.4.1, the platinum particles display kinetic stability at temperatures ~550°C and below – the temperature is insufficient to cause particle mobility and significant growth. By taking advantage of this slow, kinetically-controlled process it should, in principle, be possible to form Pt-BHA nanocomposites with average platinum particles sizes in the interesting "nano-effect" regime of around 3 nm. In this section, the ability to control the Pt

nanoparticle diameter by adjusting the calcination temperature inside of a narrow window in demonstrated.

Table 3: *Average particle diameter and standard deviation, determined from TEM micrographs, for 10 wt% Pt-BHA catalysts calcined between 475 – 575 °C. Data courtesy of Yi Zhang.*

Calcination Temperature [°C]	Conditions	Average particle diameter [nm]
475	5 vol% O_2, 80 min	2.9 ± 0.8
475	5 vol% O_2, 30 min	3.1 ± 0.8
500	5 vol% O_2, 30 min	3.3 ± 1.0
530	5 vol% O_2, 30 min	4.0 ± 1.1
575	5 vol% O_2, 30 min	4.5 ± 1.3
575	5 vol% O_2, 30 min	4.7 ± 1.4

Pt-BHA nanocomposites containing 10 wt% Pt, which were pre-calcined at 350^{o}C for 5 hours to remove the majority of remaining surfactant, are calcined in 5 vol% of oxygen in Helium at flow rate of 30 SCCM in a narrow window between 475-575°C. This temperature window is chosen based on previously presented results which indicated incomplete surfactant removal at temperatures below 450°C, and strong Pt particle growth above 600°C (section 4.4.1). Based on those previous results (see **Figure 17**), an average particle diameter of 3-7 nm is expected for this temperature window. After calcination, each catalyst is reduced at 350°C in pure hydrogen for 30 minutes, and heated in helium at ~570°C for 1 hour. The resulting powder is examined with TEM microscopy, and the average particle diameter is determined by counting more than 150 individual Pt particles. The results of this characterization are shown in **Table 3**. The average particle size increases monotonically from 2.9 to 4.7 nm as the calcination temperature increases from 475 to 575°C. The standard deviation of the particle size also increases with temperature but remains relatively small, ranging from 0.8 to 1.4 nm. Additionally, the particle size distribution is not strongly affected by the length of time of the

calcinations. Nearly identical particle size distributions (differing by only 0.2 nm) are found for samples calcined at 475°C for both 30 and 80 minutes, as well as for the sample calcined at 575°C for 30 minutes repeatedly. This seems to indicate that the platinum particles are stable at each of these temperatures, and further growth is not expected for continued calcination at the same temperature.

The results confirm that very narrow particle size distributions can be obtained in the "nano-effect" regime for Pt-BHA nanocomposites. Materials calcined in the manner described are expected to be crucial for the evaluation of catalytic activity vs. particle size, especially for low-temperature reactions (e.g. preferential oxidation of CO).

4.4.3 BHA pore structure vs. temperature

It is hypothesized that the BHA (a high-temperature stable ceramic material) is imparting its stabilization onto the Pt particles at high temperature. In this way, the pore network can be viewed as a template for Pt particle growth. It was previously established that BHA is a mesoporous material with pure textural porosity[13]. This means that the material consists of a collection of dense BHA nanoparticulates (with no internal porosity). Narrow spaces between the nanoparticulates are termed "pore necks", while larger voids within the packing arrangement of the nanoparticulates are termed "pore cages". The smaller pore necks are expected to be more restrictive to the growth of Pt particles. In order to determine the nature of the interaction between the Pt particles and BHA pore necks, the pore structure of BHA is investigated via BJH analysis of nitrogen desorption isotherms. The desorption isotherm can be used to directly measure the size of the pore necks for this structure of nanocomposite material[140].

The pure BHA material was calcined in the same temperature range (200-1200°C) as the Pt-BHA material in section 4.4.1, and the pore size distributions are plotted in **Figure 18**. The size distributions are split between low temperatures (200-600°C, left graph) and high temperatures (600-1100°C, right graph) for clarity. At low temperatures (200-400°C), the pore necks strongly increase in volume at constant pore size. Between 400°C and 900°C there is no change in the diameter or volume of the pore necks. At 900°C and above the pore necks grow significantly in diameter and their volume decreases.

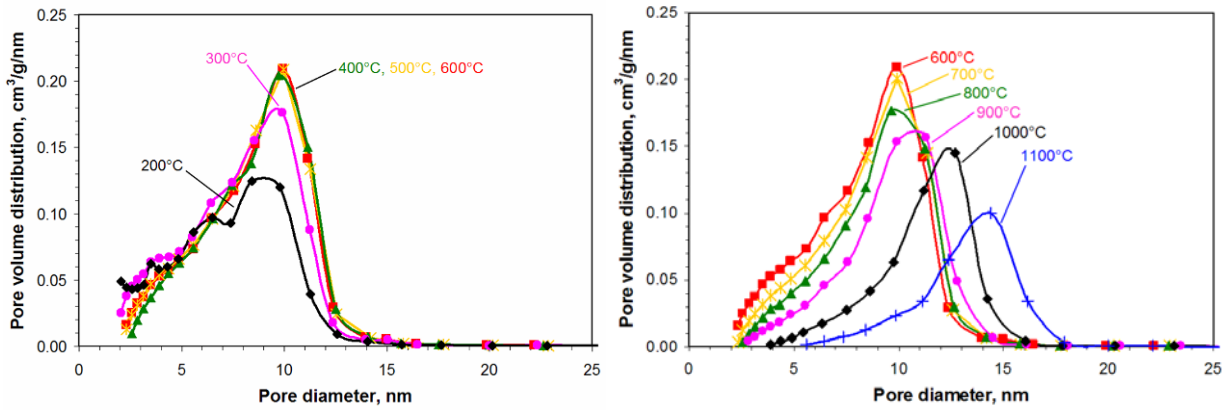

Figure 18: *Comparison of the size of the pore necks of pure (containing no metal) BHA at calcination temperatures between 200-600°C (left graph) and 600-1100°C (right graph). The size of the BHA pore necks were determined from BJH analysis of nitrogen desorption isotherms after 5 hours of calcination at each of the temperatures listed.*

The increasing volume of the pore structure at low temperatures can be attributed to surfactant removal via the calcination process (as discussed previously in section 4.4.1). The intermediate regime (between 400-900°C), where the BHA material is completely stable, is particularly interesting in terms of templating of Pt particles. In this same temperature range the Pt particles also reach a stable size (see discussion of Pt "stabilization" regime above). The strong thermal stability of the BHA correlates strongly with restricted growth of Pt particles at temperatures between 650°C and 950°C. The idea that the BHA pores are responsible for

restraining particle growth is strengthened by the fact that the average Pt particle size (≈13-15nm) is slightly larger than the average pore size (≈10-11nm) in this temperature range. The particles are unable to grow further because the pore necks are too small to allow particle migration. At 900°C and above the pore necks of the BHA begin to expand, and this is attributed to the onset of pre-crystallization of the BHA material at these elevated temperatures. This explanation is likely because full crystallization of BHA occurs at ~1200°C as documented previously[13]. Additionally, destabilization of the BHA structure above 900°C correlates directly with the temperature at which increased sintering of the Pt particles begins to occur (see **Figure 17**). A thorough investigation of this particle "caging" effect is discussed in the following section.

4.4.4 Particle caging effect

In this section, Pt particle size distributions are directly compared to BHA pore size distributions in order to definitively establish that the BHA pore necks are leading to a Pt particle caging effect. The size distribution of Pt particles is measured at both 15 minutes and 5 hours at 600°C. Earlier studies of calcination conditions established that after 15 minutes at ~600°C the residual surfactant has been removed from the Pt-BHA structure (see section 4.2.1.2), and the surface of the Pt particles is accessible for reactions (see section 4.4.1 and **Figure 10** above). Continued calcination at this temperature is expected to lead to substantial sintering and a wide dispersion of Pt particle sizes. The pore size distribution for pure BHA calcined at 600°C for 5 hours is overlaid with particle size distributions for Pt-BHA after 15 minutes (top graph) and after 5 hours (bottom graph) at the same temperature in **Figure 19**.

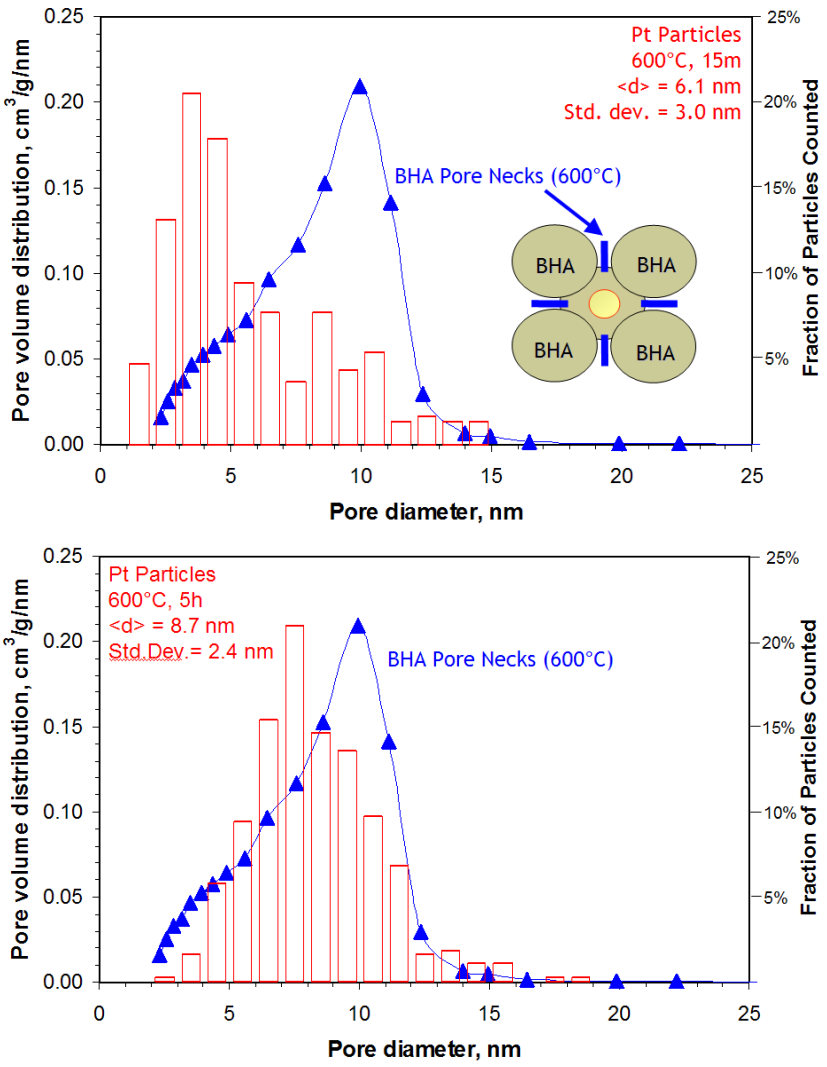

Figure 19: *Comparison between Pt particle size in Pt-BHA (histogram, right y-axis) and the size of pure (containing no metal) BHA pore necks (triangles, left y-axis). Top plot: Pt particles after 15 minutes of calcination at 600°C. Bottom plot: after 5 hrs. In all plots the size of the BHA pore necks were determined from BJH analysis of the nitrogen desorption isotherm after calcination at 600°C. Pt particle statistics were determined from TEM micrographs.*

The size distribution of the BHA pore necks at 600°C (line graph with triangles in both graphs of **Figure 19**) begins at 2 nm, reaches a maximum around 10 nm, and tapers off sharply – no pores are observed above ~17 nm. In comparison, the platinum particles after 15 minutes of calcination (top bar graph in **Figure 19**) appear across a wide range of sizes from 1 nm to 15 nm

- the largest particles observed correlate well with the largest pore neck diameter observed. The particle size distribution is skewed toward smaller particles, leading to an average particle size of 6.1 nm. After 5 hours of calcination (bottom bar graph in **Figure 19**), the average particle size increases to 8.7 nm. The range of particle sizes does not increase significantly – particles are observed from 2-19 nm. The smallest particles (those that are smaller than the majority of the pore necks) have grown significantly leading to a size distribution that is well distributed well around the average – the strong skewing observed after 15 minutes is no longer evident. However, the largest particles observed after 5 hours of calcination (~18-19 nm) are only slightly larger than the size of the largest pore necks (~17 nm). One would expect (for the case of unrestrained growth) that the largest particles observed after 15 minutes would grow substantially after 5 hours, yet instead the largest particles observed are only slightly larger than those in the material calcined for 15 minutes. Only a very small fraction (< 1%) of particles are larger than the widest pore necks. This is a strong indication that particle sintering is severely restricted at this temperature for platinum particles near the maximum size of the pore necks of the ceramic structure, and that the pore necks are responsible for this sintering resistance.

The dispersion of the platinum particle size distribution after calcination provides further evidence of a pore caging effect. A standard deviation of 3.0 nm is observed after 15 minutes of calcination at 600°C. The standard deviation decreases to 2.4 nm after 5 hours of calcination. This is counter to the typical behavior of particles that undergo an increase in average size – typically the standard deviation increases with increasing particle size[141, 142]. The narrowing of the particle size distribution after 5 hours of calcination is a strong indication that the hypothesis is correct – pore necks are restraining the growth of the largest particles (~15 nm), while the

smallest particles are undergoing further growth until they are also restrained. This leads to the narrowing of the platinum particle size distribution that is observed.

The strong correlation between the pore structure and platinum particle size provides evidence that the platinum particles reside within the pore cages of the BHA and are restrained from growth by the size of the pore necks. This conclusion is further supported by TEM, which is used to obtain high-magnification images of the Pt-BHA structure. To overcome the 2D nature of standard TEM images and obtain information about the 3D structure of the nanocomposite, a series of images is taken after tilting and rotating the sample within the microscope. In this way, direct visual evidence of the platinum particles "caged" within the ceramic can be obtained. A cartoon is presented in **Figure 20** that shows how these measurements are made and how they reveal information about the 3D structure.

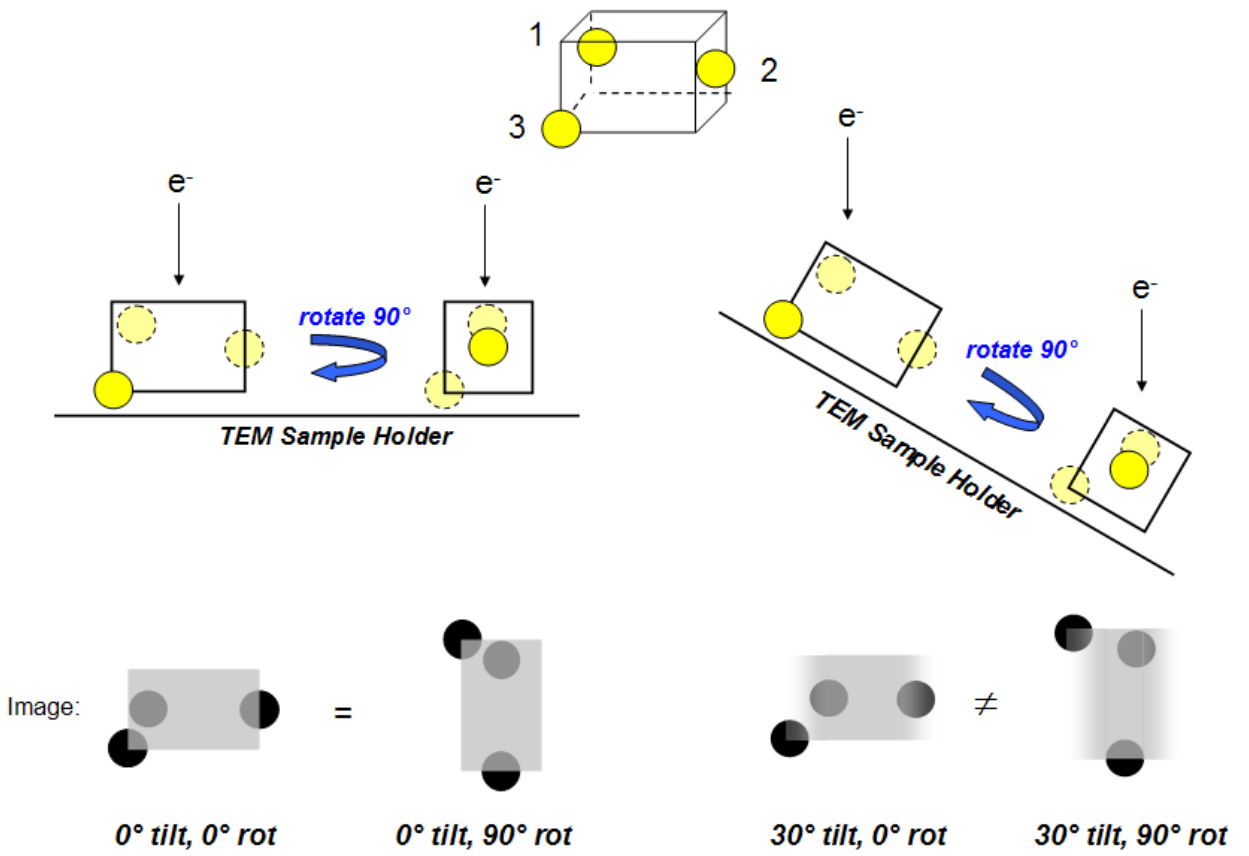

Figure 20: *Cartoon depicting tilt-rotation measurements using the TEM. The top image depicts the structure of a hypothetical particulate of Pt-BHA with yellow spheres representing Pt particles and the transparent rectangular box representing the BHA. The middle shows the orientation of the Pt-BHA particulate on the TEM sample holder as it is both tilted and rotated. At the bottom, the resulting TEM images from each type of sample holder manipulation are shown.*

The cartoon depicts a hypothetical Pt-BHA particulate that has platinum particles (yellow circles) residing in 3 different possible orientations within the ceramic (rectangular prism). One particle resides completely "caged" within the ceramic (labeled 1), one is partially "caged" in the side of the ceramic (labeled 2), and one rests outside of the ceramic structure on the corner (labeled 3). Each of these cases is possible in the real Pt-BHA structure, and the depiction presented here should allow the reader to understand how each of these orientations will be observed in the tilt-rotation experiment. In the middle row of the cartoon, a side-projection of

the hypothetical Pt-BHA particle resting on the TEM sample holder is depicted. From left to right these orientations are shown: [0° tilt, 0° rotation], [0° tilt, 90° rotation], [30° tilt, 0° rotation], and [30° tilt, 90° rotation]. In each of these orientations the electron beam is aimed vertically down through the particulate, producing a different image for each orientation (shown in the final row).

A rotation of the sample holder with no tilt does not produce a change in the image, as both [0° tilt, 0° rotation] and [0° tilt, 90° rotation] are the same image simply rotated 90° (comparing the 1st and 2nd images in the bottom row). Hence, simple in-plane rotations are not sufficient to obtain 3-dimensional information about the sample. However, this is in direct contrast with what is observed by a rotation *after the sample is tilted*. First of all, by tilting the sample holder we observe a change in the image (comparing the 1st and 3rd images in the bottom row). These changes arise from the fact that the particles are now at different depths within the ceramic structure relative to the electron beam. The left and right (shorter) sides of the ceramic appear faded because the projection of the particulate on either side is thinner. Additionally, the inter-particle distances change – particle 1 appears further to the right of particle 3, and particle 2 is appears horizontally closer to particle 1. Further changes are observed by *rotating the sample holder while it remains tilted* (comparing the 3rd and 4th images in the bottom row). Right away, it is clear that this manipulation produces a different image which provides 3-dimensional spatial information, *contrary to when the sample is rotated without tilt*. The longer sides of the ceramic appear to fade out because the material is thinner in those directions with respect to the orientation of the electron beam. The particles again appear to shift in position in relationship to one another. Particle 1 shifts away from particle 3 horizontally, and particle 1 and 2 are no longer aligned parallel to the sides of the ceramic.

The changes observed in this simple hypothetical particulate can provide insight into the orientation of particulates observed in more uniquely-shaped real-life samples. By observing the relative transparency of the ceramic material we can gain information about the shape and thickness of the particulate. By observing shifts in the positions of the particles in the TEM images, we can learn about the orientation of the platinum particles with respect to each other and to the ceramic itself. A few broad conclusions can be made. Particles "caged" within the structure (like particle 1) will always appear to be covered by a layer of ceramic material. Particles that are partially "caged" in the structure (like particle 2) will sometimes transition to being covered by ceramic as the orientation of the sample holder changes. Finally, particles resting on the top of the particulate (particle 3) will typically appear to have a portion of the particle appear uncovered by ceramic, especially when the particle lies on the outer edge of the ceramic particulate.

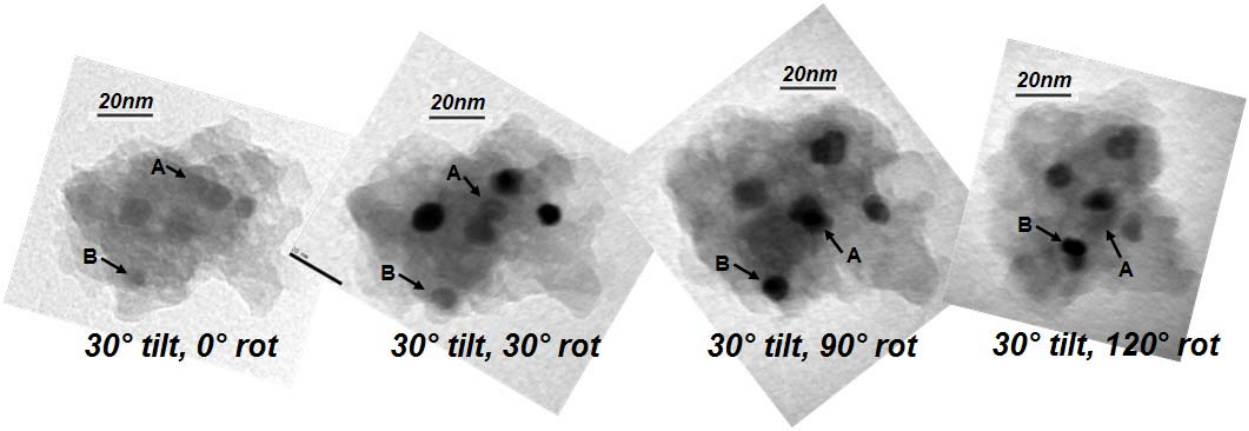

Figure 21: *TEM images of 10 wt% Pt-BHA as the sample holder is tilted by 30° and then rotated from 0 to 120°. Special thanks to Andreas Kulovits for assistance in obtaining these TEM images.*

Figure 21 shows a series of TEM images of 10 wt% Pt-BHA as the sample is subjected to a 30° tilt and a rotation from 0 to 120°. The positions of two particles A and B are labeled on

the TEM images. Particle A appears to be completely "caged" within the BHA structure. In all images it is covered with a transparent grey layer of BHA. In addition, the positioning of particle A relative to the other (relatively fixed-in-position) particles changes as the sample is rotated, from toward the upper half of the particle at [30° tilt, 0° rotation] to the lower center at [30° tilt, 120° rotation]. This apparent particle movement implies that the particle is at a different depth within the BHA from the other particles – because particle A is further from the axis of rotation it appears to "move" more than the other particles within the structure. Particle B appears to be partially "caged" in the side of this particular Pt-BHA particulate. At both [0° tilt, 0° rotation] and [30° tilt, 0° rotation] the particle appears covered by the BHA substrate. As the rotation proceeds, the particle gets progressively darker and begins to shift toward the center of the particulate once [30° tilt, 120° rotation] is reached. This is consistent with the particle being "caged" in the side of the particulate and only being fully visible once the particulate has been rotated so particle B is facing toward the electron beam. It is possible to differentiate between partial burial (believed to be the case here) and simply resting of the platinum particle on the side of the particulate. If the platinum particle were resting on the outside of the pore structure, we would expect to see it protrude from the side of the particulate as the rotation is made. Instead, we observe a smooth transition from it appearing behind the ceramic to appearing in front of it. This evidence of partial burial is important when we consider the method by which these TEM images are obtained. The larger Pt-BHA particulates that result from the synthesis (with diameters up to 500 microns) are crushed by mortar and pestle before being dispersed on the TEM grid. Thus the pieces of material observed in TEM are part of a larger Pt-BHA structure. The strong evidence of *partial* "caging" we frequently observe in these broken-off pieces almost certainly translate into *complete* "caging" in the larger Pt-BHA particulate prior to crushing.

Figure 22 is a cartoon depicting this phenomenon, where particle A which is completely caged within the BHA framework prior to crushing for TEM, but appears to be partially caged after the crushing procedure cleaves the BHA across particle A's diameter.

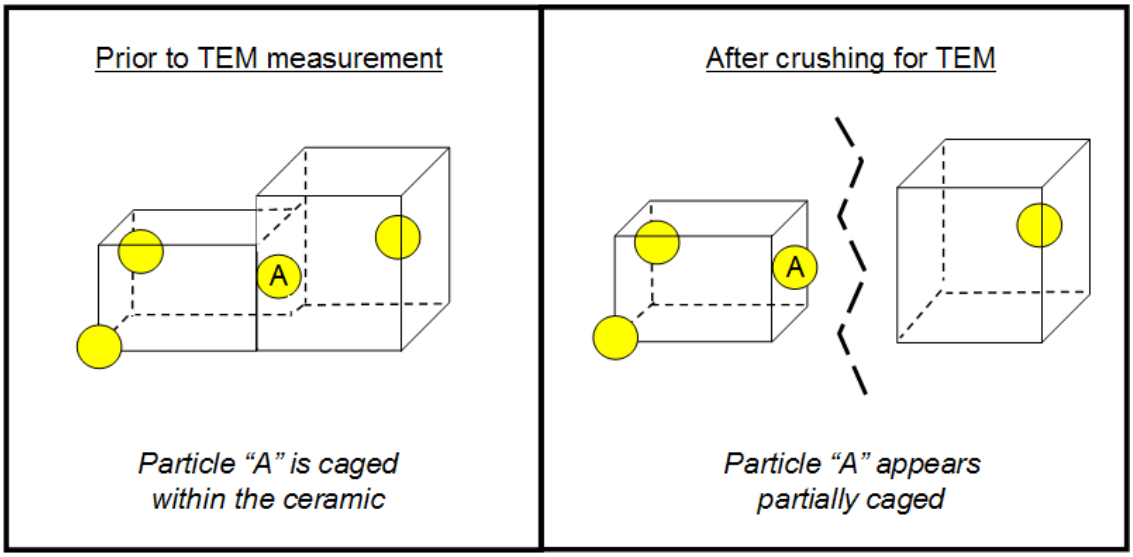

Figure 22: *Cartoon depicting platinum particles (yellow spheres) within the BHA framework (transparent rectangular boxes) before and after the particulate is crushed for the TEM measurement.*

Both particles A and B in the sample TEM images shown in **Figure 21** provide strong evidence of particle "caging" within the BHA framework – a necessary condition for the thermal stabilization mechanism discussed above.

If the growth of noble metal nanoparticles is restrained by the necks of the (highly stable) pore structure at 600°C, what happens when the pore structure destabilizes at higher temperatures (as observed in **Figure 18** above 900°C)? One would expect further growth of the Pt particles as the pore necks become large enough to allow coalescence between neighbor particles within the structure. For two 15 nm particles which sinter, an 18.9 nm particle should result (assuming spherical particles and based strictly on geometric considerations). Coalescence of multiple nearby particles would result in even further particle growth. To experimentally

determine the effect that this type of destabilization of the BHA structure has on the Pt particles, a sample of Pt-BHA and pure BHA are each calcined for 1000°C for 5 hours. Nitrogen porosimetry is used to evaluate the pore structure of the pure BHA, while TEM micrographs are used to obtain the distribution of the Pt particles. The results are overlaid in **Figure 23**. In this case, the pore structure of the BHA is evaluated with both nitrogen adsorption and desorption, with the BJH analysis of the adsorption curve resulting in the pore structure of both the pore necks as well as the pore cages of the material.

Indeed, the size of the Pt particles grows significantly, with an average particle diameter of 18.8 nm observed (in excellent agreement with the expected size of two 15 nm particles coalescing, calculated above). The width of the particle distribution increases substantially as well, with particles ranging from 5 nm to 40 nm, and a standard deviation of 9.2 nm. A large fraction of particles (56.8%) are still within the size envelope of the pore necks (4 – 17nm) and the vast majority of particles (95.1%) reside within the envelope of the pore necks and cages (2 – 33 nm).

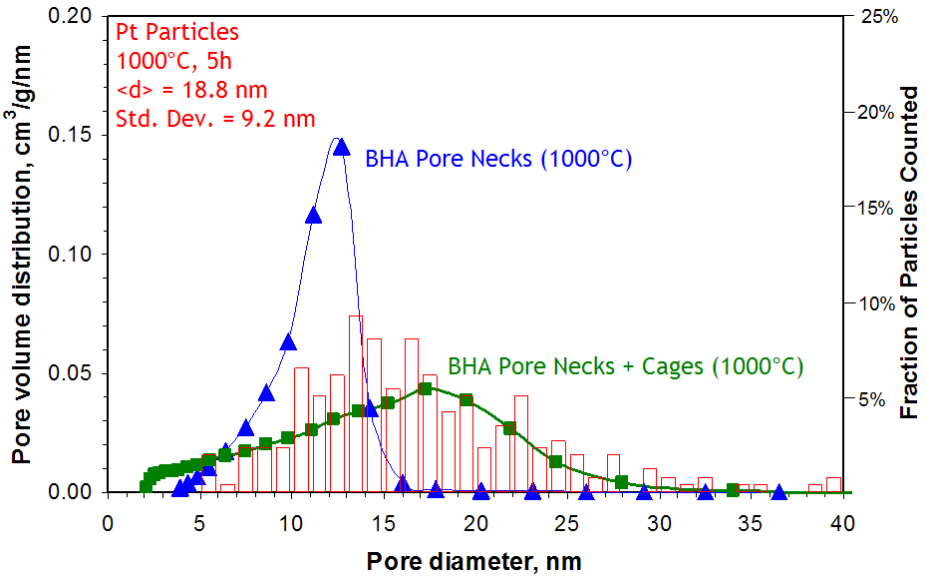

Figure 23: *Comparison between Pt particle size in Pt-BHA (histogram, right y-axis), and the size of pure (containing no metal) BHA pore necks (triangles, left y-axis) and pore cages (squares, left y-axis). The size of the BHA pore necks were determined from BJH analysis of the nitrogen desorption isotherm, while the pore cages were determined from the nitrogen adsorption isotherm. The nitrogen porosimetry was conducted after 5 hours of calcination at 1000°C. Pt particle statistics were determined from TEM micrographs.*

The results show significant nanoparticle sintering occurs after the BHA structure has begun to destabilize at around 900°C. The pore necks have become larger in size because of the onset of pre-crystallization at these elevated temperatures (see section 4.4.3, **Figure 18**). Consequently, the platinum particles are now able to resume sintering by making their way through the (newly expanded) pore necks. However, this sintering is still constrained by the structure of the BHA matrix – specifically, the pore cages. The explanation is the following: a larger particle begins to form via agglomeration of multiple platinum particles in close proximity. The particles that agglomerate to form the larger one are free to sinter due to expansion of the previously restraining pore necks. Eventually this newly-formed, sintered particle becomes large enough to nearly fill the size of the pore cage. The pore cage then prevents further agglomeration, and the larger particle is again restrained from further sintering.

These results indicate that there is a strong driving force for the Pt particles to remain nanosized (with sizes corresponding to the sizes of the pore cages of the BHA structure), even at temperatures as high as 1000°C. The strong sintering resistance of the Pt particles is at least partially responsible for the high activity and stability of Pt-BHA catalysts under high-temperature reaction conditions (e.g. 1000°C for CPOM). A physical caging phenomenon is the most likely explanation for this stabilization effect.

4.4.5 Particle caging in Ni-BHA

Because the particle stabilization is the result of purely physical caging effect (rather than a chemical one) it should be broadly applicable towards the stabilization of nanoparticles. The only condition necessary for the stabilization of a wide variety of catalytically active metals is the ability to form a similar structure to that of BHA – nanoparticles of metal distributed homogeneously throughout a thermally-stable, sponge-like ceramic with textural porosity (necks and cages). This section outlines the formation of thermally stable Ni-BHA nanocomposites and provides evidence that particle caging is also responsible for the high-temperature stability of nickel nanoparticles.

Nickel metal is an important material for a wide variety of industrial reactions, from hydrogenation to polymerization. It has also gained attention recently as an oxygen carrier for use in a clean energy application termed Chemical Looping Combustion (CLC). In CLC, an oxygen carrier (NiO in this case) is used to oxidize a fuel stream, while in a separate reactor the spent oxygen carrier (Ni) is re-oxidized in a stream of air. This process allows for flame-free combustion of fuel, thus eliminating the formation of NOx. It also produces a sequestration ready CO_2 stream as a by-product, thus avoiding energy penalties for CO_2 separation, making it

unique amongst many emerging energy production technologies. Further discussion of CLC can be found elsewhere, as it is outside of the scope of this thesis[143, 144].

Ni-BHA materials were formed in an identical manner to Pt-BHA, except $Ni(NO_3)_2$ replaces H_2Cl_6Pt as the metal salt component (Further details about Ni-BHA as well as the synthesis of other metal-BHA combinations can be found in Appendix D). A TEM micrograph of the resulting material after synthesis and calcination at 800°C is shown in **Figure 24**. Ni-BHA samples are reduced in hydrogen gas at the same calcination temperature to reduce NiO to Ni since Ni metal particles are easier to image than NiO. The structure shows many similarities to previously obtained micrographs of Pt-BHA. Dense nickel particles (dark spheroidal shapes) are observed throughout the lighter, less-dense BHA ceramic phase. The particles appear to be similarly embedded within the framework of the BHA, rather than resting on the outside of it.

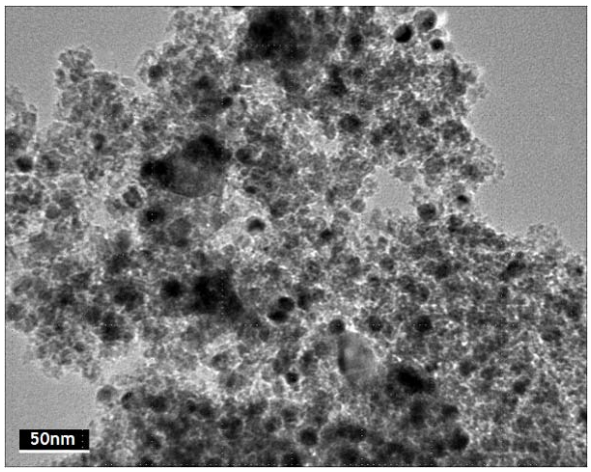

Figure 24: *TEM micrograph of 30 wt% Ni-BHA calcined at 800°C*

A comparison between the BHA pore structure and Ni particle size is used to confirm that a caging effect is present in Ni-BHA similar to Pt-BHA. Samples of Ni-BHA and pure BHA are each calcined for 800°C for 5 hours. The Ni-BHA is reduced briefly (30 mins) in hydrogen at 800°C to assist particle resolution in TEM. Nitrogen porosimetry is used to evaluate the pore

structure of the pure BHA, while TEM micrographs are used to obtain the distribution of the Ni particles. The results of both measurements are overlaid in **Figure 25**. The Ni particles have an average particle diameter of 10.8 nm with a narrow size distribution (standard deviation of 5.1 nm). Similar to Pt-BHA, the vast majority of particles (95.6%) reside within the envelope of the pore necks (3 – 18 nm).

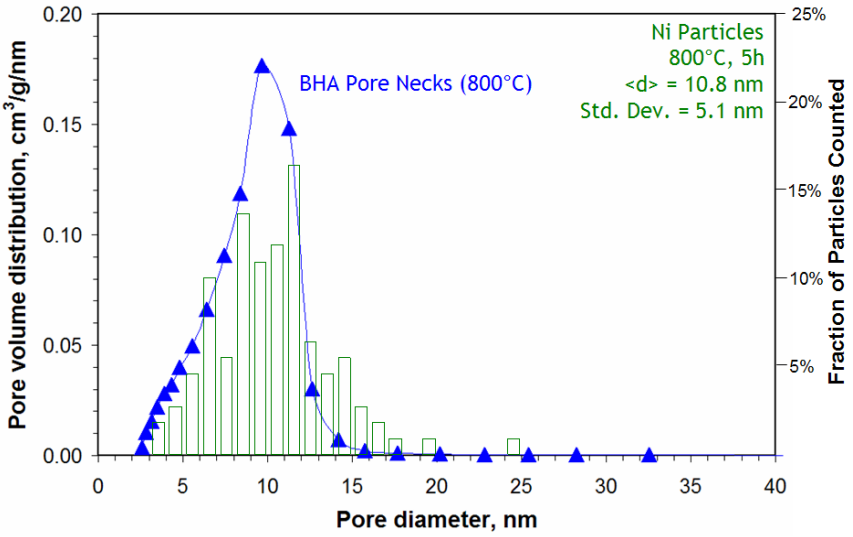

Figure 25: *Comparison between Ni particle size in Ni-BHA (histogram, right y-axis) and the size of pure (containing no metal) BHA pore necks (triangles, left y-axis). Ni particles statistics were determined using TEM micrographs taken after 5 hours of calcination at 800°C in air, followed by reduction in H_2 for 1 hour at 800°C. The size of the BHA pore necks were determined from BJH analysis of the nitrogen desorption isotherm after 5 hours of calcination at 800°C.*

At 800°C, the structure of the BHA remains stable (see **Figure 18**) and the sizes of pore necks have not begin to increase. Hence, the Ni particles remain trapped by the necks of the BHA.

A chemical looping combustion (CLC) oxygen carrier must be able to withstand high-temperature conditions (T > 800°C) as well as an environment which continuously alternates between strongly reducing and strongly oxidizing. To be an effective carrier, it must maintain its ability to quickly incorporate and release oxygen in these stressful conditions. For nanoscale

materials, particle sintering is particularly detrimental because it leads to larger particles which are slower to oxidize. It is logical to assume that a material, such as Ni-BHA, which can maintain metal nanoscale characteristics at high temperatures, will be a highly effective oxygen carrier for CLC.

Simulated CLC reaction is used to test the potential of Ni-BHA nanocomposites for this reaction. Ni-BHA nanocomposite, pre-calcined at 900°C, is placed within a thermogravimetric analysis chamber. The material is subjected to periodically changing flows of air and hydrogen gas over the course of 1000 minutes at 900°C. The weight change is monitored over time, and the results are plotted in **Figure 26**. When the material has a larger mass the active phase is NiO, and when the mass is lowest Ni metal is present. The presence of each of these phases is confirmed by XRD. The graph shows that the amount of Ni available for oxidation and reduction does not change throughout the course of the testing, as indicated by the constant difference between the mass of the Ni and NiO during the course of the experiment.

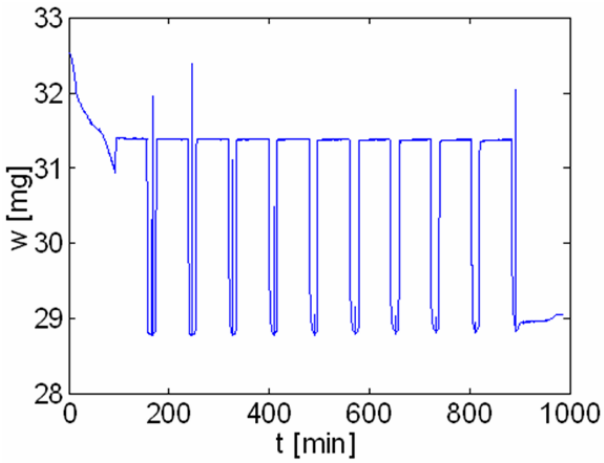

Figure 26: *TGA Analysis Ni-BHA (right plot) as the sample is cycled between oxidizing (Air) and reducing (H_2) conditions at 900°C. The larger mass corresponds to NiO, while the smaller mass represents Ni metal (confirmed by XRD).*

These results confirm the stability of nanocomposite Ni-BHA under the stressful conditions of continuous oxidation and reduction at high-temperature. The unique structure of the Ni-BHA nanocomposite results in caging of the Ni particles, just as with Pt-BHA discussed previously. This caging effect performs the same function as it does with Pt-BHA – strong suppression of thermal sintering. This suppression prevents growth of the Ni nanoparticles and allows it to be completely oxidized and reduced in each cycle over the 1000 minutes of testing at 900°C.

4.4.6 Summary

The sizes of Pt particles in Pt-BHA nanocomposite do not increase uniformly with calcination temperature. Across a wide range of high-temperature conditions (600-1000°C) the particles remain surprisingly stable and nano-sized. Strong correlation between Pt particle size in Pt-BHA and the pore necks of pure BHA has established a plausible explanation for the stable size of the Pt particles. The reason for this stability is found to be a particle caging effect – attributable to the narrow pore necks of the supporting BHA matrix. At lower temperatures ($T<900°C$) the pore necks prevent particle sintering by blocking particle migration. Above 900°C, the particles sinter to fill the pore cages, and are once again thermally stabilized. The particles are only able to grow beyond the nanoscale regime after the BHA structure crystallizes and the neck-and-cage structure is no longer present ($T > 1200°C$). This effect is also seen in similarly structured Ni-BHA – indicating the fundamental nature of the particle stability, and the tremendous active metal stabilization potential of this class of materials. These metal-BHA nanocomposites are expected to be effective and stable catalysts and oxygen carriers for numerous high temperature reactions with industrial relevance. The following section discusses

the results of testing these materials in two such reactions – catalytic methane combustion and water-gas shift.

4.5 REACTIVE EVALUATION

As discussed above, powdered nanocomposite Pt-BHA catalysts demonstrate excellent thermal stability and increased activity in high-temperature CPOM (see section 4.1). The stability of these materials, in particular the active, nano-scale noble metal component, is the result of a particle caging effect by the pore necks and cages of the BHA matrix (see section 4.4.4). Those previous studies demonstrate that these materials have the potential to be effective catalysts in extreme conditions. In order to further test the utility of these novel nanocomposites, two additional reaction systems are studied: methane combustion and water-gas shift. These reactions are both important reactions for clean energy production. Methane combustion, like CPOM, runs at very high temperatures (T>700°C) so it serves as a further test of the thermal stability of the nanocomposite. Water-gas shift, while not operating at as high of temperatures (typically T < 500°C), is a test of another important parameter of catalyst stability, that of hydrothermal stability – due to the presence of steam in the reactant mixture.

4.5.1 Methane combustion

Catalytic combustion reduces NO_x emissions by lowering the flame temperature needed to fully oxidize a fuel stream. Much catalytic combustion work to-date has been with thermally-stable, yet relatively inactive ceramics (thermally stabilized aluminas, such as BHA fall in this

category). The use of more active noble metal catalysts (e.g. Pt) has been limited by the strong exothermic nature of the reaction, leading to a large adiabatic temperature rise (~276K for 1 vol% CH_4). This strong temperature rise promotes sintering of the active metal component, resulting in deactivation of the catalyst. The thermal stability of noble metals in Pt-BHA-type nanocatalysts is thus highly desirable for this reaction. The experimental procedures used to test methane combustion are outlined in the experimental section (sec. 3.3.3).

A number of different nanocomposite and commercially available catalysts are used to test a wide variety of factors in methane combustion. A list of these catalysts, including composition, pre-treatment conditions, average Pt particle diameter (from TEM, where applicable), and Pt specific surface area (from CO pulse chemisorption) is given in **Table 4**.

Table 4: *Catalysts used in methane combustion experiments. All catalysts (including those commercially purchased) were reduced in pure H_2 at the same calcination temperature prior to use. Average particle diameter was determined using images from TEM.*

Catalyst Type	Nominal Loading	Pre-treatment	Average Pt Particle Diameter [nm]	Pt specific surface area [m^2/g Pt]
BHA	n/a	Air, 600°C, 5 h	--	--
Pt/Al_2O_3	1 wt% Pt	Reduction at 600°C	7.2	85.2
Pt-BHA	1 wt% Pt	Air, 600°C, 5 h	6.7	31.7
Pt-BHA	10 wt% Pt	Air, 500°C, 15 m	5.4	53.1
Pt-BHA	10 wt% Pt	Air, 600°C, 15 m	9.0	84.0
Pt-BHA	10 wt% Pt	Air, 700°C, 5 h	12.9	10.3
Pt-BHA	10 wt% Pt	Air, 1000°C, 3 h	28.0	0.7
CeO_2-BHA	10 wt% CeO_2	Air, 700°C, 5 h	--	--
Pt-CeO_2-BHA	10 wt% CeO_2, 1 wt% Pt	Air, 700°C, 5 h	11.9	19.8

A pure BHA catalyst is used as a control catalyst. BHA is somewhat catalytically active in this reaction, as described in previous research[38]. However, the BHA ceramic exhibits very

low activity, so the addition of small amounts of noble metal is expected to strongly increase its activity.

Amongst Pt catalysts, a 1 wt% Pt-BHA is compared with a commercially available 1 wt% Pt/Al_2O_3 (Aldrich). Both catalysts have similar particle sizes – around 7 nm as measured by TEM. However, the Pt specific surface area of the commercial catalysts is nearly 3 times larger than the Pt-BHA catalyst. The reason for this large disparity in specific surface areas can be explained by the unfortunate presence of a population of larger particles with diameters around 20 nm (see top left plot of platinum particle size for 1 wt% Pt-BHA shown in **Figure 29**). These larger particles have low specific surface area and consume a large portion of the total weight of platinum available, thus resulting in a much lower overall specific surface area.

Additionally, a batch of Pt-BHA with 10 wt% Pt is used to examine the effect of particle size on the catalyst activity – various calcination treatments are used to achieve a variety of Pt particle size distributions (mean diameter ranging from 5.4 nm to 28.0 nm). Additionally, both pure and 1 wt% Pt- loaded BHA nanocomposites are doped with 10 wt% ceria (the appropriate amount of cerium nitrate hexahydrate is added during the aging stage of the microemulsion) to compare with undoped samples. Zarur et al previously found that CeO_2-doped BHA initiated light-off of a 1 wt% methane stream at dramatically lower temperature (~400°C vs. ~700°C undoped)[38].

The amount of Pt metal present in the nanocomposite is expected to strongly affect the activity of the catalyst. In order to establish the increase in activity with Pt metal loading, a 1 vol% methane stream is ignited over pure BHA, 1 wt% and 10 wt% Pt-BHA catalysts. The 1 wt% Pt-BHA was calcined at 600°C prior to reaction, resulting in 6.7 nm particles. The 10 wt% Pt-BHA is also calcined at 600°C prior to reaction, resulting in 9.0nm platinum particles. The

resulting methane conversion curves are plotted in **Figure 27**. The velocity of the gas stream is adjusted based on the measured Pt surface area of each catalyst. For pure BHA, a gas hourly space velocity (GHSV) of ~60,000h^{-1} is used. For each of the Pt catalysts, a space velocity of ~366,000h^{-1} per square meter of Pt surface area is used.

The pure BHA sample ignites the methane stream (defined as 10% methane conversion) at just below 600°C, with full conversion occurring at ~700°C. This result is very similar to that obtained by Zarur and Ying for methane combustion over nanostructured BHA[38]. For the samples loaded with platinum, the ignition curve shifts to lower temperatures. Because the flow rate of reactive gases is normalized to the Pt surface area, it is expected that both 1 and 10 wt% samples show similar ignition characteristics. For both 1 wt% and 10 wt% loadings of platinum, ignition occurs around 500°C, with full conversion occurring just below 600°C for 1 wt% Pt, and just above 600°C for 10 wt% Pt. The ignition curves for both platinum catalysts lie within the bounds of measurement error, except at conversions greater than 70%, where the 1 wt% catalyst reaches full conversion at ~30°C lower temperature than the 10 wt% catalyst. There is a possibility this small improvement for the 1 wt% catalyst is the result of the smaller average particle size (6.7 vs. 9.0 nm) for this catalyst. These smaller particles have a larger fraction of edge and corner sites on their surface – and these are generally considered more active catalytically[145]. These results indicate that the platinum metal improved the methane combustion activity of the BHA catalyst by lowering the ignition temperature for both loadings by ~100°C. Only a small amount of active Pt surface area (and thus, a small amount of expensive Pt metal) is necessary to strongly improve the activity of the BHA catalyst.

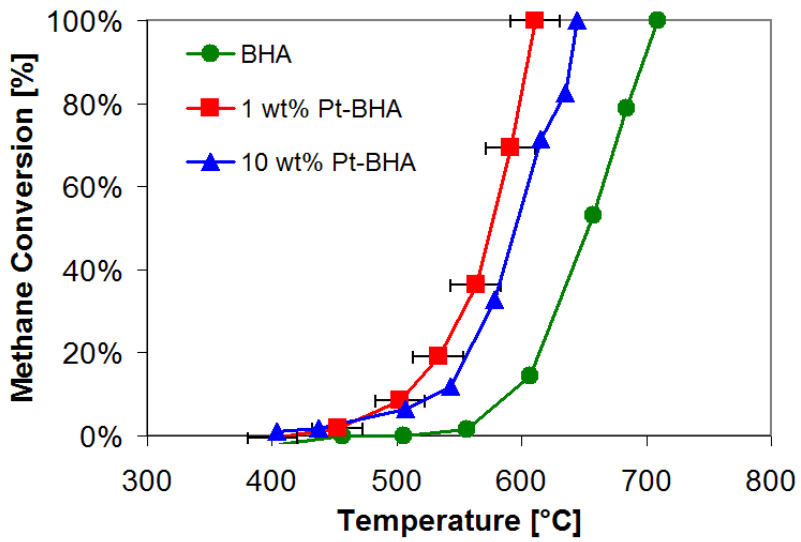

Figure 27: *Methane conversion as a function of temperature for pure BHA, 1 and 10 wt% Pt-BHA (9.0 nm particle size). For pure BHA, GHSV ≈ 60,000 h^{-1}, for Pt-BHA the flow rate is adjusted to normalize the gas velocity to the amount of Pt surface area, ~366,000h^{-1} per square meter of Pt surface area. Error bars indicate +/- 20°C associated with the placement of the thermocouple in proximity to the catalyst bed.*

At the high temperatures necessary for methane combustion, significant sintering of the Pt metal is expected. However, our previous characterization of Pt-BHA indicates that the Pt particles contained within the ceramic framework are very stable in the temperature range of 600-900°C. This inherent stability is equally important for a good methane ignition catalyst as the previously observed strong improvement in activity.

The stability of 1 wt% Pt-BHA for catalytic combustion is compared with a commercially available 1 wt% Pt/Al_2O_3 catalyst. This lower weight loading was chosen because a low Pt weight loading is crucially important for an industrially relevant methane combustion catalyst. Higher loadings will lead to increased catalyst cost. Both 1 wt% Pt catalysts are pre-calcined as indicated in **Table 4** (above) – Pt-BHA is calcined in air and reduced for 1 hour in hydrogen at 600°C, while the commercial Pt/Al_2O_3 is reduced for 1 hour at 600°C. The ignition curve is measured under these initial treatment conditions, and the catalyst is then subjected to

calcination in air at 800°C in order to induce sintering and catalyst deactivation. After 2, 24, and 48 hours of calcination at this temperature, additional ignition curves are measured for each catalyst. In this way, the deactivation of the catalyst can be measured over time. The resulting methane conversions are plotted in **Figure 28**. The velocity of the gas stream is adjusted based on the measured Pt surface area of each catalyst. The Pt-BHA catalyst has a much lower Pt surface area, so the flow rate is lowered to account for the reduced accessibility of the active surface.

The left plot of **Figure 28** tracks the commercial Pt/Al_2O_3 catalyst. Initially, the catalyst is very active – ignition is achieved at ~350°C, and full conversion just below 600°C. Significant deactivation occurs after just 2 hours of calcination at 800°C, especially at low temperatures – ignition is not achieved until ~500°C. Full conversion is also delayed to just above 600°C. Further deactivation takes place after high-temperature treatment for 24h. Initial conversion is delayed until nearly 600°C, with full conversion occurring ~640°C. After 48h the catalyst has similar activity as after 24h, suggesting that the catalyst has finally stabilized. The right graph tracks the methane conversion for the Pt-BHA catalyst. Initially the catalyst is significantly less active than the commercial catalyst – ignition is not reached until ~530°C, with full conversion achieved at ~650°C. The calcination at 800°C for 2h also deactivates this catalyst – ignition is delayed until ~570°C, and full conversion is delayed until ~680°C. After this initial deactivation, the catalyst remains stable after further high-temperature treatment for 24 and 48h. It should also be noted that when comparing the deactivated commercial catalyst with pure-BHA (dashed curve, both plots), no reduction of ignition temperature is observed, and there is only a ~50°C reduction in the temperature of full conversion. The deactivated 1 wt% Pt-BHA material has nearly an identical ignition profile as the pure BHA material.

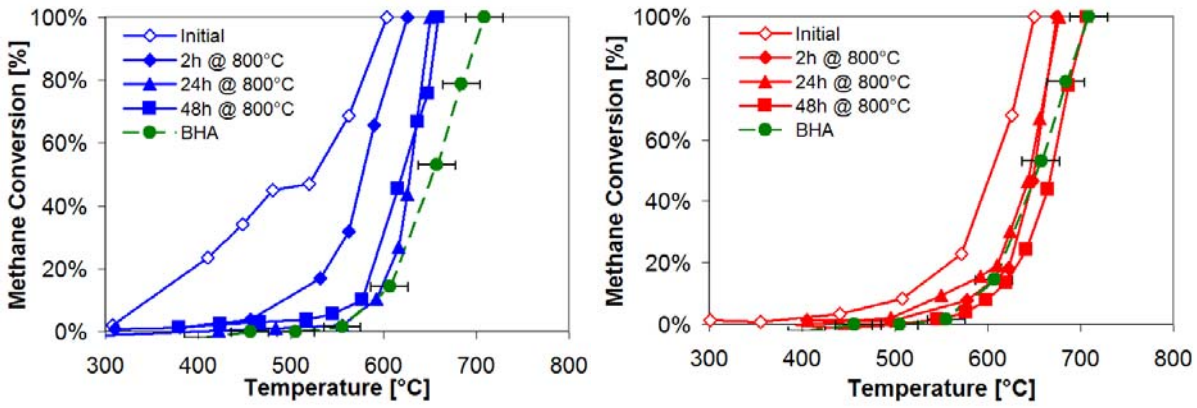

Figure 28: *Methane conversion as a function of temperature for 1 wt% Pt/Al_2O_3 (left graph) and 1 wt% Pt-BHA (right graph). Catalyst stability was tested by heating each catalyst in flowing air at 800°C for 2, 24, and 48 hours. Pure BHA is plotted on both graphs for reference. Flow rates normalized to platinum surface area, GHSV ≈ 13,000 for Pt-BHA, 60,000 h^{-1} for Pt/Al_2O_3. GHSV ≈ 60,000 for pure BHA. Error bars indicate +/- 20°C associated with the placement of the thermocouple in proximity to the catalyst bed.*

These results indicate that initially the commercial catalyst, which has small platinum particles distributed on the exterior of the alumina support, is an excellent methane conversion catalyst. However, the activity of the catalyst decreases dramatically due to Pt sintering (as seen in TEM, see **Figure 29** below), as expected for unstabilized Pt particles at 800°C. The Pt-BHA catalyst is much less active at low-temperatures, even after compensating for the lower measured platinum surface area in this catalyst. This is an indication that internal mass transfer limitations might be playing a role for this catalyst, which contains Pt particles distributed in a porous ceramic framework. The deactivation of the 1 wt% Pt-BHA catalyst is much less pronounced than in the commercial catalyst, but this is likely a result of its poor initial activity. Finally, the fact that both catalysts are not significantly more active than pure BHA after deactivation indicates that Pt particles are not sufficiently stabilized, even in the Pt-BHA nanocomposite.

The size of the platinum particles in 1 wt% Pt catalysts is measured before and after deactivation. The size of the platinum particles gives an indication of the amount of deactivation

that occurs due to sintering. A TEM image of the materials is taken before any reaction, and after the final ignition curve is measured after 48h of treatment at 800°C. The platinum particles are measured and counted from the images, and histograms are plotted in **Figure 29**.

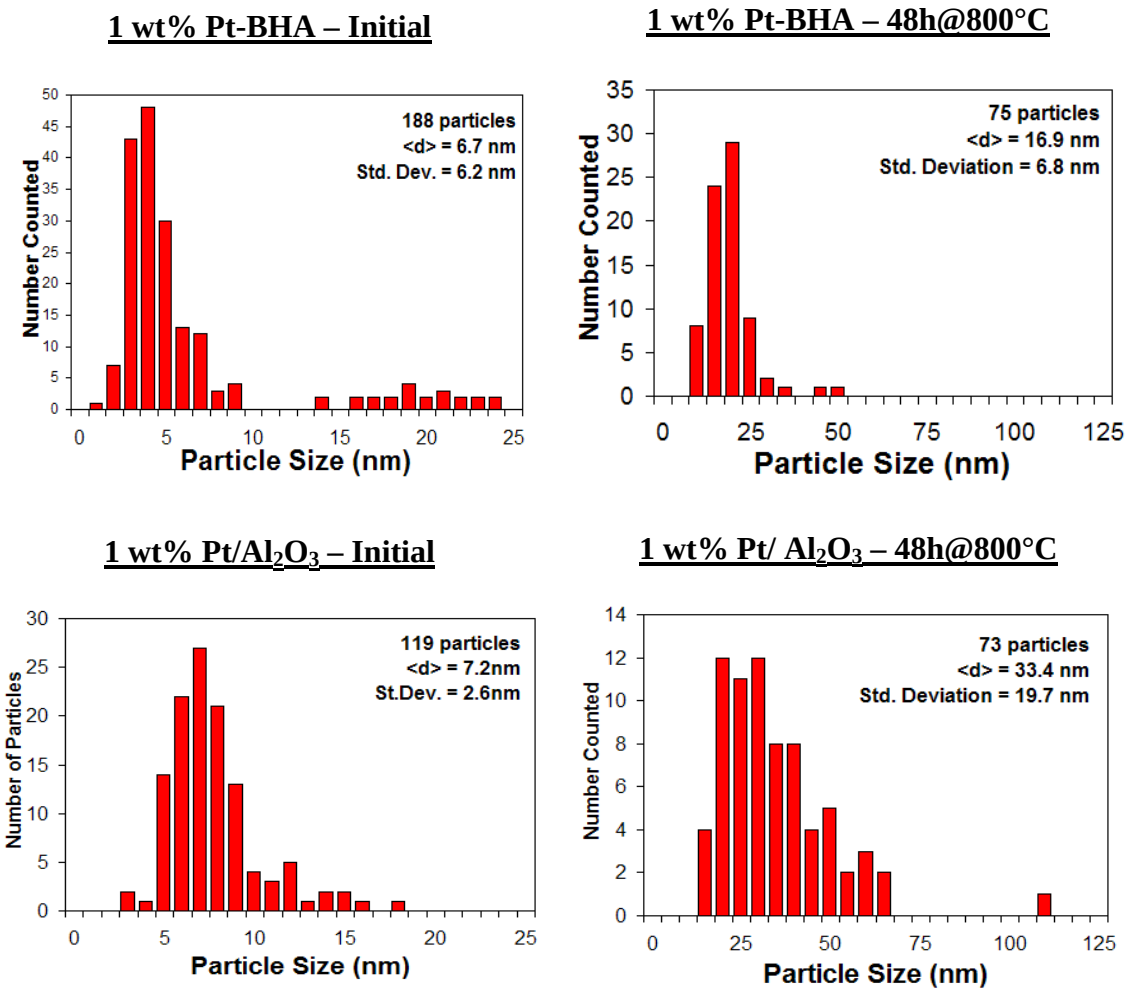

Figure 29: Particle size distributions for 1 wt% Pt based catalysts used in methane combustion. The distribution is determined from TEM micrographs. Top: Pt-BHA. Bottom: Pt/Al_2O_3. Left: as initially used in methane combustion. Right: after methane combustion following 48h at 800°C in flowing air.

As indicated previously, the size of the particles is similar in both catalysts prior to reaction. The Pt-BHA catalyst has an average particle size of 6.7 nm, with a broad standard

deviation of 6.2 nm due to the presence of a population of larger particles ~20 nm. As mentioned before, this distribution of larger particles also serves to lower the platinum specific surface area for this catalyst. These larger particles are not typical of Pt-BHA catalysts in general, and likely result from an uncontrolled aspect of this particular synthesis. In that way, it is unfortunate that the reactive testing was performed on this batch of 1 wt% Pt-BHA. The Pt/Al_2O_3 commercial catalyst has a slightly larger average particle size of 7.2 nm, with a much lower standard deviation of 2.6 nm. After the 48h treatment at 800°C, there is a strong increase in particle size for both catalysts. In Pt-BHA the average particle size increases to 16.9 nm. The standard deviation remains relatively stable at 6.8 nm, however. In the commercial catalyst, severe sintering occurs, resulting in particles with average diameter 33.4 nm and a much larger dispersion as indicated by a standard deviation of 19.7 nm.

The results of this particle size analysis confirm that deactivation is stronger over Pt/Al_2O_3 due to rapid particle sintering in high-temperature treatment. This also further confirms the previously measured thermal stability of Pt-BHA catalysts. Furthermore, the failure of the platinum-loaded catalyst to significantly improve performance over the pure BHA material might have an explanation linked to the Pt particle size. Both catalysts experience sintering which results in the removal of particles with diameter < 10 nm (after the 48h treatment). These smaller particles are expected to be the most active for the reaction, due to a larger fraction of Pt atoms without full atomic coordination (step edge and corner atoms). Further confirmation of this effect can be seen in the initial activity measured for both catalysts. The Pt-BHA catalyst has a small but significant population of larger particles (~20nm). These larger particles contain a large fraction of the total Pt atoms available, with significantly lower surface area. This leads

to a Pt-BHA catalyst which is less active initially. The commercial catalyst has a very narrow particle size distribution of particles ~ 7 nm, and the result is a much more active catalyst.

The alternative explanation for the low activity of 1 wt% Pt-BHA (before deactivation) is the possibility of internal mass transfer limitations (MTL) limiting the methane conversion. MTL may arise because of the configuration of the Pt-BHA material – Pt particles "caged" within a ceramic framework with narrow mesopores. The tortuous path that a methane molecule must travel inside the Pt-BHA particulate combined with the rapid kinetics of methane combustion at high-temperatures lead to the possibility of strong internal MTL. The size of the Pt-BHA particulate is expected to have a strong effect on the presence of internal MTL, based on the well-known relationship between the effectiveness factor, η, and the Thiele modulus, ϕ, for spherical particulates and first order kinetics[146]:

$$\eta = \text{observed rate constant/intrinsic rate constant} = \frac{3}{\phi}\left(\frac{1}{\tanh\phi} - \frac{1}{\phi}\right)$$

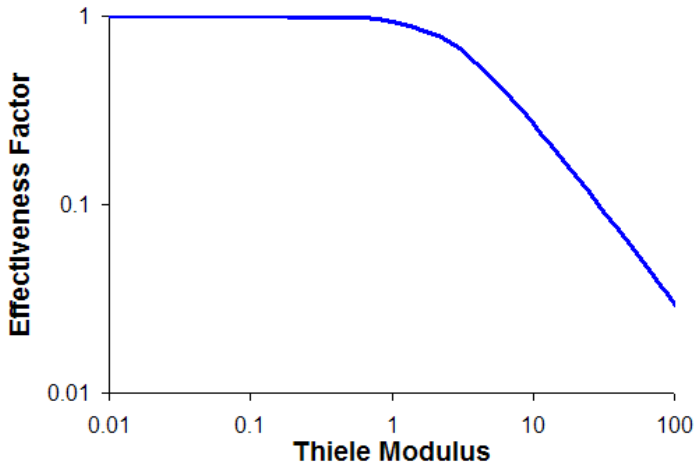

Figure 30: *Effectiveness factor as a function of Thiele modulus for spherical catalyst particulates and first order kinetics. Based on correlations from Post et al.*[146]

Figure 30 plots the effectiveness factor as a function of Thiele. From the plot, it is clear that one observes intrinsic reaction kinetics when the Thiele modulus is below a value of 1. The Thiele modulus (which can be expressed as a Damköhler number Da = ϕ^2) can be considered a measure of the ratio of the relative reaction rate to the relative diffusion rate within a catalyst particulate. The Damköhler number is expressed as:

$$Da = \phi^2 = \frac{D_P^2 k^0}{4D}$$

Where D_P is the diameter of the catalyst particles, k^0 is the intrinsic rate constant of the reaction, and D is the diffusion constant for the gases in the reaction. From this relationship it is clear that for large particulates there is a greater possibility of observing non-intrinsic (mass transfer limited) reaction kinetics. This is further exacerbated in methane combustion reaction because of the high intrinsic reaction rates expected for high temperatures.

The relationship between particulate diameter, Thiele modulus, and effectiveness factor provides a simple test for internal MTL – by varying the particulate size fraction (that is, the typically micrometer-sized primary particulates placed into the reactor) and observing the activity of the catalyst. If MTLs are present, one should observe a change in the activity of the catalyst for different particle sizes. If the activity does not change, the effectiveness factor is close to a value of 1 – and intrinsic reaction activity on that catalyst is being measured.

To proceed with testing for MTLs in Pt-BHA catalysts for methane combustion, the 1 wt% catalyst is divided into 4 subsets via sieving based on the diameter (D_P) of the secondary Pt-BHA particulates – approximately 63 microns, smaller than 180 μm, between 180 and 500 μm, and larger than 500 μm. The smallest size fraction was sieved to have 37% of its particles more

than, and 62% less than 63 microns. The commercial catalyst contained 30 wt% of its particles with D_P greater than 63 microns, and 70 wt% less than 63 microns. A direct size fraction-based comparison with the commercial catalyst is important because it allows us to compare the two different morphologies of this material - active metal residing on the outside surface of the alumina particulates (as in Pt/Al_2O_3), and Pt particles "caged" internally within ceramic BHA (as in Pt-BHA). The larger size fractions represent cases with higher probability of mass transfer limitations. The same mass of catalyst (~0.09g) is used in each case, with a similar flow rate to earlier testing (**Figure 28**) resulting in a GHSV of 60,000 h^{-1}. The methane conversion is monitored as a function of reaction temperature for each catalyst, and the result is plotted in

Figure 31.

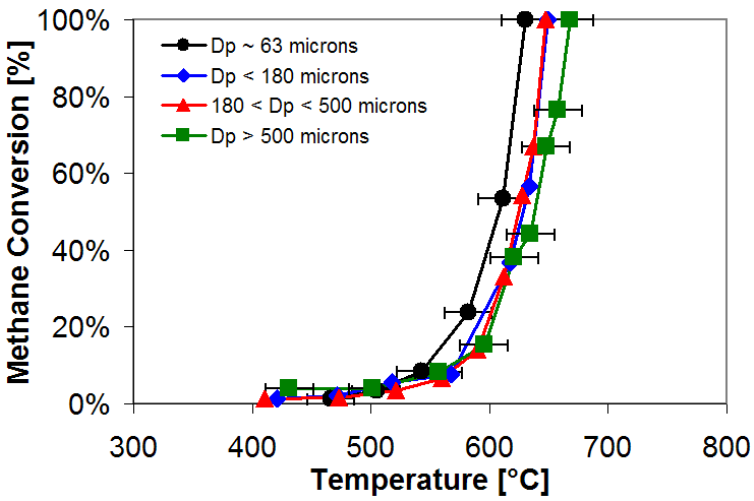

Figure 31: *Methane conversion as a function of temperature for 1 wt% Pt-BHA divided into 4 different particulate size fractions to identify the presence of internal mass transfer limitations. GHSV ≈ 60,000 h^{-1} for all catalysts. Error bars indicate +/- 20°C associated with the placement of the thermocouple in proximity to the catalyst bed.*

The methane conversion is identical within experimental error for each of the four particulate size fractions. Ignition of the methane stream is reached at ~580°C, and full

conversion at ~640°C. These results indicate that MTL are not responsible for the lower activity of Pt-BHA compared to commercial Pt/Al_2O_3 catalysts. Other factors, such as the increased monodispersity and absence of larger Pt particles (~20 nm) in the commercial catalyst, must be responsible for its higher activity.

Previous catalyst research with nanomaterials has often found the presence of a nanoparticle size effect – an increase in activity for particles of a particular nanoscale dimension[6]. Earlier measurement of activity in 1 wt% Pt/Al_2O_3 catalysts indicated that a particle size effect could be responsible for the rapid loss of activity in these materials (see explanation of histograms in **Figure 29**). In order to test for the presence of this effect, 10 wt% Pt-BHA catalysts are treated in a variety of ways in order to produce particles with a wide range of average particle sizes – from 5.4 nm to 28.0 nm. The treatments used and the sizes achieved are outlined above in **Table 4**. Each of the catalysts is used to ignite a 1 vol% methane stream and the methane conversion is plotted as a function of reaction temperature in **Figure 32**. The flow rate of reactant gas is adjusted to account for variation of the Platinum surface area for each of the catalysts.

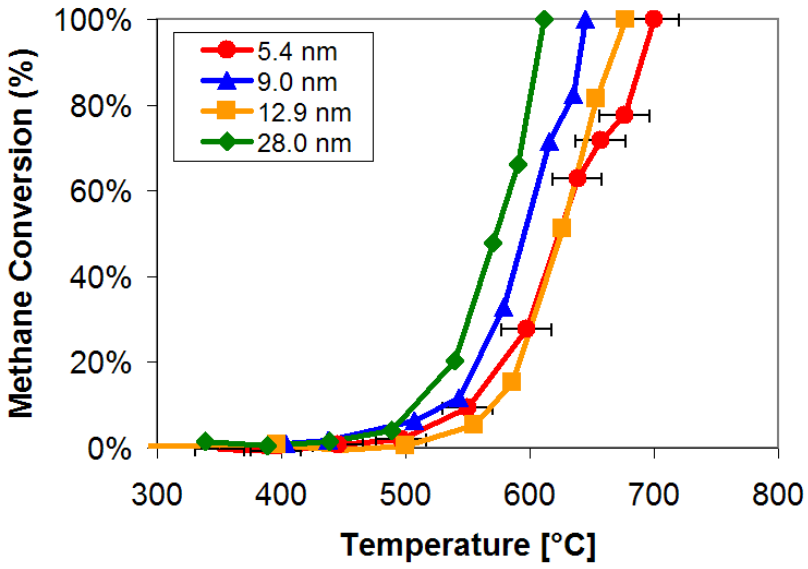

Figure 32: *Methane conversion as a function of temperature for 10 wt% Pt-BHA with different average particle sizes. The flow rate is adjusted for each catalyst sample to normalize the gas velocity to the amount of Pt surface area, ~366,000h^{-1} per square meter of Pt surface area. Error bars indicate +/- 20°C associated with the placement of the thermocouple in proximity to the catalyst bed.*

The catalyst with the largest average particle size (28.0 nm) has the highest activity, with full conversion reached at ~600°C. The catalyst with 9.0 nm particles reaches full conversion ~630°C. Both the 5.4 nm and 12.9 nm Pt-BHA materials show similar activity, with full conversion at ~680°C. There is no clear progression of methane conversion with average nanoparticle size. The results of this testing are inconclusive, and it is not possible to identify the presence of a nanosize effect for this reaction. A couple of factors are possibly leading to the inconclusive results. First, the highest reaction temperature is higher than the calcination temperature for both of the smallest particle sizes. This results in sintering of the Pt particles *in-situ* and therefore it is unclear if the ignition curve measured is representative of the initially indicated average Pt particle size. Secondly, because of the extremely low measured Pt surface area for the largest particle size fraction (~28.0 nm) it was necessary to use a much lower gas

flow rate. This resulted in a much lower overall GHSV (non-normalized GHSV ~13,000 h^{-1} vs. ~184,000 h^{-1} for the other three sizes). At this lower gas velocity, the residence time of the gases within the catalyst bed is increased, allowing more reaction to take place. This is the likely explanation for the increased activity of this particular catalyst. Determination of particle size effects under these high-temperature conditions (where particle sintering is significant) is problematic at best.

Previously, Zarur and Ying observed dramatic lowering of methane ignition temperature after doping BHA powders with CeO_2[38]. In that context, ceria-doped hexaaluminates containing highly active Pt nanoparticles have great potential as methane combustion catalysts. To that end, a 10 wt% ceria doped BHA was prepared by adding cerium nitrate hexahydrate during the aging of the BHA gel in the microemulsion synthesis. A 1 wt% Pt, 10 wt% ceria catalyst is prepared in a similar manner, with the platinum salt being added to the water phase of the microemulsion as described previously. Each of these new catalysts is used to ignite a 1 vol% methane stream. The results are compared to similar previous measurements of pure BHA and 1 wt% Pt-BHA in **Figure 33**. All catalysts are tested with GHSV = 60,000 h^{-1} (no normalization for Pt surface area was done in this case).

All of the modified BHA materials (platinum, ceria, and Pt-ceria) show similar methane conversion behavior. Conversion of 10% of the initial stream is achieved at ~500°C, and full conversion is reached at ~600°C. This ignition behavior is significantly improved from the pure BHA material – which reaches similar conversions at temperatures ~100°C greater. However, the ceria-doped material did not reduce the ignition temperature as low as in the Ying paper, where 10% conversion was achieved at $T \approx 425°C$[38].

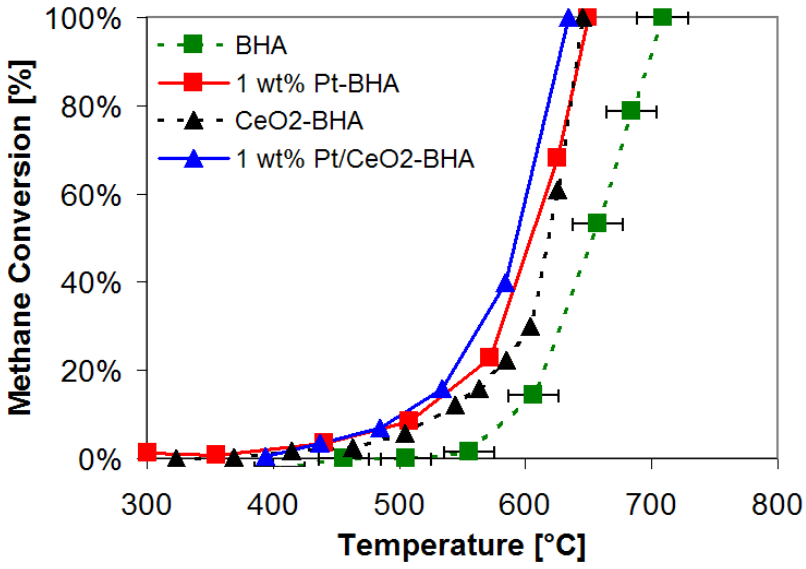

Figure 33: *Methane conversion as a function of temperature for BHA, 1 wt% Pt-BHA, CeO_2-BHA, and 1 wt% Pt-CeO_2-BHA. Calcination: Pt/Al_2O_3 - reduced at 600°C (H_2), Pt-BHA and pure BHA - calcined at 600°C for 5h (Air), reduced at 600°C (H_2). GHSV ≈ 60,000 h^{-1} for all catalysts.*

The result of this investigation is that 10% ceria-doped BHA is as effective for methane combustion as 1 wt% Pt-BHA. The ceria doped material is cheaper to produce, given the very high price of Pt, and it is expected to be much more stable in high temperature treatment, given the high thermal stability of ceria. Interestingly, the Pt/CeO_2-BHA catalyst does not significantly improve on the activity of either of the singularly doped BHAs. However, this similar activity is reached with less accessible Pt surface area than the 1 wt% Pt-BHA catalyst (19.8 m^2/g Pt vs. 31.7 m^2/g), indicating a higher activity in the ceria doped material.

4.5.2 Water-gas shift

As discussed in the background section, the water-gas shift reaction is another important reaction for the production of clean energy and hydrogen, where its main purpose is to increase the H_2/CO ratio of syngas mixtures at low to intermediate temperatures (200-500°C). Because of the mild exothermicity of the reaction (-41kJ/mol), it is equilibrium limited at high temperatures where reaction rates are high (see equilibrium curve in **Figure 34**). Unfortunately, many traditional water-gas shift catalysts, including FeO, Cu, and CoO-MoO based catalysts, do not exhibit suitable activity at low temperatures where equilibrium is not limiting[95]. This presents a practical challenge to water-gas shift in industrial practice: operate at low temperature with low reactivity but no equilibrium limitations, or operate at high-temperature with sufficient reactivity but be limited by the reaction equilibrium. In practice, a two reactor system of low and high temperature water-gas shift is used, each having separate catalysts and reaction conditions. There is therefore a strong desire to find a WGS catalyst which has high activity at temperatures below 250° to prevent equilibrium limitations and greatly simplify the overall process.

Recently, work by Flytzani-Stephanopoulos and coworkers has shown that Au and Pt ceria materials show high activity below 200°C, with activity being traced back to the Au (or Pt) – ceria interface[101-103]. Additionally, they found that Pt based catalysts are typically more active than their Au counterparts[105]. These results provide an interesting starting point for the investigation of Pt and Au nanocomposite structures in the WGS reaction. We have already shown that Pt-BHA nanocomposites are active and stable catalysts for CPOM (sec. 4.1) and methane combustion (sec. 4.5.1). These materials have a highly homogeneous distribution of platinum particles throughout the BHA structure (sec. 4.1), leading to a large Pt-support interface – which is expected to be important for high WGS activity based on Flytzani-Stephanopoulos

work. Additionally, the synthesis of Pt-BHA has been shown to be highly flexible – leading to the formation of nickel and other metal-BHAs (sec. 4.4.5 and Appendix E) as well as ceria modified BHA (sec. 4.5.1). The nanoscale characteristic of these materials, combined with the ability to tailor both the active metal and ceramic phases, make them worthy of investigation in WGS reaction.

The experimental procedure used for WGS testing is outlined in detail in section 3.3.2. Briefly, a mixture of 21.8% H_2O, 9.4% CO, 21.8% H_2, 6.0% CO_2, and 24.8% He is flowed over ~0.05g of catalyst material in a temperature-controlled reactor oven. After condensing out the water remaining after reaction, the gas mixture is analyzed by GC in order to determine the CO conversion and atomic balances. The catalysts used in this testing are listed in **Table 5**.

Table 5: *Catalyst composition and pre-treatment conditions prior to use in water-gas shift experiments.*

Catalyst Type	Nominal Loading	Pre-treatment
Pt-BHA	1 wt% Pt	Air, 5h @ 600°C → H_2, 1h @ 600°C
Pt-Al_2O_3	1 wt% Pt	H_2, 1h @ 600°C
Pt/CeO_2-BHA	1 wt% Pt, 10 wt% CeO_2	Air, 5h @ 700°C → H_2, 1h @ 500°C
Au/CeO_2-BHA	2 wt% Au, 10 wt% CeO_2	Air, 5h @ 600°C → H_2, 1h @ 600°C
Au-CeO_2	2 wt% Au	Air, 5h @ 600°C → H_2, 1h @ 600°C

A series of platinum catalysts are tested (**Table 5**, rows 1-3). The standard 1 wt% Pt-BHA material is formed via sol-gel reaction within a reverse microemulsion. Platinum deposited on alumina powder (1 wt%, Aldrich) is tested as representative of a conventional platinum catalyst. Ceria-modified Pt-BHA (Pt/CeO_2-BHA), which was discussed above as a methane combustion catalyst (see discussion of **Figure 33**), is also tested. This material was calcined at slightly higher temperature (700°C vs. 600°C for the other catalysts studied here) due to the higher temperature conditions of the methane combustion work that the Pt/CeO_2-BHA was

previously used for. Because 700°C is situated within the "plateau" of platinum particle stability (see **Figure 17**) we do not expect a strong change in the activity of this catalyst due to the increased calcination temperature.

Additionally, two types of Au nanocomposites are evaluated (**Table 5**, rows 4-5). Ceria modified Au-BHA was formed by using $AuCl_3$ as a precursor salt in the typical sol-gel microemulsion synthesis, with cerium nitrate hexahydrate being added to during the aging process (similar to the ceria-modified Pt-BHA synthesis mentioned in the previous paragraph). Au-CeO_2 is formed by completely replacing the BHA precursors with cerium nitrate hexahydrate in the sol-gel microemulsion method.

The CO conversions obtained for the various platinum-based catalysts are shown in **Figure 34**. The equilibrium composition for the inlet gas mixture is determined across a wide range of reaction temperatures and is plotted to indicate where the reaction is equilibrium limited. This equilibrium curve is determined via a STANJAN solver (http://navier.engr.colostate.edu/tools/equil.html) which minimizes the Gibbs free energy for the gas mixture. A blank reactor tube, containing no catalytic material – only the quartz glass felt used to hold the catalyst in place – is also tested.

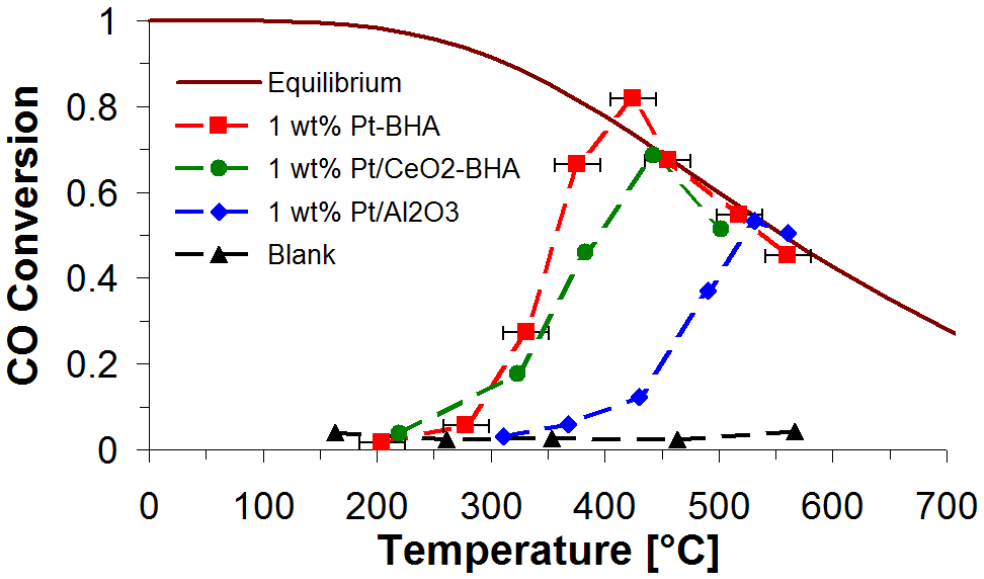

Figure 34: *CO Conversion as a function of reaction temperature for various platinum-based WGS shift catalysts. Equilibrium conversion is plotted for the inlet gas mixture as a function of temperature. A blank sample is included as a control, and it contained only quartz glass plugs and no catalyst material. Approximately 0.05g of each catalyst is used in the testing resulting in GHSV between ~46,000 h^{-1} and ~81,000 h^{-1}. Error bars indicate +/- 20°C associated with the placement of the thermocouple in proximity to the catalyst bed.*

The blank reactor (triangles) shows minimal activity across the range of temperatures tested, indicating that the WGS reaction does not take place on the reactor walls or packing material and that the homogeneous gas-phase reaction is negligibly slow at these conditions. The 1 wt% Pt-BHA (squares) and 1 wt% Pt/CeO_2-BHA (circles) both show comparable CO conversion – with the latter being slightly less active at high temperatures. Both of these catalysts show the onset of ~10% CO conversion at a temperature of 300°C, and increasing from there until the reaction becomes equilibrium limited at T > 400°C. The conventional Pt/Al_2O_3 catalyst is much less active than either of the nanostructured materials. 10% CO conversion is reached at T ~ 425°C for this material, with equilibrium limitations becoming important above T ~525°C.

These results, at least for low-temperature WGS reaction, do not compare favorably with literature. Neither of the platinum nanocomposite materials show substantial activity at 300°C, while Deng and Flytzani-Stephanopoulos found that 2.2 at% Pt-ceria (modified with La) showed CO conversion of ~40%, while 0.8 at% Pt-ceria (unmodified) had initially ~60% CO conversion[114]. We speculate that small particle sizes and correspondingly high metal dispersion of these catalysts, because of the low initial calcination temperature (400°C), is responsible for this large difference in activity. Deng *et al.* do not present TEM images of their Pt-ceria based catalysts, but it is safe to assume that they are at least comparable in size to Pt particles in Pt-BHA at 400°C – around 3 nm (see 4.4.1). In contrast to that, the standard calcination conditions for the nanocomposite materials (T~600°C) produces nanoparticles with diameters ~9 nm which are not active in WGS at 300°C in the present study.

In their work, the Flytzani-Stephanopoulos group found that both of the Pt-based catalysts they tested showed significant deactivation during start-up and shutdown. The 2.2 at% Pt catalyst's CO conversion was reduced by 50% after a single start-up/shut-down, and this behavior is believed to result from the formation of carbonates or formates during shut-down that block active sites[114]. In order to establish if this behavior is also experienced in the platinum nanocomposites tested here, as well as to establish the stability of these nanocomposites, a series of prolonged reaction studies were undertaken. Each of the platinum-based catalysts was allowed to run at 450°C for ~ 24 hours after the initial CO oxidation activity was measured (plotted in **Figure 34**). The catalysts were each shut down after that activity measurement, and then re-started for this study. The CO oxidation was measured at half-hour intervals during this time, normalized by the initial activity during steady state reaction at this temperature, and plotted in **Figure 35**.

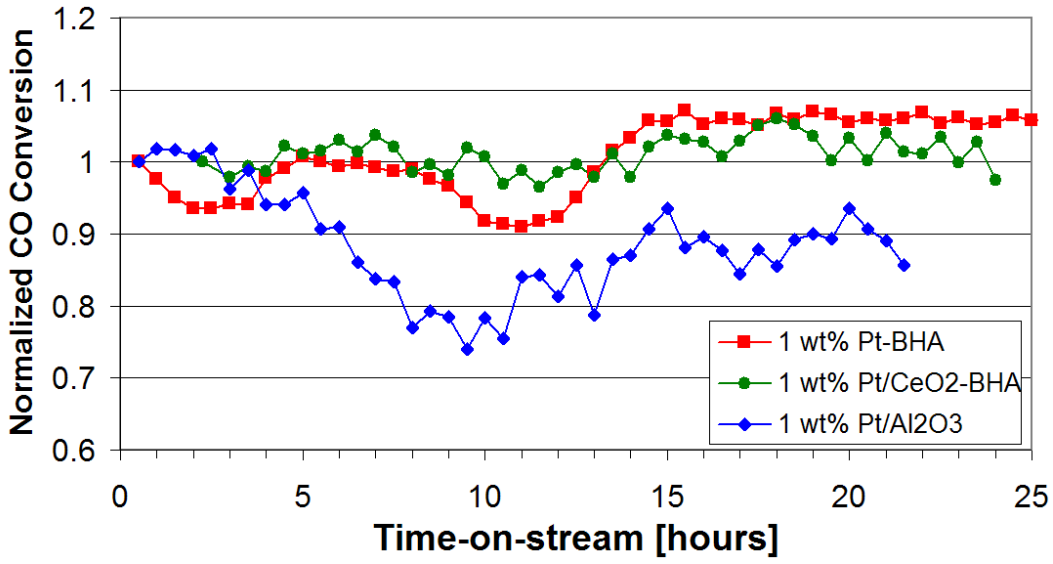

Figure 35: *CO conversion as a function of time-on-stream for platinum based WGS catalysts. The CO conversion is normalized by dividing each data point by the initial CO conversion after steady-state was reached. Approximately 0.05g of each catalyst is used in the testing resulting in GHSV between ~46,000 h^{-1} and ~81,000 h^{-1}. Each test was run at ~450°C.*

The 1 wt% Pt-BHA sample stabilizes at ~107% of its initial activity in this testing, indicating that the material is stable even after shut-down/start-up. The Pt/CeO_2-BHA catalyst also demonstrated stable behavior during the 24 hours of testing, maintaining its full initial activity. The conventional Pt/Al_2O_3 catalyst does experience slight deactivation during the course of the test – decreasing to ~80% of initial activity before recovering to ~90% near the end of the ~22 hours of testing. This indicates that the nanocomposite catalysts are both more resistant to deactivation than the commercial catalyst, as well as being more active. It should also be noted that the deactivation measured here was during the course of the reaction, and not due to start-up/shut-down dynamics. None of the catalysts here experienced noticeable changes in activity when restarting the reactor, contrary to what was seen in the Flytzani-Stephanopoulos work.

Au- based catalysts were also synthesized and tested in WGS reaction. In this case, both Au catalysts are combined in a nanostructure with ceria, as it is believed in some studies that the gold-ceria interface – specifically a Au-O-Ce structure with atomically dispersed gold – is responsible for catalyst activity[101]. Other studies, however, conclude that nanocrystalline gold accounts for a great deal of the activity seen in Au-CeO_2 catalysts[104]. The CO conversion of these materials in WGS reaction is plotted in **Figure 36** in comparison with Pt/CeO2-BHA.

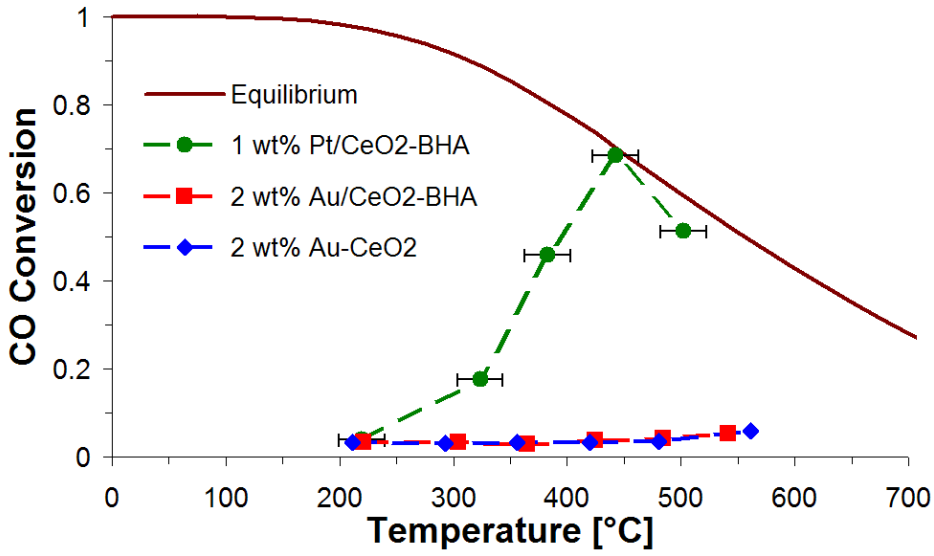

Figure 36: *CO Conversion as a function of reaction temperature for various ceria-based WGS shift catalysts. Equilibrium conversion is plotted for the inlet gas mixture as a function of temperature. Approximately 0.05g of each catalyst is used in the testing resulting in GHSV between ~64,000 h^{-1} and ~162,000 h^{-1}. Error bars indicate +/- 20°C associated with the placement of the thermocouple in proximity to the catalyst bed.*

It is clear from the graph that Au-ceria based catalysts did not demonstrate activity for WGS at all – even for higher temperatures. These Au catalysts are calcined at 600°C, much higher than 400°C seen in the Flytzani-Stephanopoulos paper. This calcination temperature

likely results in larger nanoparticles of Au with a strong decrease in the amount of highly-active atomically-dispersed gold atoms.

A TEM image of the Au-CeO_2 catalyst calcined at 500°C is included in **Figure 37**. In this material, it is difficult to distinguish the metallic gold particles from the dense ceria support. Future testing using EDX to distinguish the gold particles from the ceria support is planned. Calcination of these materials at lower calcination temperature may allow the retention of atomically dispersed gold. A complication arises because of the need to remove surfactant that remains from the microemulsion based synthesis – the calcination will need to be at least above ~450°C (see sec. 4.2).

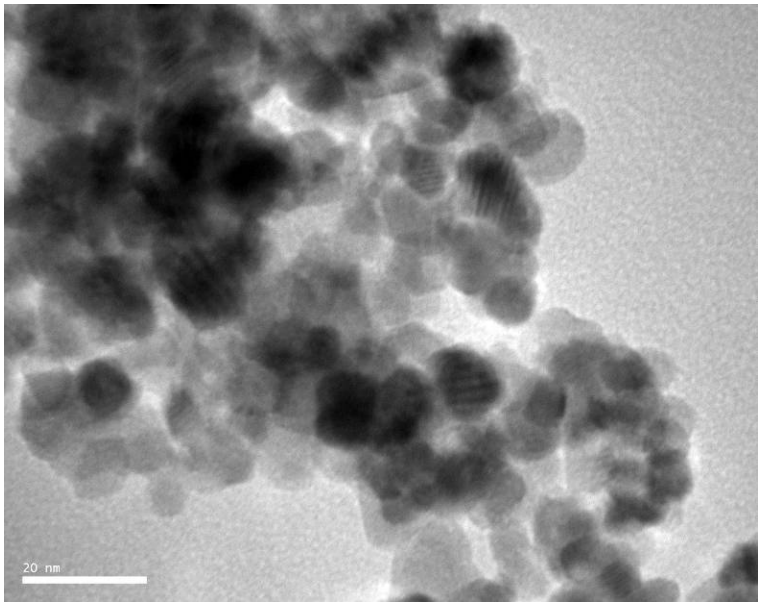

Figure 37: *TEM image of Au-CeO_2 calcined at 500°C.*

These preliminary studies successfully demonstrated the potential of nanocomposite catalysts for the water-gas shift reaction. The stability of Pt-based nanocomposites is promising, but future efforts will need to focus on improving their activity at low temperatures. This is particularly important because of the conundrum facing the water-gas shift reaction system: is it

preferable to operate at low temperatures with low reactivity, or at high-temperatures with equilibrium limitations? Clearly, a water-gas shift catalyst which is both highly active and stable at low-temperatures would be preferable because it would remove the equilibrium limitations and the need to operate a second high-temperature water-gas shift reactor altogether. The literature in this area indicates that the size of the active component and the interaction of that component with the support are both crucial to the catalysts activity[102, 104], and future studies should focus on understanding and improving nanocomposite catalysts with these factors in mind.

5.0 SILICA BASED NANOMATERIALS

Silica is an important catalytic support material in heterogeneous catalytic reactions because it is chemically inert and shows high thermal stability. Mesoporous silica structures such as MCM-41 have great potential for catalysis due to their tunable pore structure which allows for shape and size selective adsorption of reactant molecules[33]. Highly selective catalysts have been created by functionalizing these mesoporous structures with metallic species (such as titania)[147, 148]. As discussed previously, however, these materials have an inherent susceptibility to mass transfer limitations due to their large aspect ratios, especially in relevant high temperature (T≈1000°C) reaction conditions. They are also limited by the thermal stability of the metallic species, which sinter in those high temperature conditions. Chapter 4.0 discussed the formation and testing of thermally stable nanocomposite structures formed with barium hexaaluminate as the ceramic phase which successfully overcame both of these limitations. This section will discuss efforts to expand on those results through the synthesis of nanostructured silica and nanocomposite metal-silicates. While the results to-date have not been particularly successful, the foundations for a successful synthesis of nanocomposite silica materials is taking shape. Important synthesis parameters such as water-to-surfactant ratio and pH have been investigated. Most recently (during the writing of this thesis), Ni- and Fe- silicates have been formed which show promising results in redox cycling. These results will be highlighted in the outlook section at the end of this chapter.

5.1 SYNTHESIS

Silica nanostructures were formed via two different methods. The first is an aqueous phase sol-gel based synthesis. This system was used to investigate the effect of various synthesis parameters on the structure of the resulting silica and metal-silica nanomaterials. The second synthesis method is based on the microemulsion templated sol-gel approach used in the formation of Pt-BHA materials discussed previously. This method is used to create metal-silica nanocomposite structures. Both methods use tetraethoxysilane (TEOS) as the silica precursor.

5.1.1 Sol-gel

The sol-gel approach is adopted from the work of Armelao[149]. A long-chain surfactant, Brij58 (2g, Aldrich), was dissolved in an HCl solution (pH=0.48, 200ml) at 50°C. After complete dissolution, TEOS (4.4g, Fluka) was added all at once under vigorous stirring. The solid product was filtered, washed with de-ionized water, and dried at room temperature for 24 hours. In some cases, reduction of the silica precursors was initiated by bubbling the solution with ammonia gas. Each sample was allowed to age for 24 hours. The solution was gravity filtered and the particulate was washed thoroughly with de-ionized water. The resulting dried powder was calcined in flowing air for 1 h at 160°C then 4 h at 600°C.

A number of different synthesis parameters were varied to determine the effect on the final product. These parameters included: pH of the aqueous solution, water-to-surfactant ratio, aging time, and reduction method.

5.1.2 Microemulsion templated sol-gel

The microemulsion templated approach is identical to that described for Pt-BHA nanocomposites (sec. 3.1) with the exception of two aspects. First, the alkoxides used for BHA were replaced with TEOS. The ingredients for a single batch of 10wt% Pt-SiO_2 are shown in **Table 6**. The second difference is the use of an additional reduction step. In the Pt-BHA synthesis, a gel would form spontaneously upon addition of the hexaaluminate precursors to the microemulsion. In TEOS the gel does not form unless the mixture is subjected to an additional reduction step. Bubbling with ammonia gas was used to reduce the synthesis and induce gel formation. All other synthesis and workup procedures were identical for the microemulsion based materials.

Table 6: *Components in the microemulsion templated sol-gel synthesis of 10wt% Pt-SiO_2*

Microemulsion		**MW [g/mol]**	**moles**	**Mass [g]**
PEPP	(surfactant)	2000.00	0.0075	15.0
1-Pentanol (>99%)	(co-surfactant)	88.15	1.9853	175.0
2,2,4 Trimethylpentane (>99%)	(oil phase)	114.23	0.3939	45.0
De-ionized H_2O (Milli-Q)	(water)	18.00	0.7111	12.8
$H_2PtCl_6 \cdot 6\ H_2O$ (>37.5% as Pt)	(metal salt)	409.82	0.0012	0.487
Silica Solution				
Tetraethoxysilane (99.99%)		208.33	0.0347	7.23
Anhydrous 2-propanol (99.5%)		60.10	1.6328	98.13

5.2 RESULTS AND DISCUSSION

5.2.1 Sol-gel based silica and parameter variation

A sol-gel based synthesis was chosen for silica because it offered numerous methods for tuning the properties of the synthesis to alter the final product. An example of this tuning is shown in **Figure 38**. Two batches of silica were formed in parallel, with all parameters being equal except for the pH of the aqueous solution prior to TEOS addition. At pH = 1.0 (left image) the gel phase took longer to form than at pH = 0.48 (right image), leading to a longer aging period as well (72 vs. 24 hours). The silica formed at pH = 1.0 shows the presence of large, dense particles of silica (dp ≈ 100nm) intermixed with finely-grained low density silica. This material had a very high specific surface area of ~1630 m^2/g. This is amongst the highest reported surface areas reported for silica nanomaterials, comparing favorably with MCM-41 and MCM-48 (~1000 m2/g)[85]. Further attempts to reproduce this highly interesting silica material are included in the outlook section. The silica formed at pH = 0.48 shows no evidence of the large silica particles. Instead, a collection of dense dp ≈ 5nm silica particulates are dispersed amongst the low density silica. The material in this case had a surface area of ~880 m^2/g, much lower than the pH = 1.0 sample, but still very high relative to other nanomaterials.

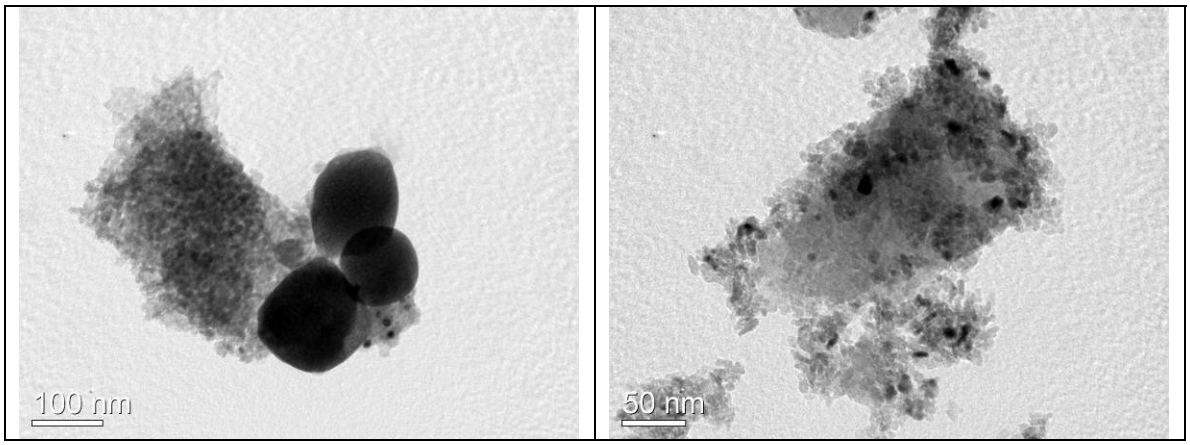

Figure 38: *TEM images of SiO_2 particles formed via the sol-gel method. Left: pH = 1.0 and aging time = 72 hours. Right: pH = 0.48 and aging time = 24 hours.*

The dramatic differences in the morphology and specific surface area of the silica formed (from only a 0.5 pH point change) demonstrate the highly tunable nature of the sol-gel method. A wide range of synthesis parameters are evaluated to determine their effect on the silica structure. Nitrogen porosimetry was chosen as a characterization tool for rapid analysis of the specific surface area and pore structure of the resulting silica materials. The results of this testing are summarized in **Table 7**. The silica yield (last column) was determined by dividing the mass of silica powder actually obtained by the mass of silica expected for 100% conversion of the TEOS. Discussion of the results of each parameter variation is given in the following sections.

Table 7: *Experimental parameters for sol-gel synthesis of silica.*

Experiment Number	R_w	pH	Aging Time (h)	Reduction Method	Specific Surface Area [m^2/g]	Avg. Pore Size [nm]	Y_{SiO2} [%]
1	4189	0.50	22.0	--	820.2	3.1	77
2	5033	0.49	22.0	--	911.6	3.1	69
3	6272	0.48	24.0	--	849.8	3.2	86
4	8347	0.50	24.0	--	921.9	3.1	69
5	12534	0.50	22.0	--	760.4	3.1	86
6	6265	0.15	23.0	--	767.4	3.2	52
7	6280	0.25	23.0	--	843.7	3.1	53
8	6242	0.60	23.0	--	803.0	3.3	39
9	6273	0.75	23.0	--	926.4	3.1	61
10*	6288	0.76	6.0	--	780.5	3.1	2
11*	6288	0.76	8.0	--	821.8	3.1	10
12*	6288	0.76	12.0	--	823.4	3.1	19
13*	6288	0.76	27.0	--	950.1	3.2	165
14**	6291	0.75	0.0	NH_3 bubble	919.1	4.1	73
15**	6291	0.75	4.0	NH_3 bubble	905.4	4.8	67
16**	6291	0.75	20.0	NH_3 bubble	897.9	5.4	67
17**	6291	0.75	24.0	NH_3 bubble	746.5	5.6	90

** indicates samples were all part of a large batch from which samples were drawn after the aging time indicated.*

*** indicates samples were all part of a large batch which was bubbled with NH_3 immediately after introduction of TEOS. Samples were drawn after the aging time indicated.*

5.2.1.1 pH

The pH of the aqueous solution represents the relative abundance of H^+ ions available for the silica polymerization to take place. Zhao *et al* found that the rate of precipitation of mesoporous silica (formed in a similar manner) was given by the following relation[150]:

$$r = k[H^+]^{0.31}[Cl^-]^{0.31}$$

They postulated a mechanism that first involved hydrolysis of the TEOS species in the acidic media, followed by oligimerization of the silica species. If this mechanism and rate law are accurate, then increasing pH number should have a negative impact on the aging time necessary for silica precipitation (i.e. for constant aging time, smaller yields will be achieved). The pH value will impact the structure of the silica if the hydrolysis of TEOS is the controlling step in the reaction mechanism. If the TEOS hydrolysis is not rate controlling, we expect pH to have relatively little impact on silica structure.

With these considerations in mind, the pH value of the sol-gel solution was varied between 0.15 - 0.75 by addition of HCl to the aqueous solution prior to TEOS addition. Solutions with pH values of 1.0 and larger did not show any precipitation of silica during the course of the experimental run. All other experimental conditions were held constant. Experiments 3, 6, 7, 8, and 9 (**Table 7**) represent the data set for this analysis. The experimental results are plotted in **Figure 39**.

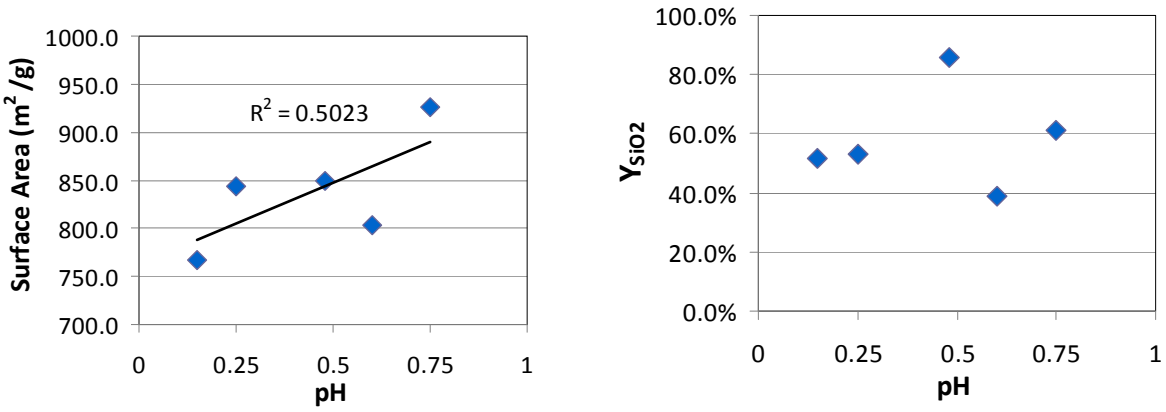

Figure 39: *Specific surface area and silica yield for sol-gel synthesis of silica with various pH values.*

The specific surface area of the silica follows an increasing trend from ~770 m^2/g for pH = 0.15 to nearly 925 m^2/g for pH = 0.75. All pH values resulted in silica with average pore size of around 3.1-3.3 nm, indicating little change to the mesopore network. The silica yield varies widely for the three samples, from ~40% for pH = 0.6 to close to 90% for pH = 0.5.

The surface area of the silica increases as the pH value increases toward a limiting value (no silica gel formed for pH > 1.0). This is an indication that H^+ ions may be detrimental to the formation of high-surface area silica. The silica yield data shows a high degree of variability, so it is difficult to draw a conclusion based on these measurements. However, the predicted trend of decreasing yield with increasing pH value is not evident.

5.2.1.2 Water to surfactant (R_W) ratio

The molar water-to-surfactant (R_W) ratio is a measure of the relative concentration of the Brij56 surfactant. As the value of R_W is increased (smaller surfactant concentration) the surfactant is expected to be present in lower concentrations on the surface of the silica particles as they form. This is expected to result in faster precipitation kinetics (increased yields for the same aging

time) because the surfactant molecules are expected to hinder the silica oligimerization process. The particles that form will be larger in size, leading to more coarsely grained silica with lower specific surface area and larger pores.

The R_W ratio was varied by changing the mass of surfactant added to the mixture while keeping the mass of TEOS and water the same. In all cases dilute mixtures of surfactant were used, resulting in large R_W values ($R_{W,min}$ = 4189). Experiments 1 through 5 (**Table 7**) represent the data set for this analysis. The results are plotted in **Figure 40**.

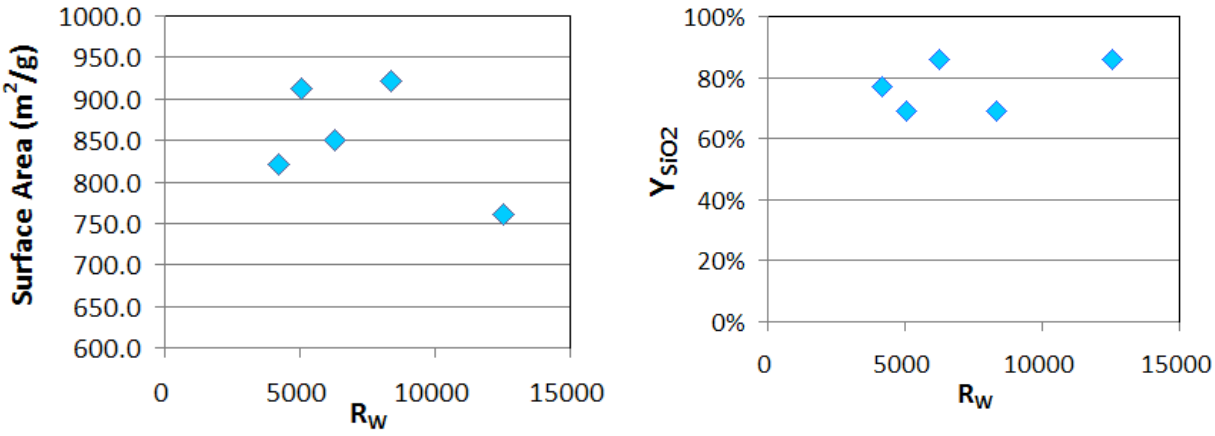

Figure 40: *Specific surface area and silica yield for sol-gel synthesis of silica with various R_W.*

The data indicate a very weak decreasing trend in specific surface area and a weak increasing trend in silica yield as the R_W value is increased. There is a large amount of variability (low R^2 values) in the data, indicating that more data should be obtained before a definitive judgment of this effect of this parameter is determined. Pore size measurements indicate no change in the pore structure of these materials, with pore diameter ~3.1nm for all samples.

With caution (due to scatter in the data), we report that the trends are as predicted. Increasing R_W value leads to less surfactant on the surface, larger particles of silica, and trends

toward lower specific surface areas. Increasing R_W also leads to increasing silica yields, presumably due to faster oligimerization of the silica in the presence of lowered surfactant concentration. Interestingly, the pore structure of the material remains unchanged across all R_W values, indicating that the concentration of surfactant is unimportant in the formation of pores. This does not eliminate the possibility that the structure and size of the surfactant is an important factor in pore formation.

5.2.1.3 Aging time

The length of time that the reaction proceeds should have an obvious affect on the silica yield, with longer aging times resulting in higher yields. More interesting is the effect the aging time has on the specific surface area and pore structure of the resulting silica. It is clear from previous studies that prolonged reaction times can lead to increased oligimerization and changes in the mesoscale architecture of the material[150]. It is likely that continued aging after the onset of precipitation will result in larger agglomerates of silica with lower specific surface area and smaller pores.

To test this hypothesis, a single batch of sol-gel silica was prepared, and aliquots were withdrawn from the batch at 6, 8, 12, and 27 hours after addition of TEOS. The experiments corresponding to this analysis are 10-13 (**Table 7**). The results are plotted in **Figure 41**.

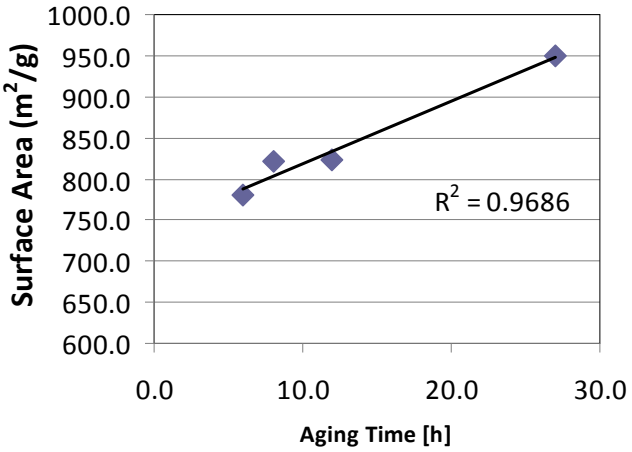

Figure 41: *Specific surface area for sol-gel synthesis of silica with increasing aging time. The line is a linear regression fit of the data, with R-square value shown.*

The data show a well-correlated increasing specific surface area with increasing aging time. Each sample was determined to have a pore size of ~3.1 nm. It was not possible to evaluate the silica yield for each aging time due to an experimental limitation. All 4 data points were measurements made by withdrawing aliquots from a single, larger batch of solution. This was done to ensure that identical synthesis parameters were present at each aging time. Because of this, the synthesis yield was much higher for the last aging time. Silica formed at earlier aging times remained on the walls of the synthesis flask, and was included in the weight of the final sample.

The increasing trend in the specific surface area is contrary to what was predicted. It appears that prolonged aging allows the silica to form a more finely structured high-surface area structure. This could be a byproduct of the use of a very dilute mixture (high R_W values) of TEOS and surfactant, since in a dilute mixture agglomeration is expected to occur more slowly. These results correlate well with the formation of very high specific surface area silica (~1630 m2/g), because that material was aged for even longer – 72 hours (see discussion of **Figure 38**

above). Interestingly, the pore size distribution is unaffected by aging time. This indicates that the increased surface area must be the result of a more extensive network of similarly sized pores, rather than as result of shrinking the pores or fundamentally altering the mesoscale structure of the silica.

5.2.1.4 Reduction method

The sol-gel method discussed relies on spontaneously occurring precipitation to occur as the silica agglomerates become too large to remain in solution. Thus the processes of nucleation and growth of the silica seeds occur simultaneously throughout the aging time. It is optimal to separate these two processes (in time) for the synthesis of uniform, high-surface area nanostructures. Rapid nucleation followed by slow particle growth allows for a homogeneous size distribution of nanoparticles. It is therefore interesting to consider the use of induced nucleation of the gel via rapid reduction.

The sol-gel synthesis was prepared as discussed above. In this experiment, however, a stream of NH_3 gas was bubbled through the solution immediately after TEOS addition. Bubbling (~1 SLM flow rate) continued until a rapid formation of white silica particulates occurred, after approximately two minutes. The NH_3 gas is a strong base, and it is expected to rapidly increase the pH of the solution. Therefore the pH listed in **Table 7** should only be considered a starting point. It should be noted that Zhao found in similar studies that basic (pH > 7) sol-gel precursor solutions generally yielded amorphous silica or silica gels, rather than crystallites[150]. This should not be considered detrimental to the formation of nanocomposite catalysts, however, as amorphous BHA serves as an excellent material for thermal stabilization of nanoscale particles (chapter 4.0). The results of nitrogen porosimetry analysis of silica formed via rapid nucleation and subsequent aging testing are shown in **Figure 42**.

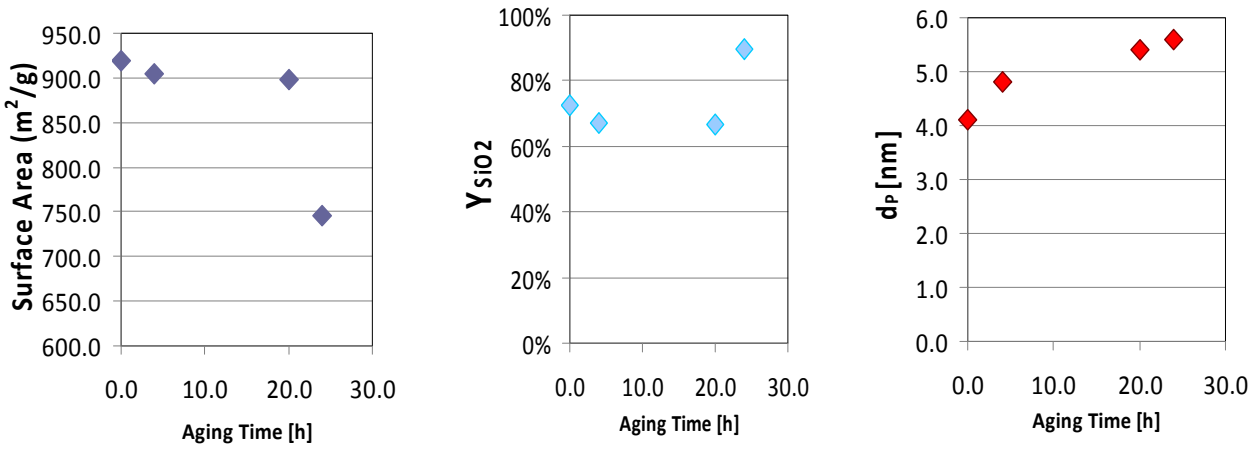

Figure 42: *Specific surface area, silica yield, and pore diameter versus aging time for sol-gel synthesis of silica with rapid reduction induced by NH_3 gas.*

The specific surface area of the synthesized silica remains at ~900 m^2/g for the first 20 hours of aging, but decreases to ~750 m^2/g by 24 hours (**Figure 42**, left graph). This correlates with an increase in silica yield, from 67% to nearly 90%, as the sample is aged from 20 to 24 hours (**Figure 42**, center graph). The pore structure of the silica increases continually throughout the aging process, from ~4 nm directly after NH_3 bubbling to nearly 6 nm after 24 hours.

The silica in this sample was produced in one flask, with a sample taken out at each aging time indicated. Because of this, a portion of the silica formed at earlier aging time remains after each sampling. There is a high probability that this silica produced at earlier times remained on the walls of the synthesis vessel, and were only measured at the last data point. A more gradually increasing yield would be expected if this sampling problem did not arise, because some of the silica measured at the last data point would be included in the earlier points. Future studies should use separate reaction vessels for each data point, to prevent this inhomogeneous sampling.

Despite this experimental limitation, the data indicate that the silica material is growing as predicted. The rapid nucleation of the silica by the NH_3 bubbling leads initially to very high surface area silica formed from smaller agglomerates. As the silica is allowed to age, the nanoparticles grow larger, leading to lower surface areas and larger pores. The process of rapid reduction of the TEOS precursor via NH_3 bubbling immediately followed by quenching (filtration/washing) shows the potential to quickly and efficiently form very high surface area silica.

5.2.1.5 Pt-SiO_2 via sol-gel synthesis

The incorporation of a well dispersed noble metal phase is an important part of the formation of a highly active catalyst. Pt metal is catalytically active for CPOM and methane combustion, and can be stabilized by a nanostructured BHA framework (see section 4.0). It is worthwhile, then, to investigate the synthesis and properties of Pt-SiO_2 nanocomposites prepared using the sol-gel method.

Hexachloroplatinic acid was dissolved into the aqueous phase of the sol-gel synthesis prior to addition of Brij58 and TEOS. The amount of salt added was adjusted to form both 1wt% and 10wt% Pt loaded silica. For these experiments, TEOS was added drop-wise over the course of one hour (following the method of Armelao *et al*[149]). NH_3 bubbling, previously used to form pure silica with high specific surface areas, was used to precipitate the Pt-silica mixture at various times during the synthesis (before aging, after aging, and without any aging). TEM was used to study the morphology and distribution of the Pt nanoparticles within the silica structure.

Figure 43 shows TEM images of sol-gel Pt-SiO_2 at both 1wt% and 10wt% Pt loading. In both cases, a distribution of ~5-10nm Pt particles is present. However, the particles are inhomogeously distributed on the structure. Some parts of the silica material are heavily loaded,

while others are completely void of nanoparticles (large sections of unpopulated silica were observed during TEM analysis). Increasing the Pt weight loading increases the quantity of particles in the populated regions, but the heterogeneities still exist. It also appears in the images that the Pt nanoparticles are located on the surface of the silica, rather than incorporated into the structure. The specific surface area and pore structure of the material is similar to that of pure silica formed via sol-gel (~730 m^2/g, 3.2 nm), indicating that the Pt salt does not significantly alter the silica formation.

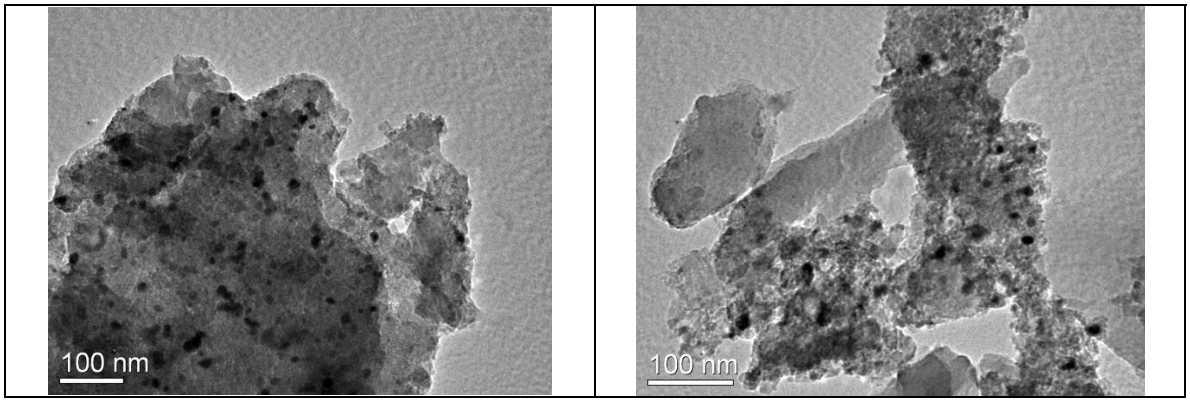

Figure 43: TEM images of Pt-SiO_2 formed via sol-gel synthesis of silica. Left: 1 wt% Pt, Right: 10wt% Pt. Both samples: pH=0.5, aging time=24h, no NH_3 bubbling, calcined at 600°C.

The results indicate that it is possible to form a nanocomposite Pt-SiO_2 material via the sol-gel synthesis; however, the material is somewhat limited. The nanoparticles are not incorporated in the ceramic structure (as with BHA), so they are not expected to be sinter resistant in high-temperature reaction conditions (~1000°C). Additionally, the Pt nanoparticles are not homogeneously distributed, possibly due to their uncontrolled reduction and precipitation within the continuous aqueous phase of the synthesis. Because of this limitation, as well as the high-surface area pure silica formed using it previously, NH_3 bubbling was explored to determine the effect that a controlled reduction has on the final nanocomposite structure.

Unfortunately, NH_3 bubbling leads to very poorly structured Pt-SiO_2. **Figure 44** shows TEM images of the resulting materials formed with NH_3 bubbling. Pt particles are very sporadic and frequently large in size (>20nm) in all three of these samples. The large particle size is likely the result of sintering of the unstabilized Pt particles at 600°C. The areas of dense Pt particle populations seen in non-bubbled samples are not present. The sol-gel synthesis does not lead to intimate contact between the nanostructured silica and Pt. Instead, it appears to induce completely separate precipitation of the silica and Pt domains. The addition of Pt does not significantly alter the surface area (between 840 and 1040 m^2/g) or the pore structure (3.1, 5.1, and 4.6 nm) of the resulting silica material compared to similarly synthesized pure silica.

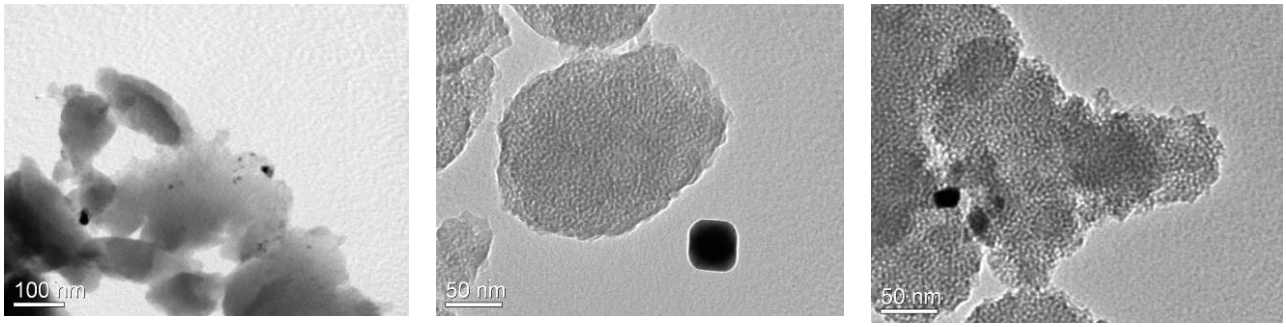

Figure 44: *TEM images of 1 wt% Pt-SiO_2 formed via sol-gel synthesis of silica with NH_3 bubbling. Left: bubbled after 24h aging. Center: bubbled before 24h aging. Right: bubbled without any aging. All samples: pH=0.5, calcined at 600°C*

5.2.2 Microemulsion templated synthesis of Pt-SiO_2

Sol-gel synthesis of Pt-SiO_2 leads to poorly distributed Pt nanoparticles, and significant growth of Pt nanoparticles after calcination at 600°C in some circumstances. Theoretically, these limitations can be overcome by performing the sol-gel reaction within the micelles of a water-in-

oil microemulsion. The individual micelles are expected to act as a template for the reaction, leading to intimate contact between the silica and Pt, and the formation of a more homogeneous nanocomposite. The benefits of performing the sol-gel reaction within a microemulsion have been previously shown for Pt-BHA nanocomposites[10-14].

10 wt% Pt-SiO_2 nanocomposites are formed via the microemulsion templated sol-gel process described previously. The TEOS precursor will not spontaneously form a gel, as in the formation of BHA from alkoxides, so a method was devised to induce gel formation. Liquid reducing agents (e.g. ammonium hydroxide) were used to perform the gellation, but the results were not reproducible (data not included). The inherent sensitivity of microemulsions to changes in composition may have led to the inconsistency of those results. Instead, bubbling with NH_3 gas is utilized because it induces the precipitation of silica without significantly altering the composition of the microemulsion. Even though bubbling with NH_3 gas was ineffective at producing Pt-SiO_2 nanocomposites for the sol-gel procedure above, the significantly different environment of the microemulsion, as well as a more systematic bubbling method warrant trying this method again. Aging of the microemulsion takes place following the bubbling procedure.

This investigation focused on two important factors in the formation of Pt-SiO_2: bubbling time and aging period. Four bubbling times (30s, 90s, 150s, and 210s) are used at two different aging times (0.5h and 23h). Longer bubbling time allows for longer contact between the microemulsion and the ammonia gas, leading to higher pH in the micelles and faster gel formation. Longer aging time is expected to lead to increased particle growth and lower specific surface areas. A range of characterization techniques, including XRD, TEM, and nitrogen porosimetry, are used to analyze the structure of the resulting materials.

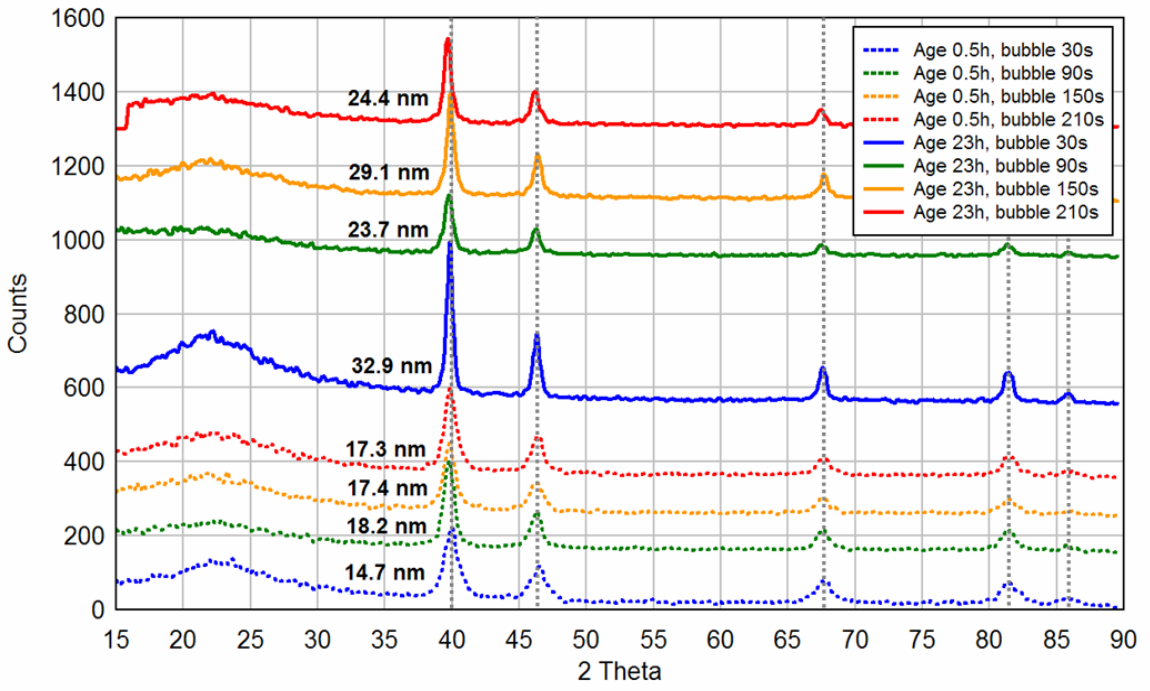

Figure 45: *X-ray diffraction patterns of Pt-SiO_2 formed via sol-gel reaction within a reverse microemulsion. Dashed vertical lines indicate Pt reflexes at 39.8, 46.2, 67.5, 81.3, and 85.7 2θ. The numbers listed are average particle sizes determined from Debye-Scherrer analysis of the 39.8 2θ reflex.*

X-ray diffraction (**Figure 45**) shows no discernable reflexes for silica crystallites, indicating that for all cases the silica remains amorphous. Reflexes for Pt indicate the presence of nano-sized domains of crystalline Pt in each of the samples measured. Debye-Scherrer line broadening analysis of the dominant Pt reflex at ~40 2θ gives an estimate of the average Pt crystallite diameter. The samples aged for 23h have larger diameter Pt crystallites (23.7-32.9 nm) than samples aged for 0.5h (14.7-18.2 nm). The effect of bubbling time on the size of the Pt crystallites is difficult to determine from these results, because no clear trend is established as the bubbling time is increased.

TEM is used to characterize the morphology of the silica and Pt, and to more accurately determine the diameter of the Pt nanocrystals. **Figure 46** shows the images and particle size

distribution for samples aged for 0.5h, while **Figure 47** shows similar data for samples aged for 23h. In all samples studied the silica is assembled in large clumps with no consistent discernable morphology. The Pt particles generally form spheroidal crystallites which vary in size depending on the aging/bubbling time. The particles reside on the surface of the silica structure, rather than within the silica matrix, similar to Pt-SiO_2 formed via the sol-gel route. One advantage of the microemulsion templated method is the homogeneous distribution of Pt particles amongst the silica material (for aging time of 0.5h), compared to the highly heterogeneous distribution that resulted from the sol-gel method.

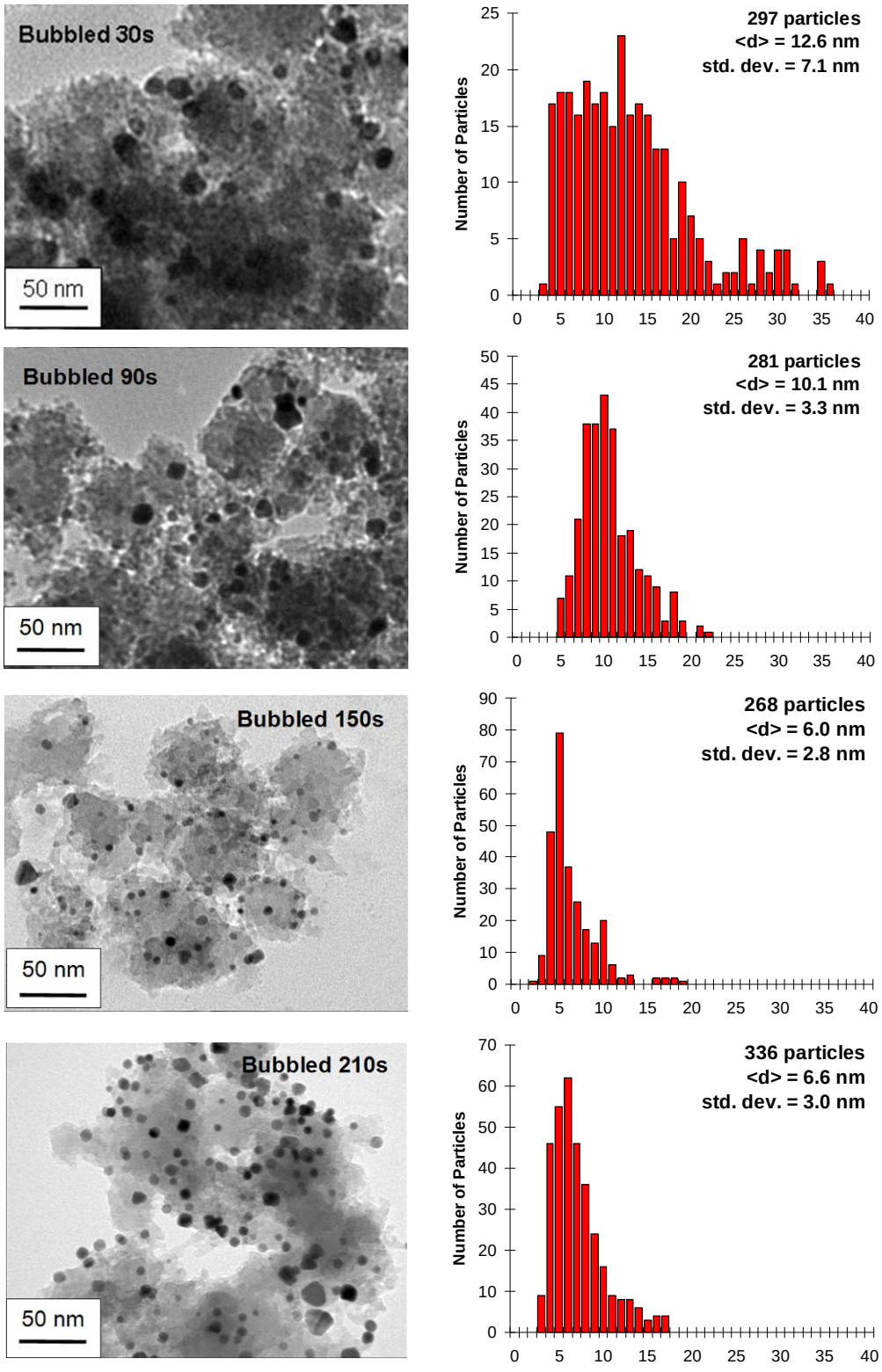

Figure 46: *Selected TEM micrographs for Pt-SiO2 catalysts and corresponding Pt particle size distributions, aged for 0.5 hours and bubbled as indicated.*

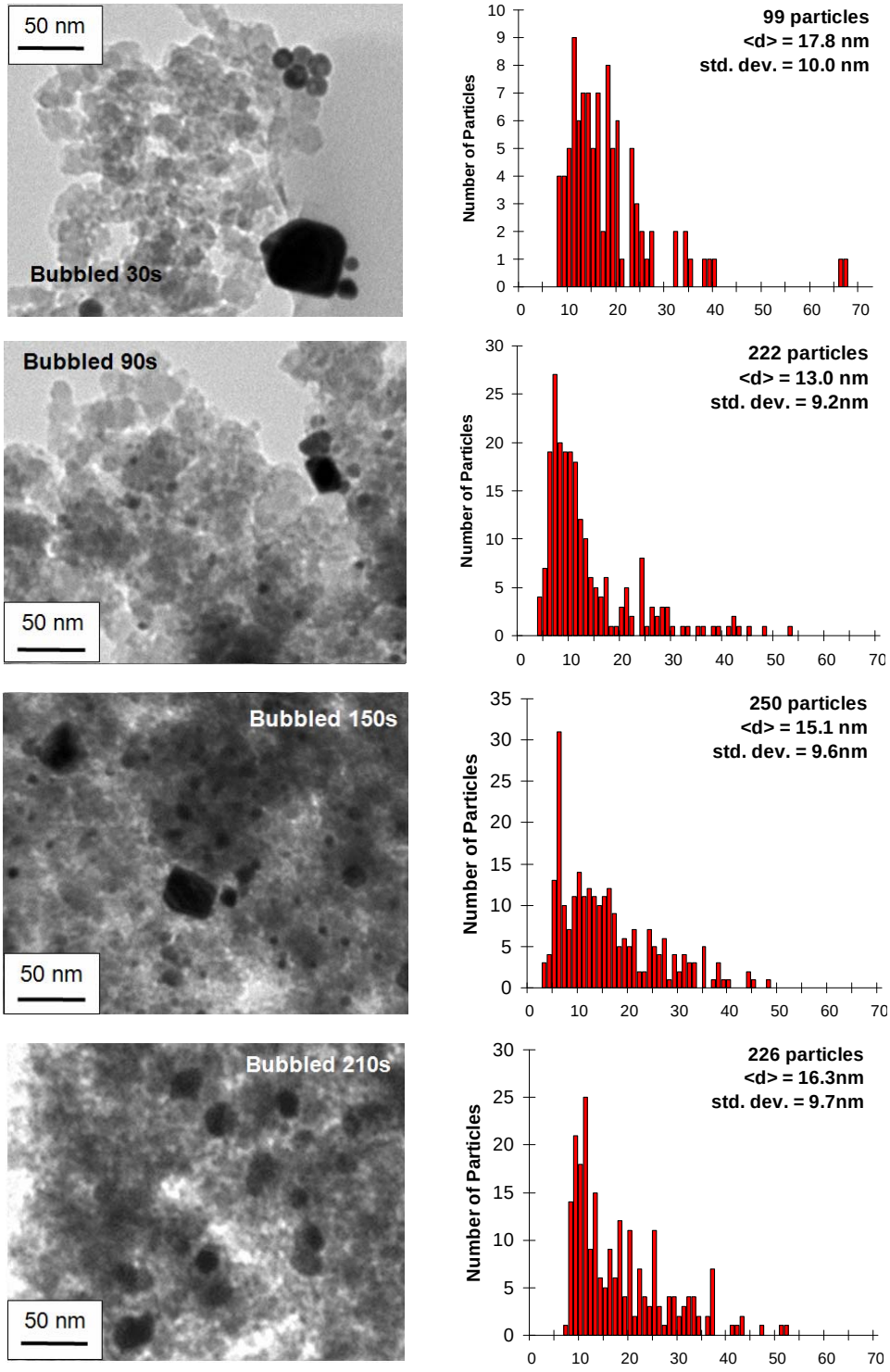

Figure 47: *Selected TEM micrographs for Pt-SiO2 catalysts and corresponding Pt particle size distributions, aged for 24 hours and bubbled as indicated.*

In samples aged for 0.5h (**Figure 46**), the average Pt particle size shows a decreasing trend as the bubbling time is increased (from ~13nm to ~7nm). Additionally, the size distribution of the particles becomes much narrower as the bubbling time increases above 30s. In samples aged for 23h (**Figure 47**), the average Pt particle size shows no discernable trend as the bubbling time is increased (varying between ~13 to ~18 nm). The size distribution of the particles aged for 23h is much broader than for the samples aged for 0.5h. All of the bubbling times measured showed a significant portion of particles with diameters larger than 40 nm. The growth of the particles leads to a less homogeneous distribution of particles, eliminating one of the main advantages of the microemulsion method.

Nitrogen porosimetry was used to evaluate the specific surface area of the Pt-SiO_2 materials at each reaction condition. **Figure 48** plots the specific surface area and average Pt particle size (determined from TEM, above) as a function of aging and bubbling time. Samples aged for 23h have both larger Pt particles (as mentioned above) and larger specific surface areas. The sample aged for 24h shows an increasing specific surface area trend as the bubbling time increases, leveling off after 150s. No other trends can be established with respect to the bubbling time.

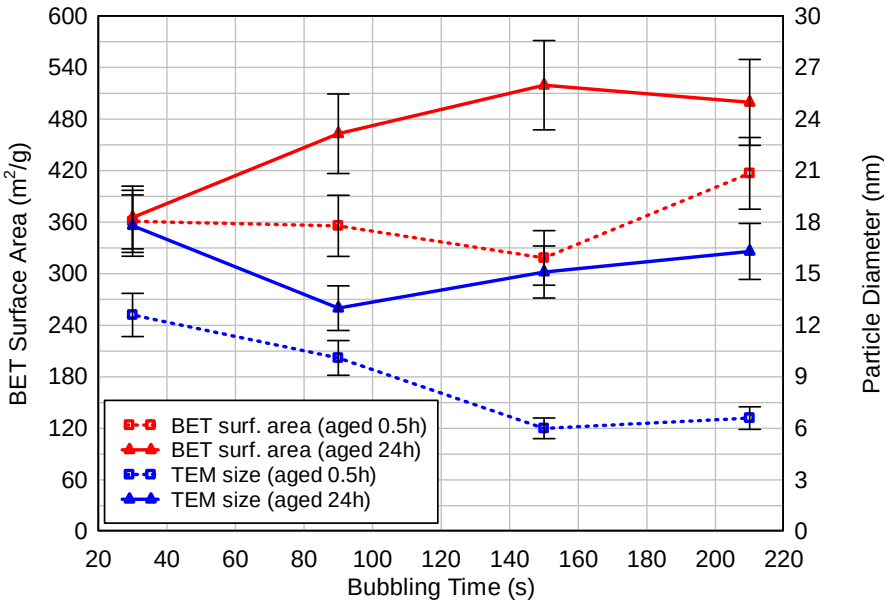

Figure 48: *Average Pt particle size determined from TEM, and BET surface area for Pt-SiO_2 materials with bubbling and aging times as indicated. Error bars indicate an approximation of the experimental error (10%).*

The stability of the platinum nanoparticles at high temperature conditions is an important concern for the application of these materials as nanocatalysts. In order to test the stability, one of the Pt-SiO_2 nanocomposites (aged 0.5h, bubbled 210s) was calcined for 5 hours at 1100°C, and XRD was used to evaluate the change in Pt particle size (**Figure 49**). The Debye-Scherrer line broadening analysis indicates that the Pt particles increased three-fold in diameter.

The data from XRD, TEM, and BET indicate that the formation of Pt-SiO_2 via sol-gel synthesis within a microemulsion was limited in success. Consistent formation of nanoscale platinum dispersed on an amorphous silica substrate was achieved. Longer aging time leads to increased platinum particle size and higher specific surface areas. Aging is an important part of forming a high-surface area nanostructure, but in this case it leads to agglomeration of the Pt precursors in solution. The increase in specific surface area may be the result of lowered silica pore occlusion due to the larger size and poorer distribution of the Pt nanoparticles. The length

of bubbling time was not a critical parameter in the synthesis. Increased bubbling time did decrease the average particle size for samples aged for 0.5h, but no other trends could be established. Despite the advantages offered by NH_3 bubbling (retention of microemulsion composition, rapid gel formation), it remains a difficult procedure to control at best. Most importantly, none of the TEM images seemed to indicate that the Pt particles were actually encaged by the silica structure, which has been shown to result in the high temperature stability seen for Pt-BHA nanocomposites. The lack of thermal stability is indicated by significant Pt particle sintering during calcination at 1100°C.

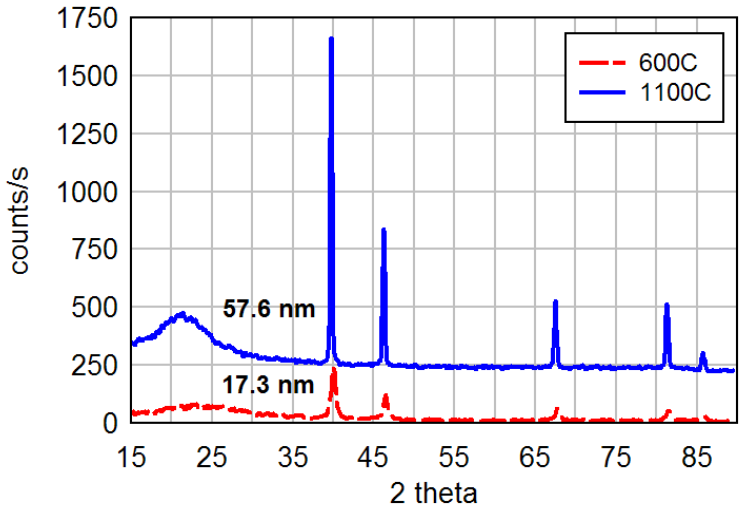

Figure 49: *XRD pattern for Pt-SiO_2, bubbled for 210s and aged for 0.5h, calcined at 600 and 1100°C.*

5.2.3 Outlook

The work on silica nanomaterials presented here has resulted in a better understanding of the challenges involved in this synthesis. By carefully varying pH, aging time, R_W, and reduction method, it has been possible to identify the effect that each has on the formation of nanoscale silica. Two different methods were used to form Pt-SiO_2 nanocomposites, both with limited success. The nanocomposites formed do not demonstrate the same particle-in-cage morphology previously seen for thermally stable Pt-BHA nanocomposites, and hence are not sinter resistant. Further work will be needed to improve the structure of these materials.

The formation of silica with particularly high specific surface area (~1630 m^2/g, **Figure 38**, left graph) should be investigated further. This specific surface area is higher than those reported in the literature for high surface area MCM-41 and MCM-48 materials[85]. The effect of extended aging time seems to be a strong increase in specific surface area, and this effect is not characterized for aging times longer than ~24 hours in the current work. The reproducible formation of silica with high surface area could then lead to high surface area metal-silicates via introduction of metal salts during the synthesis procedure. These nanocomposite catalyst materials would have potential as active catalysts due to the combination of high surface area and high active metal dispersion.

Recently, the formation of Ni and Fe silicates has been explored with some success. The synthesis procedure followed closely the previously reported synthesis of Pt-SiO_2 via the sol-gel method (section 5.2.1.5). A pH of 0.75, R_W value of 4189, aging time of 24h, and 30 wt% metal weight loading of the appropriate nitrate salt (Ni- or Fe-) was used. Both samples were bubbled with NH_3 to induce precipitation of the metal-silicate material, gravity filtered and washed with de-ionized water, and subsequently dried under high-vacuum.

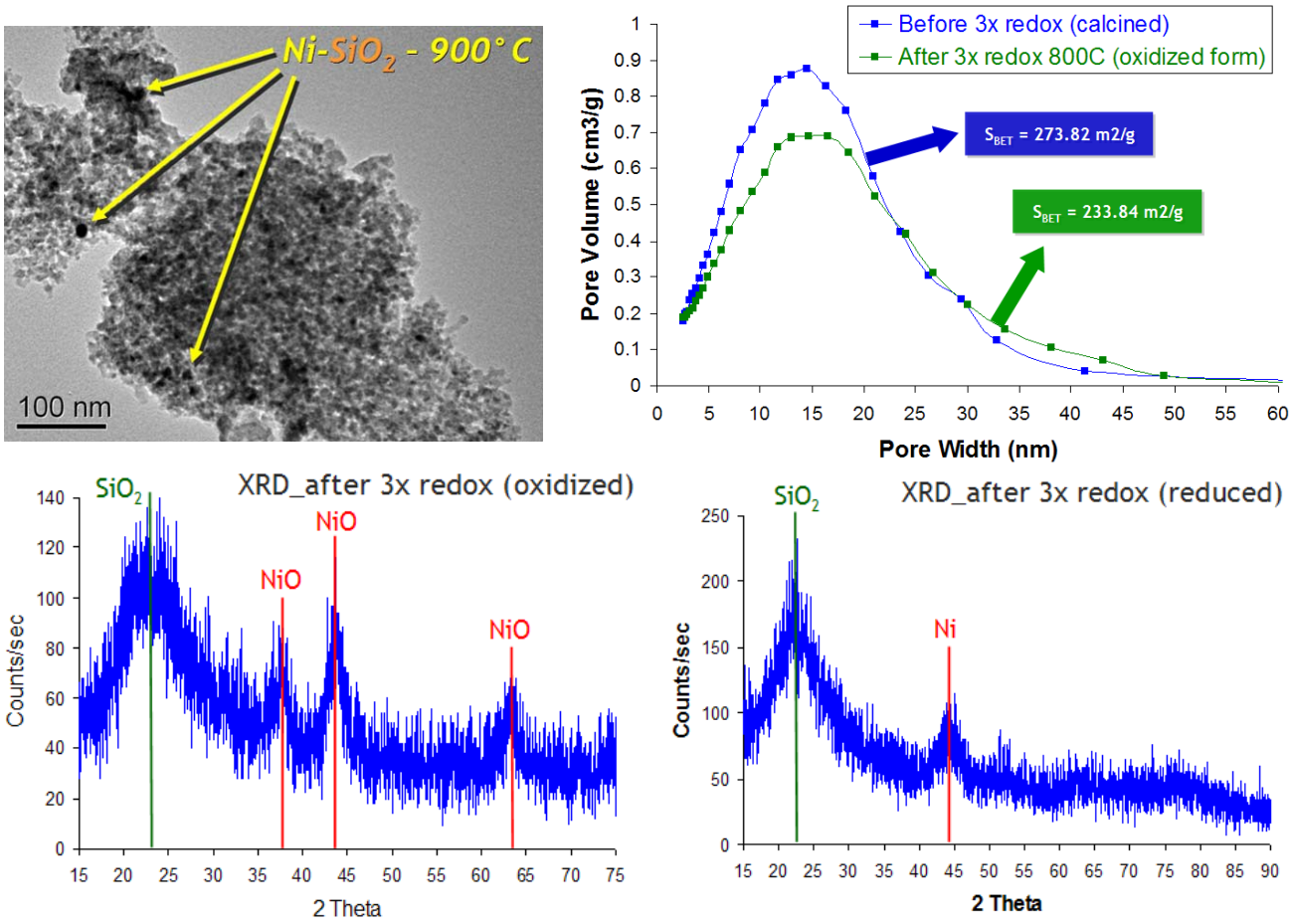

Figure 50: *Summary of results for Ni-SiO_2. Top left: TEM image showing the presence of nanoscale Ni particles within the silica framework. Top right: pore size distributions of the material before and after redox cycling, obtained from BJH analysis. Bottom left: XRD pattern of NiO-SiO_2 after redox cycling and oxidation. Bottom right: XRD pattern of Ni-SiO_2 after redox cycling and reduction.*

The results of characterization of Ni-SiO_2 formed via the sol-gel method are shown in Figure 50. The TEM image (top left) taken after calcination at 900°C shows the presence of nanoparticles of Ni distributed in the porous silica framework. The simple fact that the particles are fairly small (~5-10 nm) at this high calcination temperature is a strong indication that the silica structure is imparting thermal stability to the nickel nanoparticles.

BJH analysis of nitrogen isotherms of the material yields pore size distributions (top right graph of Figure 50). The analysis is performed before and after 3 reduction-oxidation cycles (oxidation: 900°C, 30 mins, Air. reduction: 900°C, 30 mins, H_2). A high surface area is measured for the Ni-SiO_2 sample, both before and after redox cycling, with the post-redox sample losing ~40 m^2/g. The pore structure remains similarly sized before and after redox, with a maximum pore volume of pores with diameters ~15 nm. The sample loses some pore volume after redox, but the structure of the pores remains roughly the same. These results highlight the high-temperature stability of the silica framework during redox cycling – indicating their potential for use in CLC cycling described previously (section 4.4.5).

XRD diffraction patterns are obtained for Ni-SiO_2 before and after redox cycling (bottom graphs of Figure 50). After three redox cycles and subsequent oxidation (bottom left) reflexes corresponding to amorphous SiO_2 and NiO are observed in the XRD pattern. The broad NiO reflexes observed indicate the nanoparticulate nature of the particles. After reduction, the XRD pattern shows the presence of amorphous SiO_2 and metallic Ni. The nickel reflex is also very broad, indicating nanoscale Ni particles are present. These results indicate that even under conditions where strong sintering of the Ni particles should be expected; the particles maintain their nanoscale size and their ability to be rapidly reduced and oxidized.

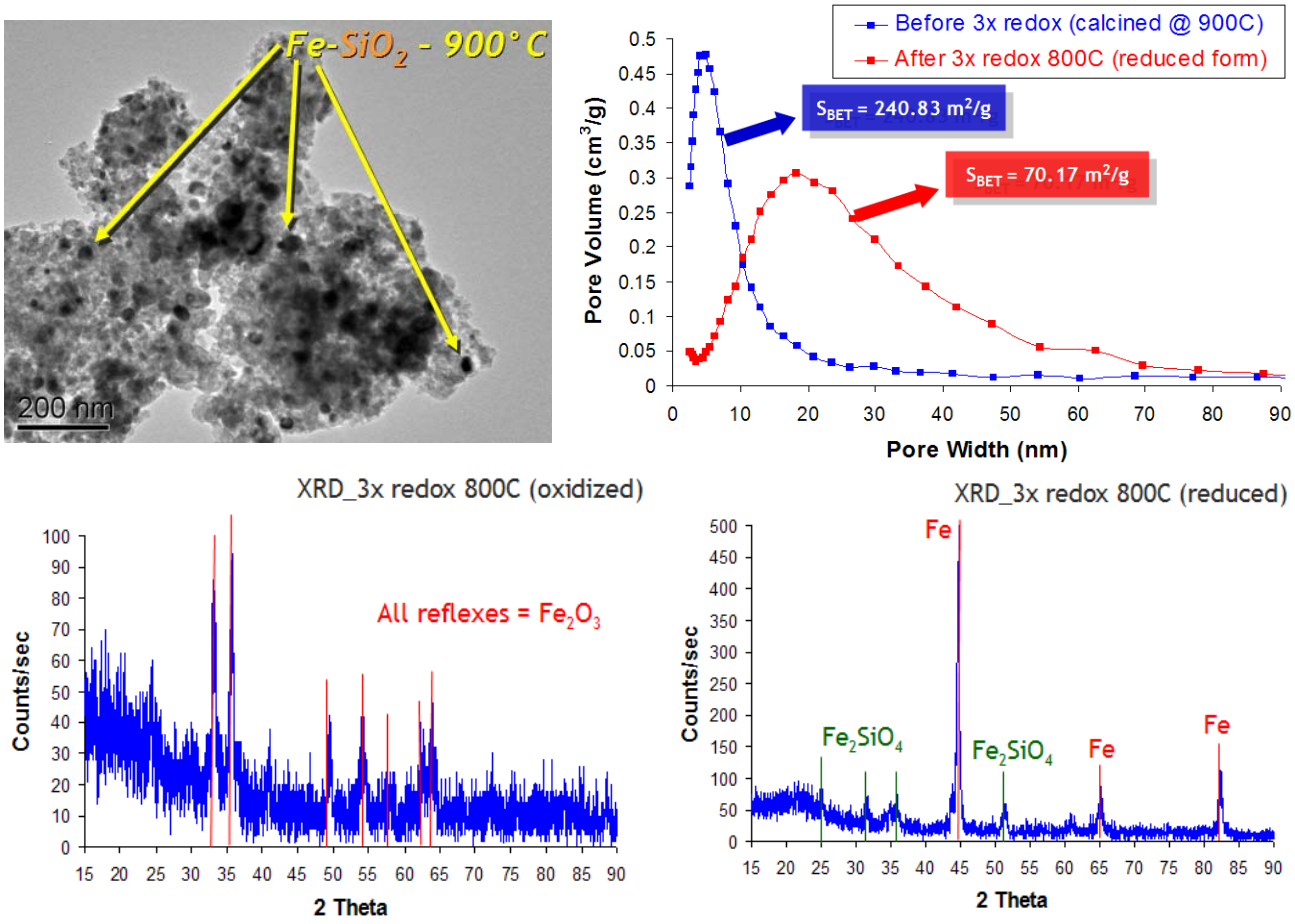

Figure 51: *Summary of results for Fe-SiO_2. Top left: TEM image showing the presence of nanoscale Ni particles within the silica framework. Top right: pore size distributions of the material before and after redox cycling, obtained from BJH analysis. Bottom left: XRD pattern of Fe_2O_3-SiO_2 after redox cycling and oxidation. Bottom right: XRD pattern of Fe-SiO_2 after redox cycling and reduction.*

The results of characterization of Fe-SiO_2 formed via the sol-gel method are shown in **Figure 51**. The TEM image (top left) taken after calcination at 900°C shows the presence of nanoparticles of Fe distributed in the porous silica framework. The particles are generally larger than nickel particles in Ni-SiO_2 but they do remain nanosized (~20 nm) at this high calcination temperature. The silica substrate does not appear to be as effective for stabilizing the iron particles.

BJH analysis of nitrogen isotherms of the material yields pore size distributions (top right graph of **Figure 51**). The analysis is performed before and after 3 reduction-oxidation cycles (oxidation: 900°C, 30 mins, Air. reduction: 900°C, 30 mins, H_2). A high surface area is measured for the Fe-SiO_2 sample before redox, but a much reduced surface area after cycling – a reduction from ~240 m^2/g to ~70 m^2/g. The pore structure also changes in size after the redox treatment, with the maximum in the pore size distribution shifting from ~5 nm to ~20 nm. This result explains at least partially the reason for lower Fe particle stability in this material. The silica ceramic is not stable when Fe particles are present, and this resulting pore restructuring at high temperature allows for subsequent growth of the Fe particles.

XRD diffraction is used to try and elucidate the reason for poor stability of the silica material in the presence of Fe nanoparticles. XRD patterns are obtained for Fe-SiO_2 before and after redox cycling (bottom graphs of **Figure 51**). After three redox cycles and subsequent oxidation (bottom left) sharp reflexes corresponding to Fe_2O_3 are observed in the XRD pattern. After reduction, the XRD pattern shows the presence of metallic Fe and interestingly, Fe_2SiO_4. This iron silicate structure is responsible for the observed poor stability of the pore structure for the Fe-SiO_2 nanocomposite. During the reduction process, iron oxide reacts with the silica substrate to form Fe_2SiO_4. During oxidation the iron silicate destabilizes and the Fe atoms are re-oxidized to Fe_2O_3:

$$\boldsymbol{Fe}_2\boldsymbol{O}_3 + \boldsymbol{SiO}_2 \underset{\boldsymbol{O}_2}{\overset{\boldsymbol{H}_2}{\Leftrightarrow}} \boldsymbol{Fe} + \boldsymbol{Fe}_2\boldsymbol{SiO}_4 + \boldsymbol{SiO}_2$$

It is important to note that the solid solution formation observed is reversible, and that the oxidizable Fe content appears to be relatively constant ~22 wt% during multiple redox cycles. Additionally, the structure of the material seems to stabilize after the initially strong reduction in specific surface area and increase in pore size. After 5 redox cycles, the specific surface area of

the Fe-SiO_2 nanocomposite levels off at ~35 m^2/g, and the pore size distribution maximum remains around 20 nm. These results indicate that Fe-SiO_2 has the potential to be a suitable material for CLC reaction. The solid-solution formation is not detrimental to the oxidizable Fe content, and does not appear to affect the stability of the material after the initial restructuring period.

There are strong parallels between both of these metal-SiO_2 materials and Ni-BHA (section 4.4.5) – all three consist of thermally stabilized metal particles distributed throughout an amorphous ceramic support. In the case of Fe- and Ni-SiO_2, there are two advantages – the synthesis does not involve the added complication of a reverse microemulsion, and the ceramic support is lower-weight SiO_2 (an important consideration for maximizing oxidizable metal weight loading for an application like CLC). These advantages make these materials worthy of future investigations.

6.0 SUPPORTED NANOCOMPOSITE CATALYSTS

6.1 INTRODUCTION

The exceptional – and sometimes even entirely novel - activity of nanomaterials in combination with recent advances in materials science have lead to an explosive development in "nanocatalysis" over the past decade[151]. However, there is an increasing disconnect between the discovery and development of nanomaterials and their industrial use. This is due to a number of significant concerns and limitations associated with the use of nanomaterials in an industrial environment. The fine powder form in which nanomaterials are typically synthesized create concerns regarding pressure drop, flow maldistribution, and fluid by-pass, as well as health and environmental concerns due to particle handling and possible particle entrainment. However, conventional procedures such as pelletizing, for example, typically result in compacting or collapsing of the catalyst structure. This undoes desired characteristics such as the large, accessible surface area. Therefore, there is an increasing need to develop materials which combine the desirable characteristics of nanomaterials with the advantages of "conventional", macroscale materials, i.e. which bridge the gap between nanoscale science and "macroscale" application.

A number of recent studies have attempted to overcome the problems associated with nano-powders through the development of hierarchical nanoscale materials. For example,

Costacurta *et al* examined mesoporous silica deposited on macroporous ceramic foams[152], and Danumeh *et al* utilized a dual-templating approach to form a hierarchical porous system consisting of cubic mesoporous walls of macro-porous silica, with application as a molecular sieve[153]. Kuang *et al* examined a similar macroporous silica with bimodal mesoporous character[154], while Sen *et al* achieved mesoporous silica with tunable pores on three different length scales in the macro-, meso-, micro-porous range from an infiltration of a macroporous polystyrene sphere template[155]. However, all of these studies focus on mesoporous silica, and none report on the stability of the resulting materials in demanding environments, such as high-temperature, reactive conditions.

Directly attaching nanoscale catalytic materials onto typical "macro"-scale support structures (monoliths, foams, felts) can be considered as a simple alternative to the direct formation of a hierarchically structured material. Such support structures are widely used and well-established in industrial catalysis. Monolithic extruded supports are predominantly used in high-throughput environmental applications, such as automotive exhaust treatment and catalytic combustion, due to the low pressure drop per unit length and attrition/crushing resistance of the structure[156]. Among their limitations, however, are poor heat transfer and lack of radial mixing[157]. Ceramic foams, on the other hand, are characterized by their irregular, open pore structure (~75-85% porous), which allows for improved radial mixing, attrition/crushing resistance, as well as low pressure drop[157]. A largely untested support material in catalysis is ceramic felt. The very open nature of the felt results in low pressure drop, while the fibrous structure offers a high surface area for coating active catalyst material. Additionally, the malleable nature of the felt offers a benefit in terms of flexible catalyst design. To our knowledge, the only systematic studies of ceramic felts as catalyst supports are those of Renken

and co-workers who examined noble metals supported on silica and aluminoborosilicate glass fibers in a wide range of catalytic oxidation and hydrogenation reactions[158-164].

These previous efforts towards a hierarchical catalyst structure have been extended by investigating the anchoring of nanocomposite Pt-BHA catalyst on different conventional and novel catalyst supports (monoliths, foams, and felts).

6.2 FORMATION OF SUPPORTED NANOCATALYST

Pt-BHA was synthesized via a reverse-microemulsion templated pathway described previously (sec. 3.0) After the washing procedure, the material was dried partially, resulting in a gelatinous form which was used in the experiments. One part of the gel was dried to completion and calcined forming a Pt-BHA powder reference material, while the rest was used for the coating procedures described below. The powder was sieved and only the fraction with d > 500 microns was used in the packed bed for reactive testing because of gas bypass issues.

Images of the uncoated support structures used are shown in **Figure 52**. Alumina and silica foam monoliths were obtained from Vesuvius Hi-Tech Ceramics. Both types of foams are white in color and have 45 pores per linear inch. Cordierite extruded monoliths were obtained from Corning Inc. The monoliths are 400 pores per square inch and initially egg shell colored. Silica felts were obtained from Technical Glass Products. The silica felts had a very open and fibrous nature. Before coating these felts, a chemical binder used in the manufacturing process had to be removed via thermal treatment (1 hour at 482°C in 2 SLM air). Alumina felts were obtained from Zircar ceramics and used as received. The alumina felts had a more densely packed structure than the silica felts.

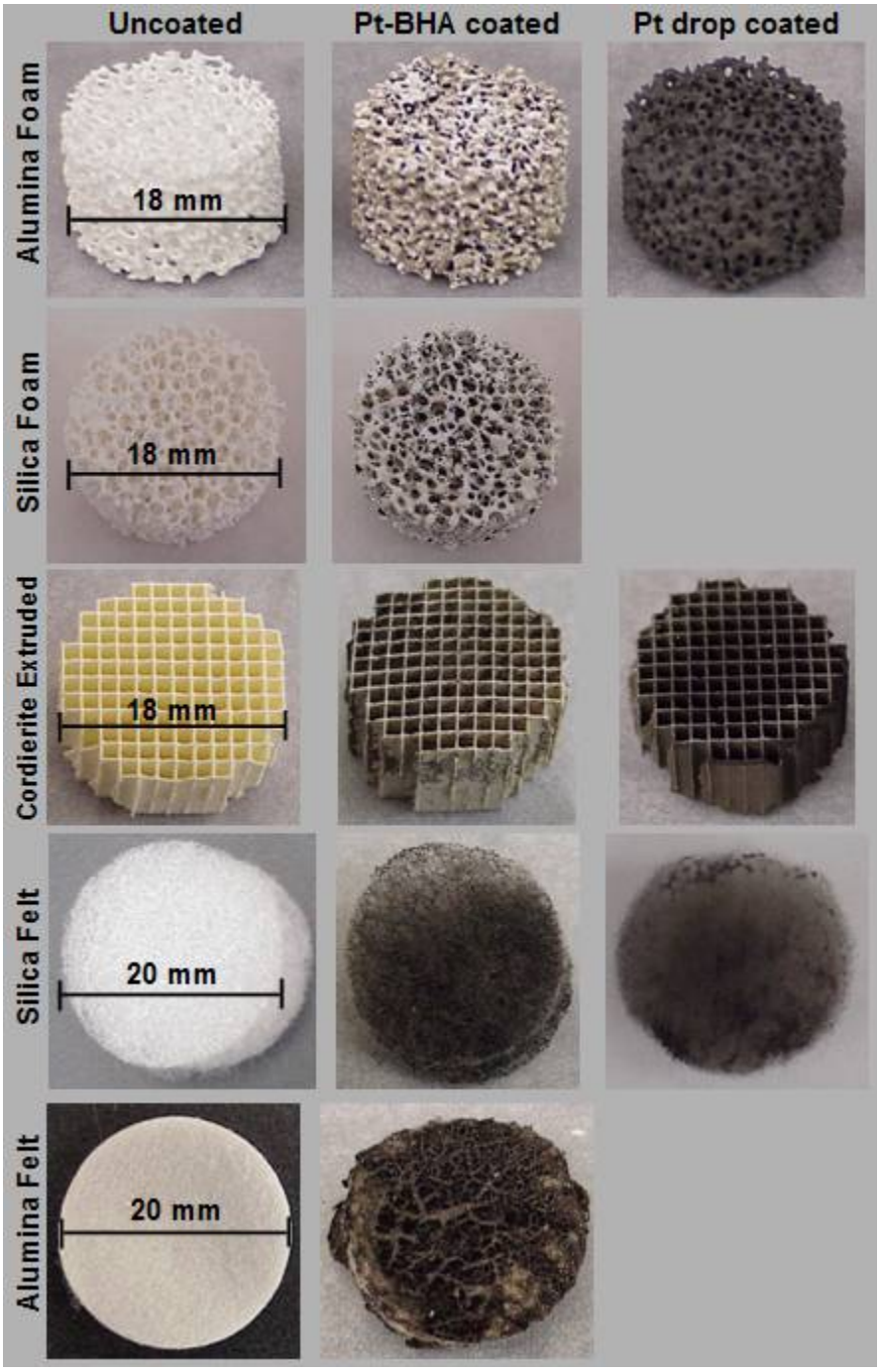

Figure 52: *Images of support structures used for coating and reactive testing. Left-most images are as-received, center are after dip coating with Pt-BHA, right-most after drop coating with Pt-salt solution.*

The dip coating was performed as follows: Each support was placed into a shallow glass vial and covered with a 2-3 ml aliquot of Pt-BHA gel. The gel was allowed to infiltrate the pore network of the support, and the catalysts were dried at ambient conditions overnight. The structures were then calcined in a flow tube oven (3 hours at 600^{o}C in 2SLM air, followed by 3 hours in 10% H_2 in N_2). As a control, separate samples of each support were drop coated with 10wt% H_2PtCl_6 in distilled water, allowed to dry, and calcined (280°C, 6 hours 1SLM N_2, 4 hours 5% H_2 in N_2). These were chosen as 'conventional' reference materials for the investigations.

6.3 RESULTS AND DISCUSSION

Visual inspection of the Pt-BHA coating was done via scanning electron microscopy using a Phillips XL30 electron microscope. Catalyst morphology and platinum particle size are determined by transmission electron microscopy (JEOL-2000FX). Samples for the transmission electron microscopic measurements were obtained by placing a drop of sample suspension in acetone on a copper type-B support grid (Ted Pella, Inc.), followed by air drying to remove the solvent. Pt particle size distributions were determined by counting individual particles in TEM micrographs with the help of ImageJ software[165]. Nitrogen porosimetry (Micromeritics ASAP 2020) was used to determine surface area, pore volume, and pore size distribution. Samples are degassed for 3 hours at 200°C under high vacuum prior to each test. The typical test involved a 6-point BET analysis for total surface area measurement and an 84-point BJH analysis for pore size and volume determination. X-ray diffraction measurements were performed with a high-resolution powder X-ray diffractometer (Phillips PW1830, USA) in line focus mode using a

monochromatic Cu radiation at the wavelength of 1.54 Å. Pulse chemisorption of CO (Micromeritics Chemisorb 2750) was used to determine active Pt surface area. Each sample was reduced in a stream of hydrogen gas at 600°C prior to pulsing with pure CO gas at room temperature.

Since the aim of the present investigation was the development of a supported nanocomposite catalyst without compromising the underlying activity of the nanoscale active component, the unsupported, highly active powder form of the nanocomposite Pt-BHA catalyst was used as reference material in the present investigation. The excellent activity, selectivity, and stability of this Pt-BHA nanocomposite powder catalysts had already previously been demonstrated in our group in detailed investigations of catalytic partial oxidation of methane to synthesis gas[14]. In the following, after a brief characterization of this reference material, various supported catalyst formulations – alumina mats, silica foams and felts, and cordierite extruded monoliths – are evaluated with regard to activity, selectivity and stability in comparison to this reference material as well as "conventionally" supported catalysts prepared by drop-coating with Pt salt solution.

6.3.1 Characterization of Pt-BHA used for coating

First, the unsupported Pt-BHA powder was characterized via TEM. The morphology of the material consists of nanoscale domains of Pt homogeneously distributed throughout a sponge-like BHA matrix, and is unchanged from that previously described in 0 above. After low-temperature calcination at T= 300°C, the average Pt particle size is 2.7 nm with a narrow size distribution (σ = .65 nm) as determined from particle size statistics shown in **Figure 53**. After calcination at T= 600°C, the particles grow to an average size of 8.7 nm and the size distribution

broadens to σ = 2.4 nm. This particle growth can be correlated with removal of residual surfactant at a calcination temperature of ~450°C, and the Pt particle size then remains essentially unchanged up to temperatures around 1000°C [13].

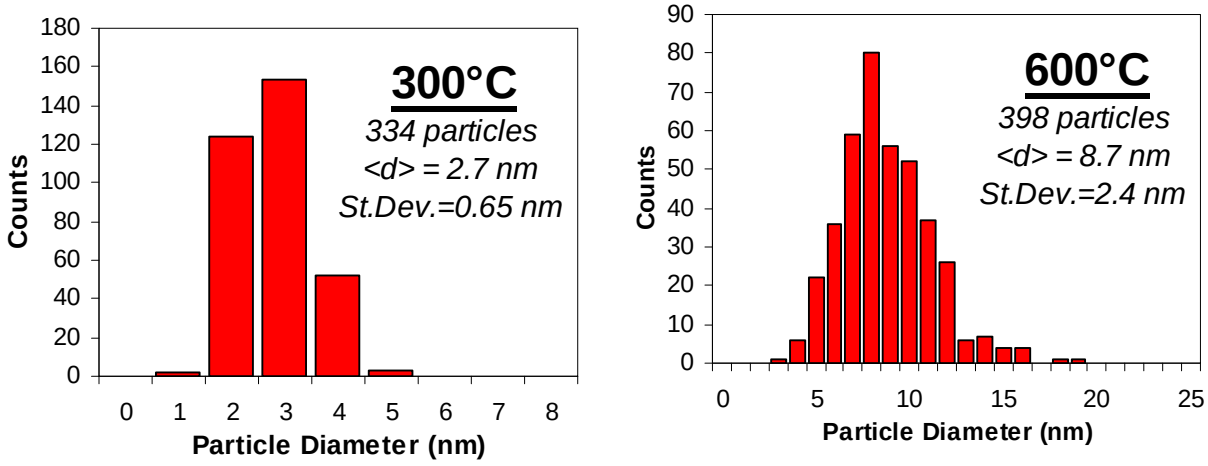

Figure 53: *Pt particle size distributions in Pt-BHA nanocomposite powder catalysts as determined from TEM images.*

6.3.2 Coating of different support structures

After supporting this Pt-BHA powder on the different support structures via dip-coating with the gel form of the uncalcined Pt-BHA (see 6.2), the supported catalysts were first characterized qualitatively via SEM.

The alumina foam-supported Pt-BHA catalyst appears to have a low dispersion of the nanocomposite on the support (first row of Figure 52). Closer inspection confirms a highly non-uniform distribution in which large amounts of material are trapped in the inner pore network (**Figure 54**, left image). It should be noted that these agglomerates are stable during normal

handling and even if the catalyst is mildly tapped onto a surface to shake loose any excess material. Vigorous tapping or other abrasion leads to further loss of catalytic material. In comparison, the alumina foam is also shown after conventional drop-coating with a Pt salt solution (first row of Figure 52). This coating leads to a metal coating with a comparatively uniform distribution of Pt on the support structure as confirmed by SEM (**Figure 54**, right image).

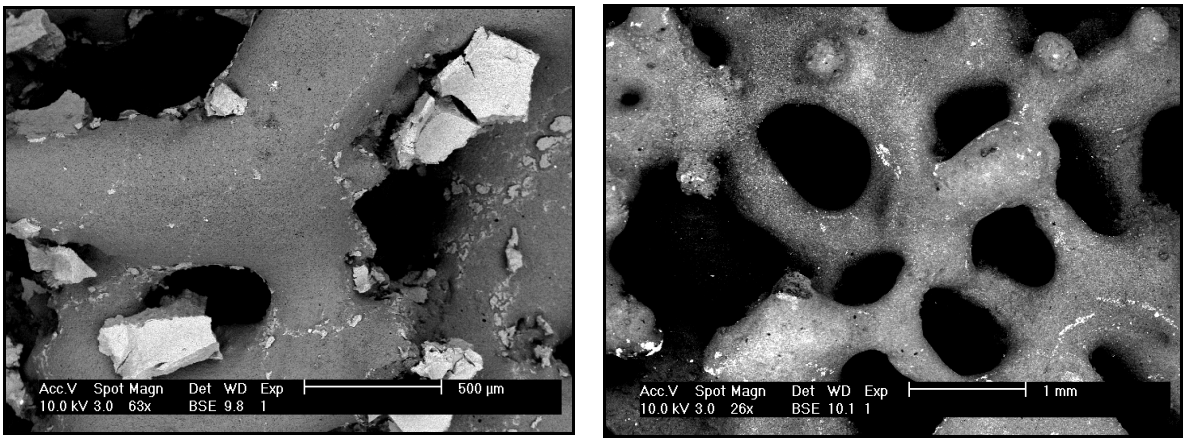

Figure 54: *SEM micrograph of alumina foams: Left: Dip coated with Pt-BHA. Right: Drop coated with Pt-salt solution.*

The silica foam supported Pt-BHA, like the alumina foam supported Pt-BHA, shows a low dispersion of the nanocomposite (second row of Figure 52), with similar mechanical stability during handling. SEM images of this structure were essentially indistinguishable from those of the alumina foam supported structure, and are therefore not shown. The silica foam was also drop coated with a Pt-salt solution. Again, the properties of this coating were indistinguishable from those of the alumina foam.

The straight-channel cordierite extruded monolith turns grey with small black flecks of Pt-BHA upon coating (third row of Figure 52). The Pt-BHA material did not have strong adhesion to the cordierite, however, loosing significant amounts of coating even during normal

handling of the supported catalyst structure. The nanocomposite is very poorly dispersed on the walls of the monolith structure, as evident in the SEM images shown in (**Figure 55**, left image). Adhesion appears to occur predominantly at points in the cordierite structure where the Pt-BHA particles can settle into a fracture or crack. In comparison, the cordierite monolith is also shown again after conventional drop-coating with a Pt salt solution (third row of Figure 52). Again this leads to a uniform metal coating with a fairly homogeneous distribution of Pt on the support structure as confirmed by SEM (**Figure 55**, right image).

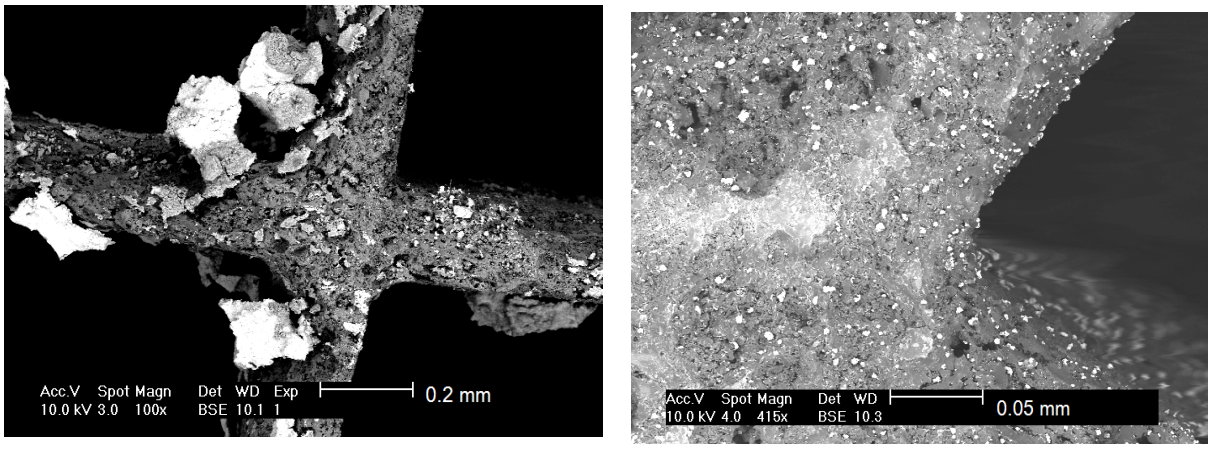

Figure 55: *SEM micrographs of cordierite monoliths. Left: Dip coated with Pt-BHA. Right: Drop coated with Pt-salt solution.*

Silica felts were also coated with the Pt-BHA nanocomposite (fourth row of Figure 52). Visual inspection indicates that the Pt-BHA appears to be well dispersed in the silica fiber structure. The catalyst is stable upon normal handling and mild tapping. Vigorous tapping of the catalyst initially removes a small amount of excess catalytic material, but the majority remains strongly bound to the fibers. SEM images of this silica felt supported Pt-BHA catalyst (**Figure 56**, top left micrograph) reveal a "chunky" texture of the material, similar to the Pt-BHA coated

foam monoliths. However a larger number of smaller chunks are adhering to the silica fibers, leading to a better overall dispersion of Pt-BHA. In fact, a closer look reveals additionally a fairly high dispersion of smaller Pt-BHA particles on the fibers (**Figure 56**, top right micrograph). Overall, this Pt-BHA dispersion appears to be significantly higher on the silica felts than on any of the other support structures.

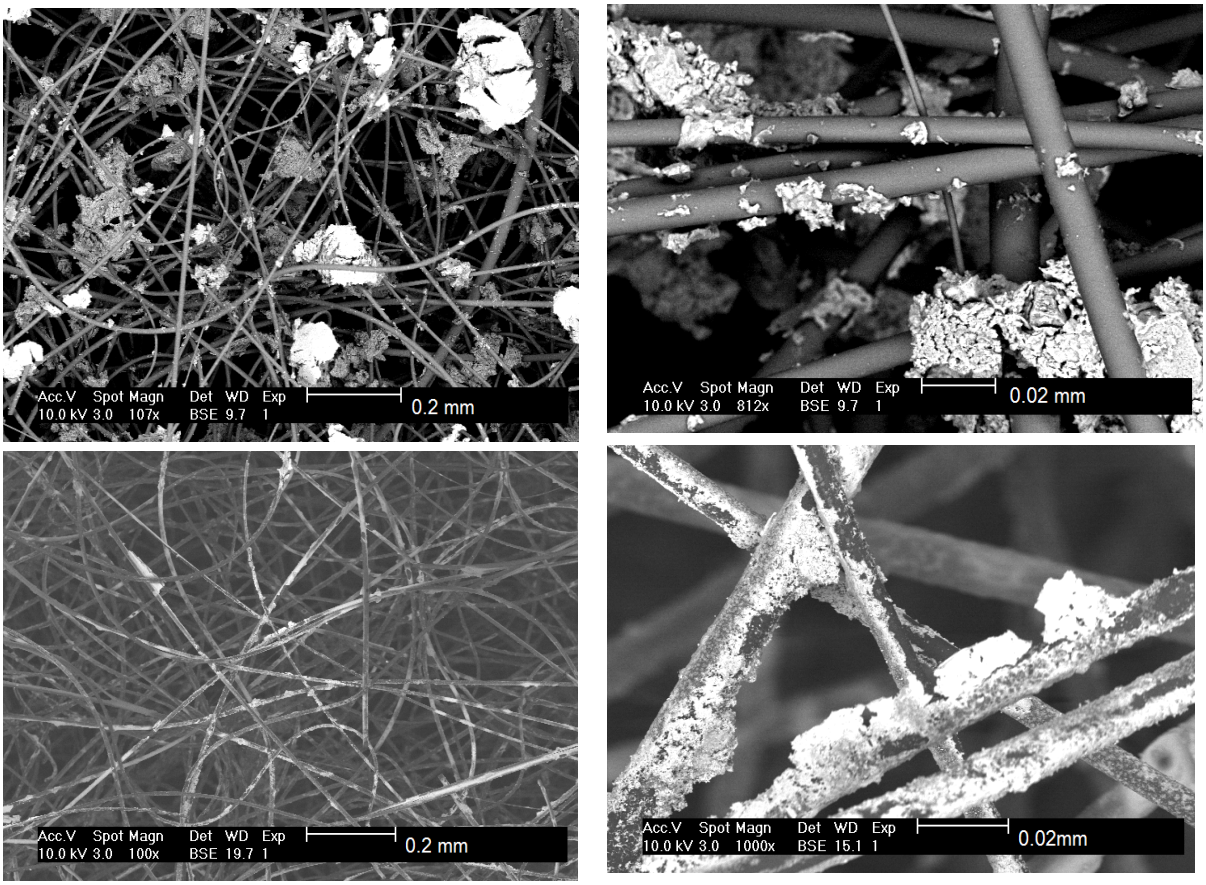

Figure 56: *SEM micrographs of silica felts. Top row: Dip coated with Pt-BHA. Bottom row: Drop coated with Pt-salt solution.*

In comparison, drop coating the silica felts with 10% H_2PtCl_6 solution leads to a blotchy Pt coating that does not appear very uniform to the naked eye (fourth row of Figure 52). Beyond

this macroscopic inhomogeneity of the coating, however, SEM reveals that each fiber is coated fairly uniformly with a thin layer of Pt (**Figure 56**, bottom row).

Finally, Pt-BHA was coated on an alumina felt (final row of Figure 52). The nanocomposite resides largely on top of the felt and does not penetrate significantly into the fibrous structure. This poor coating is likely due to the fact that the alumina felt is significantly denser than the silica felt, resulting in poor penetration of the coating solution into the fibrous structure. Correspondingly, the mechanical stability of the nanocomposite coating on this structure is very limited even during mild handling. Because of this poor stability, this support was not further analyzed and was also not included in the reactive testing.

Overall, these observations seem to indicate that the physical structure of the support is more important for the adhesion of the nanocomposite than the chemical nature, since alumina- and silica-based supports behave very similar in the coating tests, while strong differences existed between the different support structure types.

6.3.3 Active platinum surface area

One of the most important characteristics of a supported catalyst is obviously the amount of exposed active surface area, in this case the total Pt surface area. Therefore, the Pt surface areas of all above described supported nanocomposite catalysts were determined via chemisorption. The results are shown in **Table 8**. Since all materials are disk shaped, their size is characterized by their respective diameter (D) and length (L). Pt weight loading (m_{Pt}) was calculated based on the ~7.5wt% Pt in the Pt-BHA nanocomposite used in the coating process. The total platinum surface area (A_{Pt}) was determined using CO pulse chemisorption, and specific surface areas (a_{Pt}) were calculated per mass of platinum and per mass of the entire catalyst (last two columns).

Table 8: *Comparison of active platinum surface area for the supported catalyst structures and the unsupported Pt-BHA powder.*

Active Component	Structure	Size D, L [mm]	m_{Pt} [mg]	A_{Pt} [m^2]	a_{Pt} (m^2/g)	
					[g Pt]	[g cat]
Pt	Alumina foam	18, 10	63	0.29	4.68	0.14
	Silica felt	20, 2	20	0.019	0.96	0.42
Pt-BHA	Alumina Foam	18, 10	1.9	0.056	29.6	0.03
	Silica foam	18, 10	2.8	0.11	37.6	0.06
	Silica felt	20, 2	4.8	0.095	19.8	1.15
Pt-BHA	powder	18, 3	38	2.2	57.4	4.31

One can see that the total amount of Pt is significantly higher for the catalysts that were drop-coated with a Pt salt than for those coated with the nanocomposite. This is not surprising since the nanocomposite contains more than 90wt% BHA and will hence result – for otherwise similar coatings – in a drastically reduced Pt weight loading. However, while one could expect a corresponding decrease in the total Pt surface area for the Pt-BHA coated catalysts; this is only true for the alumina foam catalyst. The silica felt supported Pt-BHA catalyst shows a significantly higher surface area than the conventionally coated felt, indicating a much higher dispersion, i.e. retention of the nanoparticulate nature of the Pt in the nanocomposite coating. This is also reflected in the Pt surface area per total catalyst weight (last column in table 1), which is higher for the Pt-BHA coated silica felt than for the one coated with pure Pt.

The superior dispersion becomes most apparent in a comparison of the specific Pt surface areas where even the nanocomposite-coated alumina foam shows a 6-fold higher specific surface

area than the conventionally coated one, while the specific Pt surface area for the silica felt is increased by as much as a factor of 20. In both cases, however, the supporting process leads to the occlusion of some of the Pt, as apparent in a comparison of their specific Pt surface areas with that of the Pt-BHA powder (last row in table 1). This is of course unavoidable in a supported catalyst, since the active phase has to adhere to the support, making the surface area at the interface between active phase and support inaccessible for the reaction. The fact that the (less stable) alumina foam catalyst shows a lower reduction in specific surface area, i.e. less occlusion than the (more stable) silica felt, indicates that a certain amount of occlusion is even a requirement for a stable adhesion of the nanocomposite to the support.

6.3.4 Reactive testing (CPOM)

Catalytic partial oxidation of methane to synthesis gas (CPOM) is chosen as test reaction to evaluate the activity and stability of these structured catalysts due to its industrial importance as well as its high-temperature and short-contact time reaction conditions. In CPOM, methane reacts directly with oxygen or air to form synthesis gas (CO and H_2) in a one-step reaction:

$$CH_4 + 0.5\ O_2 = CO + 2\ H_2\ (\Delta H_R^0 = -37\ kJ/mol)$$

making it a promising alternative to the traditional industrial route to syngas via steam reforming of methane (SRM)[89]. CPOM is typically catalyzed by noble metals (Pt, Rh), runs auto-thermally due to its mild exothermicity, and is characterized by very high reaction temperatures (>1000K), extremely short contact times (<10 ms), and very high reaction rates. These features of the reaction, as well as our lab's previous experience with CPOM[91-94] make it an ideal test reaction for these nanocomposite materials.

All reactive testing was conducted in a quartz-metal hybrid reactor. Typical reaction temperatures were between 700-1000°C (autothermal) for all configurations tested. Mass flow controllers (MKS Instruments Inc.) were used to feed the reactants (methane and synthetic air) at a total flow rate of 4 SLM. This resulted in residence times between 9 and 38 ms for the different catalyst configurations (at standard inlet conditions). More details of the reactive setup are contained in section 3.3.

Experimental results for the CPOM testing are shown in **Figure 57**, where methane conversion (left graph), hydrogen selectivity (center) and CO selectivity (right graph) are shown as a function of molar methane-to-oxygen ratio (O_2:N_2 = 1:4) for adiabatic operation at a total flow rate of 4 SLM (standard liters per minute). Oxygen conversion is always complete at the experimental conditions and is hence not shown.

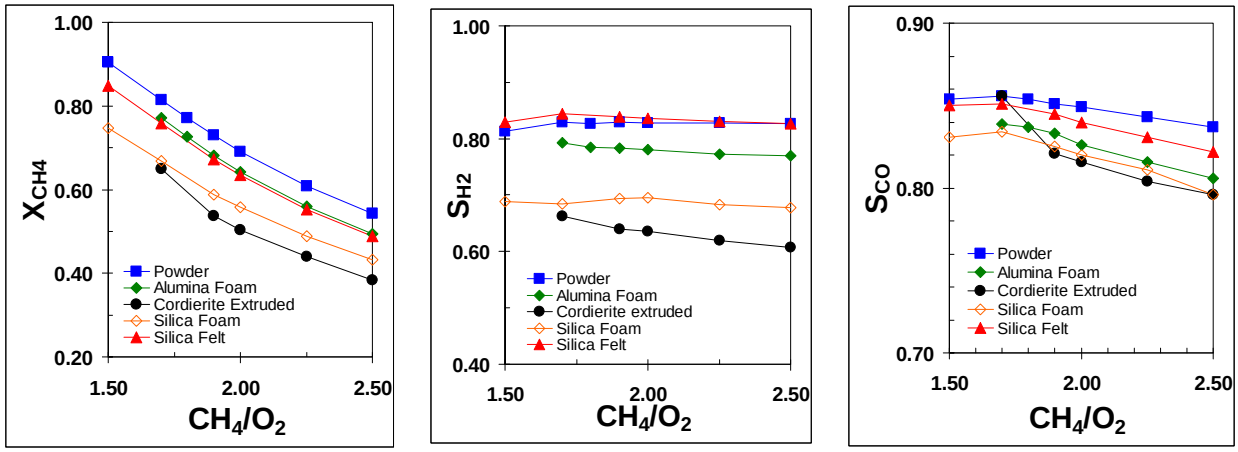

Figure 57: *Methane conversion (left), hydrogen selectivity (center), and carbon monoxide selectivity (right) versus molar CH_4:O_2 ratio for the supported nanocomposite catalysts in CPOM. Total flow rate = 4.0 SLM, N_2:O_2 = 4:1, autothermal operation.*

Methane conversion (left graph) decreases monotonically with increasing CH_4/O_2 ratio for all catalysts. This is a well-known trend in CPOM[14, 166], and is explained by the fact that oxygen is

the limiting reactant in this reaction system, and hence increasing oxygen availability with decreasing CH_4/O_2 ratio results in higher methane conversion. Methane conversion for the powder, foam monolith, and silica felt are identical within experimental error (+/-3%). The extruded monolith and silica foam monolith perform poorly compared with the other nanocomposite catalysts, with methane conversions as much as 20% and 15% less (respectively) than Pt-BHA powder.

Hydrogen selectivity (center graph) remains almost constant at ~80% (+/-3%) for the powder, alumina foam, and silica felt for all CH_4/O_2 ratios tested. Again the cordierite extruded monolith and silica foam monolith show significantly lower selectivity than the other supports. This is in agreement with the lower conversions over this catalyst, since a less selective reaction, i.e. a higher degree of total oxidation, consumes more of the limiting reactant (oxygen) due to the stoichiometry of the total oxidation reaction and hence results in lower methane conversion.

Finally, CO selectivity (right hand graph) shows similar values of ~80-85% with a slight decreasing trend with CH_4/O_2 ratio for all catalysts across the whole range of CH_4/O_2 ratios.

These conversions and selectivities are well in excess of those reported previously for conventionally prepared supported Pt catalysts[13, 14, 166-171]. Strong improvements in methane conversion (by up to 20%) and even more pronounced improvements in hydrogen selectivity (by up to 40% from the conventional catalysts to the nanocomposite powder) are observed across the whole range of methane-to-oxygen ratios. The results over the Pt-BHA nanocomposite powder furthermore are in good agreement with our previous results over a similar type of catalyst[14], attesting to not only the excellent catalytic activity and selectivity of these nanocomposite catalysts, but also to the well-controlled and highly reproducible synthesis procedure.

Temperatures measured at the back-edge of the various catalysts (not shown here) ranged between 730-830°C for Pt-BHA powder, 750-830°C for alumina foam-supported Pt-BHA, 790-900°C for the silica foam, 920-1010°C for the cordierite extruded monolith, and 700-810°C for the silica felt. The temperatures increased monotonically as the methane-to-oxygen ratio decreased from 2.5 to 1.5 due to the increasing methane conversion for leaner mixtures. The average temperature is furthermore strongly affected by changing hydrogen selectivities between the different catalysts and as a function of methane-to-oxygen ratio. This is expected since lower selectivity for hydrogen indicates a higher degree of methane combustion, which is a strongly exothermic process.

Overall, the results indicate that Pt-BHA supported on extruded cordierite monoliths and silica foam monoliths are relatively poor CPOM catalysts. In addition, rapid deactivation was observed over the extruded cordierite monolith to the point where a second ignition of the CPOM reaction after prolonged operation was not possible any more. The low reactivity and poor stability of the extruded monolith appear to reflect the difficulty involved in coating the structure, which leads to low Pt-BHA loadings, poor dispersion of nanocomposite, and diminished catalytic stability. The reasons for the poor performance of the silica foam catalyst are not entirely clear from the present results, as the catalyst showed similar coating, stability, and surface areas as the alumina foam catalyst, yet significantly lower activity and selectivity in the reaction.

In contrast to that, the alumina foam and silica felt supported catalysts offer similar reactivity to the unsupported Pt-BHA powder at a total Pt weight loading that is around an order of magnitude lower. While one could conclude that one could use 10-times less powder, this is not possible as the catalyst bed was already only 3 mm long and a further reduction (even by much

less than a factor of ten) would lead to significant problems with maldistribution of the shallow bed and strong gas bypass and channeling. This points to one of the main advantages of using supported nanocomposite powders: using a support structure allows the use of very small amounts of catalyst while maintaining a well-defined flow pattern and uniform distribution of the catalyst in the reactor. Given the highly reactive nature of nanoparticles, this is a significant consideration well beyond the system studied in the present investigation.

In order to obtain a direct comparison between a conventional supported Pt catalyst and the nanocomposite-based catalysts, the two most reactive catalysts, the silica felts and alumina foam monoliths, were also evaluated with regard to activity and selectivity in CPOM after drop-coating with H_2PtCl_6. The results are shown in **Figure 58**, where methane conversion and H_2 and CO selectivity are shown as a function of CH_4/O_2 ratio in comparison to the results over the equivalent Pt-BHA supported catalysts. One can see that while in both cases the nanocomposite catalysts (closed symbols) outperform the conventional catalysts (open symbols), this improvement is small (albeit significant) for the alumina foam monolith but very pronounced for the silica felt. Again, it should be noted that the nanocomposite catalyst contains more than an order of magnitude less Pt than the drop-coated catalyst (**Table 8**). The results hence demonstrate that the supported nanocatalysts offers strongly improved activity and selectivity with much lower noble metal requirement than their drop-coated counterparts. In particular the silica felt supported nanocomposite catalyst showed a highly attractive combination of excellent activity and selectivity with good mechanical stability and very easy and flexible handling.

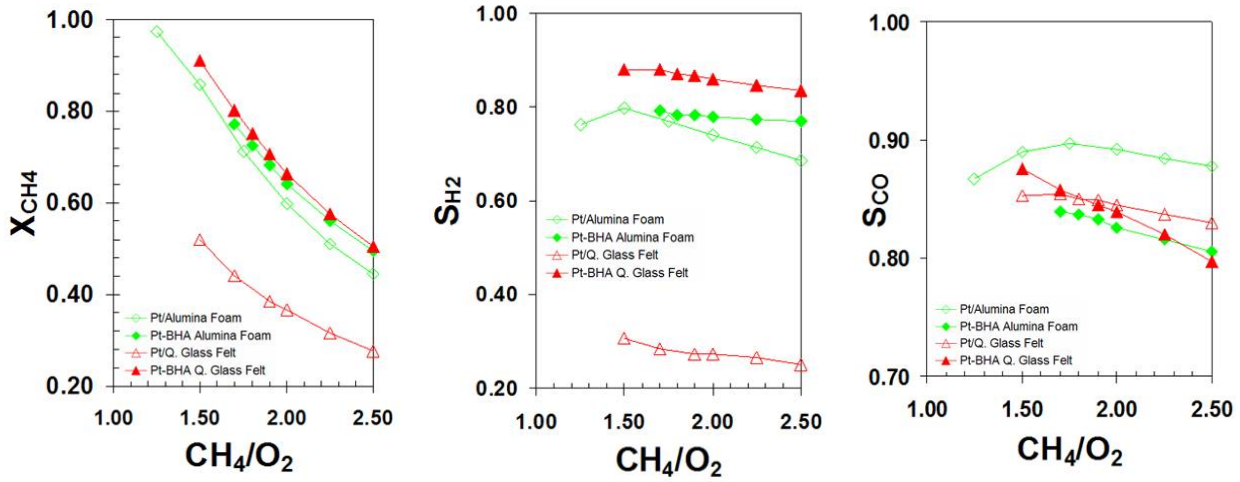

Figure 58: *Methane conversion (left), hydrogen selectivity (center), and carbon monoxide selectivity (right) versus molar CH4:O2 ratio for alumina foam and silica felts coated by drop coating with aqueous platinum solution and dip coating with Pt-BHA gel. Total flow rate = 4.0 SLM, N2:O2 = 4:1, autothermal operation.*

6.3.5 Catalyst stability

Beyond activity and selectivity of the supported nanocomposite structures, the stability of these materials in long-term high-temperature reactive atmospheres is a key concern. As discussed in the introduction, stability at reactive conditions is a major concern in particular for nanoscale catalyst materials due to their inherent thermodynamic instability. It is hence important to be certain that the exceptional high-temperature stability of the Pt-BHA nanocomposite powders is not compromised in the attempt to design a hierarchical catalyst structure through supporting these powders on monolithic structures.

Because of the strong improvements in activity and selectivity seen for the Pt-BHA coated silica felt over the Pt-salt drop coated silica felt, we focused on the stability of this relatively novel type of supported catalyst. Long term (>20 hours) CPOM reactive testing of silica felt with Pt-BHA was performed at a molar ratio CH_4:O_2 = 2.0 (N_2:O_2 = 4:1) and total flow

rate of 4.0 SLM. Additionally, the effect of weight loading on catalyst stability was investigated by testing silica felts with "low" (0.0305g), "medium" (0.0523g), and "high" (0.0800g) loadings of Pt-BHA.

Figure **59** shows the results of the catalyst stability testing for the low (left graph), medium (center) and high weight-loading felts (right graph) as methane conversion (triangles) and hydrogen and CO selectivities (squares and diamonds, respectively) versus molar CH_4:O_2 ratio.

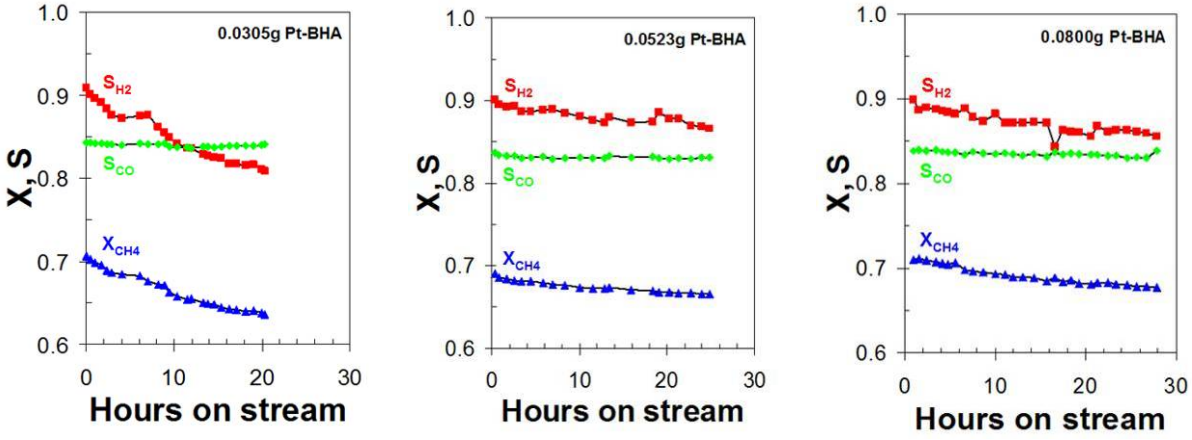

Figure 59: *Methane conversion (triangles), hydrogen selectivity (squares), and carbon monoxide selectivity (diamonds) for silica felts with different weight-loading of Pt-BHA nanocomposite in extended operation stability testing. Left: low weight loading (0.0305g Pt-BHA), center: medium weight-loading (0.0523g Pt-BHA), right: high weight-loading (0.0800g Pt-BHA). CH4:O2 = 2.0, N2:O2 = 4:1, total flow rate = 4 .0 SLM, autothermal operation.*

One observes for the low weight-loading sample (left-most graph) a strong deactivation during the course of the experiment (~21 h) as indicated by the decrease in methane conversion and hydrogen selectivity by about 10%. This trend is weakened in the medium weight-loading sample (~3% decrease in H_2 selectivity and ~2% decrease in CH_4 conversion over ~23 h, center graph), and remains unchanged upon further increase from the medium to the high weight-loading (right-most graph). Carbon monoxide selectivity remains stable ~84% for each of the

three catalysts. In agreement with these observations, catalyst temperatures increased over the course of the 20 hours, with a significant increase (from ~750 to ~840°C) for the "low" weight-loading, and a much more moderate increase (from ~730 to ~760°C) for the "medium" and "high" samples.

In order to establish the reason for the deactivation experienced during the long term stability testing of silica felt supported Pt-BHA, a series of characterization studies (SEM, BJH, XRD, TEM) were performed to evaluate these composite materials before and after reactive testing.

SEM images of the various weight-loading catalysts after running the stability experiment ("high" weight-loading pictured in **Figure 60**) show that the texture and dispersion of the Pt-BHA material remains about the same as before reaction (compare to **Figure 56**). The deactivation hence does not appear to be due to loss or sintering of the Pt-BHA agglomerates on the silica fibers.

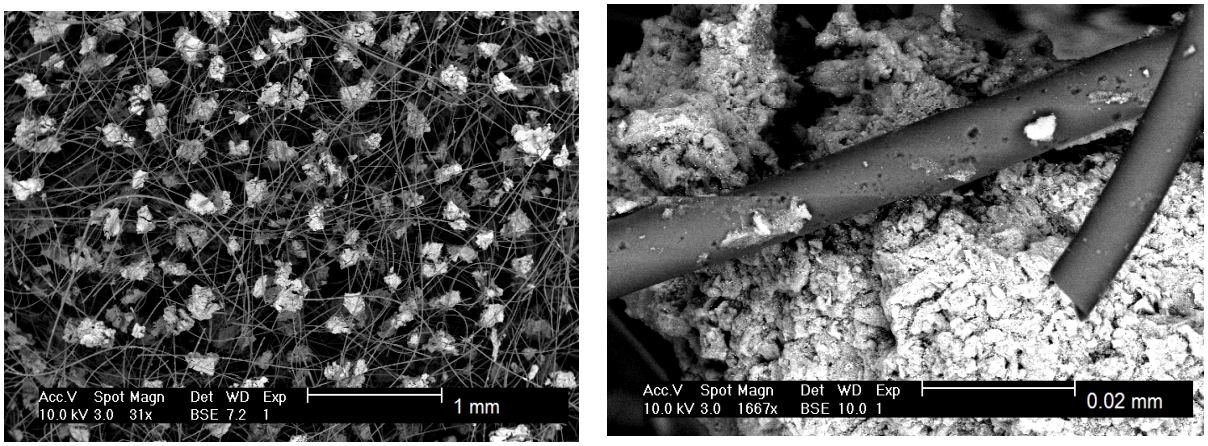

Figure 60: *SEM photos of silica felt strands after extended operation (>20 hours) in partial oxidation of methane. CH_4:O_2 = 2.0, N_2:O_2 = 4:1, total flow rate = 4 .0 SLM, autothermal operation.*

Nitrogen porosimetry was used to further evaluate the pore structure of the Pt-BHA agglomerates attached to the silica felt for a fresh sample and a sample that had undergone long term CPOM reaction testing (~20 h on-stream). The results are plotted in **Figure 61**. The adsorption and desorption isotherms for the fresh and post-CPOM samples are both typical type IV isotherms, indicating a mesoporous material with textural porosity. A Barrett–Joyner–Halenda (BJH) analysis of the desorption branch of the isotherm shows that the fresh sample (circles) has a smaller total pore volume than the post-reaction sample (squares; 0.377 cm^3/g vs. 0.392 cm^3/g), as well as a smaller average pore size (8.6 nm vs. 12.8 nm), and a larger specific surface area (106.2 m^2/g vs. 82.2 m^2/g, determined by BET analysis).

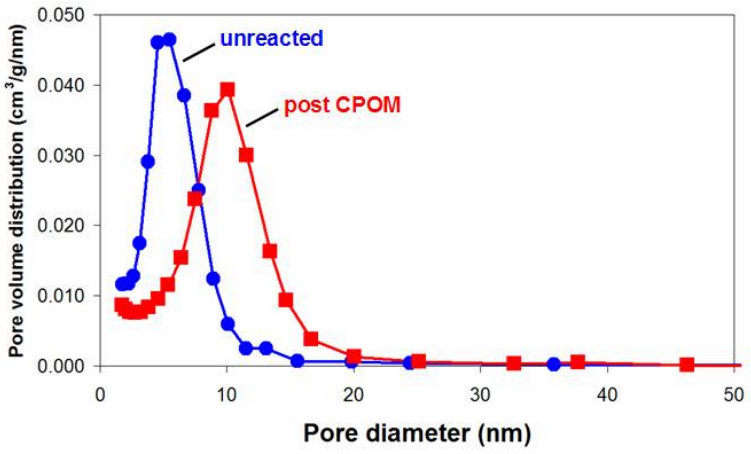

Figure 61: *Nitrogen porosimetry of Pt-BHA drop coated on silica felts (Circles: as prepared. Squares: after ~20 hours of CPOM reaction at ~800°C). Top: Nitrogen isotherm indicating a typical mesoporous material (adsorption, closed symbols; desorption, open symbols). Bottom: BJH analysis of desorption curve showing the pore size distribution.*

The results for the fresh sample are essentially unchanged from previous results for the pure Pt-BHA material[13] indicating that the structure of the Pt-BHA nanocomposite material is unaffected by the coating process. However, the results show a significant degree of

restructuring of the material upon exposure to reaction conditions. This restructuring is due to changes in the BHA pore structure at temperatures in excess of ~800°C, as also previously observed for a pure BHA material[172]. This restructuring leads to somewhat increased pore sizes and correspondingly decreased total surface area of the samples. Since the CPOM reaction exposes the catalyst to temperatures well in excess of 800°C, it is not surprising to find a similar pore restructuring in the present samples. Overall, however, the results indicate that the catalyst structure remains intact.

X-ray diffraction (**Figure 62**) of the fresh sample shows no discernible reflexes except for a broad feature at ~20°, indicative of amorphous silica from the silica felt itself. No reflexes representing BHA can be detected. This diffuse background does not change upon exposure to reaction conditions, in agreement with our previous finding that the BHA structure remains largely amorphous below ~1,210°C[13]. The Pt nanoparticles are too small to be picked up by XRD before reaction. After long-term CPOM reaction, distinct Pt reflexes appear. A Debye-Scherrer fit of the dominant Pt reflex at ~40° 2 theta yields a Pt particle size of 24.6 nm, well in excess of the expected particle size which is in the order of about 10 nm (see figure 3, right graph). However, this agrees with previous observations on these materials, where we found that while the majority of the Pt nanoparticles are well stabilized inside the porous BHA structure, a small fraction of Pt particles on the outer perimeter of the Pt-BHA agglomerates are not sufficiently held in place and hence sinter at higher temperatures. Since XRD is a volume sensitive technique, and since volume scales with the cube of the particle diameter, even a few sintered particles result in a strong apparent particle size increase.

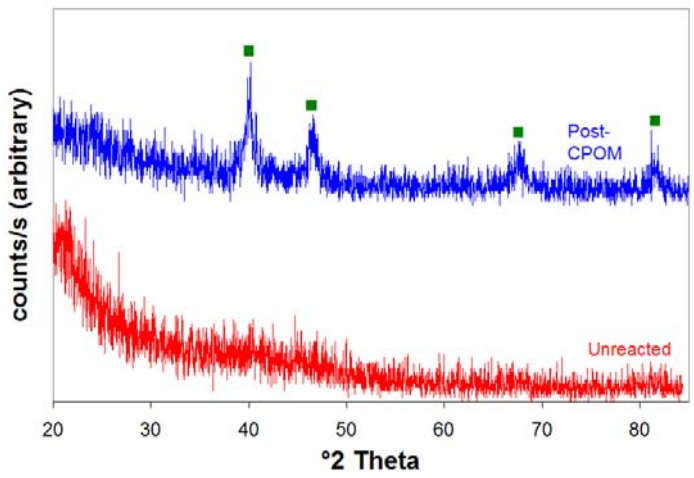

Figure 62: *X-ray diffraction patterns for unreacted and post-CPOM reaction silica felts coated with Pt-BHA. Squares indicate the location of metallic platinum reflexes.*

To confirm this hypothesis, Pt particle size distributions in the silica felt supported Pt-BHA before and after long-term exposure to CPOM were determined directly via TEM for both a low and a high weight-loading sample (**Figure 63**). The results show that the Pt particle sizes remain indeed small and unchanged within experimental error (d_P ~ 8-9 nm with σ ~ 2 nm) for both catalyst samples. However, we also observe a very small, but significant, population of large Pt particles (d_P > 100 nm) in TEM (not shown) and a depletion of the outer perimeter of the Pt-BHA particulates of Pt nanoparticles after exposure to high temperatures (see previous TEM images of Pt-BHA powders, section 0above), confirming the above explanation of the large particle sizes determined via XRD.

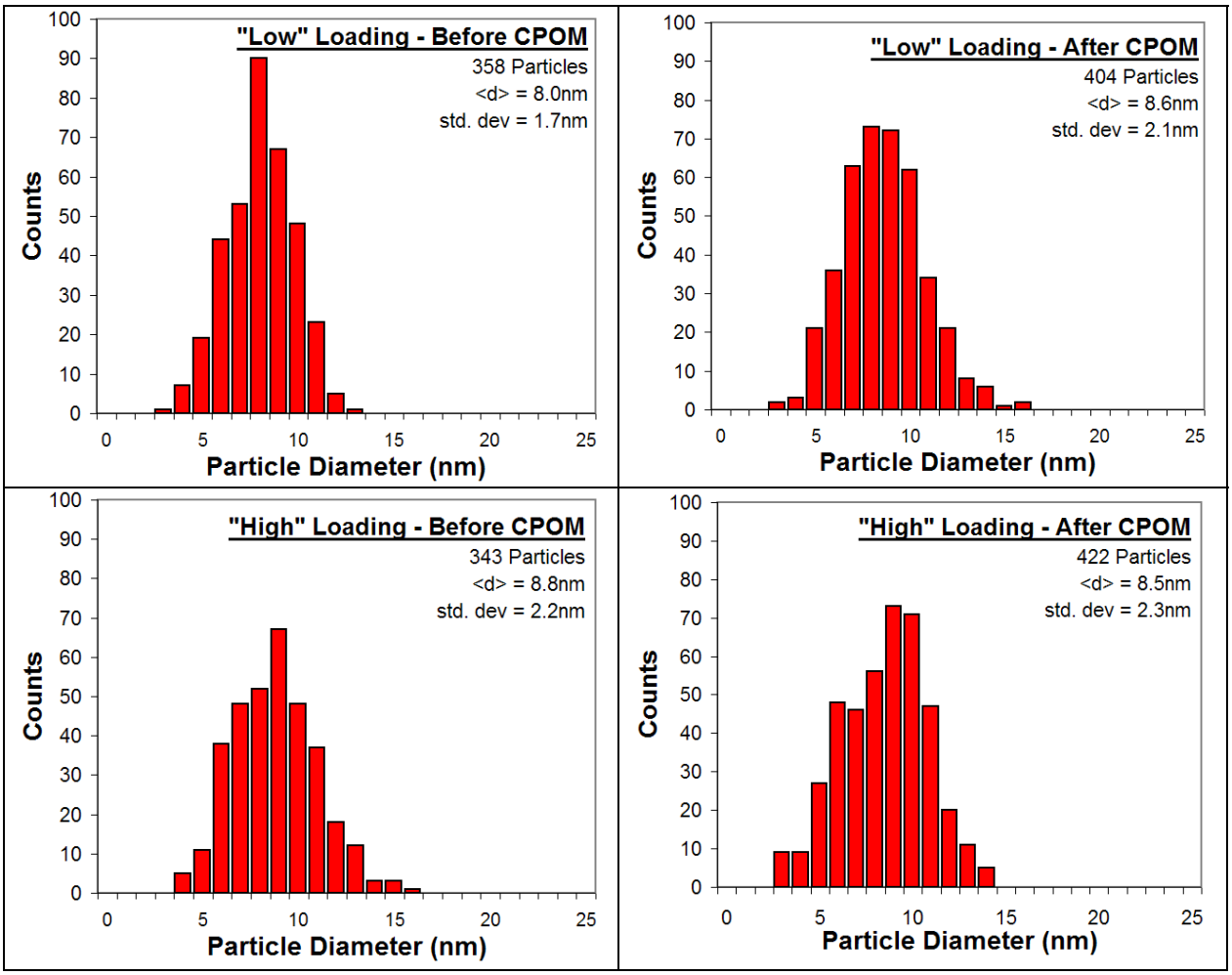

Figure 63: *Pt particle size distributions for "low" and "high" weight loading Pt-BHA coated silica felts – both before and after ~20 hours of CPOM testing - as determined from TEM images.*

These results point toward an explanation for why the medium and high weight-loading samples show a much less pronounced deactivation. These catalysts have sufficient platinum material remaining even after this "selective sintering" process to support the reaction and hence are able to sustain the reaction. Furthermore, this suggests that the deactivation process is limited to an initial decrease in activity – correlated with the (limited) agglomeration of unstable Pt nanoparticles – after which a stable, though slightly lower, level of activity should be reached. While we have previously demonstrated the long-term (>100 h) stability of the Pt-BHA

powders[14], no attempt was made at a longer term stability test in the present study beyond the ~20 hour studies presented here.

Overall, the results indicate that strong stabilizing effect of 'caging' the Pt nanoparticles inside the pore network of the nanocomposite that we observed before (see 4.4.4, above) is not compromised by the supporting process, and that the presented, simple form of supporting the nanocomposite powder results in a highly active, stable, and easy-to-handle catalyst.

7.0 SUMMARY AND OUTLOOK

7.1 SUMMARY

The goal of this thesis was to develop a further understanding and promote potential application of nanocomposite catalysts in clean energy processes. Because of the high temperature of many energy related processes, we investigated the origin of the tremendous thermal stability of platinum particles within nanocomposite Pt-barium hexaaluminate catalysts. To increase understanding of nanomaterials synthesis, we investigated the effect of changing various synthesis parameters on the material structure. To promote industrial application of nanocatalysts, we attached nanomaterials to structured supports and tested these supported nanocatalysts in catalytic partial oxidation of methane. Finally, we intended to extend the application of nanocomposite catalysts by testing them in other clean energy applications, including catalytic methane combustion and water-gas shift.

The results of detailed characterization studies of Pt-BHA nanocomposites were presented in detail in this thesis. These results are particularly important given the impact that these properties has on the activity and stability of these materials as catalysts. A particular focus was placed upon the effect of calcination conditions on the properties of the resulting material. Short duration (15 min) calcination in air proves to be sufficient to completely remove residual surfactants as combustion products while retaining small particle size. Longer treatment

in air results in further growth of the platinum particles, indicating that particle sintering is thermodynamically favored but limited by kinetics at ~600°C. Calcination in hydrogen removed residual surfactant in the form on hydrogenation products, but failed to remove the most strongly bound surfactant residues from the surface of the platinum particles. The residual surfactant restricts particle sintering in these materials.

Further characterization of the Pt-BHA nanocomposite focused on the size of the platinum particles at elevated temperatures. The stability of these particles is important for the applicability of these materials for many important clean energy reactions. A plateau of platinum particle stability – retention of platinum particles with diameters ~15 nm – is found to exist between 600-1000°C. In this plateau the particles are thermally stabilized because particle migration is suppressed due to a particle "caging" effect attributed to the narrow pore necks of the BHA ceramic. As the structure of the BHA begins to expand ~900°C the platinum particles resume further sintering, but are once again restrained by the size of the pore cages. Only once the BHA crystallizes at ~1210°C do the platinum particles begin to experience uncontrolled thermal sintering.

These metal-BHA nanocomposites were tested in two important clean energy applications – methane combustion and water-gas shift. In methane combustion, a low 1 wt% loading of Pt-BHA was able to lower the ignition temperature by 100°C than over pure BHA. This 1 wt% Pt-BHA catalyst exhibited thermal stability that is a characteristic of this novel class of materials, as well as no indications of internal mass transfer limitations. In water-gas shift, Pt-BHA nanocomposites were not as active as atomically dispersed Pt-CeO2 catalysts at low temperature (300°C), yet they did remain much more stable during shut-down/restart conditions.

Investigations of the formation of metal – SiO_2 nanocomposites yielded an enhanced understanding of the important parameters for sol-gel synthesis of silicate materials. This understanding resulted in the formation of Ni-SiO_2 and Fe-SiO_2 nanocomposites with excellent thermal stability during oxidation-reduction cycling at 800°C.

A study was presented on the supporting of a Pt-BHA powder onto a range of different, conventional and novel support materials (silica and alumina felts and foams, and extruded cordierite monoliths). The Pt-BHA coated alumina foam and silica felt showed improved methane conversion and hydrogen selectivity in CPOM reaction with over an order of magnitude less Pt loading, while the silica felt supported material experienced only mild deactivation during 25 hours of reaction. The presented work can be regarded as a step towards bridging the gap between nanoscale science and (macroscopic) technical application via hierarchical structuring of catalysts from the nano- to the macroscale as summarized in Figure 64. In particular, such supported nanocomposite catalysts hold great potential for use in demanding environments, such as high-temperature, high-throughput conditions in fuel processing and similar energy-related applications.

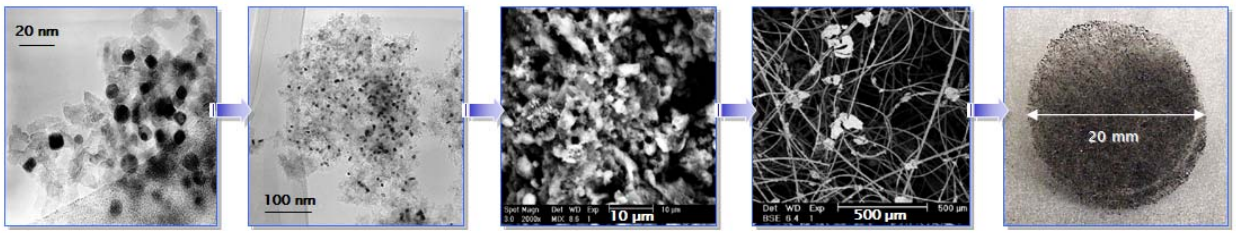

Figure 64: *TEM and SEM images and photo of the Pt-BHA coated silica felt catalyst, illustrating the hierarchical structuring of the catalyst across many length scales from the nanoscale (left) to the macroscale (right). From left to right: TEM images of Pt nanoparticles embedded in BHA; TEM image of Pt-BHA nanocomposite particulate; SEM image of the macropore structure of a nanocomposite particle; SEM image of Pt-BHA coated silica fibers; photo of the Pt-BHA coated silica felt catalyst.*

7.2 OUTLOOK

A fundamental understanding of how one can tailor the properties of the nanocomposite structure by changing the parameters of the synthesis has thus far eluded discovery. Section 4.3 and the accompanying Appendix D show how water-to-surfactant ratio and hydrophilic chain length can produce changes in the pore structure and platinum particle size, but more work is needed to understand the underlying mechanisms. Insight might be gained by examining additional parameters such as the hydro*phobic* chain length of the microemulsion surfactant; a series of experiments with SPAN and TWEEN type surfactants, which are available in a variety of different hydrophobic chain lengths, may complement and enhance the understanding of the previously investigated XP type surfactants (structure of surfactants shown in Appendix A).

One particular aspect of tailoring the properties of the nanocomposite should gain special attention. We can trace the stability of metal nanoparticles at high-temperature to a "caging" effect that depends on the size of the pore necks within the BHA ceramic. Hypothetically, if one could tailor a similarly structured ceramic but which only contained pore necks with diameters ~3 nm, one would be able to create a catalyst which combines the novel nanoparticle effects seen in this size range (e.g. nanogold for CO oxidation by Haruta), with the tremendous thermal stability seen in the present work. This catalyst would have great potential for a wide variety of high-temperature reactions.

Recent work has pointed out a method to simplify the formation of high-temperature stabilized metal nanocomposites. Because the particle "caging" effect only depends on the structure of the ceramic material, it is therefore possible to first form the ceramic material and then add the necessary metal nanoparticles later. Thus, the microemulsion synthesis and, more

importantly – the surfactant removal – can be avoided altogether. This is highlighted by the investigation of drop-coating pure BHA materials (see Appendix E.2) – where Fe, Cu and Ni drop coated BHA look strikingly similar to their microemulsion templated counterparts. Parameters such as pH of the drop coating solution and the method of coating deserver further investigation given the promising results seen in this initial investigation.

Continuing investigations of nanocomposite materials as water-gas shift catalysts should be pursued in order to expand on the preliminary results shown here. The stability of Pt-BHA and Pt-ceria nanocomposites during start-up/shut-down is promising, but their lack of low temperature (T<300°C) activity is somewhat surprising. The lack of any WGS activity over Au-ceria nanocomposites is also surprising, considering the wealth of literature describing the high activity of this type of catalyst. Future investigations should focus on the particle size in both Au and Pt catalysts and the nature of the interaction between the particles and the ceramic substrate, as these factors appear to play a crucial role in this reaction.

In the future, nanocomposites should be expected to play a key role in photocatalysis and photovoltaic materials. Photovoltaics can be regarded as the cleanest energy application – they require no fossil fuels, produce no harmful emissions, and generate electricity from the abundant energy of the sun. However, many challenges remain, especially regarding appropriate photoactive materials. Focus has been on TiO_2 because of its high chemical stability, abundance in nature (and correspondingly low cost), and experimental results indicating effectiveness of TiO_2 for degradation of pollutants in water and air[173]. Grätzel and coworkers pioneered the use of TiO_2 as a photovoltaic through the invention of a solar cell capable of producing electricity at 12% efficiency using a ruthenium-based organic dye as a sensitizer[174]. While their result is widely regarded as a key step forward for photovoltaics, it also highlights one of the main

disadvantages of TiO_2 – its large band gap (3.2 eV) results in adsorption only in the UV spectra, leading to low efficiency unless a photosensitizing dye or other means are employed to promote further photon adsorption[175].

While the use of dyes has been successful in some cases, the strong photodegradation of most organic dyes, and the careful nature with which the dye must be applied (less than a monolayer of coverage) limit their practical application[176]. These limitations have led to recent studies of using semiconductor nanocrystals (quantum dots, QD) such as CdS, CdSe, InP and InAs, to increase the sensitivity of high band gap semiconductors such as TiO_2[176-179]. QDs have a unique ability to tune the size of the band gap via changing the spatial dimensions of the dot, thus allowing for maximum solar adsorption in the visible spectra. The nano- characteristic of both the TiO_2 and the QD in this class of composite material is of great importance. A nanostructured TiO_2 provides a higher surface area for increased light harvesting as well as increased surface contact between the titania and the quantum dots[175]. Likewise, the nanosized quantum dots have tunable band gaps and never show the presence of an electron-withdrawing depletion layer due to their nano-characteristic[175]. Synthesis techniques for these complex materials are varied and numerous, indicating the large amount of interest in this area. For CdSe QDs alone, one finds examples of adsorption of the QDs onto TiO_2 using bi-functional surface modifiers[180], growth of the QDs on the TiO2 from a chemical bath[181], attachment of CdSe to ZnO using short linker molecules[182], and the growth of ZnS/CdSe core-shell structures[183, 184] all with various levels of success.

In another case, $ZnFe_2O_4$-TiO_2 nanostructures were formed for the simple reason that both components had previously been shown to be promising solar energy materials. These nanocomposite materials showed enhanced photoactivity, which the investigators attributed to

inhibition of anatase-to-rutile restructuring in the TiO_2 by the $ZnFe_2O_4$[185]. Anatase is known to be significantly more photoactive than rutile TiO_2. The origins of this higher photoactivity possibly arise from the smaller electron effective mass that has been inferred from electrical and optical measurements of anatase[186]. This smaller electron mass allows for increased mobility of the electrons in anatase, resulting in the band-like conduction and increased photoactivity observed.

The ability to form a homogeneous distribution of metal or bimetallic nanoparticles on or within a nanostructured photovoltaic ceramic is therefore a key aspect of the successful implementation of photovoltaic technology. Thus, one can view the sol-gel microemulsion technique used to form nanocomposite Pt-BHA outlined in this dissertation as a suitable starting point for the formation of nanocomposite QD-TiO_2 structures. The substantial work to-date in tailoring the structure of the metal (see appendix E.1) and ceramic components (see chapter 5.0), leads one to believe that a structure such as CdSe-TiO_2 is possible using this technique. Clearly the direct formation of a bimetallic CdSe structure will be a challenge, as previous efforts in our group to form bimetallic species from a microemulsion have resulted in separate domains of each metal rather than a true bimetallic. If this and other challenges can be overcome, it should be possible to form a nanocomposite material which should be a viable candidate for photovoltaic applications. In addition, the high level of success for Pt-BHA in gas phase reactions should translate into similar behavior for nanocomposite CdSe-TiO_2 in gas phase photocatalytic reaction. An example would be photocatalytic reduction of CO_2 with water over modified TiO_2 nanomaterials, a reaction which has been studied recently by a number of groups[187-190]. This reaction converts the greenhouse gas CO_2, which is the leading contributor to global warming, into a potential fuel source (methane or methanol) – truly a clean energy application.

The investigations and results presented in this thesis have led to further understanding of nanocomposite materials, developed their potential as clean energy catalysts, and laid the foundation for future investigations in this field. We believe strongly that continued research will unlock new and exciting possibilities for these novel materials.

APPENDIX A

SURFACTANTS USED

Table 9: *Surfactants Utilized in the Synthesis of Nanocomposite Materials.*

surfactant	properties
Lutensol AO3 *(Triethylene glycol tridecyl/pentadecyl ether)* 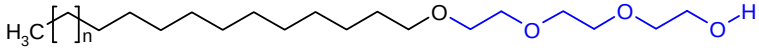	HLB: 8 n = 1(67%), 3 (33%) MW: ca. 340 g/mol *BASF*
Lutensol XP30 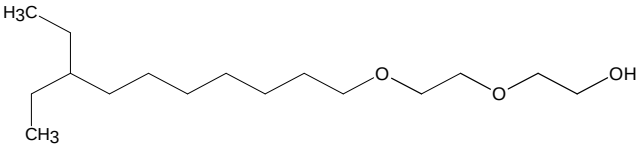	HLB: 8 MW: ca. 290 g/mol *BASF*
Lutensol XP50 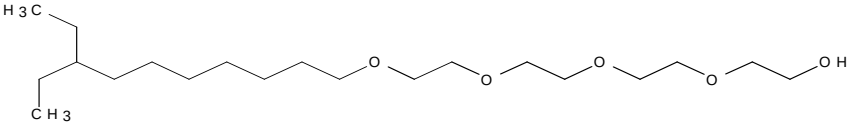	HLB: 10 MW: ca. 370 g/mol *BASF*
Lutensol XP70 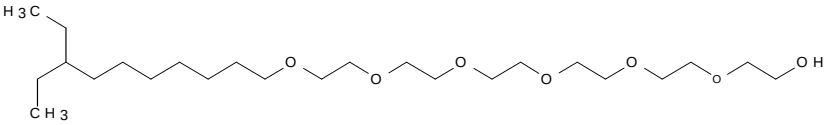	HLB: 12 MW: ca. 445 g/mol *BASF*

Span 80 [sorbitan oleate] * 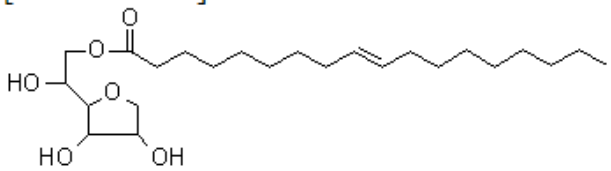	HLB: 4.3 MW: 428.6 g/mol *Fluka*
Tween 85 [sorbitan trioleate poly(ethylene oxide)] * ($w + x + y + z$ is approx 20) 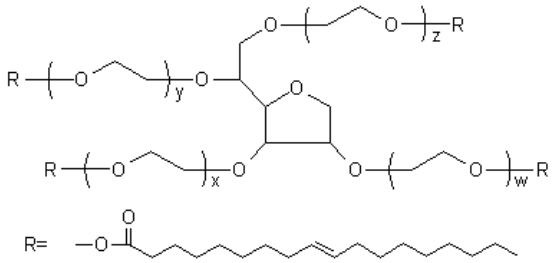	HLB: 11 MW: n/a *Fluka*
PEPP *((Polyethylene glycol)-block-(polypropylene glycol)-block-(polyethylene glycol))* 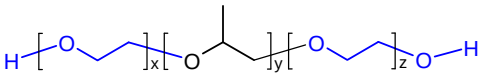	HLB: 1 – 7 (PEG-PPG-PEG) MW: ca. 2000 g/mol PEG: 10% *Aldrich*

APPENDIX B

PARAMETERS FOR GC AND RELATED CALCULATIONS

B.1 CATALYTIC PARTIAL OXIDATION OF METHANE

B.1.1 Calculation of conversion, selectivity, and atomic balance

Using molar quantities, methane conversion is defined as:

$$X_{CH4} = \frac{[CH_4]_{in} - [CH_4]_{out}}{[CH_4]_{in}}$$

Assuming CO, CO_2, and CH_4 are the only carbon containing species in the system, and that no coke formation occurs within the reactor (none was observed), one can substitute:

$$[CH_4]_{in} = [CH_4]_{out} + [CO]_{out} + [CO_2]_{out}$$

Leading to the following equation for methane conversion, containing only molar fractions in the exit stream which are easily determined from the GC measurement, and not relying on inlet concentrations (which are not directly measured):

$$X_{CH4} = \frac{[CO]_{out} + [CO_2]_{out}}{[CH_4]_{out} + [CO]_{out} + [CO_2]_{out}}$$

The CO and H_2 selectivity can be calculated directly from the definition of selectivity (the molar ratio of desired product to all products formed). For the reaction of methane to CO or CO_2, this yields the following equation which can be determined from the GC measurement:

$$S_{CO} = \frac{[CO]_{out}}{[CO]_{out} + [CO_2]_{out}}$$

For the reaction of CH_4 to H_2 or H_2O, this yields the following equation which can be determined from the GC measurement:

$$S_{CO} = \frac{[H_2]_{out}}{[H_2]_{out} + [H_2O]_{out}}$$

For atomic balances, there are 3 main balances to consider: C/H, C/O, and C/N. C/H is used to calculate the water concentration in the exit stream, and is fixed at ¼ based on the methane feed. C/O can be calculated at the inlet and exit from the following equations:

$$C/O_{in} = \frac{\dot{N}_{CH4,in}}{2 \cdot \dot{N}_{Air,in} \cdot 0.215}$$

$$C/O_{out} = \frac{[CO]_{out} + [CO_2]_{out} + [CH_4]_{out}}{2 \cdot [CO_2]_{out} + [H_2O]_{out} + [CO]_{out} + 2 \cdot [O_2]_{out}}$$

Similarly, the C/N atomic balance can be determined from:

$$C/N_{in} = \frac{\dot{N}_{CH4,in}}{2 \cdot \dot{N}_{Air,in} \cdot 0.785}$$

$$C/N_{out} = \frac{[CO]_{out} + [CO_2]_{out} + [CH_4]_{out}}{2 \cdot [N_2]_{out}}$$

The C/O and C/N balances were determined for each experimental run, and generally closed to within +/-5%.

B.1.2 GC-Oven Setup

The GC system consists of two Shimadzu GC-14B running in parallel. It is designed to measure the composition of CH_4, O_2, N_2, H_2, H_2O, CO and CO_2. However, the measurement of H_2O was not used in the present study, because the H_2O was condensed prior to entering the GC system in order to prevent column degradation or damage. The parameters for the GC oven/detector system are listed in **Table 10**.

Table 10: *GC oven and detector parameters for CPOM.*

Parameter	***Oven 1***	***Oven 2***
Initial oven temperature	40°C	40°C
Injection temperature	250°C	200°C
Detector temperature	250°C	80°C
TCD temperature	100°C	80°C
TCD current	100 mA	65 mA
TCD polarity	1	2
Gas pressures [kPa]:		
Air (FID)	60	
H_2 (FID)	80	
Carrier gas (column)	240 H_2	190 Ar

The configuration of the GC is as follows. Oven 1 separates CH_4, O_2, N_2, H_2O, CO and CO_2 but not H_2, because it is used as the carrier gas for this oven. Two columns, one Haysep P and one Molesieve 13X (both 3m long, 18 in. diameter), are used to perform the separation. Because the Molesieve 13X column is incompatible with CO2 and H2O, these gases are separated first in the Haysep P column and bypass the Molesieve 13X column altogether. The relative order of detection is CO_2 (from the Haysep P), CH_4, O_2, N_2, CO, (all from the Molesieve 13X), and finally H_2O (again from the Haysep P). Oven 2 separates H_2 from all other components using 2 Haysep P (3m long, 18 in. diameter) operating in series.

B.2 WATER-GAS SHIFT REACTION

B.2.1 Calculation of conversion and atomic balance

For this reaction system the inlet concentrations of H2, He, CO and CO_2 are determined by feeding the reaction mixture to the GC directly while bypassing the reactive zone at room temperature. Helium is used as an internal standard to calculate the exit gas compositions. The exit gas flow rate, after water condensation, can be determined:

$$F_{out} = \frac{[He]_{in} F_{in}}{[He]_{GC}}$$

The exit gas compositions can be determined from the exit gas flow rate and the concentrations of the reactant species measured from the GC (denoted $[X]_{GC}$):

$$[X]_{out} = \frac{[X]_{GC} F_{out}}{F_{in}} \quad \text{X = CO, } CO_2\text{, } H_2\text{, He}$$

Note: this is only valid because it is assumed WGS is the only reaction occurring and it does not involve a change in the number of moles. CO conversion can now be calculated as:

$$X_{CO} = \frac{[CO]_{in} - [CO]_{out}}{[CO]_{in}} = \frac{\xi}{F_{CO,in}}$$

Using the inlet flow rate of CO, the extent of reaction, ξ, can be evaluated. The concentration of water leaving the reactor can thus be determined:

$$[H_2O]_{out} = \frac{F_{H_2O,out}}{F_{out}} = \frac{F_{H2O,in} - \xi}{F_{out}}$$

The atomic balances of interest, C/H and C/O, can be calculated (j = in or out):

$$C/O_j = \frac{[CO]_j + [CO_2]_j}{2 \cdot [CO_2]_j + [H_2O]_j + [CO]_j}$$

$$C/H_j = \frac{[CO]_j + [CO_2]_j}{2 \cdot [H_2]_j + 2 \cdot [H_2O]_j}$$

The balances are determined for each experimental run, and generally close to within +/-10%.

B.2.2 GC-Oven Setup

The GC used is an Agilent 3000A Micro GC. It is capable of measuring the composition of CH_4, O_2, N_2, H_2, CO, CO_2, ethane, ethylene, and acetylene. H_2O must be condensed prior to entering the GC system in order to prevent column degradation. The parameters for the GC system are listed in **Table 11**.

Table 11: *GC oven and detector parameters for WGS.*

Parameter	***Channel 1***	***Channel 2***
Carrier gas	Argon	He
Column type	Molecular Sieve	Plot u
Injection type	Backflush	Fixed volume
Inlet temperature	40°C	40°C
Injection temperature	250°C	200°C
Column temperature	110°C	70°C
Detector type	TCD	TCD
Detector sensitivity	Standard	High
Column pressure	40 psi	15 psi
Post run pressure	40 psi	25 psi
Backflush time	9.5 s	---
Sample time	10 s	10 s
Injection time	10 ms	30 ms
Run time	150	120
Post-run time	10	60

The configuration of the GC is as follows. Channel 1 (Molecular sieve column) separates (in order of relative detection) H_2, O_2, N_2, CH_4, CO and CO_2, while channel 2 (Plot U column)

separates CO2, ethylene, ethane, and acetylene. The total run time is relatively short (3 minutes), which facilitates rapid analysis of multiple reaction zones, or continuous monitoring of a single reaction zone.

B.3 METHANE COMBUSTION

B.3.1 Calculation of conversion and atomic balance

Using molar quantities, methane conversion is defined as:

$$X_{CH4} = \frac{[CH_4]_{in} - [CH_4]_{out}}{[CH_4]_{in}}$$

Because of the large excess of oxygen used in this reaction, it is 100% selective to CO_2 and H_2O (condensed and not detected in GC), and the only carbon containing species observed in the GC are CH_4 and CO_2. No coke formation was observed in the reactor, so one can substitute:

$$[CH_4]_{in} = [CH_4]_{out} + [CO_2]_{out}$$

Leading to the following equation for methane conversion, containing only molar fractions in the exit stream which are easily determined from the GC measurement:

$$X_{CH4} = \frac{[CO_2]_{out}}{[CH_4]_{out} + [CO_2]_{out}}$$

The atomic balances of interest are C/O and C/N. C/H is meaningless since the only hydrogen-containing product (water) is not detected in the GC. C/O can be calculated at the inlet and exit from the following equations:

$$C/O_{in} = \frac{\dot{N}_{CH4,in}}{2 \cdot \dot{N}_{Air,in} \cdot 0.215}$$

$$C/O_{out} = \frac{[CO_2]_{out} + [CH_4]_{out}}{2 \cdot [CO_2]_{out} + [H_2O]_{out} + 2 \cdot [O_2]_{out}}$$

The outlet water concentration can be back-calculated assuming a constant C/H ratio. Similarly, the C/N atomic balance can be determined from:

$$C/N_{in} = \frac{\dot{N}_{CH4,in}}{2 \cdot \dot{N}_{Air,in} \cdot 0.785}$$

$$C/N_{out} = \frac{[CO_2]_{out} + [CH_4]_{out}}{2 \cdot [N_2]_{out}}$$

The C/O and C/N balances were determined for each experimental run, and generally closed to within +/-5%.

B.3.2 GC-Oven Setup

The setup is identical to the GC used for Water-gas shift.

APPENDIX C

VARIOUS TECHNIQUES FOR RESIDUAL SURFACTANT REMOVAL

C.1 WASHING

The standard Pt-BHA catalyst was placed into a fritted glass suction filter and covered with washing solvent. The slurry was manually stirred for 30 seconds after which the solvent was removed. The solvents used were water, acetone, and CH_2Cl_2 in that order, and each was repeated three times per batch. One subset of a batch of catalyst was washed immediately prior to calcination, and another subset was washed immediately following calcination. This was performed to see the effect of removing residual surfactant prior to calcination and also removing residual carbonaceous species remaining after calcination.

Figure 65 shows the specific surface area obtained from nitrogen porosimetry experiments on Pt-BHA materials washed in this manner at various temperatures. Both unwashed pure BHA and Pt-BHA washed prior to calcination show a decline in surface area at lower calcination temperatures, while other samples have steadily decreasing surface area across the entire temperature profile (from 350-500 m2/g @ 300°C to 125-250m^2/g. @ 900°C) These measurements are a strong indication that some of the mesopores of these samples remain blocked by residual surfactant at low calcination temperatures. This reveals that residual

surfactant may be a hindrance to the catalytic ability of these materials, and that this washing technique may be an important step toward removing it. It also indicates that this technique is not completely effective at removing the surfactant from the catalyst surface.

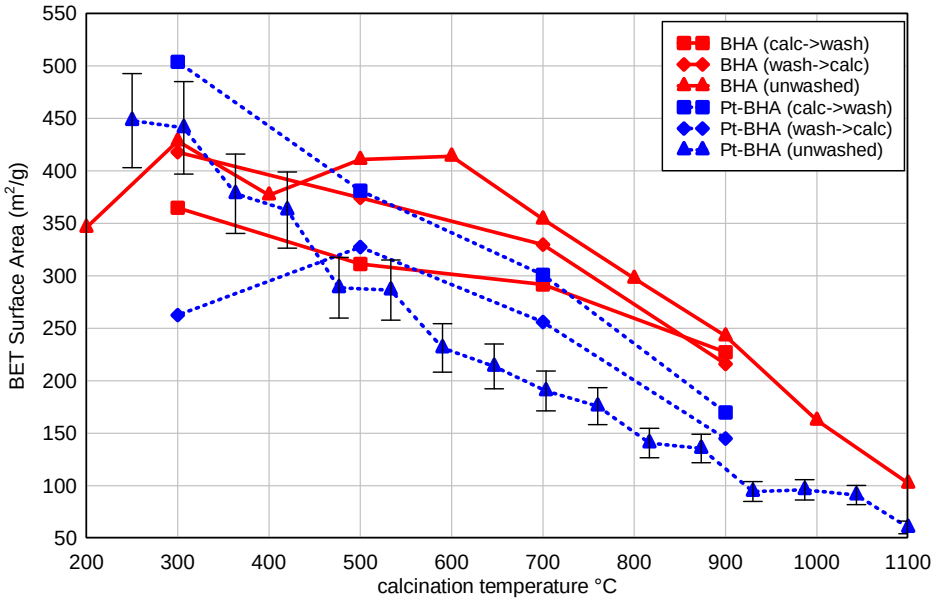

Figure 65: *BET total surface area measurements of washed and unwashed Pt-BHA and pure BHA. Error bars indicate 10% error in BET a rough estimate of the experimental variability of the measurements.*

BJH analysis of the nitrogen adsorption isotherms was used to obtain the pore structure of the washed and unwashed BHA. The results shown in **Figure 66** clearly indicate that the washing procedure has very little effect on the pure BHA nanocomposite. The pore necks all have the same diameter within experimental error in each of the three experiments. The pore cages also are virtually identical, with some slight variations in total pore volume. Combustion of surfactant in the pores of pure BHA does not appear to play a significant role in the structure of the pore system. This further supports the hypothesis that the surfactant selectively adheres to the Pt and influences the structure.

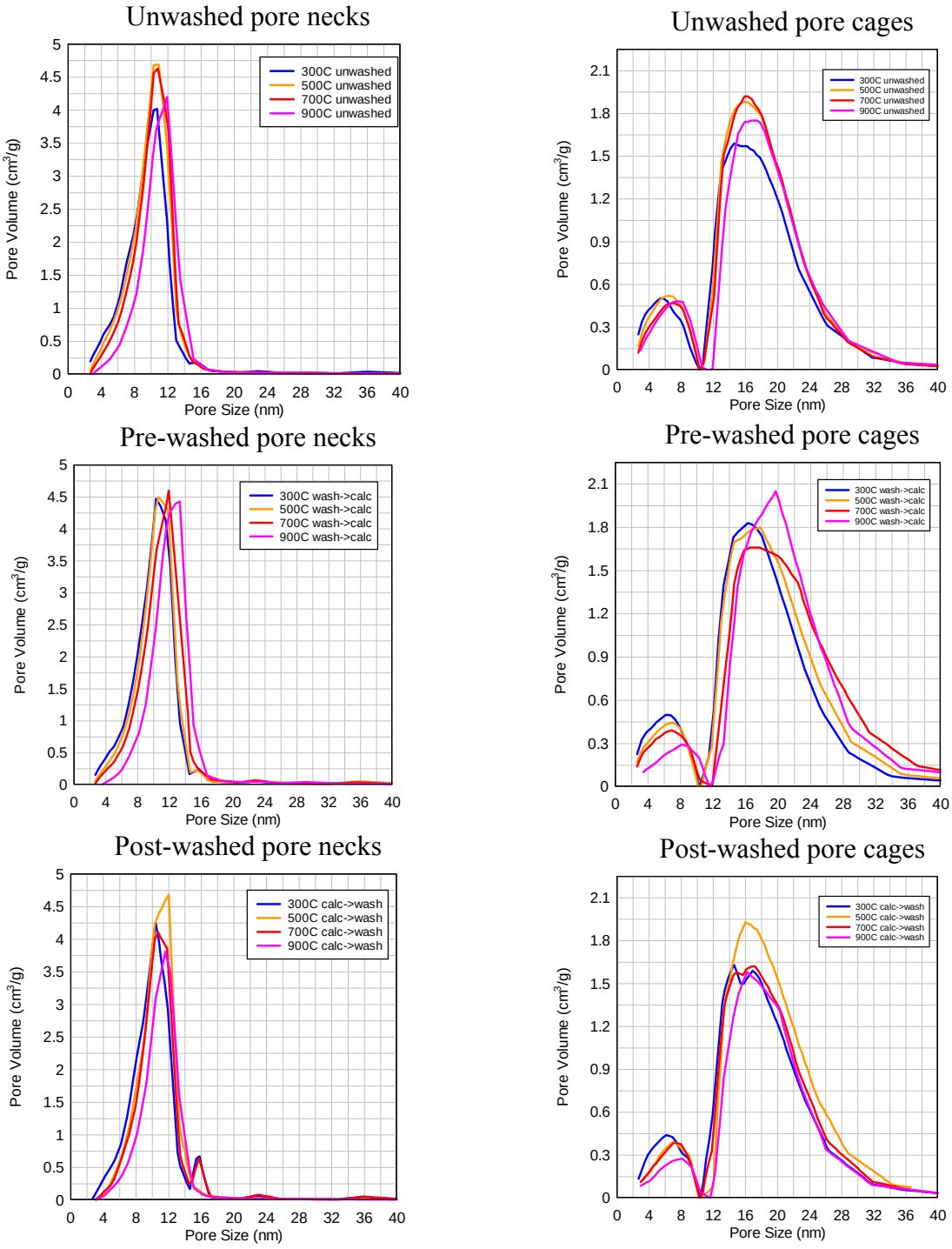

Figure 66: *Pore size distributions, obtained from BJH analysis of nitrogen adsorption, for various washing procedures conducted on pure BHA.*

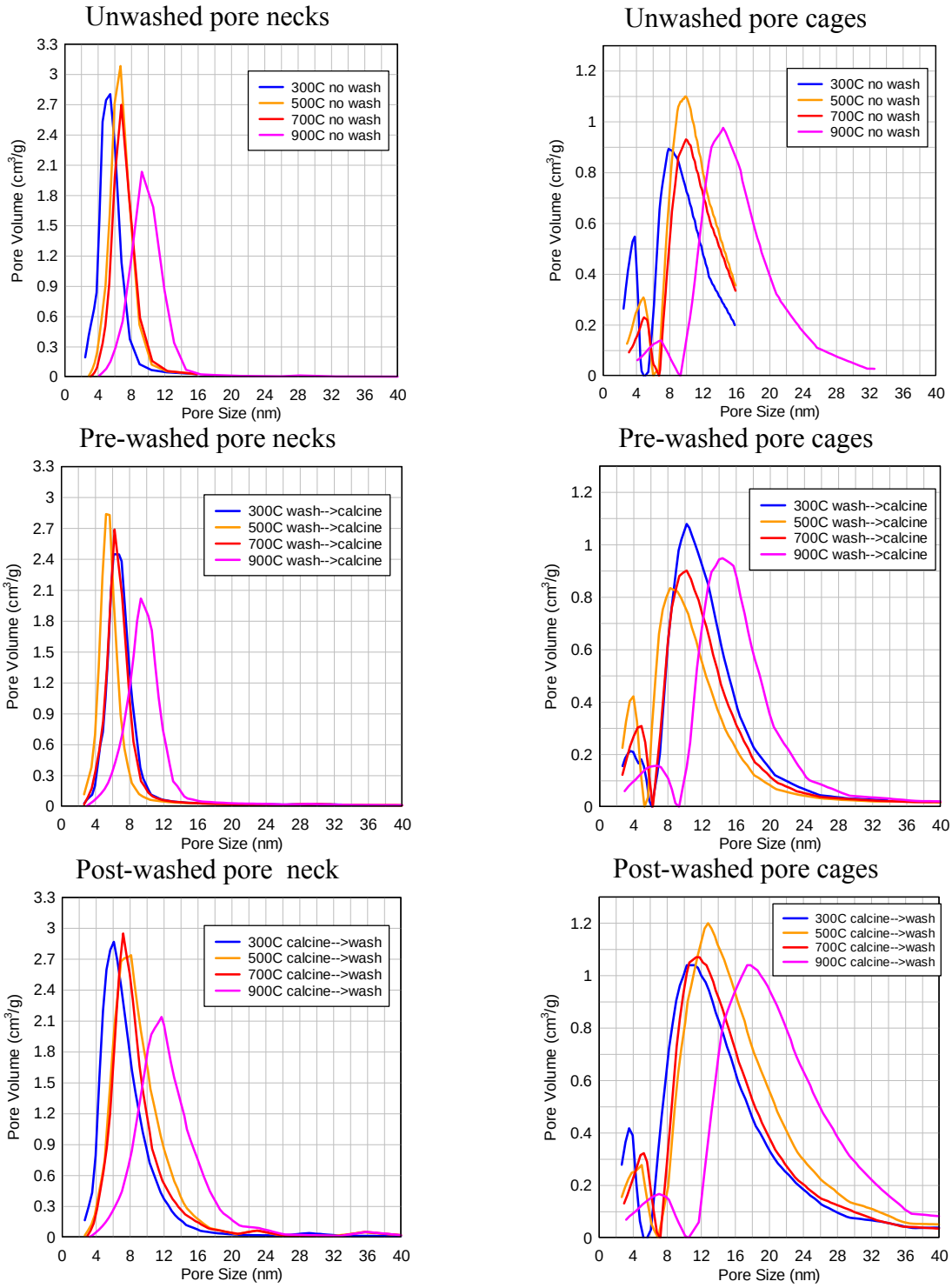

Figure 67: *Pore size distributions, obtained from BJH analysis of nitrogen adsorption, for various washing procedures conducted on 10 wt% Pt-BHA.*

Similar pore size distribution data for Pt-BHA are shown in **Figure 67**. The pore necks for all 3 procedures show very little difference in diameter or volume. The pore cages in the post-washed samples are wider and less defined at each temperature point when compared to the pre-washed and unwashed samples. The pore cages in the pre-washed and unwashed samples are roughly the same size at each temperature, with the 900°C point having a broader distribution in the unwashed sample. If one assumes that the slight widening of the pores is due to removal of surfactant (or residual carbon remaining after surfactant combustion), these results seem to indicate that the washing procedure is effective at removing the residual carbon left-over from calcination, and poor at removing the surfactant prior to calcination.

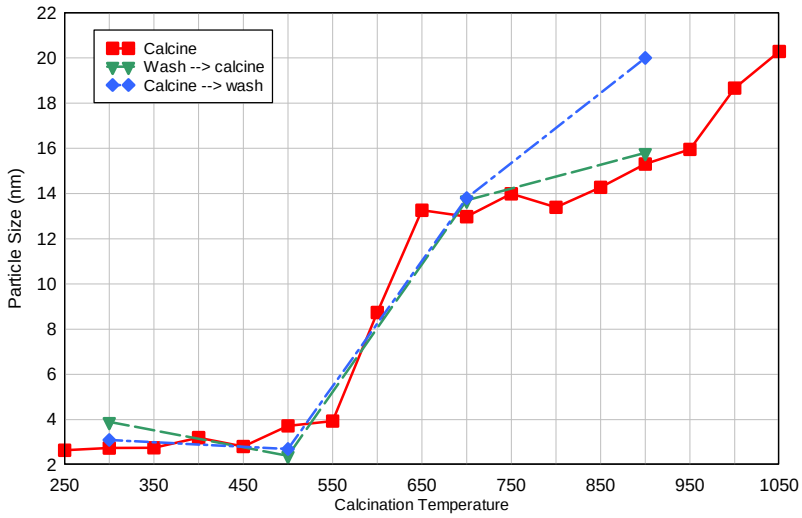

Figure 68: *TEM particle size determination at various calcination temperatures for 10 wt% Pt-BHA: unwashed, washed before, and washed after calcination.*

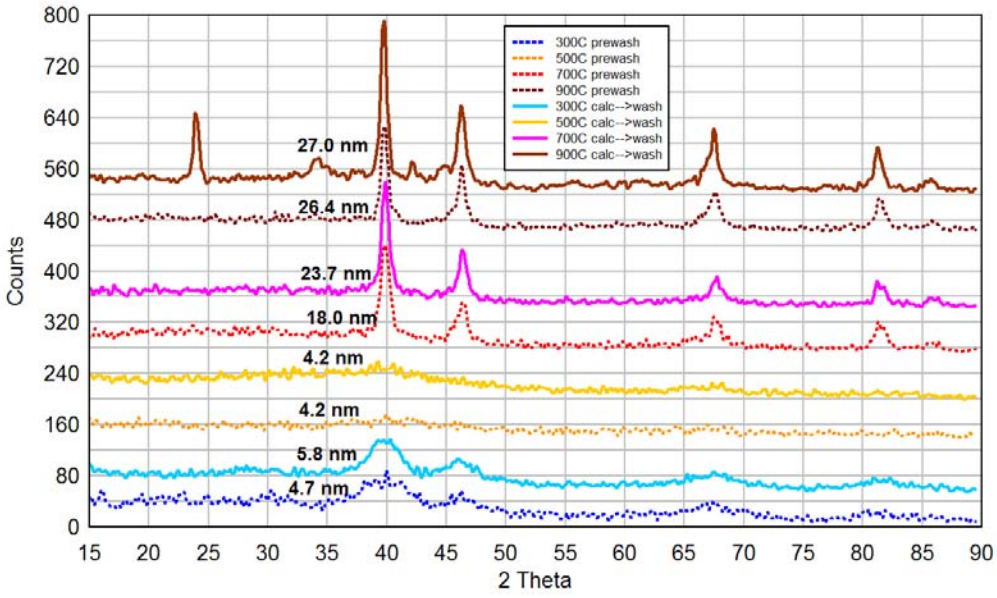

Figure 69: *XRD diffraction patterns for pre- and post- washed Pt-BHA. Numbers listed are calculations of the average Pt particle diameter from line broadening (Debye-Scherrer) analysis of the 40 2 theta peak.*

The effect of the washing procedure on the Pt particle size (as determined from TEM images) is shown in **Figure 68**. Parallel calculation of Pt particle size from line broadening analysis (Debye-Scherrer) of the 40 2θ Pt XRD reflex is presented in **Figure 69**. There are two interesting phenomena in this data. First, the particles decrease in size when the calcination temperature is increased from 300 to 500°C. The XRD patterns rule out the possibility of the measured TEM size being skewed by experimental artifacts such as a thin layer of surfactant on the surface of the nanoparticles. This effect is interesting and unexplained and is a potential candidate for future investigations. The second noteworthy effect is the larger particle size (by about 4nm) in the post-calcination washed samples at 900°C. This coincides with the formation of a new crystalline $BaCO_3$ phase, as seen in the XRD diffraction data (reflexes at ~24, ~34, and ~42 2θ). The cause of the appearance of this phase remains unknown. If the appearance of this

phase corresponds with a significant destabilization of the BHA structure, it may be an explanation for the appearance of larger Pt particles observed in the post-calcination washed sample. . In general, the washing procedure does not strongly affect the size of Pt particles observed, except the aforementioned increase in size increase at 900°C for post-calcination washed Pt-BHA.

XRD was also used to further investigate the appearance of $BaCO_3$ (witherite) in pure BHA, and the results are shown in **Figure 70**. Washing pure BHA before calcination favors the appearance of witherite at low temperatures (300 and 500C), while washing the sample after calcination favors the appearance of witherite at high temperatures (700C and 900C). A possibility is that the witherite formed in one sample is high-temperature stable, while the other is destabilized at high-temperature. Further research into why this species appears and how it affects the porosity and Pt particle size is necessary.

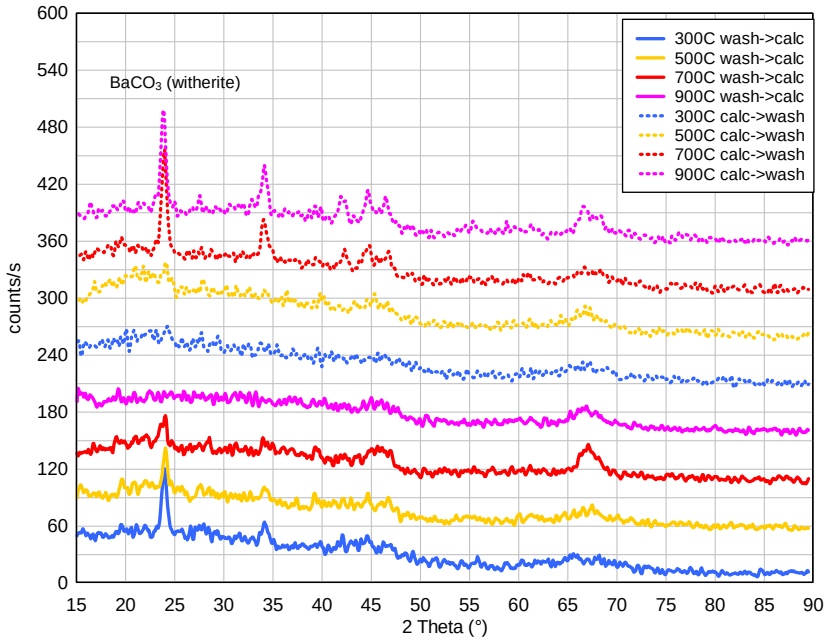

Figure 70: *XRD diffraction patterns for pre- and post- washed pure BHA showing the presence of BaCO3 witherite crystalline phase.*

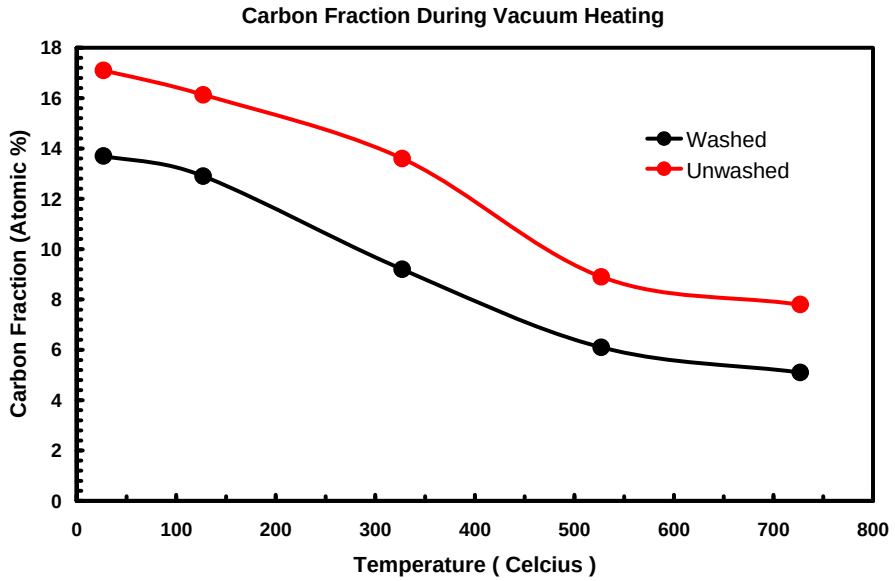

Figure 71: *XPS determination of carbon fraction for pre-washed and unwashed Pt-BHA [results from Chris Matranga, NETL]*

XPS analysis of both unwashed and washed Pt-BHA was performed in order to quantify the amount of residual carbon before and after the washing technique. The results are shown in **Figure 71**, indicating that the unwashed Pt-BHA contains ~17% carbon prior to washing, and washing only removes ~3-4% of this carbon. The washing technique is thus largely ineffective at removing surfactant residue from the Pt-BHA catalyst. A worthy goal of future investigations is to find a washing technique that can remove 100% of the surfactant prior to calcination.

C.2 REFLUXING

An alternative to the washing technique for Pt-BHA is also investigated, in which the freeze-dried catalyst was refluxed in CH_2Cl_2 at 50°C three times, followed by refluxing in acetone at

65°C three additional times. **Figure 72** shows the pore size distribution for this sample calcined at 300C compared to the previous washing technique for Pt-BHA. The refluxing technique reveals a bi-modal distribution of pore necks and pore cages within the structure of the nanocomposite. Also, the total volume of the pore cages has decreased significantly. This data is a strong indication that the refluxing technique has a significant impact on the removal of surfactant from the Pt-BHA nanocomposite, and thus on the development of the pore structure. Calcination of refluxed catalysts at increased temperatures to completely burn off any remaining surfactant (T>450°C) will be important for establishing the meaning of these results. Further investigation of Pt particle size and analysis of residual surfactant after refluxing would be worthwhile.

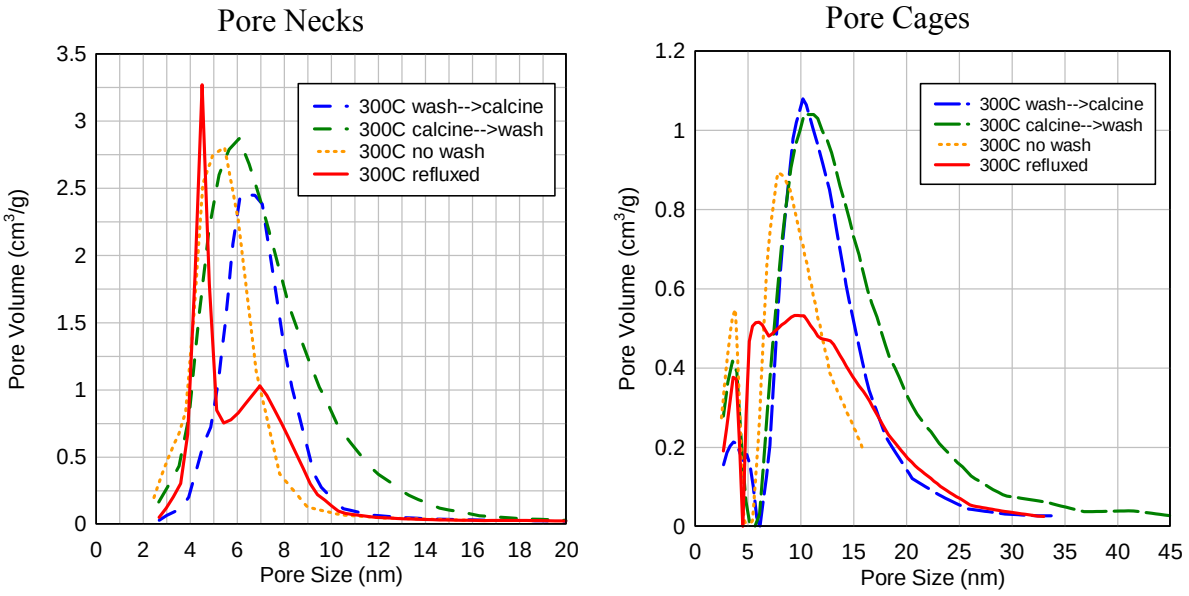

Figure 72: *Pore size distributions, obtained from BJH analysis of nitrogen adsorption isotherms, for unwashed, washed, and refluxed Pt-BHA. Calcination was performed at 300°C.*

C.3 OXYGEN PLASMA TREATMENT

An oxygen plasma sterilizer/sterilizer (PDC-32G, courtesy Dr. Valenkar, University of Pittsburgh Chemical Engineering) is used to attempt to remove surfactant prior to calcination. A small amount of uncalcined 10 wt% Pt-BHA is placed into a small weighing dish which is inserted into the oxygen plasma sterilizer. The sample was periodically removed from the chamber to measure mass loss due to surfactant removal. After ~15 minutes the mass loss had leveled off, and 67.8% of the sample had been removed by the treatment method.

The treatment was effective at removing mass from the sample, so CO pulse chemisorption analysis is used to determine the platinum surface area available. The technique revealed that the uncalcined sample had only 2.1 m^2/g Pt metal, which was much lower than previously measured for Pt-BHA nanocomposites. The oxygen plasma treatment does not appear to be able to remove surfactant from the surface of the Pt particles, but is effective at removing a large portion of organic material from the structure. Further testing, and possible combination with washing and/or refluxing techniques would be recommended.

C.4 OZONOLYSIS

The strong oxidizing potential of ozone is used to attempt to remove the surfactant material at room temperature. However, ozone treatment (4 wt% ozone in O_2 at 1 atm) is unsuccessful at removing the surfactant at room temperature [XPS study by Chris Matranga, NETL]. Heat treatment to 427°C was necessary to remove the surfactant material in both ozone and pure oxygen treatments.

APPENDIX D

THE EFFECT OF SYNTHESIS PARAMETERS ON THE PROPERTIES OF THE PT-BHA NANOCATALYST

D.1 WATER TO SURFACTANT RATIO

One of the most important parameters in the microemulsion templated synthesis chosen is the molar ratio of water to surfactant. This ratio directly affects the size of the water micelles which function as nano-sized reactors for the formation of Pt and BHA nanoparticles. Smaller R_W ratio will result in smaller micelles, and theoretically a finer grain size. A larger R_W ratio will result in larger micelles and lamellar structures at very high ratios, and theoretically a coarser grain structure transitioning to a needle-like structure as lamellar structures become more prevalent.

In order to determine how this important ratio affects the structure of Pt-BHA nanocomposites, the following test was conducted. Pt-BHA was synthesized using the standard procedure outlined in the experimental section with a few exceptions. Lutensol XP30 replaced the PEPP and pentanol surfactant system in order to reduce the number of variables in this experiment. The Lutensol XP30 surfactant does not require a co-surfactant to form a stable microemulsion. By using it, the need to adjust the ratio of surfactant to co-surfactant is circumvented. The quantities of all other components were held constant, with the exception of

the Lutensol XP30 which was varied to obtain the desired R_W ratio. The values of R_W were chosen around the microemulsion – emulsion transition curve, as shown in **Figure 73**.

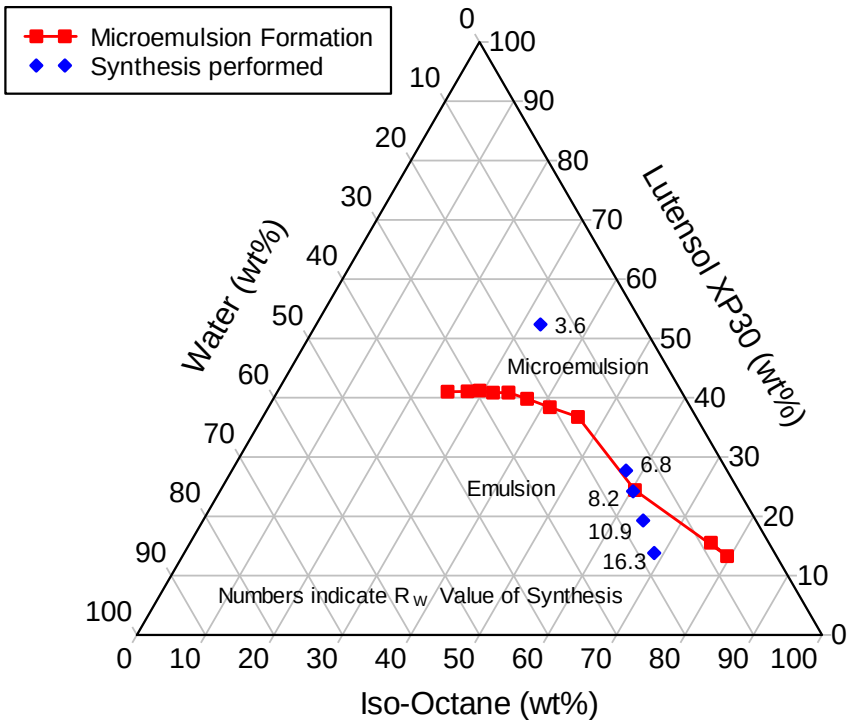

Figure 73: *Phase Diagram for the Water-Iso-Octane-Lutensol XP30 system. The squares indicate the transition point from a clear, thermodynamically stable microemulsion to a translucent kinetically stable emulsion in a scouting study for this system.*

The results of the R_W testing are shown in **Figure 74**. The BET surface area follows a continually decreasing trend as the ratio is increased. This is exactly what is expected as the grains of the ceramic grow larger due to the larger micelle size. The Pt particle size determined from the XRD patterns indicates that the Pt particles themselves are unaffected (within experimental error) by the change in the amount of surfactant. This is an interesting result, because it indicates the possibility of tailoring the ceramic material while maintaining the same Pt particle size for the Pt-BHA nanocomposite catalyst. The TEM particle size follows the same trend as the Debye-Scherrer data, but the size increases substantially at R_w=16.3. This could

indicate the first signs of the ceramic becoming more needle-like in structure, leading to destabilization of the Pt particles from the matrix.

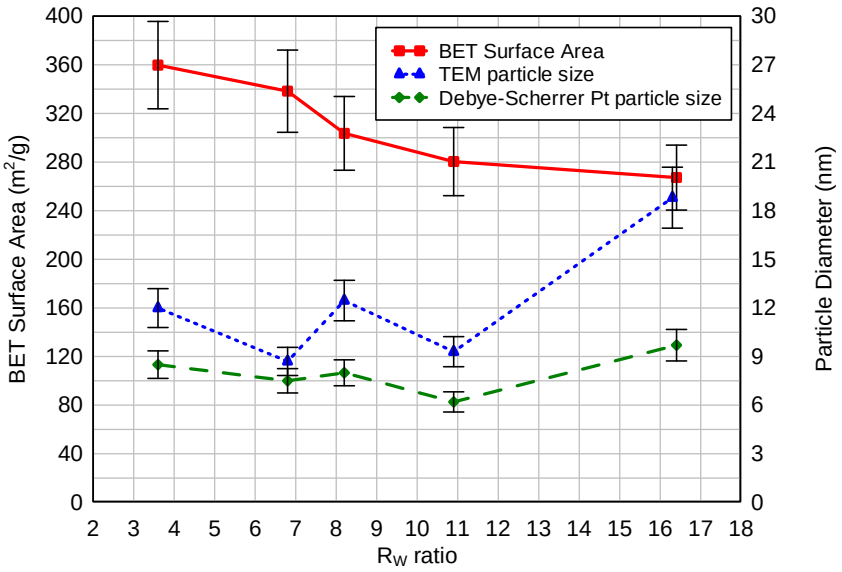

Figure 74: *BET, TEM, and XRD data for Pt-BHA catalysts synthesized at various R_W values using Lutensol XP30 as surfactant. Each catalyst was calcined for 5 hours in air at 600°C prior to measurement. Error bars indicate 10% error in BET and Debye-Scherrer, and 5% error in TEM, a rough estimate of the experimental variability of the measurements.*

Qualitative evaluation of TEM micrographs should yield the shape and structure of the primary ceramic particles. This will give an indication of the influence that changing the R_W ratio has on the final product. The micrographs shown in **Figure 75** were selected as representative of each batch of material. As the R_W ratio is increased, the primary ceramic particle size seems to grow. This is difficult to quantify, because it is hard to separate each ceramic particle visually from its nearest neighbors. Nevertheless, the growth the particles is clearly evident when one scans from R_W = 3.6 to 16.3. Further increasing the R_W value should lead to needle-like structures which should be a more open and porous structure. Materials synthesized in this manner may have application in mass transfer limited reaction systems.

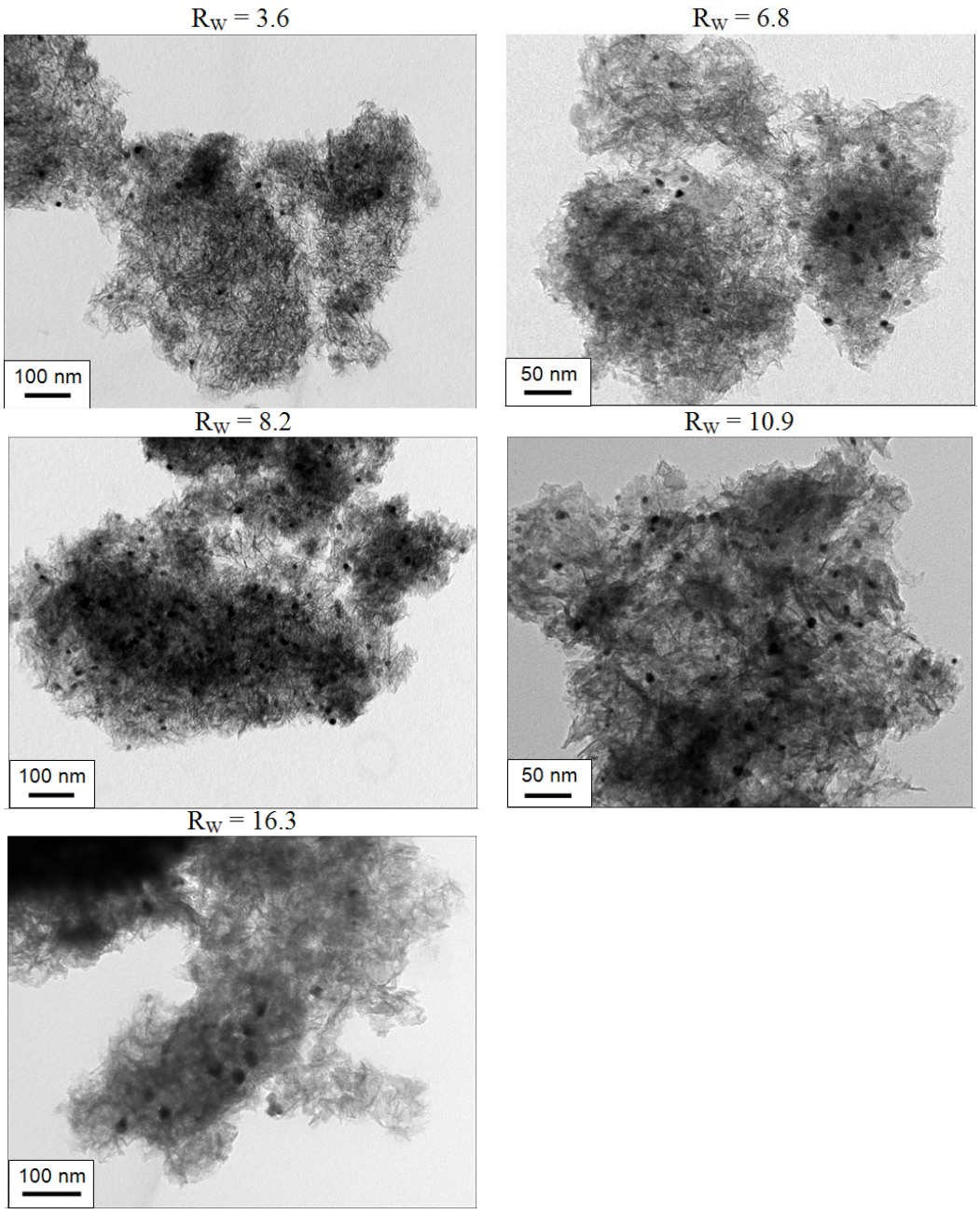

Figure 75: *Selected TEM micrographs of Pt-BHA nanocomposites formed from microemulsions having R_W ratios indicated.*

BJH analysis of nitrogen adsorption isotherm was used to evaluate the pore structure of the Pt-BHA ceramic as a function of R_W value. The resulting pore size distributions are shown in **Figure 76**. Contrary to the expected condition – increasing RW value leads to increased

primary BHA particle sizes, and thus larger pores – the pores of Pt-BHA decrease in size and volume as the R_W value of the microemulsion is increased from 3.6 to 16.4, with the most pronounced effect seen in the transition from 3.6 to 6.8 (see Figure 76). These results may indicate that a larger fraction of platinum is incorporated within the BHA framework as the R_W value is increased, resulting in a lower measured pore volume and the obstruction of larger pores. An independent evaluation of the wt% of platinum incorporated in the structure, such as inductively coupled plasma atomic emission spectroscopy (ICP-AES) would be necessary to confirm this hypothesis.

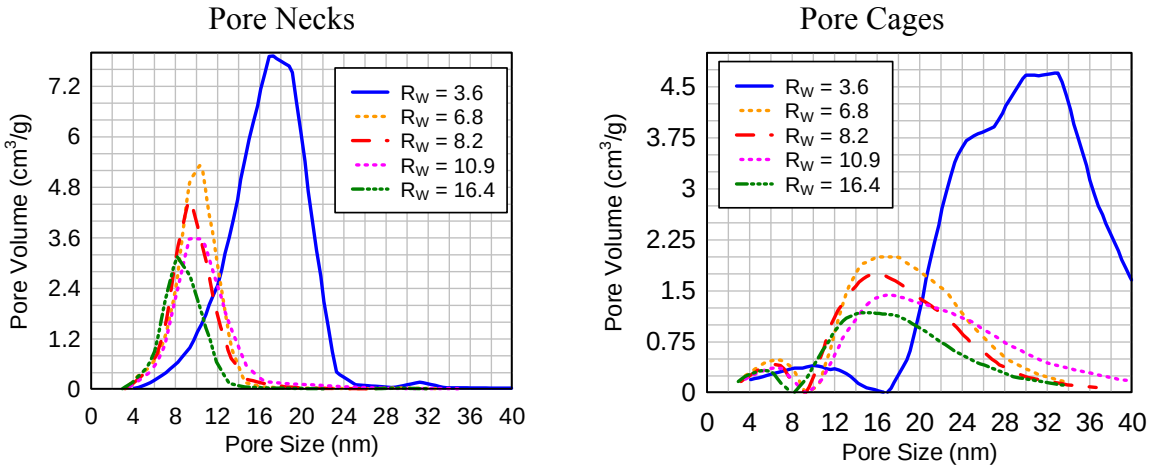

Figure 76: Pore size distributions for Pt-BHA catalysts synthesized with Lutensol XP30 at the indicated R_W values.

D.2 SURFACTANT STRUCTURE: HYDROPHILIC CHAIN LENGTH

One of the key ways to tailor the structure of the final nanocomposite is to change the properties of the surfactant. This is similar to changing the water/surfactant ratio, in that it changes the inherent properties of the microemulsion, and therefore, the final ceramic structure. With increasing hydrophilic chain length, we expect that the interior of the water micelles will be more

densely populated with surfactant chains. This may manifest itself in reduced diffusion of reactants into the micelle, so longer aging times might be necessary. Additionally, swelling of the micelle to accommodate the larger mass of surfactant is also possible. We hypothesize that the final ceramic particle size should roughly correlate with the micelle diameter, so increasing the hydrophobic-chain length should result in larger primary ceramic particles.

Three types of ethoxylated surfactants were obtained from BASF: Lutensol XP30, Lutensol XP50, and Lutensol XP70 (for structure and properties, see Appendix A). These surfactants differed only in the length of the hydrophilic ethoxy chain. A standard batch of Pt-BHA is synthesized as described in the experimental section, with one exception – the PEPP/pentanol surfactant is replaced with a molar amount of XP30/50/70 to yield an R_W of 8.4.

The BET surface area (**Figure 77**) is constant within experimental error for all three degrees of ethoxylation. The XRD data (**Figure 77**) reveal a strange behavior where the smallest particles (using Debye-Scherrer analysis) appear in the sample prepared using the intermediate chain-length XP50 surfactant. However, the TEM images indicate that the XP30 sample has the largest particles, which are roughly double (~12.5nm vs. 6.5nm) the particles formed in the XP50 and XP70 microemulsions.

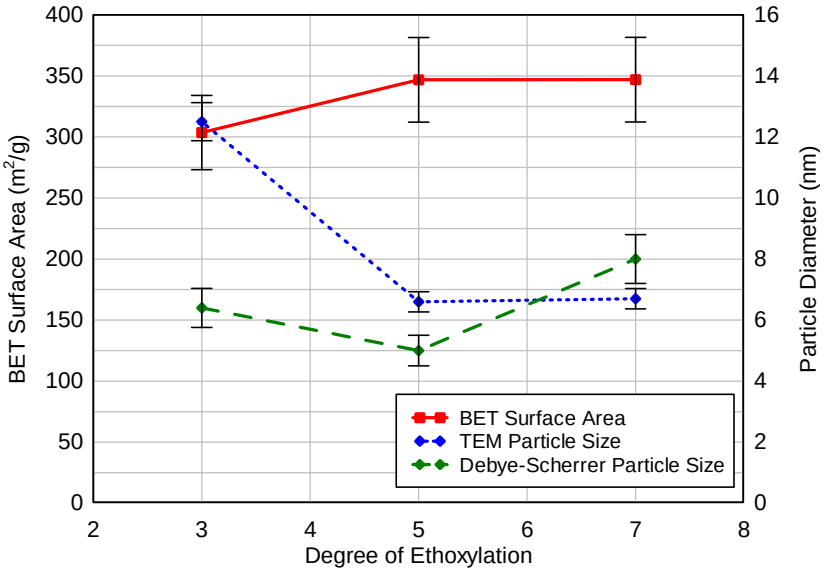

Figure 77: *BET and Debye-Scherrer data for Pt-BHA catalysts synthesized with surfactants having varying degrees of ethoxylation. Error bars indicate 10% error in BET and Debye-Scherrer, and 5% error in TEM, a rough estimate of the experimental variability of the measurements.*

The pore size distribution is determined using BJH analysis, and the results are shown in **Figure 78**. These results indicate more counter-intuitive behavior. The nanocomposite made from XP50 surfactant has larger pores than both the XP30 and XP70 samples. It is not clear why the surfactant with an intermediate degree of ethoxylation would have significantly larger pore volume than the other two surfactants tested.

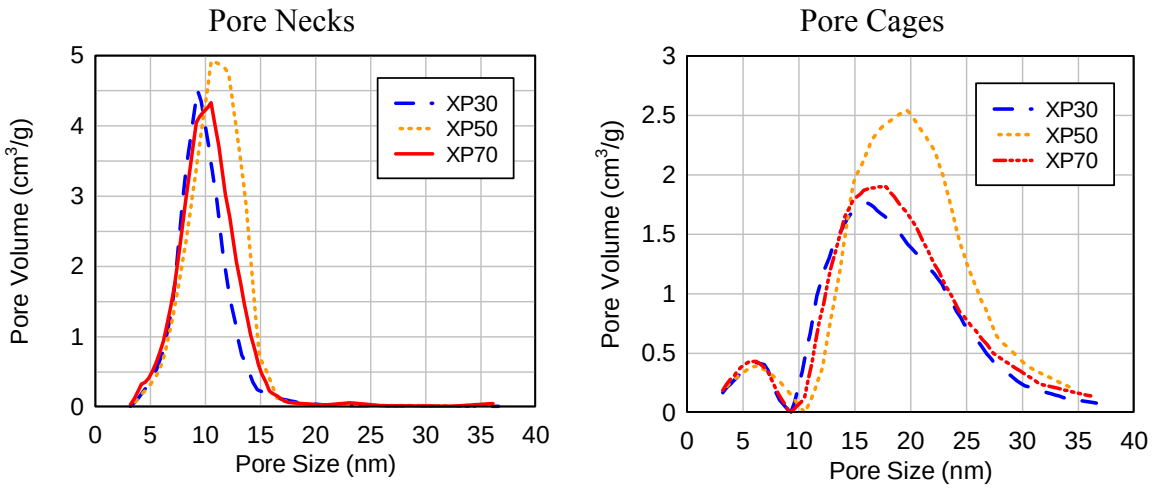

Figure 78: *Pore size distributions for Pt-BHA catalysts synthesized with surfactants having varying degrees of ethoxylation.*

TEM images of the samples that resulted from the synthesis of Pt-BHA with each of the surfactants are shown in **Figure 75**. The XP30 sample seems to have a more needle-like texture, while the XP50 and XP70 samples contains more spherically shaped clumps of ceramic particles. This behavior is clearly related to the structure of the surfactant, but it is not clear why the shorter ethoxy chains of the XP30 should lead to needle-like ceramic, and the longer ethoxy chains of the XP70 lead to spheres. Perhaps the needle-like structures result from faster diffusion kinetics through the micelle.

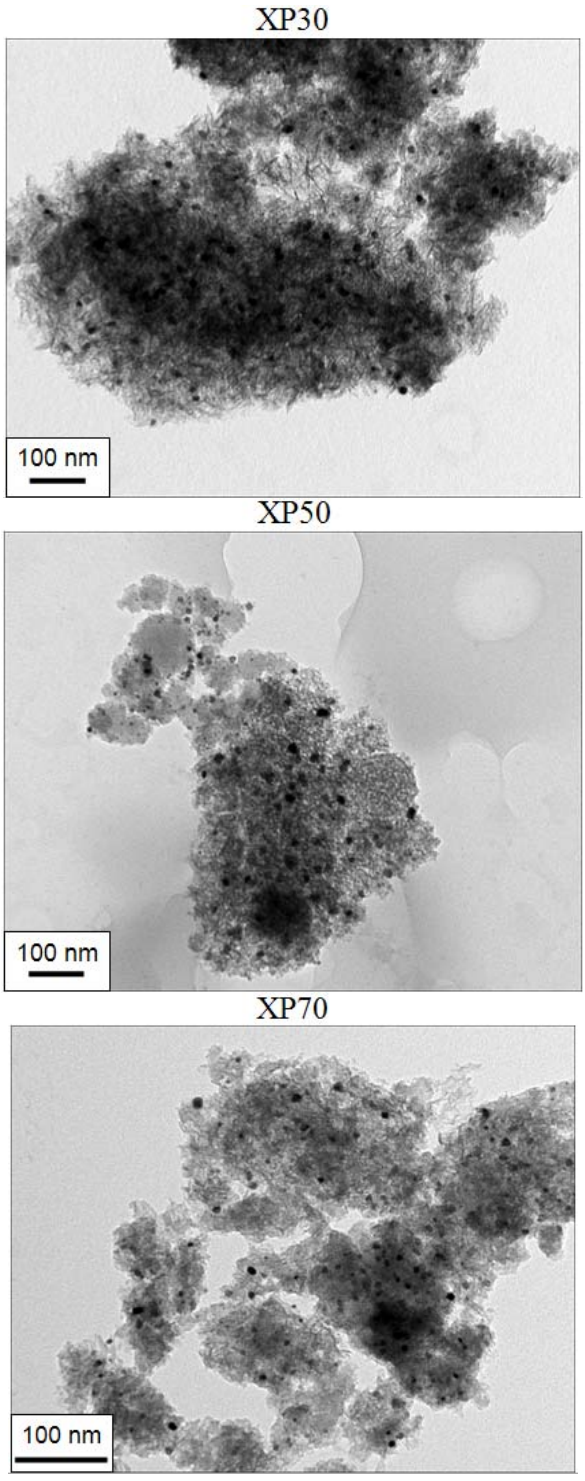

Figure 79: *Selected TEM micrographs of Pt-BHA nanocomposites formed from microemulsions using the type of surfactant indicated.*

These results indicate that more research is necessary into this parameter. A comparison of these catalysts at a lower water-to-surfactant ratio (larger surfactant concentration) might enhance the effect seen in changing the surfactant structure. Finally, other surfactant properties – hydrophobic chain length, average molecular weight, amount of branching, etc. – are worthy of future studies.

APPENDIX E

OTHER METAL-CERAMIC NANOCATALYSTS

The purpose of this section is to catalogue some of the other metal-ceramic nanomaterials that we synthesized in the course of this thesis, but were not discussed in the body text. Their synthesis and characterization is listed here as a reference point for future research in this field.

E.1 MICROEMULSION TEMPLATED

E.1.1 Au-BHA

A 10 wt% Au-BHA catalyst was synthesized by replacing H_2PtCl_6 in **Table 1** with $AuCl_3$ and following the same procedure outlined in section 3.1. A deep purple color was observed in the microemulsion after addition of the alkoxide mixture. After calcination at 600°C, the catalyst powder is dark red in color. The material is imaged with TEM (**Figure 80**). The Au particles are present in the structure, but appear to be more localized than the homogeneous distribution observed for Pt-BHA. Larger particles of gold are also prevalent, indicating that particle sintering is not fully restrained in this nanocomposite. This sample is labeled CAT105 amongst

the samples in the lab, and in the data book of catalyst synthesis (information provided for future researchers to easily locate this sample in the lab).

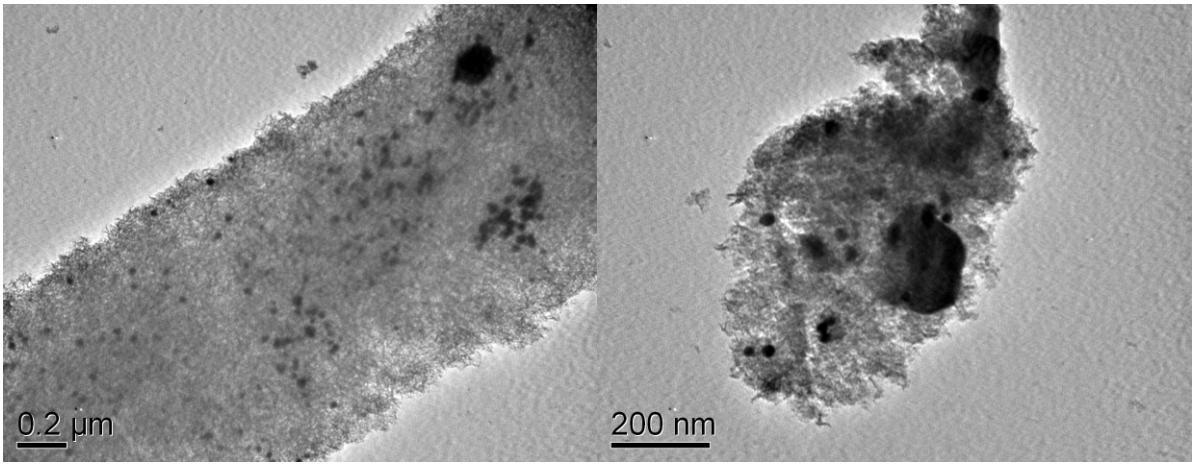

Figure 80: *TEM micrographs of Au-BHA nanocomposite after calcination/reduction at 600°C.*

E.1.2 Co-BHA

A 30 wt% Co-BHA catalyst was synthesized by replacing H_2PtCl_6 in **Table 1** with $Co(NO_3)_2$ and following the same procedure outlined in section 3.1. After oxidation at 800°C, the catalyst powder is dark blue in color, while after reduction at the same temperature the material is black. The material is imaged with TEM (**Figure 81**). The Co particles have diameter ~10nm and appear to be homogeneously distributed in the BHA. This sample is labeled Co-BHA 022806 for reference purposes.

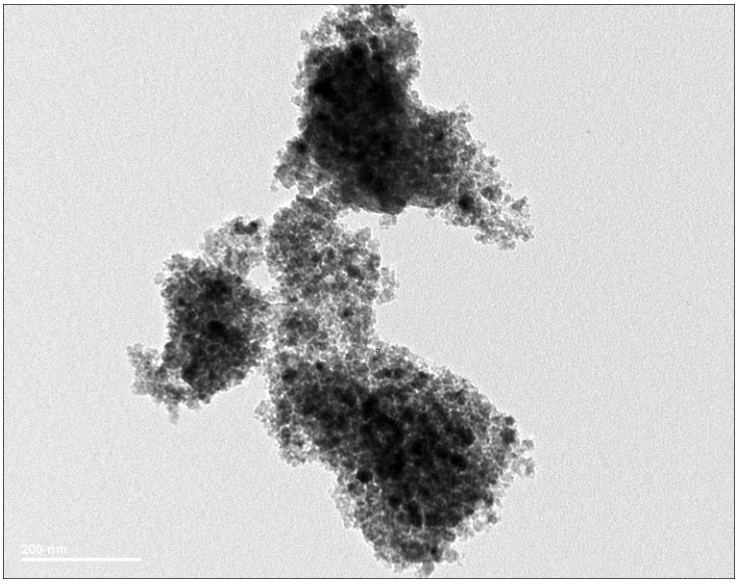

Figure 81: *TEM micrograph of Co-BHA nanocomposite after calcination/reduction at 800°C.*

E.1.3 Cu-BHA

A 50 wt% Cu-BHA catalyst was synthesized by replacing H_2PtCl_6 in **Table 1** with $Cu(NO_3)_2$ and following the same procedure outlined in section 3.1 except for one modification. Because of the large amount of $Cu(NO_3)_2$ salt added, it was necessary to increase the amount of water in the microemulsion to 16.1g in order to ensure complete salvation of the metal salt. After oxidation at 900°C, the catalyst powder is light blue in color, while after reduction at the same temperature the material is black. The material is imaged with TEM (**Figure 82**). The Cu particles are much larger in this sample; likely due to the calcination temperature being close to the melting point of copper (1083°C), but appear to be fairly well distributed throughout the BHA. This sample is labeled Cu-BHA 032806 for reference purposes.

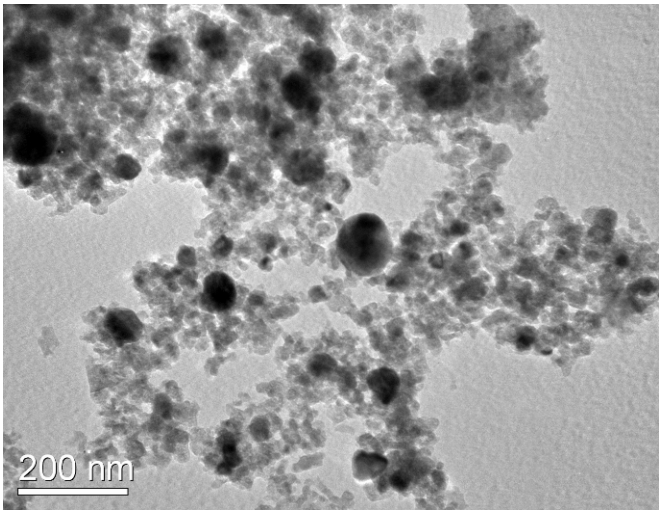

Figure 82: *TEM micrographs of Cu-BHA nanocomposite after calcination/reduction at 900°C.*

E.1.4 Fe-BHA

A 10 wt% Fe-BHA catalyst was synthesized by replacing H_2PtCl_6 in **Table 1** with $FeCl_3$ and following the same procedure outlined in section 3.1. After oxidation at 800°C, the catalyst powder is orange-red in color, while after reduction at the same temperature the material is black. The material is imaged with TEM (**Figure 83**). As one can see from the images, there is a wide distribution in the iron particle size, and they are less homogeneously distributed than for Pt-BHA. This sample is labeled Fe-BHA cat070b for reference purposes.

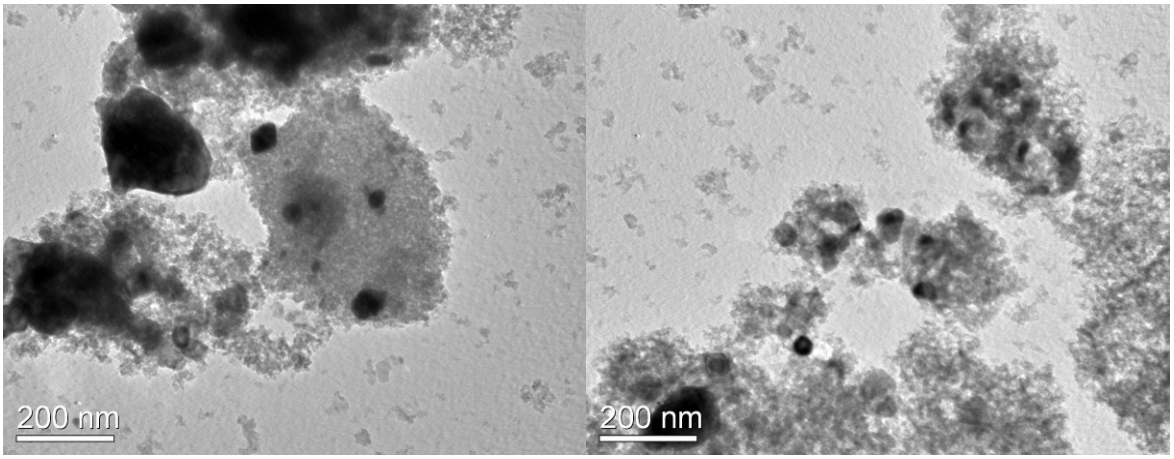

Figure 83: *TEM micrographs of Fe-BHA nanocomposite after calcination/reduction at 800°C.*

E.1.5 Pd-BHA

A 10 wt% Pd-BHA catalyst was synthesized by replacing H_2PtCl_6 in **Table 1** with $PdCl_2$ and following the same procedure outlined in section 3.1. When the microemulsion was mixed, some sediment formed and was filtered before addition of the metal alkoxides. After oxidation at 800°C, the catalyst powder is dark brown-black in color, while after reduction at the same temperature the material is black. The material is imaged with TEM (**Figure 84**). There is very little evidence of metallic Pd nanoparticles anywhere on the BHA structure. From these results, it seems likely that the sediment formed in the microemulsion was Pd rich and was therefore not incorporated into the nanocomposite because it was filtered off. Future synthesis should alter the amount of water in the microemulsion in order to accommodate the Pd-salt. This sample is labeled Cu-BHA cat069b for reference purposes.

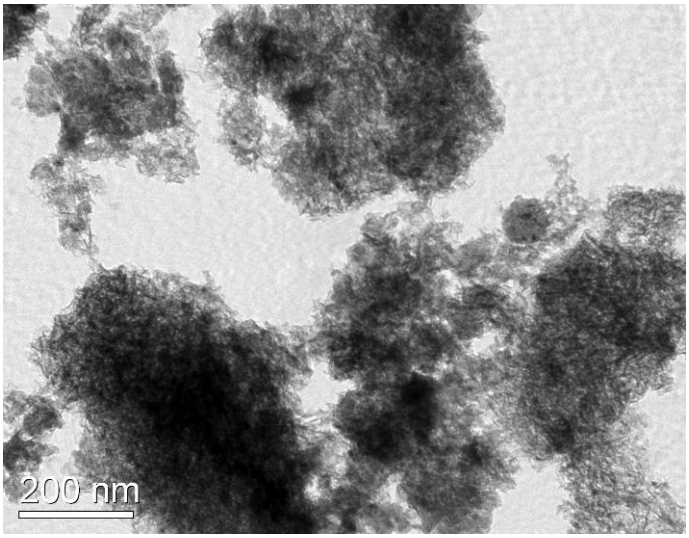

Figure 84: *TEM micrograph of Pd-BHA nanocomposite after calcination/reduction at 800°C.*

E.1.6 Zn-BHA

A 10 wt% Zn-BHA catalyst was synthesized by replacing H_2PtCl_6 in **Table 1** with $Zn(NO_3)_2$ and following the same procedure outlined in section 3.1. Zn is an interesting metal to test in this case, because of its low melting point of 419°C. Because of this we expect metal volatilization at very low temperatures and strong sintering. After calcination at 200°C, the catalyst powder is pale yellow in color, while after calcination at 600°C the material is white. The material is imaged with TEM at both temperatures with the results shown in **Figure 85**. At 200°C the Zn material is present in large particles, typically 100-200 nm in size. In some of the images, it appears like the Zn metal is "wetting" the surface of the BHA – the metal particles appear to fill and coat the surface and pores of the BHA. This is likely a result of substantial pre-melting at the calcination temperature resulting in particle sintering. After calcination at 600°C, it is clear that these materials no longer contain Zn metal – the calcination temperature is above the

melting point, and no Zn particles are detected in TEM. These samples are from both cat043 and cat051 for reference purposes.

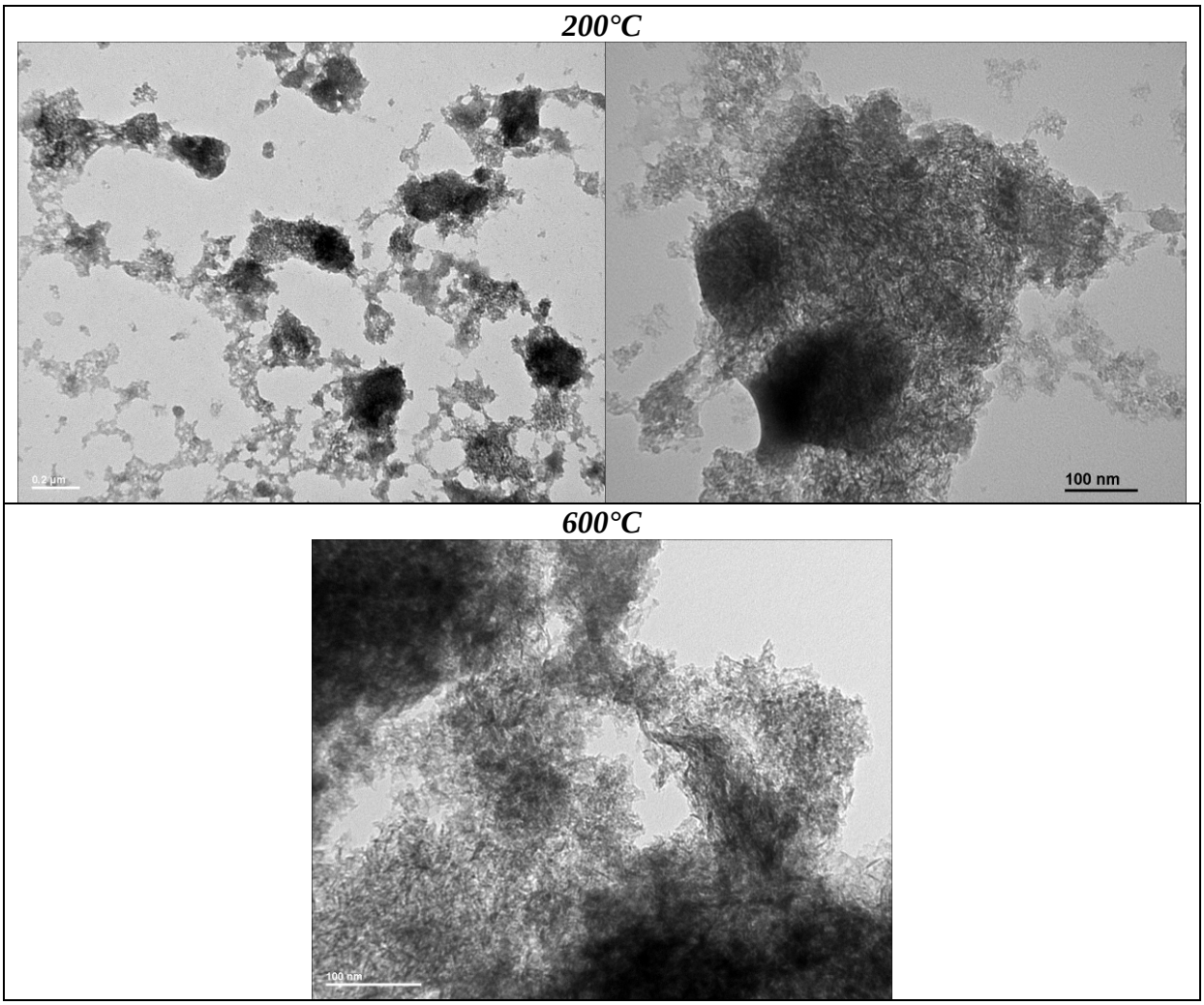

Figure 85: *TEM micrograph of Zn-BHA nanocomposite after calcination/reduction at 200 and 600°C.*

E.2 DROP COATING OF PURE BHA

In section 4.4.4 we describe the method of thermal stabilization of particles within the BHA structure – a particle caging effect due simply to the physical configuration of the BHA structure. In that section, we also demonstrate that both Pt and Ni metal nanoparticles can be stabilized, indicating to some extent the universal nature of the pore caging effect. Here, we attempt to simplify the procedure for incorporating metal nanoparticles into the BHA framework – by drop coating the pure BHA material with a variety of metal salt solutions.

In this manner, we attempt to eliminate the complications arising from the use of a microemulsion based synthesis to control the morphology of the nanocomposite. By changing the concentration and pH of the metal salt solution, as well as the manner in which the particles are introduced into the BHA framework, we obtain better control over the final material properties. Ideally, a single batch of pure nanostructured BHA would be formed and then "injected" with the appropriate metal nanoparticles. The following procedure is used for preliminary testing of this drop-coating technique:

Procedure:

1. Pre-calcine pure BHA at 700°C.
2. Determine amount of various salt solutions to yield ~20wt% loading.
3. Apply a few drops of metal salt solution to BHA (enough to wet the BHA)
4. Allow sample to dry on a hot plate ~80°C
5. Repeat steps 3 and 4
6. Calcine samples for 5h in air @ 700°C, reduce for 1h in H2.
7. Take TEM images.

The following salts are used for preparing the 10 wt% metal salt solutions (pH of the solution listed in parenthesis): $Pd(NO_3)_2$ (0.42), H_2Cl_6Pt (0.60), $FeCl_3$ (1.05), $Cu(NO_3)_2$ (3.16), and $Ni(NO_3)_2$ (4.60). TEM images of the resulting materials are shown in **Figure 86**.

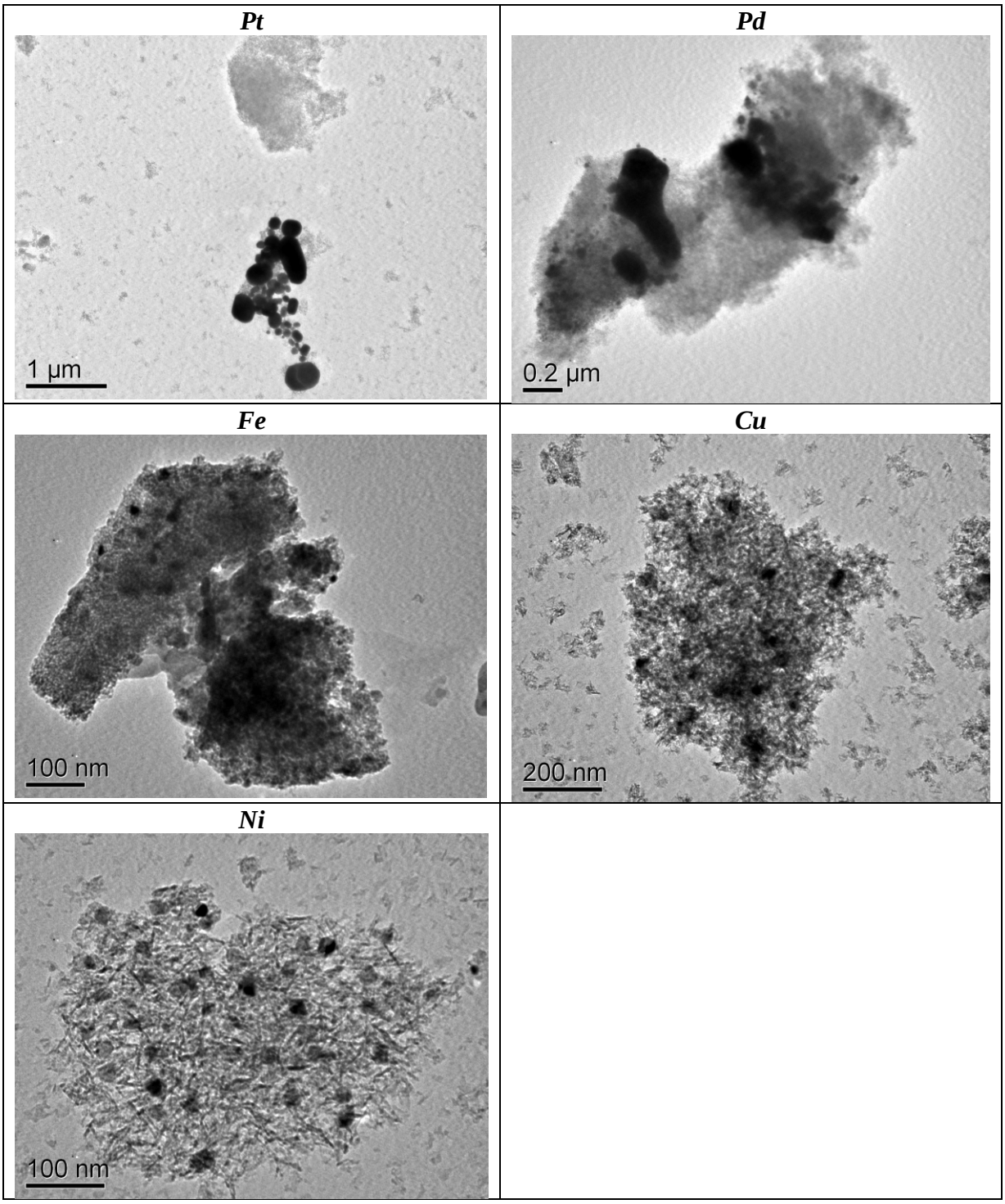

Figure 86: *TEM micrograph of drop-coated nanocomposite catalysts after calcination/reduction at 700°C.*

We observe from the TEM images that both Pt and Pd drop-coated BHA (top row of **Figure 86**) have very poor dispersion of the metal – the particles are not nano-sized and they are very inhomogeneously distributed. However, the Fe, Cu, and Ni drop-coated BHA (bottom 2 rows) show very similar characteristics to the previously obtained materials synthesized directly in the microemulsion. Nanoparticles of each of the metals are observed to be well dispersed, with particle sizes typically around 10-20 nm.

This technique is promising for future investigations. The pH of the solutions is one particularly interesting factor. Both of the failed drop coating experiments had pH values lower than 1, while the successful experiments had pH of 1.05 and higher. An investigation of drop coating with different metals with pH held constant would be useful for determining the effect of this parameter. Additionally, the concentration of the metal salt solution might have an influence on the morphology or dispersion of the metal nanoparticles, so it is worthy of future investigation. Finally, the technique used for drop coating could be improved. When simply dropping the solution onto the dried BHA, often times slightly more than is needed to wet the material is added, thus resulting in metal salt drying outside of the pore structure. This is not ideal. One suggestion to improve on this procedure involves placing the dried BHA in a basket which could be dipped and removed from the metal salt solution. In this way, the BHA could be saturated with solution and extraneous drying would be virtually eliminated.

BIBLIOGRAPHY

[1] Zittel, W. and J. Schindler, *Crude Oil: The Supply Outlook*. 2007, Energy Watch Group.

[2] Koppelaar, R., *World Production and Peaking Outlook*. 2006, Peak Oil Netherlands.

[3] Bernstein, L., et al., *Fourth Assessment Report, Climate Change 2007: Synthesis Report*. 2007, Intergovernmental Panel on Climate Change.

[4] Anastas, P. and J. Warner, *Green Chemistry, Theory and Practice*. 1998, Oxford: Oxford University Press.

[5] Haruta, M., et al., *Gold catalysts prepared by coprecipitation for low-temperature oxidation of hydrogen and of carbon monoxide.* Journal of Catalysis, 1989. **115**(2): p. 301-309.

[6] Valden, M., X. Lai, and D.W. Goodman, *Onset of catalytic activity of gold clusters on titania with the appearance of nonmetallic properties.* Science, 1998. **281**(5383): p. 1647-1650.

[7] Bell, A.T., *The impact of nanoscience on heterogeneous catalysis.* Science, 2003. **299**(5613): p. 1688-1691.

[8] Arenz, M., et al., *The effect of the particle size on the kinetics of CO electrooxidation on high surface area Pt catalysts.* Journal of the American Chemical Society, 2005. **127**(18): p. 6819-6829.

[9] Wang, Z.L., T.S. Ahmad, and M.A. El-Sayed, *Steps, ledges and kinks on the surfaces of platinum nanoparticles of different shapes.* Surface Science, 1997. **380**(2-3): p. 302-310.

[10] Kirchhoff, M., *Synthesis and Characterization of Novel High-Temperature Stable Nanocomposite Catalysts.*, in *NSTI Nanotechnology 2004*. 2004: Boston.

[11] Kirchhoff, M., U. Specht, and G. Veser, *Microemulsion-templated Synthesis of Highly Active High-Temperature Stable Partial Oxidation Catalysts*, in *Solid State Ionics 2002*, P. Knauth, Editor. 2002, MRS Publishing.

[12] Kirchhoff, M., U. Specht, and G. Veser, *Novel Sol-Gel Derived Catalyst Systems for High-Temperature Partial Oxidation of Methane*, in *Innovation in the Manufacture and Use of Hydrogen*, G. Emig, Editor. 2003, DGMK Publishing: Hamburg.

[13] Kirchhoff, M., U. Specht, and G. Veser, *Engineering high-temperature stable nanocomposite materials.* Nanotechnology, 2005. **16**(7): p. S401-S408.

[14] Schicks, J., et al., *Nanoengineered catalysts for high-temperature methane partial oxidation.* Catalysis Today, 2003. **81**(2): p. 287-296.

[15] *Department of Energy EIA - World supply and consumption*. 2006 [cited; Available from: http://www.eia.doe.gov/emeu/international/contents.html.

[16] Logothetidis, S., *Nanotechnology in medicine: The medicine of tomorrow and nanomedicine.* Hippokratia, 2006. **10**(1): p. 7-21.

[17] Rittner, M.N., *Market analysis of nanostructured materials.* American Ceramic Society Bulletin, 2002. **81**(3): p. 33-36.

[18] Kruis, F.E., H. Fissan, and A. Peled, *Synthesis of nanoparticles in the gas phase for electronic, optical and magnetic applications - A review.* Journal of Aerosol Science, 1998. **29**(5-6): p. 511-535.

[19] Ichinose, N., Y. Ozaki, and S. Kashu, *Superfine Particle Technology*. 1992, Berlin: Springer Verlag.

[20] Klabunde, K.J., *Nanoscale Materials Chemistry*. 2001, New York: Wiley-Interscience.

[21] Vollath, D. and D.V. Szabo, *Coated nanoparticles: A new way to improved nanocomposites.* Journal of Nanoparticle Research, 1999. **1**(2): p. 235-242.

[22] Cao, G., *Nanostructures and Nanomaterials: Synthesis, Properties and Applications*. 2004, London, UK: Imperial College Press. 448.

[23] Tseng, A.A., A. Notargiacomo, and T.P. Chen, *Nanofabrication by scanning probe microscope lithography: A review.* Journal of Vacuum Science and Technology B: Microelectronics and Nanometer Structures, 2005. **23**(3): p. 877-894.

[24] Makino, T., et al., *Size classification of Si nanoparticles formed by Pulsed Laser Ablation in helium background gas.* Applied Physics A: Materials Science and Processing, 1999. **69**(7).

[25] Caswell, K.K., C.M. Bender, and C.J. Murphy, *Seedless, surfactantless wet chemical synthesis of silver nanowires.* Nano Letters, 2003. **3**(5): p. 667-669.

[26] Zhang, J.-R., D. Gu, and Y.-X. Yang, *Wet-chemical synthesis of ATO nanoparticle.* Gongneng Cailiao/Journal of Functional Materials, 2002. **33**(3): p. 300-302.

[27] Pratsinis, S.E., *Flame aerosol synthesis of ceramic powders.* Progress in Energy and Combustion Science, 1998. **24**(3): p. 197-219.

[28] Stark, W.J., et al., *Flame aerosol synthesis of vanadia-titania nanoparticles: Structural and catalytic properties in the selective catalytic reduction of NO by NH3.* Journal of Catalysis, 2001. **197**(1): p. 182-191.

[29] Schuth, F., *Non-siliceous mesostructured and mesoporous materials.* Chemistry of Materials, 2001. **13**(10): p. 3184-3195.

[30] Schuth, F., *Superstructures of mesoporous silicas.* Current Opinion in Colloid and Interface Science, 1998. **3**(2): p. 174-180.

[31] Linden, M., et al., *Recent Advances in Nano- and Macroscale Control of Hexagonal, Mesoporous Materials.* Journal of Porous Materials, 1998. **5**(3-4): p. 177-193.

[32] Ciesla, U. and F. Schuth, *Ordered mesoporous materials.* Microporous and Mesoporous Materials, 1999. **27**(2-3): p. 131-149.

[33] Kresge, C.T., et al., *Ordered mesoporous molecular sieves synthesized by a liquid-crystal template mechanism.* Nature, 1992. **359**(6397): p. 710-712.

[34] Beck, J.S., et al., *A new family of mesoporous molecular sieves prepared with liquid crystal templates.* Journal of the American Chemical Society, 1992. **114**(27): p. 10834-10843.

[35] Nguyen, S.V., et al., *Mesoporous silica supported LaCoO3 perovskites as catalysts for methane oxidation.* Microporous and Mesoporous Materials, 2002. **54**(1-2): p. 51-61.

[36] Zarur, A.J., H.H. Hwu, and J.Y. Ying, *Reverse Microemulsion-Mediated Synthesis and Structural Evolution of Barium Hexaaluminate Nanoparticles.* Langmuir, 2000. **16**(7): p. 3042-3049.

[37] Zarur, A.J., et al., *Phase Behavior, Structure, and Applications of Reverse Microemulsions Stabilized by Nonionic Surfactants.* Langmuir, 2000. **16**(24): p. 9168-9176.

[38] Zarur, A.J. and J.Y. Ying, *Reverse microemulsion synthesis of nanostructured complex oxides for catalytic combustion.* Nature, 2000. **403**(6765): p. 65-67.

[39] Hanaoka, T., et al., *Control of the rhodium particle size of the silica-supported catalysts by using microemulsion.* Applied Catalysis A: General, 2000. **190**(1-2): p. 291-296.

[40] Eriksson, S., et al., *Preparation of catalysts from microemulsions and their applications in heterogeneous catalysis.* Applied Catalysis A: General, 2004. **265**(2): p. 207-219.

[41] Tanori, J. and M.P. Pileni, *Control of the shape of copper metallic particles by using a colloidal system as template.* Langmuir, 1997. **13**(4): p. 639-646.

[42] Pileni, M.P., *Nanosized particles made in colloidal assemblies.* Langmuir, 1997. **13**(13): p. 3266-3276.

[43] Li, T., et al., *Preparation of Ag/SiO2 nanosize composites by a reverse micelle and sol-gel technique.* Langmuir, 1999. **15**(13): p. 4328-4334.

[44] Ikeda, M., et al., *Preparation of size-controlled Pt catalysts supported on alumina.* Catalysis Letters, 1999. **58**(4): p. 195-197.

[45] Abarkan, I., T. Doussineau, and M. Smaihi, *Tailored macro/micro structural properties of colloidal silica nanoparticles via microemulsion preparation.* Polyhedron, 2006. **25**(8): p. 1763-1770.

[46] Chattopadhyay, P. and R.B. Gupta, *Supercritical CO2-based formation of silica nanoparticles using water-in-oil microemulsions.* Industrial & Engineering Chemistry Research, 2003. **42**(3): p. 465-472.

[47] Kosak, A., et al., *In situ synthesis of magnetic MnZn-ferrite nanoparticles using reverse microemulsions.* Journal of Magnetism and Magnetic Materials, 2004. **272-276**: p. 1542-1544.

[48] Lee, M.-H., S.-G. Oh, and S.-C. Yi, *Preparation of Eu-doped Y2O3 luminescent nanoparticles in nonionic reverse microemulsions.* Journal of Colloid and Interface Science, 2000. **226**(1): p. 65-70.

[49] Sun, Y.-P., P. Atorngitjawat, and M.J. Meziani, *Preparation of silver nanoparticles via rapid expansion of water in carbon dioxide microemulsion into reductant solution.* Langmuir, 2001. **17**(19): p. 5707-5710.

[50] Ji, M., et al., *Synthesizing and dispersing silver nanoparticles in a water-in- supercritical carbon dioxide microemulsion.* Journal of the American Chemical Society, 1999. **121**(11): p. 2631-2632.

[51] Fricke, J. and T. Tillotson, *Aerogels: Production, characterization, and applications.* Thin Solid Films, 1997. **297**(1-2): p. 212-223.

[52] Husing, N. and U. Schubert, *Aerogels - Airy Materials: Chemistry, Structure, and Properties.* Angewandte Chemie - International Edition, 1998. **37**(1-2): p. 22-45.

[53] Ward, D.A. and E.I. Ko, *Preparing Catalytic Materials by the Sol-Gel Method.* Ind. Eng. Chem. Res., 1995. **34**(2): p. 421-433.

[54] Kistler, S.S., *Coherent Expanded Aerogels and Jellies.* Nature, 1931. **127**(3211): p. 741.

[55] Lopez, T., et al., *Improved mechanical stability of supported ru catalysts: Preparation by the sol-gel method.* Journal of Catalysis, 1992. **136**(2): p. 621-625.

[56] Azomoza, M., et al., *Synthesis of high surface area supported Pt/SiO2 catalysts from H2PtCl6·6H2O by the sol-gel method.* Catalysis Today, 1992. **15**(3-4): p. 547-554.

[57] Paul, B.K. and S.P. Moulik, *Microemulsions: An overview.* Journal of Dispersion Science and Technology, 1997. **18**(4): p. 301-367.

[58] Ingert, D. and M.-P. Pileni, *Limitations in producing nanocrystals using reverse micelles as nanoreactors.* Advanced Funtional Materials, 2001. **11**(2): p. 136-139.

[59] Boutonnet, M., et al., *PREPARATION OF MONODISPERSE COLLOIDAL METAL PARTICLES FROM MICROEMULSIONS.* Colloids and Surfaces, 1982. **5**(3): p. 209-225.

[60] Boutonnet, M., et al., *Novel method of catalyst preparation for selective hydrogenation of unsaturated aldehydes.* Applied Catalysis A: General, 1996. **135**(1).

[61] Ojeda, M., et al., *Synthesis of Rh nano-particles by the microemulsion technology particle size effect on the CO + H2 reaction.* Applied Catalysis A: General, 2004. **274**(1-2): p. 33-41.

[62] Kishida, M., et al., *Hydrogenation of carbon dioxide over metal catalysts prepared using microemulsion.* Catalysis Today, 1996. **29**(1-4 SPEC. ISS.): p. 355-359.

[63] Kishida, M., et al., *Novel preparation of metal-supported catalysts by colloidal microparticles in a water-in-oil microemulsion; catalytic hydrogenation of carbon dioxide.* Chem. Commun., 1995. **7**: p. 763-765.

[64] Persson, K., et al., *Preparation of alumina-supported palladium catalysts for complete oxidation of methane.* Applied Catalysis A: General, 2003. **249**(1): p. 165-174.

[65] You, Z., I. Balint, and K.-I. Aika, *Catalytic combustion of methane over microemulsion-derived MnO x-Cs2O-Al2O3 nanocomposites.* Applied Catalysis B: Environmental, 2004. **53**(4): p. 233-244.

[66] Rymes, J., et al., *Microemulsions in the preparation of highly active combustion catalysts.* Catalysis Today, 2002. **75**(1-4): p. 297-303.

[67] Escudero, M.J., et al., *Development and performance characterisation of new electrocatalysts for PEMFC.* Journal of Power Sources, 2002. **106**(1-2): p. 206-214.

[68] Liu, Z., et al., *Synthesis and characterization of PtRu/C catalysts from microemulsions and emulsions.* Journal of Materials Chemistry, 2002. **12**(8): p. 2453-2458.

[69] Ikeda, M., et al., *Thermal stability of Pt particles of Pt/Al2O3 catalysts prepared using microemulsion and catalytic activity in NO-CO reaction.* Catalysis Communications, 2001. **2**(8): p. 261-267.

[70] Bonnemann, H., et al., *Nanoscale colloidal metals and alloys stabilized by solvents and surfactants Preparation and use as catalyst precursors.* Journal of Organometallic Chemistry, 1996. **520**(1-2): p. 143-162.

[71] Dick, K., et al., *Size-Dependent Melting of Silica-Encapsulated Gold Nanoparticles.* J. Am. Chem. Soc., 2002. **124**(10): p. 2312-2317.

[72] Cassiers, K., et al., *A detailed study of thermal, hydrothermal, and mechanical stabilities of a wide range of surfactant assembled mesoporous silicas.* Chemistry of Materials, 2002. **14**(5): p. 2317-2324.

[73] Liu, Y. and T.J. Pinnavaia, *Aluminosilicate nanoparticles for catalytic hydrocarbon cracking.* Journal of the American Chemical Society, 2003. **125**(9): p. 2376-2377.

[74] Liu, Y., W. Zhang, and T.J. Pinnavaia, *Steam-stable aluminosilicate mesostructures assembled from zeolite type Y seeds [8].* Journal of the American Chemical Society, 2000. **122**(36): p. 8791-8792.

[75] Liu, Y., W. Zhang, and T.J. Pinnavaia, *Steam-Stable MSU-S Aluminosilicate Mesostructures Assembled from Zeolite ZSM-5 and Zeolite Beta Seeds.* Angewandte Chemie - International Edition, 2001. **40**: p. 1255-1258.

[76] Bartholomew, C.H., *Mechanisms of catalyst deactivation.* Applied Catalysis A: General, 2001. **212**(1-2): p. 17-60.

[77] Pawlow, P.Z., Phys. Chem., 1909. **65**: p. 545.

[78] Borel, J.-P., *Thermodynamical size effect and the structure of metallic clusters.* Surface Science, 1981. **106**: p. 1.

[79] Nanda, K.K., et al., *Higher Surface Energy of Free Nanoparticles.* Physical Review Letters, 2003. **91**(10): p. 1061021-1061024.

[80] Campbell, C.T., S.C. Parker, and D.E. Starr, *The effect of size-dependent nanoparticle energetics on catalyst sintering.* Science, 2002. **298**(5594): p. 811-814.

[81] Corma A., et al., *Hydrocracking of Vacuum Gasoil on the Novel Mesoporous MCM-41 Aluminosilicate Catalyst.* Journal of Catalysis, 1995. **153**(1): p. 25-31.

[82] Schuth, F., A. Wingen, and J. Sauer, *Oxide loaded ordered mesoporous oxides for catalytic applications.* Microporous and Mesoporous Materials, 2001. **44-45**: p. 465-476.

[83] Zhu, J., et al., *Encapsulation of metal (Au, Ag, Pt) nanoparticles into the mesoporous SBA-15 structure.* Langmuir, 2003. **19**(10): p. 4396-4401.

[84] Kónya, Z., et al., *Nanocrystal Templating of Silica Mesopores with Tunable Pore Sizes.* Nano Letters, 2002. **2**(8): p. 907-910.

[85] Kónya, Z., et al., *Synthetic Insertion of Gold Nanoparticles into Mesoporous Silica.* Chem. Mater., 2003. **15**(6): p. 1242-1248.

[86] Eguchi, K. and H. Arai, *Recent advances in high temperature catalytic combustion.* Catalysis Today, 1996. **29**(1-4): p. 379-386.

[87] Coppens, M.-O., J. Sun, and T. Maschmeyer, *Synthesis of hierarchical porous silicas with a controlled pore size distribution at various length scales.* Catalysis Today, 2001. **69**(1-4): p. 331-335.

[88] Wender, I., *Reactions of synthesis gas.* Fuel Processing Technology, 1996. **48**(3): p. 189-297.

[89] Hickman, D.A. and L.D. Schmidt, *Production of syngas by direct catalytic oxidation of methane.* Science, 1993. **259**(5093): p. 343-346.

[90] Bharadwaj, S.S. and L.D. Schmidt, *Catalytic Partial Oxidation of Natural-Gas to Syngas.* Fuel Processing Technology, 1995. **42**(2-3): p. 109-127.

[91] Liu, T. and G. Veser. *Temperature dynamics during catalytic partial oxidation of methane in a reverse-flow reactor*. in *ACS Division of Fuel Chemistry, Preprints*. 2005. San Diego, CA.

[92] Neumann, D., M. Kirchhoff, and G. Veser, *Towards an efficient process for small-scale, decentralized conversion of methane to synthesis gas: combined reactor engineering and catalyst synthesis.* Catalysis Today, 2004. **98**(4): p. 565-574.

[93] Neumann, D. and G. Veser, *Catalytic partial oxidation of methane in a high-temperature reverse-flow reactor.* AIChE Journal, 2005. **51**(1): p. 210-223.

[94] Veser, G., J. Frauhammer, and U. Friedle, *Syngas formation by direct oxidation of methane. Reaction mechanisms and new reactor concepts.* Catalysis Today, 2000. **61**(1): p. 55-64.

[95] Newsome, D.S., *WATER-GAS SHIFT REACTION.* Catalysis reviews Softcover ed., 1980. **21**(2): p. 275-281.

[96] Li, Y., Q. Fu, and M. Flytzani-Stephanopoulos, *Low-temperature water-gas shift reaction over Cu- and Ni-loaded cerium oxide catalysts.* Applied Catalysis B: Environmental, 2000. **27**(3): p. 179-191.

[97] Qi, X. and M. Flytzani-Stephanopoulos, *Activity and stability of Cu-CeO2 catalysts in high-temperature water-gas shift for fuel-cell applications.* Industrial and Engineering Chemistry Research, 2004. **43**(12): p. 3055-3062.

[98] Wang, X., et al., *In situ studies of the active sites for the water gas shift reaction over Cu-CeO2 catalysts: Complex interaction between metallic copper and oxygen vacancies of ceria.* Journal of Physical Chemistry B, 2006. **110**(1): p. 428-434.

[99] Wen, W., et al., *In situ time-resolved characterization of novel Cu-MoO2 catalysts during the water-gas shift reaction.* Catalysis Letters, 2007. **113**(1-2): p. 1-6.

[100] Jacobs, G., et al., *Water-gas shift: Comparative screening of metal promoters for metal/ceria systems and role of the metal.* Applied Catalysis A: General, 2004. **258**(2): p. 203-214.

[101] Deng, W., et al., *Low-content gold-ceria catalysts for the water-gas shift and preferential CO oxidation reactions.* Applied Catalysis A: General, 2005. **291**(1-2): p. 126-135.

[102] Fu, Q., et al., *Activity and stability of low-content gold-cerium oxide catalysts for the water-gas shift reaction.* Applied Catalysis B: Environmental, 2005. **56**(1-2 SPEC. ISS.): p. 57-68.

[103] Wang, X., et al., *In situ time-resolved characterization of Au-Ce O2 and Au O x -Ce O2 catalysts during the water-gas shift reaction: Presence of Au and O vacancies in the active phase.* Journal of Chemical Physics, 2005. **123**(22): p. 1-5.

[104] Kim, C.H. and L.T. Thompson, *On the importance of nanocrystalline gold for Au/CeO2 water-gas shift catalysts.* Journal of Catalysis, 2006. **244**(2): p. 248-250.

[105] Jacobs, G., et al., *Low temperature water-gas shift: Examining the efficiency of Au as a promoter for ceria-based catalysts prepared by CVD of a Au precursor.* Applied Catalysis A: General, 2005. **292**(1-2): p. 229-243.

[106] Jacobs, G., et al., *Water-gas shift: In situ spectroscopic studies of noble metal promoted ceria catalysts for CO removal in fuel cell reformers and mechanistic implications.* Applied Catalysis A: General, 2004. **262**(2): p. 177-187.

[107] Jacobs, G., et al., *Low temperature water-gas shift: In situ DRIFTS-reaction study of ceria surface area on the evolution of formates on Pt/CeO2 fuel processing catalysts for fuel cell applications.* Applied Catalysis A: General, 2003. **252**(1): p. 107-118.

[108] Jacobs, G., et al., *Low temperature water-gas shift: Kinetic isotope effect observed for decomposition of surface formates for Pt/ceria catalysts.* Applied Catalysis A: General, 2004. **269**(1-2): p. 63-73.

[109] Jacobs, G., et al., *Water-gas shift catalysis: Kinetic isotope effect identifies surface formates in rate limiting step for Pt/ceria catalysts.* Applied Catalysis A: General, 2004. **268**(1-2): p. 255-266.

[110] Jacobs, G., et al., *Low temperature water gas shift: Type and loading of metal impacts forward decomposition of pseudo-stabilized formate over metal/ceria catalysts.* Catalysis Today, 2005. **106**(1-4): p. 259-264.

[111] Jacobs, G., et al., *Low-temperature water-gas shift: Impact of Pt promoter loading on the partial reduction of ceria and consequences for catalyst design.* Journal of Catalysis, 2005. **229**(2): p. 499-512.

[112] Ricote, S., et al., *Low temperature water-gas shift: Characterization and testing of binary mixed oxides of ceria and zirconia promoted with Pt.* Applied Catalysis A: General, 2006. **303**(1): p. 35-47.

[113] Jacobs, G., et al., *Low temperature water-gas shift: Comparison of thoria and ceria catalysts.* Applied Catalysis A: General, 2004. **267**(1-2): p. 27-33.

[114] Deng, W. and M. Flytzani-Stephanopoulos, *On the issue of the deactivation of Au-ceria and Pt-ceria water-gas shift catalysts in practical fuel-cell applications.* Angewandte Chemie - International Edition, 2006. **45**(14): p. 2285-2289.

[115] Liu, P. and J.A. Rodriguez, *Water-gas-shift reaction on metal nanoparticles and surfaces.* Journal of Chemical Physics, 2007. **126**(16).

[116] Liu, P. and J.A. Rodriguez, *Water-gas-shift reaction on molybdenum carbide surfaces: Essential role of the oxycarbide.* Journal of Physical Chemistry B, 2006. **110**(39): p. 19418-19425.

[117] Pfefferle, W.C., *CATALYTIC COMBUSTOR: AN APPROACH TO CLEANER COMBUSTION.* J Energy, 1978. **2**(3): p. 142-146.

[118] McCarty, J.G., et al., *Stability of supported metal and supported metal oxide combustion catalysts.* Catalysis Today, 1999. **47**(1-4): p. 5-17.

[119] Machida, M., K. Eguchi, and H. Arai, *Effect of structural modification on the catalytic property of Mn-substituted hexaaluminates.* Journal of Catalysis, 1990. **123**(2): p. 477-485.

[120] Machida, M., K. Eguchi, and H. Arai, *Catalytic properties of BaMAl11O19-[alpha] (M = Cr, Mn, Fe, Co, and Ni) for high-temperature catalytic combustion.* Journal of Catalysis, 1989. **120**(2): p. 377-386.

[121] Dalla Betta, R.A., *Catalytic combustion gas turbine systems: The preferred technology for low emissions electric power production and co-generation.* Catalysis Today, 1997. **35**(1-2): p. 129-135.

[122] Arai, H. and M. Machida, *Recent progress in high-temperature catalytic combustion.* Catalysis Today, 1991. **10**(1): p. 81-94.

[123] Eguchi, K. and H. Arai, *Low temperature oxidation of methane over Pd-based catalysts - Effect of support oxide on the combustion activity.* Applied Catalysis A: General, 2001. **222**(1-2): p. 359-367.

[124] Widjaja, H., et al., *Oxidation of methane over Pd/mixed oxides for catalytic combustion.* Catalysis Today, 1999. **47**(1-4): p. 95-101.

[125] Widjaja, H., et al., *Oxidation of methane over Pd-supported catalysts.* Catalysis Today, 1997. **35**(1-2): p. 197-202.

[126] McCarty, J.G., *Kinetics of PdO combustion catalysis.* Catalysis Today, 1995. **26**(3-4): p. 283-293.

[127] Winsor, P.A., Trans. Faraday Soc., 1948. **44**.

[128] Paul, B.K. and S.P. Moulik, *MICROEMULSIONS: AN OVERVIEW.* Journal of Dispersion Science and Technology, 1997. **18**(4): p. 301 - 367.

[129] Rasband, W. *ImageJ Software http://rsb.info.nih.gov/ij/.* 2005 [cited 2005; Available from: http://rsb.info.nih.gov/ij/.

[130] Goworek, J., A. Kierys, and R. Kusak, *Isothermal template removal from MCM-41 in hydrogen flow.* Microporous and Mesoporous Materials, 2007. **98**(1-3): p. 242-248.

[131] Sinfelt, J.H., in *Advances in Catalysis*, D.D. ELEY, H. PINES, and P.B. WEISZ, Editors. 1973, Academic Press.

[132] Wootsch, A. and Z. Paal, *Reactions of n-Hexane on Pt Catalysts: Reaction Mechanism as Revealed by Hydrogen Pressure and Compensation Effect.* Journal of Catalysis, 2002. **205**(1): p. 86-96.

[133] Wanke, S.E. and P.C. Flynn, *SINTERING OF SUPPORTED METAL CATALYSTS.* Catal Rev, 1975. **12**: p. 93-135.

[134] Mercera, P.D.L., et al., *Zirconia as a support for catalysts. Evolution of the texture and structure on calcination in air.* Applied catalysis, 1990. **57**(1): p. 127-148.

[135] Mercera, P.D.L., et al., *Stabilized tetragonal zirconium oxide as a support for catalysts. Evolution of the texture and structure on calcination in static air.* Applied catalysis, 1991. **78**(1): p. 79-96.

[136] Parmaliana, A., et al., *Temperature-programmed reduction study of NiO-MgO interactions in magnesia-supported Ni catalysts and NiO-MgO physical mixture.* Journal of the Chemical Society, Faraday Transactions, 1990. **86**(14): p. 2663-2669.

[137] Sen, F. and G. Gokagac, *Different sized platinum nanoparticles supported on carbon: An XPS study on these methanol oxidation catalysts.* Journal of Physical Chemistry C, 2007. **111**(15): p. 5715-5720.

[138] Xue, B., et al., *Growth of Pd, Pt, Ag and Au nanoparticles on carbon nanotubes.* Journal of Materials Chemistry, 2001. **11**(9): p. 2378-2381.

[139] Briot, P., et al., *Effect of particle size on the reactivity of oxygen-adsorbed platinum supported on alumina.* Applied catalysis, 1990. **59**(1): p. 141-152.

[140] Thomas, J.M. and W.J. Thomas, *Principles and Practice of Heterogeneous Catalysis*. 1996: Wiley-VCH.

[141] Tsantilis, S., H.K. Kammler, and S.E. Pratsinis, *Population balance modeling of flame synthesis of titania nanoparticles.* Chemical Engineering Science, 2002. **57**(12): p. 2139-2156.

[142] Mueller, R., et al., *Growth of zirconia particles made by flame spray pyrolysis.* AIChE Journal, 2004. **50**(12): p. 3085-3094.

[143] Ishida, M. and H. Jin, *New advanced power-generation system using chemical-looping combustion.* Energy, 1994. **19**(4): p. 415-422.

[144] Ishida, M. and H. Jin, *A novel chemical-looping combustor without NOx formation.* Industrial and Engineering Chemistry Research, 1996. **35**(7): p. 2469-2472.

[145] Narayanan, R. and M.A. El-Sayed, *Shape-dependent Catalytic Activity of Platinum Nanoparticles in Colloidal Solution.* Nano Letters, 2004. **4**(7): p. 1343-1348.

[146] Post, M.F.M., et al., *Diffusion limitations in Fischer-Tropsch catalysts.* AIChE Journal, 1989. **35**(7): p. 1107-1114.

[147] Tanev, P.T., M. Chibwe, and T.J. Pinnavaia, *Titanium-containing mesoporous molecular sieves for catalytic oxidation of aromatic compounds.* Nature, 1994. **368**(6469): p. 321-323.

[148] Maschmeyer, T., et al., *Heterogeneous catalysts obtained by grafting metallocene complexes onto mesoporous silica.* Nature, 1995. **378**(6553): p. 159-162.

[149] Armelao, L., et al., *Synthesis and structural evolution of mesoporous silica-silver nanocomposites.* Nanotechnology, 2007. **18**(15).

[150] Zhao, D., et al., *Nonionic Triblock and Star Diblock Copolymer and Oligomeric Surfactant Syntheses of Highly Ordered, Hydrothermally Stable, Mesoporous Silica Structures.* J. Am. Chem. Soc., 1998. **120**(24): p. 6024-6036.

[151] Haruta, M., *Size- and support-dependency in the catalysis of gold.* Catalysis Today, 1997. **36**(1): p. 153-166.

[152] Costacurta, S., et al., *Hierarchical porosity components by infiltration of a ceramic foam.* Journal of the American Ceramic Society, 2007. **90**(7): p. 2172-2177.

[153] Danumah, C., et al., *Synthesis of macrostructured MCM-48 molecular sieves.* Microporous and Mesoporous Materials, 2001. **44-45**: p. 241-247.

[154] Kuang, D., T. Brezesinski, and B. Smarsly, *Hierarchical porous silica materials with a trimodal pore system using surfactant templates.* Journal of the American Chemical Society, 2004. **126**(34): p. 10534-10535.

[155] Sen, T., et al., *One-pot synthesis of hierarchically ordered porous-silica materials with three orders of length scale.* Angewandte Chemie - International Edition, 2003. **42**(38): p. 4649-4653.

[156] Heck, R.M., S. Gulati, and R.J. Farrauto, *The application of monoliths for gas phase catalytic reactions.* Chemical Engineering Journal, 2001. **82**(1-3): p. 149-156.

[157] Patcas, F.C., G.I. Garrido, and B. Kraushaar-Czarnetzki, *CO oxidation over structured carriers: A comparison of ceramic foams, honeycombs and beads.* Chemical Engineering Science, 2007. **62**(15): p. 3984-3990.

[158] Kiwi-Minsker, L., et al., *Glass fiber catalysts for total oxidation of CO and hydrocarbons in waste gases.* Catalysis Today, 1999. **54**(1): p. 39-46.

[159] Yuranov, I., et al., *Oscillatory behavior during CO oxidation over Pd supported on glass fibers: Experimental study and mathematical modeling.* Chemical Engineering Science, 2000. **55**(15): p. 2827-2833.

[160] Hoeller, V., et al., *Three-phase nitrobenzene hydrogenation over supported glass fiber catalysts: Reaction kinetics study.* Chemical Engineering and Technology, 2000. **23**(3): p. 251-255.

[161] Kiwi-Minsker, L., et al., *Pt and Pd supported on glass fibers as effective combustion catalysts.* Catalysis Today, 2000. **59**(1-2): p. 61-68.

[162] Hoeller, V., et al., *Fibrous structured catalytic beds for three-phase reaction engineering hydrodynamics study in staged bubble columns.* Catalysis Today, 2000. **60**(1): p. 51-56.

[163] Kiwi-Minsker, L., et al., *Supported glass fibers catalysts for novel multi-phase reactor design.* Chemical Engineering Science, 1999. **54**(21): p. 4785-4790.

[164] Louis, B., et al., *Synthesis of structured filamentous zeolite materials via ZSM-5 coatings of glass fibrous supports.* Catalysis Today, 2001. **69**(1-4): p. 365-370.

[165] *http://rsb.info.nih.gov/ij/ last accessed on 11/02/07*. [cited 11/02/2007]; Available from: http://rsb.info.nih.gov/ij/.

[166] Friedle, U. and G. Veser, *A counter-current heat-exchange reactor for high temperature partial oxidation reactions.* Chemical Engineering Science, 1999. **54**(10): p. 1325-1332.

[167] Vernon, P.D.F., et al., *Partial oxidation of methane to synthesis gas.* Catalysis Letters, 1990. **6**(2): p. 181-186.

[168] Huff, M., P.M. Torniainen, and L.D. Schmidt, *Partial oxidation of alkanes over noble metal coated monoliths.* Catalysis Today, 1994. **21**(1): p. 113-128.

[169] Horn, R., et al., *Methane catalytic partial oxidation on autothermal Rh and Pt foam catalysts: Oxidation and reforming zones, transport effects, and approach to thermodynamic equilibrium.* Journal of Catalysis, 2007. **249**(2): p. 380-393.

[170] Mallens, E.P.J., J.H.B.J. Hoebink, and G.B. Marin, *An investigation on the reaction mechanism for the partial oxidation of methane to synthesis gas over platinum.* Catalysis Letters, 1995. **33**(3-4): p. 291-304.

[171] Mallens, E.P.J., J.H.B.J. Hoebink, and G.B. Marin, *The reaction mechanism of the partial oxidation of methane to synthesis gas: A transient kinetic study over rhodium and a comparison with platinum.* Journal of Catalysis, 1997. **167**(1): p. 43-56.

[172] Sanders, T. and G. Veser, *In preparation.* In preparation, 2007.

[173] Agrios, A.G. and P. Pichat, *State of the art and perspectives on materials and applications of photocatalysis over TiO2.* Journal of Applied Electrochemistry, 2005. **35**(7-8): p. 655-663.

[174] O'Regan, B. and M. Gratzel, *A low-cost, high-efficiency solar cell based on dye-sensitized colloidal TiO2 films.* Nature, 1991. **353**(6346): p. 737-740.

[175] Gratzel, M., *Photoelectrochemical cells.* Nature, 2001. **414**(6861): p. 338-344.

[176] Vogel, R., K. Pohl, and H. Weller, *Sensitization of highly porous, polycrystalline TiO2 electrodes by quantum sized CdS.* Chemical Physics Letters, 1990. **174**(3-4): p. 241-246.

[177] Plass, R., et al., *Quantum Dot Sensitization of Organic-Inorganic Hybrid Solar Cells.* J. Phys. Chem. B, 2002. **106**(31): p. 7578-7580.

[178] Shen, Q., D. Arae, and T. Toyoda, *Photosensitization of nanostructured TiO2 with CdSe quantum dots: effects of microstructure and electron transport in TiO2 substrates.* Journal of Photochemistry and Photobiology A: Chemistry, 2004. **164**(1-3): p. 75-80.

[179] Vogel, R., P. Hoyer, and H. Weller, *Quantum-Sized PbS, CdS, Ag2S, Sb2S3, and Bi2S3 Particles as Sensitizers for Various Nanoporous Wide-Bandgap Semiconductors.* J. Phys. Chem., 1994. **98**(12): p. 3183-3188.

[180] Robel, I., et al., *Quantum Dot Solar Cells. Harvesting Light Energy with CdSe Nanocrystals Molecularly Linked to Mesoscopic TiO₂ Films.* J. Am. Chem. Soc., 2006. **128**(7): p. 2385-2393.

[181] Diguna, L.J., et al., *High efficiency of CdSe quantum-dot-sensitized Ti O2 inverse opal solar cells.* Applied Physics Letters, 2007. **91**(2).

[182] Leschkies, K.S., et al., *Photosensitization of ZnO Nanowires with CdSe Quantum Dots for Photovoltaic Devices.* Nano Lett., 2007. **7**(6): p. 1793-1798.

[183] Dabbousi, B.O., et al., *(CdSe)ZnS Core-Shell Quantum Dots: Synthesis and Characterization of a Size Series of Highly Luminescent Nanocrystallites.* J. Phys. Chem. B, 1997. **101**(46): p. 9463-9475.

[184] Hines, M.A. and P. Guyot-Sionnest, *Synthesis and Characterization of Strongly Luminescing ZnS-Capped CdSe Nanocrystals.* J. Phys. Chem., 1996. **100**(2): p. 468-471.

[185] Yuan, Z.H. and L.D. Zhang, *Synthesis, characterization and photocatalytic activity of ZnFe2O4/TiO2 nanocomposite.* Journal of Materials Chemistry, 2001. **11**(4): p. 1265-1268.

[186] Tang, H., et al., *Electrical and optical properties of TiO2 anatase thin films.* Journal of Applied Physics, 1994. **75**(4): p. 2042-2047.

[187] Anpo, M., et al., *Photocatalytic Reduction of CO2 with H2O on Titanium Oxides Anchored within Micropores of Zeolites: Effects of the Structure of the Active Sites and the Addition of Pt.* J. Phys. Chem. B, 1997. **101**(14): p. 2632-2636.

[188] Pathak, P., et al., *Improving photoreduction of CO2 with homogeneously dispersed nanoscale TiO2 catalysts.* Chemical Communications, 2004. **10**(10): p. 1234-1235.

[189] Saladin, F., L. Forss, and I. Kamber, *Photosynthesis of CH4 at a TiO2 Surface from Gaseous H2O and CO2.* J. Chem. Soc. Chem. Commun., 1995: p. 533-534.

[190] Wu, J.C.S., H.-M. Lin, and C.-L. Lai, *Photo reduction of CO2 to methanol using optical-fiber photoreactor.* Applied Catalysis A: General, 2005. **296**(2): p. 194-200.